Geometric Singular Perturbation Theory and Averaging: Analysing Torus Canards in Neural Models

Kerry-Lyn Roberts

A thesis presented in fulfillment
of the requirements for the degree of
Doctor of Philosophy

School of Mathematics and Statistics
Faculty of Science
University of Sydney

April 2018

Acknowledgments

It has been a long four and half years, with many highs an lows. I would not have completed this thesis without the help and support of many people.

To my fellow inmates in room 807: I'm sure I would have finished a lot earlier if it wasn't for you guys. But the PhD experience would have been far less enjoyable. Thank you all for the friendship, distraction, laughs, card games and all the extra weight I gained in shared Thai, Japanese, Korean and Vietnamese lunches!

To my friends and family outside university: Thank you for always supporting and believing in me, lending a listening ear, driving to McDonald's at 2am, and making me laugh so much that I forgot about the stresses of PhD life.

To the many academics who have helped me throughout my PhD: Thank you to Hinke Osinga, Bernd Krauskopf, Harry Dankowicz, and Mathieu Desroches for technical support and assistance. Thank you to my associate supervisor Robby Marangell. Thank you to Jonathan Rubin for a rewarding collaboration from which much of my thesis followed.

And finally, thank you to my supervisor Martin Wechselberger. Thank you so much for all the countless hours you devoted to meetings, listening to me complain (especially about AUTO), fine tuning and attending all my talks, reading and editing my drafts, and giving advice. I'm sure there were times when you wanted to hit me over the head with that (large) manilla folder full of my work, but thank you for being patient. Thank you for sparking my interest in dynamical systems and mathematical biology all those years ago in undergrad, it has been quite the journey and an absolute pleasure working with you!

Abstract

Neuronal bursting, an oscillatory pattern consisting of repeated spikes interspersed with periods of rest, is a pervasive phenomenon in brain function which is used to relay information between neurons and other cells in the body. Mathematical models of bursting typically take the form of singularly perturbed systems of ordinary differential equations, which are well suited to analysis by geometric singular perturbation theory (GSPT). There are numerous types of bursting models, which are classified by a slow/fast decomposition and identification of fast subsystem bifurcation structures. Of particular interest are so-called fold/fold-cycle bursters, where burst initiation and termination occurs at a fold of equilibria and fold of periodic orbits, respectively. Such bursting models permit torus canards, special solutions which track a repelling manifold of periodic orbits of the fast subsystem.

In this thesis we analyse two fold/fold-cycle bursters, the Wilson-Cowan-Izhikevich model and the Butera model. Using numerical averaging in combination with GSPT, we construct an averaged slow subsystem and identify the bifurcations corresponding to the transitions between bursting and spiking activity patterns. In both models we find that the transition involves toral folded singularities (TFS), the averaged counterparts of folded singularities. In the WCI model, we show that the transition occurs at a degenerate TFS, resulting in a torus canard explosion, reminiscent of the classic canard explosion in the van der Pol oscillator. The TFS identified in the Butera model are generic (i.e. occurring on open parameter intervals), and using numerical continuation methods, we continue them and construct averaged bifurcation diagrams. We identify three types of folded-saddle node (FSN) bifurcations which mediate the transition between various activity patterns: FSN type I, II, and III. Type I and II are common in neural applications and have been studied extensively; both possess canards and give rise to the delay phenomenon. On the other hand, type III is novel and studied here for the first time. In the final part of this thesis, we utilise the blow-up technique and dynamic bifurcation theory to extend current canard theory to the FSN III case.

Contents

Chapter 1

Introduction

Neuronal bursting, a pattern characterised by alternating periods of rapid spiking and rest, is an ubiquitous phenomenon via which neurons communicate and relay information to various parts of the body. As bursting is a multi-scale phenomenon, mathematical models typically take the form of slow/fast (or singularly perturbed) ordinary differential equations. Such multi-scale models can be decomposed into fast and slow subsystems, and classified based on the fast subsystem bifurcation structures. This thesis focuses on a particular type of bursting model, the *fold/fold-cycle* burster. Using techniques from averaging and geometric singular perturbation theory, we investigate special solutions of fold/fold-cycle bursters, known as *torus canards*, in various neural models.

1.1 Motivation: Neural Dynamics

Neurons are the basic signalling unit of the brain, and the average human brain consists of around 10^{11} neurons. The primary role of a neuron is to transmit information to other neurons, muscle and gland cells within the nervous system. Indeed, each neuron receives input from about $10,000$ other neurons. Networks of interconnected neurons work together to coordinate movement, modulate heart and breathing rhythms, control hormone production and much more.

A typical mammalian neuron consists of a cell body or soma, axon, and dendrites; see Figure 1.1. When stimulated past a threshold, neurons produce *action potentials* – electrical transmembrane currents which alter the membrane potential of the neuron. The electrical activity is caused by the movement of charged ions across the cell membrane via structures known as *ion channels*, proteins embedded in the membrane which create pores. The channels are ion selective, but some are permeable to more than one type of ion, which for example may share a common positive (or negative) charge. Ion channels are typically *gated*, and these gates open and close in response to various stimuli like membrane voltage, mechanical stress and ligand binding. Electrical signals or action potentials propagate down the length of a neuron's axon, to the branching axon terminals which form chemical synapses with other neurons. Many axons are covered with an insulating myelin sheath, which accelerates the propagation of electrical signals along the axon. Chemical synapses are the junction or contact points were the electrical signal of one neuron is transmitted via chemical
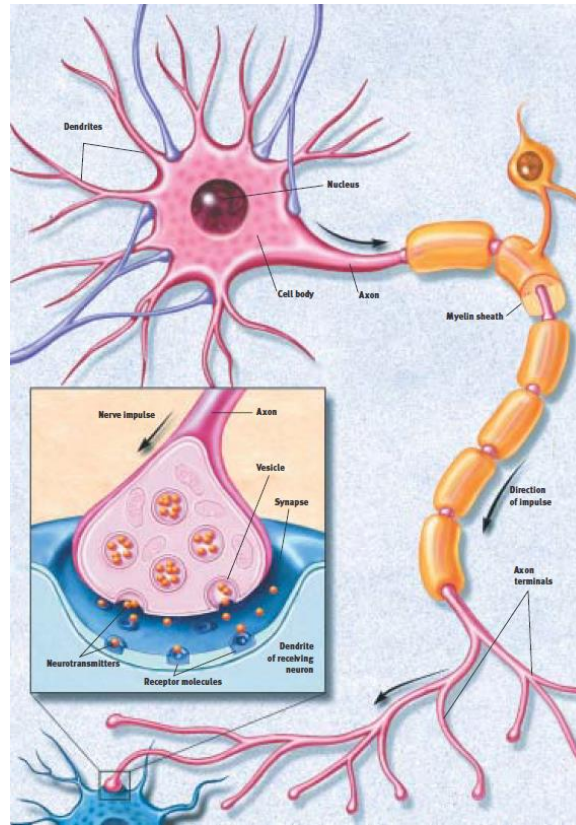
Figure 1.1: Structure of a neuron and synaptic transmission. Neurons typically receive stimulus from other neurons at the dendrites. Electrical signals then propagate down the axon to the terminals, which connect with neighbouring neuron's dendrites, forming a chemical synapse. There neurotransmitters are released which facilitate communication with other cells. Figure adapted from [57].

neurotransmitters to the dendrites of another receiving neuron. Once the action potential reaches the synapse of a sending neuron, it triggers the release of neurotransmitters. These chemical agents traverse the synaptic cleft (or gap) and bind to receptors on the receiving neuron. Typically, the binding of the neurotransmitter induces a synaptic current which may alter the membrane potential of the receiving neuron. This process facilitates the relay of information from one neuron to another.

The binding of neurotransmitters to a receiving neuron induces the opening/closing of specific gated ion channels, which in turn generates a flux of ions. This ion flux produces changes in the receiving neuron's membrane potential called *post synaptic potentials* (PSP). The strength of a PSP is proportional to the strength of the propagating action potential. Depending on the type of neurotransmitter, these PSP can be inhibitory (IPSP) or excitatory (EPSP). Significant EPSPs trigger the propagation of the action potential in the receiving neuron. Neurons which produce an action potential in response to stimuli are termed *excitable*, and the study of factors which affect the generation of such an action potential is known as *neural excitability*.

Neurons can exhibit a wide variety of electrical activity patterns which are useful in

2
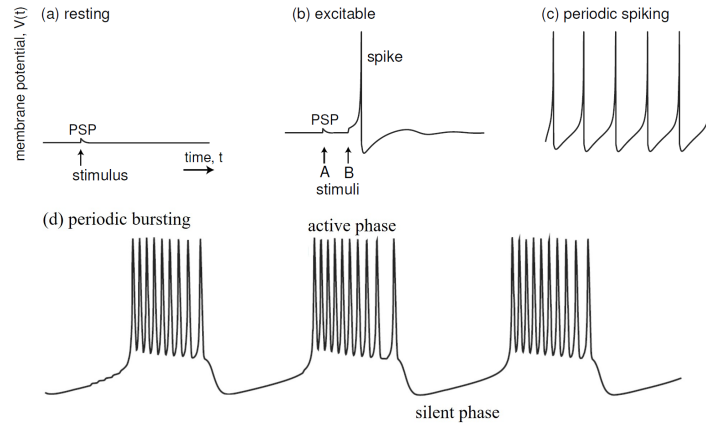
Figure 1.2: Resting, excitable, periodic spiking and periodic bursting activity patterns. The membrane potential is plotted on the y-axis versus time on the x-axis. Figure adapted from [55].

relaying information; see Figure 1.2. These patterns include:

- Quiescence or resting: the membrane potential is at rest, or exhibits small amplitude 'subthreshold' oscillations.

- Excitable: a single action potential (or series of action potentials) are generated in response to stimuli.

- Periodic spiking: the periodic firing of action potentials or *spikes*.

- Periodic bursting: periods of fast spiking (the *active phase*) interspersed with quiescence (the *silent phase*).

Most neurons are capable of bursting through stimulation or manipulation (for example, pharmacologically), however, others are intrinsically capable of bursting. Some well known examples of intrinsic bursters include cat primary visual cortical neurons [81], thalamic reticular neurons [97], cat thalamocortical relay neurons [73], mammalian respiratory neurons in the pre-Bötzinger complex [20], and trigeminal interneurons from the rat brainstem [27]. Typically, bursting occurs because of the interplay between fast and slow membrane currents. During the active phase of bursting, the intrinsic slow membrane currents build up and eventually hyperpolarise the cell, resulting in the termination of the active phase. In the silent phase, these currents slowly decay until the neuron has recovered and is ready to burst again.

1.2 Mathematical Modelling of Neuronal Dynamics

As bursting is ubiquitous in neuroscience, many mathematical models of the phenomenon have been developed. One method of obtaining bursting behaviour in neuronal models is via timescale separation. In other words, the models are singularly perturbed systems (of

3

ordinary differential equations) which take the the form

$$\begin{aligned}
\dot{x} &= \varepsilon g(x, z), \\
\dot{z} &= f(x, z),
\end{aligned} \tag{1.1}$$

where the small parameter ε creates a timescale separation. Much of this thesis focuses on analysing such systems. The vector $z \in \mathbb{R}^m$ models the fast variables which generate spiking during the active phase (for example, the membrane potential). The vector $x \in \mathbb{R}^n$ models the slow variables which are responsible for the slow modulation of the spiking behaviour. Slow/fast bursting models of the form (1.1) are well suited to analysis using geometric singular perturbation theory (GSPT).

The basic premise of GSPT is to dissect (1.1) into slow and fast subsystems, which are of lower dimension than the original model. Setting $\varepsilon = 0$ in (1.1) gives the *fast subsystem*

$$\dot{z} = f(x, z), \tag{1.2}$$

where the slow variables are treated as parameters. Many underlying mechanisms of bursting can be understood by analysing the fast subsystem (1.2) and treating $x \in \mathbb{R}^n$ as slowly varying bifurcation parameters. This method was pioneered by Rinzel [85] who grouped the variables such that there was only one slow variable. The transition from the active phase to the silent phase of bursting occurs as the slow variation of x drives the fast subsystem through bifurcations of equilibria and periodic orbits. Depending on the type of bifurcations, various kinds of bursting with distinctive qualitative features are possible.

1.3   Classification of Bursting Models

The classification of bursters according to fast system bifurcations was first suggested by Rinzel [86], who identified three kinds of bursters; later Bertram et al. [10] identified another. However, it was Izhikevich [54] who provided a comprehensive classification. Izhikevich classified bursting models according to codimension-one bifurcations of the fast subsystem (1.2), with respect to x, which were involved in the initiation and termination of the active phase. More specifically, bursters are qualitatively distinguished based on the following topology:

- Initiation: the bifurcation of the quiescent state (usually an equilibrium) that results in the transition to an oscillatory state (usually a periodic orbit).

- Termination: the bifurcation of the attracting oscillator which results in termination of the active phase and transition to quiescence.

The driving force behind bursting behaviour is bistability, i.e. the coexistence of quiescent and oscillatory states. Slow variation of x moves the fast subsystem through the bifurcations associated with initiation/termination of bursting. These bifurcations essentially 'kick' solutions from one attractor to another. When the quiescent state is an equilibrium and the oscillatory state is a limit cycle of the fast subsystem, the model is said to exhibit *point-cycle* bursting. Based on Izhikevich's classification scheme, there are 16 different types of point-cycle bursters for $m = 2$ (i.e. two fast variables), and 120 different types for $m > 2$. We refer the reader to [54, 55] for details concerning all the different bursting types.
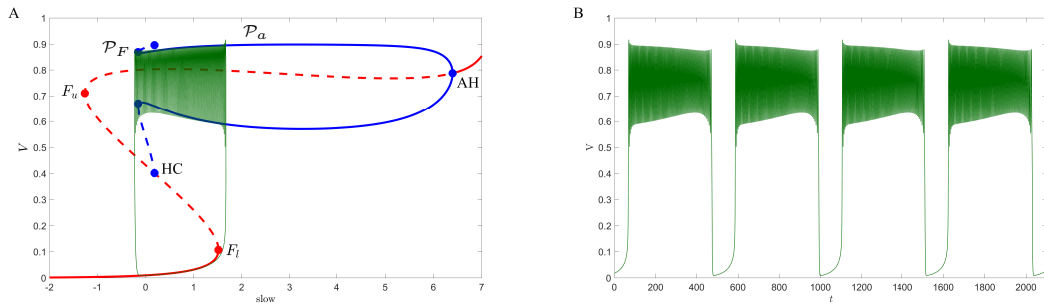
Figure 1.3: *A:* Bifurcation structure of the fast subsystem (with respect to the slow variable) of the WCI model. Plotted on the y-axis is one of the fast variables which represents the membrane potential V. Branches of equilibria are shown in red, while branches of periodic orbits are shown in blue. Solid lines denote stable branches and dashed lines denote unstable branches. A time trace of the full system (for $\varepsilon \neq 0$) is overlayed in green. Bursting is initiated at the saddle-node (fold) bifurcation F_l, where trajectories transition to the attracting family of periodic orbits $\mathcal{P}_a$. Termination of the active phase occurs at the fold of periodic orbits, labelled $\mathcal{P}_F$. The WCI model exhibits fold/fold cycle bursting. *B:* Time trace of the bursting trajectory.

This thesis focuses on the analysis of one particular type of point-cycle burster: the fold/fold-cycle burster. A classic example of a minimal fold/fold-cycle burster is the 2-fast/1-slow Wilson-Cowan-Izhikevich (WCI) model, which we will study in detail in Chapter 4. The fast subsystem bifurcation structure (with respect to the slow variable) of this model can be seen in Figure 1.3A. It is evident from this figure the fast subsystem exhibits the essential ingredient for bursting: bistability of an equilibrium and periodic attractor. The active phase of bursting is initiated at fold bifurcation of equilibria (labelled F_l). Bursting solutions in the silent phase (on the equilibrium attractor) 'fall off' near the fold and transition to the active phase (an attracting family of periodic orbits). The termination of the active phase occurs at a fold of periodic orbits (labelled $\mathcal{P}_F$) where trajectories 'jump off' and return to the equilibrium attractor. The fold of the family of periodic orbits in the fast subsystem creates a distinctive 'top-hat' appearance, and hence this type of bursting is sometimes referred to as 'top-hat bursting'.

One of the main goals in studying these bursting models from a slow/fast perspective is understanding the underlying dynamics in the quiescent and active phases, as well as the transition between the two, for non-zero ε. In the silent phase, the dynamics of the full system (for $\varepsilon \neq 0$) are well understood as a slow drift along the equilibrium attractor of the fast subsystem (1.2). As solutions approach the equilibrium fold bifurcation, they transition from a slow to a fast timescale (via an intermediate timescale), and 'jump' to the periodic attractor. Naturally, the jumping behaviour facilitates the transition between the quiescent and active phases; this phenomenon is well understood in the context of GSPT [64, 100]. During the active phase of bursting, solutions of the full system rapidly oscillate near the fast subsystem periodic attractor, but this fast motion is accompanied by a slow drift. Classical GSPT fails to quantify this slow drift in the active phase; to remedy this issue, other techniques must be used.
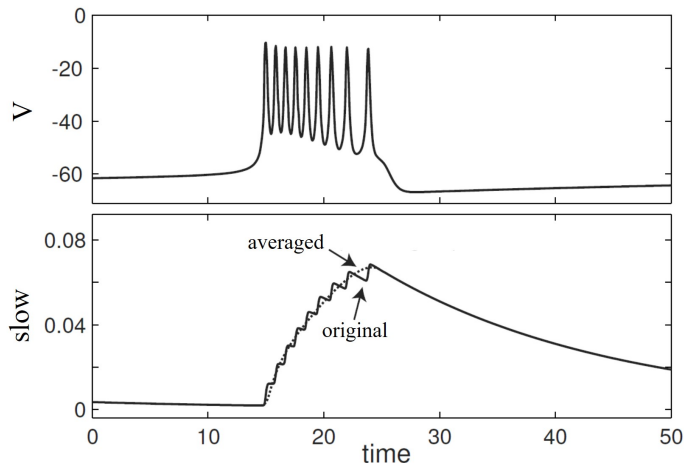
5

Figure 1.4: Time traces of a model burster (the $I_{NaP} + I_K + I_{K(M)}$ burster). The top panel shows the time trace of the membrane potential V. The bottom panel shows the time traces of the original slow variable (solid) compared to the averaged slow variable (dashed). Figure adapted from [55].

1.4 Averaging

How can we approximate the slow evolution of x during the active oscillatory phase of bursting? The averaging technique is powerful tool which can be used in conjunction with GSPT to address this question. In brief, the averaging procedure is carried out by integrating the slow equation in (1.1) over a periodic solution of the fast subsystem (1.2), yielding a new subsystem

$$\dot{X} = \frac{\varepsilon}{T(X)} \int_0^{T(X)} g(X, z) dt. \tag{1.3}$$

which is referred to as the *averaged slow subsystem*. Note that X distinguishes the averaged variable from the original variable x; the two are not equivalent. To be mathematically precise, averaging is carried out via a near-identity coordinate transformation, which transforms the original system (1.1) to (1.3). The use of averaging in ordinary differential equations (so-called *classical averaging*) dates back as far as the works of Laplace and Lagrange [71] on celestial mechanics. However, the theory of averaging in the context of singularly perturbed systems was developed in the 1960s by Pontryagin and Rodygin [83]. They proved that the slow motion $x(t)$ and the averaged slow motion $X(t)$ are $\mathcal{O}(\varepsilon)$ close under certain conditions. One caveat of Pontryagin and Rodygin's theory is the restriction to hyperbolic periodic orbits of the fast subsystem. From a GSPT point of view, Pontryagin and Rodygin's work is the periodic equivalent of Fenichel theory [40, 56], which explains the slow motion on hyperbolic equilibrium manifolds. Recent work [104] has made progress towards extending averaging theory to non-hyperbolic periodic orbits, such as a fold bifurcation of periodic orbits, which is an essential feature of a fold/fold-cycle burster.

Intuitively, the averaging procedure 'smooths out' the wiggling behaviour of the slow variables during the active oscillatory phase of bursting (see Figure 1.4). However, the averaged slow subsystem (1.3) provides an approximation to the slow x dynamics near the oscillatory attractor which responsible for spiking behaviour during the active phase of

bursting. From a GSPT point of view, it is more productive to think of averaging in this manner. Returning to Figure 1.3A, we see that during the active phase of bursting solutions move slowly left along the oscillatory attractor until they fall off near the fold (of periodics). Averaging allows us to quantify this slow motion which is essential in generating the bursting pattern. Mathematically speaking, hyperbolic equilibria of (1.3) correspond to hyperbolic periodic orbits (which have the same stability type) of the original system (1.1) [47]. In other words, stable equilibria of the averaged subsystem correspond to periodic spiking states of the full system. Similar conclusions also extend to more complicated hyperbolic attractors. Periodic bursting typically corresponds to the absence of (stable) averaged equilibria, and thus the averaged slow subsystem is a useful tool in distinguishing periodic bursting and spiking. Like the fast subsystem, the averaged slow subsystem reduces the complexity of the original system (in this case the slow dynamics) and aids our understanding of the underlying dynamic mechanisms that govern bursting.

1.5   Canard Theory

Associated with GSPT is *canard theory*, the study of *canards* which are special solutions of singularly perturbed systems that connect attracting and repelling invariant manifolds. These curious creatures were first discovered by a group of French mathematicians [7] in their study of the van der Pol oscillator [103] with constant forcing. The etymology of 'canard' will become apparent when we investigate the van der Pol oscillator in Section 2.7.1. Historically, canards have been studied using various methods such as non-standard techniques [7, 33], matched asymptotics [38, 75] and GSPT [37, 65]. This thesis focuses on analysing canards and their properties from a GSPT standpoint.

Seemingly counter-intuitively, canards typically track a repelling invariant manifold for a significant amount of time. In the case of 'classical canard theory', these invariant manifolds involve equilibria. Canards can act as separatrices and organise the dynamics in phase space. They often generate rich and complex behaviour in neural models, and many other applications. Recent studies of neural models [60, 18] and other singularly perturbed systems have identified a new flavour of canards, so-called *torus canards*, solutions which instead drift across a fold of periodics, connecting attracting and repelling manifolds of periodic orbits. Efforts to extend well-known results of 'classical' canard theory to torus canards are ongoing [104]. Some progress has been made via extension of the averaging technique to non-hyperbolic folds of periodic orbits. This is exactly the type bifurcation involved in the termination of bursting for fold/fold-cycle bursters, and they are the perfect candidates for torus canards. Much of this thesis focuses on identifying torus canards in two particular neural models, the Wilson-Cowan-Izhikevich model and the Butera model, a model of two coupled respiratory neurons. In these models, torus canards facilitate the transition from bursting to spiking (via a *torus canard explosion*), and this thesis aims to unravel the associated complex dynamics through a combination of GSPT and numerical averaging.

Closely related to canards are *folded singularities*, degenerate fold bifurcations of the fast subsystem which allow canards to cross between attracting and repelling manifolds [99, 111]. The averaged counter parts of folded singularities are called *toral folded singularities*, and their dynamics have been formally analysed in systems with two fast variables [104]. Using a

numerical continuation approach, we identify toral folded singularities in the Butera model, which has more than two fast variables. The numerical detection of toral folded singularities in higher dimensional models is an important (and novel) procedure. Furthermore, we numerically implement the averaged slow subsystem of both the Butera and WCI model. This allows for the detection and crucially the continuation of averaged equilibria, another important extension of current numerical averaging techniques. As a result, we are able to construct bifurcation diagrams of the averaged slow subsystem which elucidates the genesis of various activity patterns and the transition between them.

Bifurcations involving fold singularities are known as *folded saddle-node* (FSN) bifurcations and they come in three types. The FSN type I and II are common in neural models and have already been analysed in detail [66, 108]. Our study of the Butera model lead to the discovery of the novel FSN III bifurcation in the context of the averaged slow subsystem. Another main objective of this thesis is to extend the results of the FSN I and II to the FSN III case. In particular, we prove the existence of canards and faux canards, show that there is delayed loss of stability due to the slow passage through an Andronov-Hopf bifurcation, and provide maximal delay estimates.

1.6 Outline

The remainder of this thesis is outlined as follows: In Chapter 2, we introduce GSPT, the mathematical framework used to analyse singularly perturbed systems. In particular, we provide a complete description of the pertinent results from canard theory. In Chapter 3, we provide an overview of the mathematical tools related to periodic solutions. We review Floquet's main theorems on linearised periodic systems and the stability properties of their solutions. We summarise averaging theory from a classical and singularly perturbed standpoint. Finally, we describe in detail the numerical implementation of averaging in slow/fast systems.

In Chapter 4, we pressent a study of a minimal bursting model, the Wilson-Cowan-Izhikevich model. We provide a brief analysis of the reduced and layer problems. We numerically implement the averaged reduced system and construct an averaged bifurcation diagram. Our analysis shows that the transition from bursting to spiking occurs via a torus canard explosion. In Chapter 5, we proceed with a study of the Butera model. We present a bifurcation analysis of the full system and the averaged reduced system. The latter provides new insights into the genesis of the different kinds of bursting and spiking patterns observed, as well as the transitions. Analysis of the averaged reduced problem reveals the novel FSN III bifurcation, as well as a higher codimension bifurcation, an organising centre, which dictates the dynamics of the model. In Chapter 6, we analyse a canonical model of the organising centre observed in our study of the Butera model. It encapsulates all the required structures and bifurcations and supports the numerical results of Chapter 5. In Chapter 7, we consider a canonical model of the FSN III bifurcation and analyse the local dynamics. Using a combination of the blow-up technique and complex time path analysis, we prove the existence of canards and faux canards. Using the way-in/way-out function, we quantify the delay phenomenon and provide maximal delay estimates. We conclude with a discussion and outline of future work in Chapter 8.

Chapter 2

Geometric Singular Perturbation Theory

Many physiological phenomena evolve over multiple timescales. For example, when neurons are stimulated past a threshold, ion channels open and there is a rapid inflow of positively charged ions that generates a spike in the membrane potential. This also triggers the slow closing of the ion channels (and the opening of other channels) which results in a rapid decrease of the membrane potential. This is followed by a slow refractory period where the neuron's membrane potential returns to a resting state. The sequence of fast and slow events described above constitutes the well known action potential. Naturally, the mathematical models of such multiscale phenomena, such as the famous Hodgkin-Huxley model, are singularly perturbed. The collection of mathematical tools used to dissect and analyse these models from a geometric standpoint, is known as *geometric singular perturbation theory* (GSPT).

Chapter 2 of this thesis is devoted to reviewing this important mathematical tool. In Section 2.1 we introduce Fenichel theory and state the main theorems. Fenichel theory breaks down at points along the critical manifold where normal hyperbolicity is lost. This occurs at generic fold points, which we discuss in Section 2.2. In Sections 2.3 and 2.4.1, we examine special structures which may occur at the fold, known folded singularities, and the resulting singular canards. Given its pervasive use in extending GSPT to nonhyperbolic points, we provide an outline of the blow-up technique in Section 2.5. In Section 2.6, we state the results for a regular fold. Finally, in Section 2.7 we present a summary of canard theory for folded singularities and folded saddle-nodes.

2.1 Fenichel Theory

This thesis is concerned with singularly perturbed systems of ordinary differential equations which take the form

$$\begin{aligned}
\dot{x} &= g(x, z, \varepsilon), \\
\varepsilon \dot{z} &= f(x, z, \varepsilon),
\end{aligned} \tag{2.1}$$

where $(x, z) \in \mathbb{R}^n \times \mathbb{R}^m$, and the functions f, $g : \mathbb{R}^n \times \mathbb{R}^m \times \mathbb{R} \to \mathbb{R}^m$ are sufficiently smooth. The variables x and z are considered slow and fast, respectively, and $0 < \varepsilon \ll 1$ is a small

parameter which induces the time scale separation between the variables. The overdot in (2.1) denotes differentiation with respect to 'slow time' τ, and hence we refer to (2.1) as the slow system. The time rescaling $\tau = \varepsilon t$ leads to the fast system

$$
\begin{aligned}
x' &= \varepsilon g(x, z, \varepsilon), \\
z' &= f(x, z, \varepsilon),
\end{aligned} \tag{2.2}
$$

where the prime denotes differentiation with respect to the 'fast time' t. When $\varepsilon \neq 0$, systems (2.1) and (2.2) are equivalent, and differ only in the speed that orbits are traversed. Solutions of systems (2.1) and (2.2) consist of a mixture of slow and fast behaviour which cannot be approximated in a single limit. The slow and fast behaviour may be approximated by taking the so-called *singular limit* $\varepsilon \to 0$ of the slow (2.1) and fast (2.2) systems, respectively. Taking the singular limit in (2.2), yields the m-dimensional *layer problem*

$$
\begin{aligned}
x' &= 0, \\
z' &= f(x, z, 0),
\end{aligned} \tag{2.3}
$$

where the slow variables act as parameters. The layer problem approximates (2.2) by allowing the fast variables to evolve independently of the slow variables, which are assumed to evolve so slowly that they are treated as parameters. Alternatively, taking the singular limit in (2.1) gives the n-dimensional differential-algebraic system

$$
\begin{aligned}
\dot{x} &= g(x, z, 0), \\
0 &= f(x, z, 0),
\end{aligned} \tag{2.4}
$$

known as the *reduced problem*, where the flow is restricted to the so-called *critical manifold* $f = 0$.

Definition 2.1 (Critical Manifold). The *critical manifold* is defined as the set of equilibria of the layer problem

$$
\mathcal{S} := \{(x, z) \in \mathbb{R}^n \times \mathbb{R}^m : f(x, z, 0) = 0\}. \tag{2.5}
$$

The reduced problem approximates (2.1) by allowing the slow variables to evolve while assuming that the fast variables evolve so rapidly that they instantaneously equilibrate to $\mathcal{S}$. Notice that the flow on $\mathcal{S}$ in the layer problem (2.3) is trivial, while the flow away from $\mathcal{S}$ is undefined in the reduced system (2.4). The critical manifold is an important geometric structure as it acts as an interface between the fast and slow dynamics of (2.3) and (2.4). The goal of *geometric singular perturbation theory* (GSPT) [40, 56] is to consolidate the slow and fast dynamics of the lower dimensional sub-systems (2.3) and (2.4), and thus elucidate the dynamics of the full $(m + n)$-dimensional system for $\varepsilon > 0$.

2.1.1 The layer problem

In general, the critical manifold $\mathcal{S}$ defines an n-dimensional manifold, i.e. the Jacobian $D_{(x,z)}f|_{\mathcal{S}}$ has full rank. Since we assume that f is sufficiently smooth, $\mathcal{S}$ is a differentiable manifold. The critical manifold is one of the most important objects in any GSPT analysis, and singularly perturbed systems are classified based on the properties of $\mathcal{S}$.

Definition 2.2 (Normal hyperbolicity)**.** A subset of the critical manifold $\mathcal{S}_h \subseteq \mathcal{S}$ is *normally hyperbolic* if all the eigenvalues of the Jacobian $D_z f|_{\mathcal{S}_h}$ have non-zero real part, i.e. all equilibria $(x, z) \in \mathcal{S}_h$ of the layer problem (2.3) are hyperbolic. Normally hyperbolic subsets of $\mathcal{S}_h$ are further classified based on their stability properties:

(i) $\mathcal{S}_a \subseteq \mathcal{S}_h$ is *attracting* if all eigenvalues of $D_z f|_{\mathcal{S}_a}$ have negative real part,

(ii) $\mathcal{S}_r \subseteq \mathcal{S}_h$ is *repelling* if all eigenvalues of $D_z f|_{\mathcal{S}_r}$ have positive real part,

(iii) $\mathcal{S}_s \subseteq \mathcal{S}_h$ is of *saddle type* if it is neither attracting or repelling.

For normally hyperbolic manifolds $\mathcal{S}_h$, there exists a uniform splitting of the the eigenvalues of $D_z f|_{\mathcal{S}_h}$. For each $p \in \mathcal{S}_h$, there are m_s eigenvalues with negative real part such that m_u eigenvalues with positive real part and $m_s + m_u = m$. This naturally leads to the definition of local stable and unstable manifolds of $\mathcal{S}_h$.

Definition 2.3. The *local stable and unstable manifolds* of $\mathcal{S}_h$, denoted by $W^s_{loc}(\mathcal{S}_h)$ and $W^u_{loc}(\mathcal{S}_h)$ respectively, are given by the unions

$$W^s_{loc}(\mathcal{S}_h) = \bigcup_{p \in \mathcal{S}_h} W^s_{loc}(p), \qquad W^u_{loc}(\mathcal{S}_h) = \bigcup_{p \in \mathcal{S}_h} W^u_{loc}(p). \tag{2.6}$$

The locally invariant manifolds $W^s_{loc}(p)$ and $W^s_{loc}(p)$ are known as *fast fibers* with *base point* $p \in \mathcal{S}_h$. The family of fast fibers form a *fibration* or *foliation* of $W^s_{loc}(\mathcal{S}_h)$ and $W^u_{loc}(\mathcal{S}_h)$, emanating from $\mathcal{S}_h$, where $\dim W^s_{loc}(\mathcal{S}_h) = n + m_s$ and $\dim W^u_{loc}(\mathcal{S}_h) = n + m_u$.

For singularly perturbed problems with normally hyperbolic critical manifolds, *Fenichel theory* [40, 56] provides the fundamental tools necessary to analyse such systems from a geometric standpoint. Before stating the theorems we define the Hausdorff distance.

Definition 2.4. The *Hausdorff distance* between two non-empty sets $V, W \subset \mathbb{R}^{m+n}$ is defined by

$$d_H(V, W) = \max \left\{ \sup_{v \in V} \inf_{w \in W} \|v - w\|, \sup_{w \in W} \inf_{v \in V} \|v - w\| \right\}$$

Fenichel's first theorem guarantees the persistence of normally hyperbolic manifolds, and their corresponding local stable and unstable manifolds, for sufficiently small $\varepsilon > 0$.

Theorem 2.1 (Fenichel's Theorem 1 [40, 56])**.** *Suppose that $\mathcal{S}_h$ is a compact normally hyperbolic critical manifold, possibly with boundary, of system (2.1). Assume that $f, g \in C^r$, for $1 \leq r < \infty$. Then for sufficiently small $\varepsilon > 0$, the following holds:*

(i) *There exists a C^r-smooth, locally invariant slow manifold $\mathcal{S}_h^\varepsilon$ that is diffeomorphic to $\mathcal{S}_h$.*

(ii) *The slow manifold $\mathcal{S}_h^\varepsilon$ has a Hausdorff distance $\mathcal{O}(\varepsilon)$ from $\mathcal{S}_h$.*

(iii) *$\mathcal{S}_h^\varepsilon$ is not usually unique, but all representations of the manifold lie at a Hausdorff distance $\mathcal{O}(e^{-K/\varepsilon})$ away from each other for some $K > 0$.*

(iv) *There exist C^r-smooth, locally invariant stable and unstable manifolds of $\mathcal{S}_h^{\varepsilon}$*

$$W_{loc}^s(\mathcal{S}_h^{\varepsilon}) = \bigcup_{p^{\varepsilon} \in \mathcal{S}_h^{\varepsilon}} W_{loc}^s(p^{\varepsilon}), \qquad W_{loc}^u(\mathcal{S}_h^{\varepsilon}) = \bigcup_{p^{\varepsilon} \in \mathcal{S}_h^{\varepsilon}} W_{loc}^u(p^{\varepsilon}), \tag{2.7}$$

that are $\mathcal{O}(\varepsilon)$ close (in terms of the Hausdorff distance) and diffeomorphic to $W_{loc}^s(\mathcal{S}_h)$ and $W_{loc}^u(\mathcal{S}_h)$ respectively.

2.1.2 The reduced problem

The layer problem (2.3) provides an approximation of the fast flow toward/away from the critical manifold $\mathcal{S}$, but at the price of trivial dynamics on $\mathcal{S}$. We now turn our attention to the reduced problem (2.4), from which we can approximate the slow flow on $\mathcal{S}$. Conversely, the trade-off is that now the flow is undefined away from $\mathcal{S}$.

Recall that for normally hyperbolic critical manifolds $\mathcal{S}_h$, the Jacobian $D_z f|_{\mathcal{S}_h}$ is nonsingular. Thus the implicit function theorem implies that $f(x, z, 0) = 0$ has a local graph representation $z = h(x)$, such that $f(x, h(x), 0) = 0$. This means that $\mathcal{S}_h$ can be represented over a single coordinate chart given by the slow variable base $x \in \mathbb{R}^n$. Then the reduced flow (2.4) on $\mathcal{S}_h$ is given by

$$\dot{x} = g(x, h(x), 0). \tag{2.8}$$

Remark 2.1. A coordinate chart on an n-dimensional manifold $\mathcal{S} \in \mathbb{R}^{n+m}$ is given by the pair (U, φ), where U is an open set of $\mathcal{S}$, and $\varphi : U \to V$ is a diffeomorphism from U to the open set $V = \varphi(U) \subset \mathbb{R}^n$. In other words, the n-dimensional manifold $\mathcal{S}$ is locally diffeomorphic to the Euclidean space of dimension n.

Fenichel's second theorem guarantees the persistence of a slow vector field on the slow manifold $\mathcal{S}_h^{\varepsilon}$ that is close (in a limiting sense) to the reduced vector field on $\mathcal{S}_h$.

Theorem 2.2 (Fenichel's Theorem 2 [40, 56])**.** *Suppose that $\mathcal{S}_h$ is a compact normally hyperbolic critical manifold, possibly with boundary, of system (2.1). Assume that $f, g \in C^r$, for $1 \le r < \infty$. Then for sufficiently small $\varepsilon > 0$, the following holds:*

(i) *The slow vector field on $\mathcal{S}_h^{\varepsilon}$ converges to the reduced vector field on $\mathcal{S}_h$ as $\varepsilon \to 0$.*

Since $\mathcal{S}_h$ has a local graph representation $z = h(x)$, it follows from Theorem 2.1 that $\mathcal{S}_h^{\varepsilon}$ also has a graph representation $z^{\varepsilon} = h(x, \varepsilon)$, for sufficiently small $\varepsilon > 0$. Thus the slow flow on $\mathcal{S}_h^{\varepsilon}$ is given by

$$\dot{x} = g(x, h(x, \varepsilon), \varepsilon). \tag{2.9}$$

In other words, for normally hyperbolic critical manifolds, we can reduce our singularly perturbed problem to a regularly perturbed problem on $\mathcal{S}_h^{\varepsilon}$. Thus we have the following corollary:

Corollary 2.1. Hyperbolic equilibria of the reduced problem (2.4) persist as hyperbolic equilibria of full system (2.1) for sufficiently small $\varepsilon > 0$.

For $\varepsilon > 0$, the evolution of the base points $p^\varepsilon \in \mathcal{S}_h^\varepsilon$ of the fast fibres $W_{loc}^s(p^\varepsilon)$ and $W_{loc}^u(p^\varepsilon)$ is governed by (2.9). Thus the individual fast fibres are not invariant under the flow of (2.1). However, the families of fast fibres $W_{loc}^s(\mathcal{S}_h^\varepsilon)$ and $W_{loc}^u(\mathcal{S}_h^\varepsilon)$ are invariant in following way:

Theorem 2.3 (Fenichel's Theorem 3 [40, 56]). *Suppose that $\mathcal{S}_h$ is a compact normally hyperbolic critical manifold, possibly with boundary, of system (2.1). Assume that $f, g \in C^r$, for $1 \le r < \infty$. Let $\cdot t$ denote the solution operator of (2.1). Then for sufficiently small $\varepsilon > 0$, the following holds:*

(i) *The foliation $\{W_{loc}^s(p^\varepsilon) : p^\varepsilon \in \mathcal{S}_h^\varepsilon\}$ is positively invariant i.e.*

$$W_{loc}^s(p^\varepsilon) \cdot t \subset W_{loc}^s(p^\varepsilon \cdot t),$$

for all $t \ge 0$ such that $p^\varepsilon \cdot t \in \mathcal{S}_h^\varepsilon$.

(ii) *The foliation $\{W_{loc}^u(p^\varepsilon) : p^\varepsilon \in \mathcal{S}_h^\varepsilon\}$ is negatively invariant i.e.*

$$W_{loc}^u(p^\varepsilon) \cdot t \subset W_{loc}^u(p^\varepsilon \cdot t),$$

for all $t \le 0$ such that $p^\varepsilon \cdot t \in \mathcal{S}_h^\varepsilon$.

Theorem 2.3 implies that a trajectory in the stable manifold $W_{loc}^s(\mathcal{S}_h^\varepsilon)$ decays exponentially towards its base point $p^\varepsilon \in \mathcal{S}_h^\varepsilon$, and this decay is inherited from the unperturbed case. The same is true for a trajectory in the unstable manifold $W_{loc}^u(\mathcal{S}_h^\varepsilon)$, except in backward time. Finally, we have the following corollary:

Corollary 2.2 ([40, 56]). Let $\alpha_s < 0$ be an upper bound for the real part of the stable eigenvalues of the critical manifold $\mathcal{S}_h$. Then there exists a constant $\kappa_s > 0$ such that, if $p^\varepsilon \in \mathcal{S}_h^\varepsilon$ and $q^\varepsilon \in W_{loc}^s(p^\varepsilon)$, then

$$||q^\varepsilon \cdot t - p^\varepsilon \cdot t|| \le \kappa_s \exp(\alpha_s t),$$

for all $t \ge 0$, such that $p^\varepsilon \cdot t \in \mathcal{S}_h^\varepsilon$.

Similarly, let $\alpha_u > 0$ be an upper bound for the real part of the unstable eigenvalues of the critical manifold $\mathcal{S}_h$. Then there exists a constant $\kappa_u > 0$ such that, if $p^\varepsilon \in \mathcal{S}_h^\varepsilon$ and $q^\varepsilon \in W_{loc}^u(p^\varepsilon)$, then

$$||q^\varepsilon \cdot t - p^\varepsilon \cdot t|| \le \kappa_u \exp(\alpha_u t),$$

for all $t \le 0$, such that $p^\varepsilon \cdot t \in \mathcal{S}_h^\varepsilon$.

When the critical manifold is a normally hyperbolic attracting manifold, i.e. $\mathcal{S}_h = \mathcal{S}_a$, Fenichel theory implies that after an initial transient time, the dynamics of (2.1) are completely described by the slow dynamics on the n-dimensional slow manifold $\mathcal{S}_h^\varepsilon$, which to leading order may be approximated by the reduced flow on $\mathcal{S}_a$. Note that the $\mathcal{S}_h = \mathcal{S}_a$ case was originally dealt with by Tikhonov [102], without the geometric context and the corresponding existence theory.

In summary, Fenichel theory guarantees that normally hyperbolic segments of the critical manifold, i.e. normally hyperbolic manifolds of equilibria of the layer problem (2.3), persist as locally invariant slow manifolds $\mathcal{S}_h^\varepsilon$ of the full problem (2.1) for sufficiently small $\varepsilon > 0$. Furthermore, the slow vector field on $\mathcal{S}_h^\varepsilon$ is an $\mathcal{O}(\varepsilon)$ smooth perturbation of the reduced vector field (2.4).

2.2   Folded Critical Manifolds

For normally hyperbolic critical manifolds, Fenichel theory provides a fairly complete picture of the dynamics of the full system. However, Fenichel theory breaks down at points along $\mathcal{S}$ where normal hyperbolicity fails, i.e. where $D_z f|_{\mathcal{S}}$ has at least one eigenvalue with zero real part. These points correspond to bifurcations of the layer problem (2.3) under variation of the parameter x.

Common examples of loss of normal hyperbolicity include fold or saddle-node bifurcations [64, 65, 99, 100, 110], Andronov-Hopf bifurcations [51, 79, 80], as well as points of self-intersection of $\mathcal{S}$ [63]. These non-hyperbolic regions can generate interesting dynamics.

Definition 2.5. The n-dimensional critical manifold $\mathcal{S}$ is *locally folded* if there exists an $(n-1)$-dimensional manifold $\mathcal{F} \subset \mathcal{S}$ defined by

$$\mathcal{F} := \{(x,z) \in \mathcal{S} \mid \operatorname{rank}(D_z f)(x,z,0) = m-1, \tag{2.10}$$

$$l \cdot [D_{zz}^2 f(x,z,0)(r,r)] \neq 0,\, l \cdot [(D_x f)(x,z,0)] \neq 0\}, \tag{2.11}$$

where l and r are the left and right nullvectors of the Jacobian $(D_z f)(x,z,0)$, respectively. The set $\mathcal{F}$ is the set of *fold points* of the critical manifold, i.e. the set of saddle-node bifurcations of the layer problem. The first condition (2.10) defines a bifurcation of the layer problem; the last two conditions (2.11) involving the left and right nullvectors define the saddle-node bifurcation which is interpreted geometrically as a fold.

Remark 2.2. The expression $(D_{zz}^2 f)(x,z,0)(r,r)$ is a *symmetric multilinear vector function* [70] such that

$$l \cdot [(D_{zz}^2 f)(x,z,0)(r,r)] = \sum_{i=1}^{m} l_i \sum_{j=1}^{m} \sum_{k=1}^{m} \frac{\partial^2 f_i}{\partial z_j \partial z_k} r_j r_k. \tag{2.12}$$

For a single fast variable ($m=1$), the set of fold points is simply

$$\mathcal{F} := \{(x,z) \in \mathcal{S} \mid f_z(x,z,0) = 0,\, f_{zz}(x,z,0) \neq 0,\, l \cdot [(D_x f)(x,z,0)] \neq 0\}. \tag{2.13}$$

The reduced problem (2.4) describes the slow flow restricted to the critical manifold $\mathcal{S}$, which necessarily lies in the tangent bundle $T\mathcal{S}$ of $\mathcal{S}$. The total time derivative of the algebraic constraint $f(x,z,0) = 0$ is given by

$$D_x f \cdot \dot{x} + D_z f \cdot \dot{z} = 0,$$

which provides the definition of a tangent vector $(\dot{x}, \dot{z})$ of an integral curve $(x(t), z(t))$ constrained to the tangent bundle $T\mathcal{S}$. Thus the reduced problem can be recast in the following form:

$$\dot{x} = g(x,z,0),$$
$$-D_z f \cdot \dot{z} = D_x f \cdot g(x,z,0), \tag{2.14}$$

where $(x,z) \in \mathcal{S}$. For normally hyperbolic segments of $\mathcal{S}$, the Jacobian matrix $D_z f$ is non-singular, i.e. $\det(D_z f) \neq 0$. Thus the inverse $(D_z f)^{-1}$ exists and is well defined for $(x,z) \in \mathcal{S}_h$. Applying $(D_z f)^{-1}$ to both sides of the equation for $\dot{z}$ in (2.14) gives

$$\dot{x} = g(x,z,0),$$
$$\dot{z} = -(D_z f)^{-1} \cdot D_x f \cdot g(x,z,0), \tag{2.15}$$

where $(x, z) \in \mathcal{S}_h$. System (2.15) can then be represented in any local coordinate chart.

In a neighbourhood of the fold $\mathcal{F}$, the Jacobian $D_z f$ is singular and the inverse $(D_z f)^{-1}$ does not exist. In such cases we cannot write the reduced problem in the form of (2.15). Instead, we employ the classical adjoint (or adjugate) of $D_z f$, which exists and is well defined along $\mathcal{F}$. The adjoint of a matrix A, denoted by $\mathrm{adj}(A)$, is defined as the transpose of the cofactor matrix of A, i.e.

$$\mathrm{adj}(A) \cdot A = A \cdot \mathrm{adj}(A) = \det(A) \cdot I.$$

Remark 2.3. The adjoint of any square matrix A is well defined when A has full rank and when A is rank one deficient. If A has full rank, then so does $\mathrm{adj}(A)$. If A is rank one deficient, then the rows of $\mathrm{adj}(A)$ are either the left nullvectors of A or the zero vector. Similarly, the columns of $\mathrm{adj}(A)$ consist of either right nullvectors or the zero vector. In other words, $\mathrm{adj}(A)$ is rank one. When $m = 1$, $A = \det(A)$ is a scalar and $\mathrm{adj}(A) = 1$.

By applying $\mathrm{adj}(D_z f)$ to both sides of the second equation in (2.14), the reduced problem can be written as

$$\begin{aligned}
\dot{x} &= g(x, z, 0), \\
-\det(D_z f) \cdot \dot{z} &= \mathrm{adj}(D_z f) \cdot D_x f \cdot g(x, z, 0).
\end{aligned} \tag{2.16}$$

Note that along $\mathcal{F}$ we have $\det(D_z f) = 0$ and system (2.16) is necessarily singular, which generically leads to a finite time blow-up. This is problematic as we want to understand the reduced dynamics in a neighbourhood of $\mathcal{F}$. The singularity along $\mathcal{F}$ can be avoided by applying the space-dependant rescaling $d\tau = -\det(D_z f) d\bar{\tau}$ to (2.16), which gives

$$\begin{aligned}
\dot{x} &= -\det(D_z f) g(x, z, 0), \\
\dot{z} &= \mathrm{adj}(D_z f) \cdot D_x f \cdot g(x, z, 0),
\end{aligned} \tag{2.17}$$

where the overdot now denotes differentiation with respect to $\bar{\tau}$. System (2.17) is known as the *desingularised reduced problem*. Notice that in regions of phase space (i.e. $\mathcal{S}$) where $\det(D_z f) > 0$, the direction of the flow in the desingularised problem (2.17) must be reversed to maintain consistency with the reduced flow (2.16). Otherwise, systems (2.16) and (2.17) are topologically equivalent.

2.3 Singularities of the Reduced Problem

With the goal of studying the reduced dynamics near $\mathcal{F}$ in mind, we define the different types of singularities of the desingularised system:

Definition 2.6. The set of *regular singularities* of (2.17) is given by

$$\mathcal{E} := \{(x, z) \in \mathcal{S} \setminus \mathcal{F} : g(x, z, 0) = 0\}. \tag{2.18}$$

Definition 2.7. The set of *regular fold points* $p \in \mathcal{F}$ of (2.17) satisfy the *transversality condition* (or *normal switching condition*)

$$\mathrm{adj}(D_z f) \cdot D_x f \cdot g \neq 0. \tag{2.19}$$

Definition 2.8. The set of *folded singularities* of (2.17) is given by

$$\mathcal{M} := \{(x, z) \in \mathcal{F} : \text{adj}(D_z f) \cdot D_x f \cdot g(x, z, 0) = 0\}. \tag{2.20}$$

In other words, folded singularities violate the transversality condition (2.19).

Generically, ordinary singularities form equilibria of both the reduced and desingularised systems. In contrast, folded singularities are equilibria of the desingularised system, but not of the reduced system. Instead they are points where both the left and right-hands sides of the $\dot{z}$-equation in (2.16) are zero, and a simple cancellation of zeros can occur. As a result, the reduced flow may cross the fold (via the folded singularity) in finite time. Thus folded singularities facilitate the movement of trajectories from one sheet of the critical manifold to another of differing stability type. This unique behaviour leads us to the definition of canards:

Definition 2.9 (Singular canards and canard Point)**.** Trajectories of the reduced problem (2.16) that move from the attracting sheet $\mathcal{S}_a$, across $\mathcal{F}$ via a folded singularity, and onto the repelling sheet $\mathcal{S}_r$ of the critical manifold, are known as *singular canards*. Trajectories of (2.16) that move instead from the repelling sheet $\mathcal{S}_r$ to the attracting sheet $\mathcal{S}_a$ of the critical manifold, are known as *singular faux canards*. The folded singularity is called a *canard point*.

Geometrically speaking, the violation of transversality (2.19) is actually equivalent to a tangency condition. A folded singularity is defined by the condition

$$\text{adj}\, D_z f \cdot D_x f \cdot g(x, z, 0) = 0, \tag{2.21}$$

where $(x, z) \in \mathcal{F}$. From Remark 2.3, left multiplication by $\text{adj}(D_z f)$ is equivalent to left multiplication by l, the left nullvector of $D_z f$. In essence, left multiplication by l ensures that we are looking in the correct fast direction to identify the fold $\mathcal{F}$. Furthermore, by the definition of $\mathcal{F}$ in (2.11), we have $l \cdot D_x f \neq 0$. Note that for one fast variable, (2.21) simplifies to $D_x f \cdot g(x, z, 0) = 0$, which clearly indicates that g is orthogonal to $D_x f$ (which is orthogonal to $\mathcal{S}$). Thus (2.21) implies that along the fold $\mathcal{F}$, at a folded singularity, the reduced flow $g(x, z, 0)$ projected onto the slow base x is tangent to $\mathcal{F} \subset \mathcal{S}$. The tangency condition at a folded singularity is illustrated in Figure 2.1. Panel A shows the reduced flow near a folded (node) singularity. Panel B shows the projection into the slow (x_1, x_2)-plane, and we can see that the reduced flow is tangent to the fold precisely at the folded singularity.

2.3.1 One slow variable

For $n = 1$ slow variables, $\mathcal{S}$ is a one dimensional manifold and $\mathcal{F}$ is a zero-dimensional manifold. In other words, the set $\mathcal{F}$ consists of isolated fold points which lie on the critical manifold. On the other hand, the set of folded singularities $\mathcal{M}$, defined by (2.20), satisfies three conditions: $f = 0$, $\det(D_z f) = 0$, and $\text{adj}(D_z f) \cdot D_x f \cdot g = 0$. Since there are only two unknown variables x and z, the above conditions cannot be fulfilled in general and $\mathcal{M}$ is degenerate. Thus an extra condition (typically involving a system parameter) is needed to make $\mathcal{M}$ generic. From Definition 2.5 and Remark 2.3 it follows that $\text{adj}(D_z f) \cdot D_x f \neq 0$. Thus the only way condition (2.20) can be satisfied is if $g = 0$. In other words, for $n = 1$
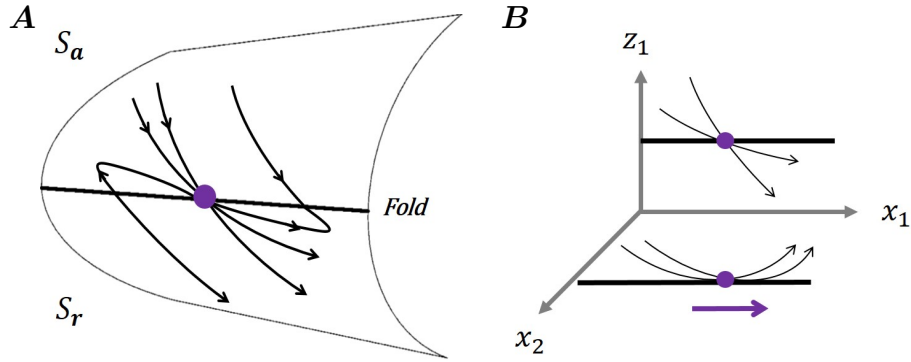
Figure 2.1: Illustrative diagram of the reduced flow near a generic folded node singularity in various projections. *A:* The critical manifold $\mathcal{S}$ (grey) is plotted in (z_1, x_1, x_2) space, with the reduced flow (black) near the folded singularity (solid purple circle). The attracting and repelling sheets of the critical manifold $\mathcal{S}_a$ and $\mathcal{S}_r$ meet at a fold (thick black line). *B:* Projections of the fold and reduced flow into the (z_1, x_1) and (x_1, x_2)-planes. In the slow (x_1, x_2) subspace, the reduced flow is tangent to the fold precisely at the fold singularity.

the set of folded singularities in fact consists of ordinary singularities interacting with $\mathcal{F}$, i.e. a bifurcation of equilibria.

In planar systems, folded singularities occur when, under the variation of a parameter, the fold point and the slow nullcline intersect. This necessarily corresponds to a bifurcation of the full system wherein an equilibrium switches stability. Linearisation of the full system about the folded singularity reveals an Andronov-Hopf bifurcation which is singular. This underpins the classic canard explosion which explains the rapid transition from quiescence to relaxation oscillations via canard cycles in the van der Pol oscillator. More details will be given in Section 2.7.1.

2.3.2 Two or more slow variables

For $n \geq 2$ slow variables, the set of folded singularities is a codimension-one subset of the fold $\mathcal{F}$. Thus $\mathcal{M}$ forms an $(n-2)$-dimensional set of equilibria of (2.17), and the linearisation of (2.17) always has $(n-2)$ zero eigenvalues (whose corresponding eigenvectors are tangent to $\mathcal{M}$). Folded singularities are then classified based on the two remaining non-zero eigenvalues:

Definition 2.10. Let $n \geq 2$, and let ν_1, ν_2 denote the non-zero eigenvalues of the linearisation of (2.17) about a folded singularity $q \in \mathcal{M}$. The folded singularity q is classified as a

- *folded node* if ν_1, $\nu_2 \in \mathbb{R}$, and $\nu_1 \cdot \nu_2 > 0$,
- *degenerate folded node* if ν_1, $\nu_2 \in \mathbb{R}$, and $\nu_1 = \nu_2$,
- *folded saddle* if ν_1, $\nu_2 \in \mathbb{R}$, and $\nu_1 \cdot \nu_2 < 0$,
- *folded saddle-node* if ν_1, $\nu_2 \in \mathbb{R}$, and ν_1, $\nu_2 = 0$,
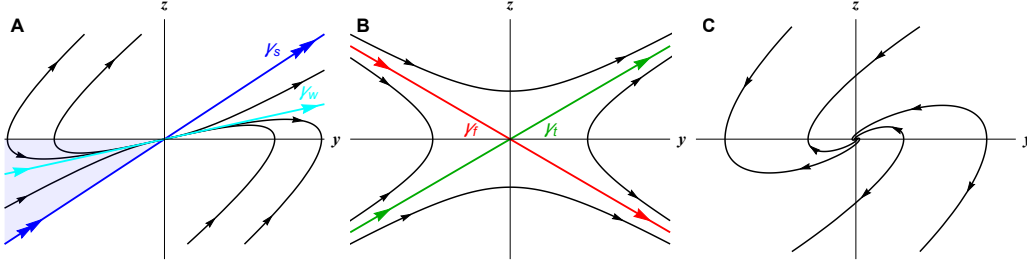- *folded focus* if ν_1, $\nu_2 \in \mathbb{C}$.

17

Figure 2.2: Reduced flow projected into the (y, z)-plane, in a neighbourhood of A: a folded node, B: a folded saddle, and C: a folded focus. In each figure, the fold is the y-axis, which separates $\mathcal{S}_a$ ($z < 0$) and $\mathcal{S}_r$ ($z > 0$). The folded node has a singular strong canard γ_s (shown in blue) and a singular weak canard γ_w (cyan). The fold and γ_s form a sector known as a funnel (the shaded blue region). The funnel is filled with singular canards that rotate around γ_w and cross the folded node tangent to it. The folded saddle has a singular (true) canard γ_t (green) and a singular faux canard γ_f (red). The folded focus has no singular canards.

Folded saddles, nodes and foci are generic singularities. On the other hand, folded saddle-nodes and degenerate folded nodes are codimension-one subsets of $\mathcal{M}$. Folded node singularities have two singular canards, the *strong canard* γ_s and the *weak canard* γ_w, which correspond to the strong and weak eigendirections of the desingularised flow. The region enclosed by the fold and γ_s is known as the *singular funnel*, and it is filled with singular canards which are 'funnelled' through the folded node tangent to γ_w. In comparison, the folded saddle singularity only has two singular canards, a (true) canard γ_t and a faux canard γ_f. See Figure 2.2 for a comparison of the reduced flow in a neighbourhood of the three different folded singularities.

Remark 2.4. A folded focus singularity has no singular canards or singular faux canards.

2.4 Local Normal forms

For systems with $m \geq 2$ fast variables, the $(m-1)$ fast hyperbolic eigendirections do not significantly alter the local dynamics near the fold. It follows that, by a centre manifold reduction, the system can be locally reduced to an $(n+1)$-dimensional system:

Theorem 2.4 (Centre manifold reduction [16, 111])**.** *Suppose system (2.1) has a critical manifold which is locally folded, as in Definition 2.5. Then there exists an $(n+1)$-dimensional centre manifold W^C in a neighbourhood of $(x_*, z_*) \in \mathcal{F}$, with the following properties:*

(i) W^C is tangent to the $(n+1)$-dimensional space spanned by the slow directions and the left nullvector of $D_z f(x_*, z_*, 0)$.

(ii) System (2.1) reduced to W^C has the form

$$
\begin{aligned}
\dot{x} &= \tilde{g}(x, z_1, \varepsilon), \\
\varepsilon \dot{z}_1 &= x_1(d_1 + \mathcal{O}(x, z_1)) + z_1^2(d_1 + \mathcal{O}(x, z_1)) + \varepsilon \mathcal{O}(x, z_1, \varepsilon),
\end{aligned}
\tag{2.22}
$$

where $x \in \mathbb{R}^n$, $z_1 \in \mathbb{R}$, and d_1, d_2 are non-zero constants.

18

Furthermore, for $n \geq 2$ slow variables, the local dynamics near a folded node or saddle singularity is described (to leading order) by the following normal form:

Theorem 2.5 (Folded saddle and folded node normal form [111])**.** *Suppose system (2.1) has a critical manifold which is locally folded, as defined in Definition 2.5, and possess a folded singularity $p \in \mathcal{M}$ of either saddle or node type. Then there exists a smooth change of coordinates that transforms (2.22) to the canonical form*

$$
\begin{aligned}
\dot{x}_1 &= \frac{1}{2}\mu(x_3, \ldots, x_n) - (1 + \mu(x_1, \ldots, x_n))z + \mathcal{O}(x_1, (x_2+z)^2, \varepsilon), \\
\dot{x}_2 &= 1 + \mathcal{O}(x_1, x_2, z, \varepsilon), \\
\dot{x}_j &= a_j + g_{j,1}(x_3, \ldots, x_n) + \mathcal{O}(x_1, x_2, z, \varepsilon), \qquad j = 3, \ldots, n \\
\varepsilon\dot{z} &= x_1(1 + z\mathcal{O}(x_2, \ldots, x_n)) + z^2(1 + \mathcal{O}(x_1, z) + \varepsilon\mathcal{O}(x_1, x_2, z, \varepsilon)),
\end{aligned}
\tag{2.23}
$$

where a_j are constants, $g_{j,1}(0, \ldots, 0) = 0$, and $\mu(x_3, \ldots, x_n)$ is the eigenvalue ratio of the folded singularity p (with respect to the desingularised reduced system).

Setting $n = 2$ in system (2.23) gives the following normal form [110] for systems with a single fast variable:

$$
\begin{aligned}
\dot{x} &= \frac{1}{2}\mu y - (1 + \mu)z + \mathcal{O}(x, \varepsilon, (y + z)^2), \\
\dot{y} &= 1 + \mathcal{O}(x, y, z, \varepsilon), \\
\varepsilon\dot{z} &= x + z^2 + \mathcal{O}(xyz, xz^2, z^3, \varepsilon(x + y + z), \varepsilon^2).
\end{aligned}
\tag{2.24}
$$

The corresponding desingularised reduced system is given by

$$
\begin{aligned}
\dot{y} &= -2z\left(1 + \mathcal{O}(y, z)\right), \\
\dot{z} &= \frac{1}{2}\mu y - (1 + \mu)z + \mathcal{O}((y + z)^2),
\end{aligned}
\tag{2.25}
$$

and the associated Jacobian evaluated at the folded singularity $(y, z) = (0, 0)$ is

$$
A(0,0) = \begin{pmatrix} 0 & -2 \\ \frac{1}{2}\mu & -(1 + \mu) \end{pmatrix}.
$$

Thus linearisation of the desingularised flow (2.25) about the origin yields eigenvalues $\lambda_1 = -1$, $\lambda_2 = -\mu$, with eigenvectors $\nu_1 = (2, 1)^T$, $\nu_2 = (2, \mu)^T$. If $\mu < 0$, the folded singularity at the origin is of saddle type, and if $\mu > 0$ the folded singularity is of node type. Notice that the parameter $\mu = \lambda_1/\lambda_2$ represents the eigenvalue ratio of the folded singularity.

2.4.1 Bifurcations of folded singularities

Bifurcations involving folded singularities are called *folded saddle-node (FSN) bifurcations*, which come in different varieties. The first type, FSN I, can be observed in system (2.24) by taking the limit $\mu \to 0$. Linearisation of the desingularised flow (2.25) at the origin now yields eigenvalues $\lambda_1 = -1$, $\lambda_2 = 0$ with eigenvectors $\nu_1 = (2, 1)^T$, $\nu_2 = (2, 0)^T$. The singularity at the origin is in fact a saddle-node bifurcation of a folded node and a folded
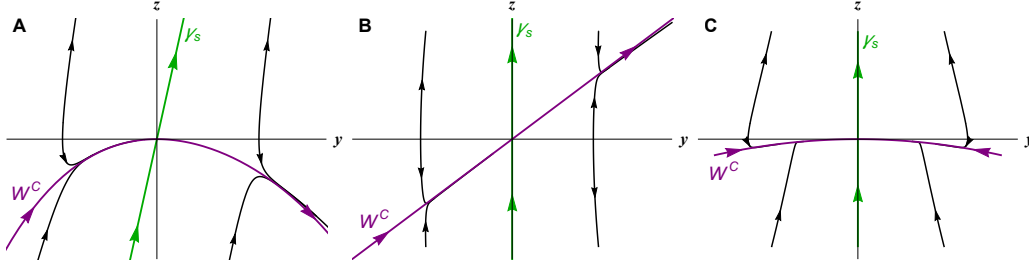
Figure 2.3: Reduced flow in a neighbourhood of a *A:* FSN I (with centre manifold W^C on $\mathcal{S}_a$), *B:* FSN II (with W^C transverse to the fold), and *C:* FSN III (with W^C on $\mathcal{S}_a$), projected into the (y, z)-plane. In all figures, the centre manifold is shown in purple and the singular canard γ_s is in green.

saddle singularity. Furthermore, the centre manifold at the origin is tangent to the fold, and there exists a singular canard (which corresponds to the eigenvector ν_1) that is transverse to both the y and z coordinate axes (see Figure 2.3A).

To observe the other types of FSN bifurcations, we employ two rescalings: Firstly, we rescale $\tilde{y} = \mu y$ in (2.24), which gives

$$
\begin{aligned}
\dot{x} &= y - (1 + \mu)z + \mathcal{O}(x, \varepsilon, (y + z)^2), \\
\dot{y} &= \frac{1}{2}\mu + \mathcal{O}(x, y, z, \varepsilon), \\
\varepsilon\dot{z} &= x + z^2 + \mathcal{O}(xyz, xz^2, z^3, \varepsilon(x + y + z), \varepsilon^2),
\end{aligned}
\tag{2.26}
$$

where we have dropped the tildes. Secondly, we rescale $\tilde{y} = \text{sgn}(\mu)\sqrt{|\mu|}y$ in (2.24), which gives

$$
\begin{aligned}
\dot{x} &= \sqrt{|\mu|}y - (1 + \mu)z + \mathcal{O}(x, \varepsilon, (y + z)^2), \\
\dot{y} &= \frac{1}{2}\text{sgn}(\mu)\sqrt{|\mu|} + \mathcal{O}(x, y, z, \varepsilon), \\
\varepsilon\dot{z} &= x + z^2 + \mathcal{O}(xyz, xz^2, z^3, \varepsilon(x + y + z), \varepsilon^2),
\end{aligned}
\tag{2.27}
$$

where we have once again dropped the tildes. Note that all three normal forms (2.24), (2.26) and (2.27) are equivalent for $\mu \neq 0$, and linearisation of the desingularised flow at the origin yields eigenvalues -1 and $-\mu$. However, taking the limit $\mu \to 0$ in systems (2.26) and (2.27) now leads to different types of FSN singularities, with a distinct geometry and structure.

Taking the limit $\mu \to 0$ in (2.26) gives the FSN II bifurcation, which is a transcritical bifurcation of an ordinary singularity and a folded singularity. The centre manifold of the FSN II is transverse to the fold and the singular canard is tangent to the z-axis. Taking the limit $\mu \to 0$ in (2.27) gives the FSN III bifurcation, which is a pitchfork bifurcation of two folded singularities and an ordinary singularity. The centre manifold of the FSN III is tangent to the fold, and the singular canard is also tangent to the z-axis. See Figure 2.3 for a comparison of the reduced flow near all three FSN bifurcations.

The FSN I and II are both common in applications, and can generate interesting dynamics. The FSN I occurs in various neural models [101, 106, 112], and generates mixed-mode oscillations (MMOs) in the forced van der Pol oscillator [12, 46, 49, 100]. The FSN II is

the unfolding of the two dimensional singular Andronov-Hopf bifurcation seen in planar slow/fast systems with degenerate folded singularities, such as the van der Pol oscillator [37, 64]. Like the FSN I, the FSN II also frequently occurs in cell models [88, 90, 91, 105, 50], and plays a role in the creation of MMOs [5, 13, 45]. Note that both types of bifurcations can occur in the same model [39, 101]. The FSN I and II have been studied in detail in [66, 76, 78, 108], and have been shown to possess canards for $\varepsilon > 0$. The FSN III bifurcation was observed for the first time, in the context of slow/fast averaging, in our study of the Butera model (a coupled neural model) [87]. The Butera model will be analysed in detail in Chapter 5 of this thesis, while Chapter 7 will be devoted to analysing a normal form of the FSN III, and formally proving the existence of canards.

2.5   The Blow-Up Technique

Recall that Fenichel theory breaks down in a neighbourhood of the fold $\mathcal{F}$ and other nilpotent singularities (i.e. singularities with a zero eigenvalue). The key to understanding the dynamics near $\mathcal{M} \subset \mathcal{F}$ is the *blow-up technique*. This method was first applied to slow/fast systems by Dumortier *et al.* [37] who studied canard cycles in the planar van der Pol system. The blow-up is a coordinate transformation which restores sufficient hyperbolicity to degenerate equilibria (such as folded singularities) to allow the use of standard dynamical systems tools. The literature is replete with examples of the application of the blow-up technique to slow-fast systems with $k = 1$, 2 slow variables; see for example [64, 65, 66, 108, 99, 110]. In [111] the blow-up technique is used to analyse a folded node/saddle singularity for $k \geq 2$ slow variables. For a rigorous formulation of the blow-up technique in a general context, see [29, 36, 89].

In this section we will outline the blow-up for a general 1-fast/2-slow system whith a folded critical manifold, trivially extended by $\varepsilon' = 0$:

$$
\begin{aligned}
x' &= \varepsilon g_1(x, y, z, \varepsilon), \\
y' &= \varepsilon g_2(x, y, z, \varepsilon), \\
z' &= x(1 + \mathcal{O}(x, y, z)) + z^2(1 + \mathcal{O}(x, y, z)) + \mathcal{O}(\varepsilon) =: f(x, y, z, \varepsilon), \\
\varepsilon' &= 0.
\end{aligned}
\tag{2.28}
$$

It is necessary to consider the extended system as ε will be explicitly included in the blow-up transformation. In the extended phase space, away from the fold curve $\mathcal{F}$, the linearisation of (2.28) along the manifold of equilibria $\mathcal{S} \times \{0\}$ yields three zero eigenvalues and one non-zero eigenvalue. On the other hand, the linearisation along $\mathcal{F}$ yields four zero eigenvalues, i.e. the entire fold and set of folded singularities $\mathcal{M} \subset \mathcal{F}$ is a degenerate set of equilibria of (2.28). Let X denote the vector field of (2.28), and without loss of generality, assume that the origin is a degenerate equilibrium, i.e. $X(0, 0, 0, 0) = 0$, $f_z(0, 0, 0, 0) = 0$. We define two blow-up transformations, the cylindrical blow-up for regular folds, and the spherical blow-up for folded singularities.

Definition 2.11. The cylindrical blow-up $\Phi_F : B_F \to \mathbb{R}^4$ of (2.28) is the mapping

$$
(x, y, z, \varepsilon) = \left(\bar{r}^\alpha \bar{x}, \bar{y}, \bar{r}^\beta \bar{z}, \bar{r}^\gamma \bar{\varepsilon} \right) =: \Phi_F(\bar{x}, \bar{y}, \bar{z}, \bar{\varepsilon}, \bar{r}),
\tag{2.29}
$$

where $B_F = \mathbb{S}^2 \times \mathbb{R} \times [0, \rho]$, $\rho > 0$, with appropriate weights $(\alpha, \beta, \gamma) \in \mathbb{N}^3$. The y-axis is blown up by Φ_F to a cylinder with

$$\bar{x}^2 + \bar{z}^2 + \bar{\varepsilon}^2 = 1.$$

Definition 2.12. The spherical blow-up $\Phi_M : B_M \to \mathbb{R}^4$ of (2.28) is the mapping

$$(x, y, z, \varepsilon) = \left(\bar{r}^\alpha \bar{x}, \bar{r}^\beta \bar{y}, \bar{r}^\gamma \bar{z}, \bar{r}^\delta \bar{\varepsilon} \right) =: \Phi_M(\bar{x}, \bar{y}, \bar{z}, \bar{\varepsilon}, \bar{r}), \tag{2.30}$$

where $B_M = \mathbb{S}^3 \times [0, \rho]$, $\rho > 0$, with appropriate weights $(\alpha, \beta, \gamma, \delta) \in \mathbb{N}^4$. The folded singularity at the origin is blown up by Φ_M to a 3-sphere with

$$\bar{x}^2 + \bar{y}^2 + \bar{z}^2 + \bar{\varepsilon}^2 = 1.$$

The spherical blow-up inflates the degenerate folded singularity at the origin to 3-sphere. On the other hand, the set of regular fold points $\mathcal{F}$ forms a manifold that must be dealt with uniformly. Thus the cylindrical blow-up treats all regular fold points simultaneously in directions transverse to the fold, and y is not rescaled. The cylindrical blow-up is essentially a trivial extension of the planar blow-up for a single regular fold point along $\mathcal{F}$.

Let Φ denote the map Φ_F or Φ_M, and let B denote B_F or B_M. Notice that Φ is proper and surjective. Furthermore, Φ defines the induced map $\Phi^* : TB \to T\mathbb{R}^4$ between the appropriate tangent bundles [99]. Since $X(0,0,0,0) = 0$, there exists a vector field $\bar{X}$ on B such that $\Phi^* \bar{X} = X$. The idea is to then analyse the vector field $\bar{X}$ on the manifold B; one could utilise spherical coordinates to do this, but coordinate charts are far more useful as they simplify calculations. Coordinate charts lead to the notion of directional blow-ups and directional charts.

Definition 2.13 ([99])**.** Let $I := \{1, \ldots, 2m\}$, $m \in \mathbb{N}$. Then *directional blow-ups* Φ_i, $i \in I$ are obtained by setting one variable on $\mathbb{S}^{m-1}$ to ± 1 in the definition of the mapping Φ. *Directional charts* $\kappa_i : B_i \to \mathbb{R}^4$, $i \in I$ are homeomorphic maps such that $B = \bigcup_{i \in I} B_i$. In chart κ_i, the blown up vector field $\bar{X}$ is described by the vector field X_i. Note that $m = 4$ in the spherical blow-up, while $m = 3$ in the cylindrical blow-up.

The directional charts κ_i cover the 3-sphere (or cylinder) with m-planes which are orthogonal to the coordinate axes. Generally, it is sufficient to consider only a few directional charts to construct a complete picture of the blow-up dynamics. For singularly perturbed problems, the so-called *classical chart* $\kappa_2 : \varepsilon = +1$ is the most important directional chart. In chart κ_2 of the spherical blow-up, $\bar{r} = \varepsilon^{-\delta}$, i.e. Φ_2 is simply an ε-dependent rescaling of (2.28). For this reason, the classical chart is also referred to as the *rescaling chart*.

Remark 2.5. We define the following notation: Let $\bar{Y}$ denote an object associated with (2.28), within the blow-up, i.e. on the blown up locus B. Let Y_i denote the object in the directional chart κ_i.

Within each directional chart κ_i, the $r_i = 0$ hyperplane corresponds to the blown-up image of the set of degenerate equilibria, i.e. $\mathbb{S}^2 \times \mathbb{R} \times \{0\}$ or $\mathbb{S}^3 \times \{0\}$. It follows that the associated vector field X_i vanishes in the $r_i = 0$ hyperplane. We thus define a local vector field and local division, which are required to desingularise the blown up vector field and obtain non-trivial dynamics.

Definition 2.14 ([99]). A *local vector field* X is defined on a compact smooth manifold B by a finite open covering $\{B_i\}$ of B with some smooth vector field X_i on each B_i, such that for each pair of indices i, $j \in I$ with $B_i \cap B_j \neq 0$, there exists a strictly positive, smooth function g_{ij} defined on $B_i \cap B_j$ such that $X_i = g_{ij}X_j$ on $B_i \cap B_j$.

Definition 2.15 ([99]). Let $\{B_i\}$ be a finite open covering of B, on which local vector fields X and $\tilde{X}$ are given by X_i and $\tilde{X}_i$. Then $\tilde{X}$ is the result of *local division* of X if there exist smooth functions $f_i : B_i \to \mathbb{R}$ such that $X_i = f_i\tilde{X}_i$ in B_i.

In our application, the functions f_i are typically powers of r_i so that f_i only vanishes on B where Φ fails to be a diffeomorphism (i.e. $\mathbb{S}^2 \times \mathbb{R} \times \{0\}$ for the cylindrical blow-up and $\mathbb{S}^3 \times \{0\}$ for the spherical blow-up). Local division is then performed by rescaling time by a power of r_i to give the desingularised vector fields $\tilde{X}_i$. The vector fields X_i and $\tilde{X}_i$ have the same phase portrait for $r_i > 0$, but $\tilde{X}_i$ may reveal non-trivial dynamics on the set $r_i = 0$.

We also define the change of coordinates which enables the tracking of objects and solutions in different charts.

Definition 2.16. Let κ_{ij} denote the change of coordinates that takes solutions in chart κ_j and maps them to chart κ_i. Then

$$\kappa_{ij} := \kappa_j \circ \kappa_i^{-1}. \tag{2.31}$$

An 'appropriate choice' of weights $(\alpha, \beta, \gamma, \delta) \in \mathbb{N}^4$ should satisfy the following requirements [99]:

(i) Local division is possible to obtain the vector fields $\tilde{X}_i$;

(ii) The dynamics in the $r_i = 0$ plane can be analysed;

(iii) Perturbation methods can be used to obtain the dynamics for $r_i > 0$;

(iv) The vector fields $\tilde{X}_i$ only have hyperbolic (or semi-hyperbolic) equilibria.

The choice of weights is problem dependent and often best determined in the classical chart. Note that if any degenerate singularities remain after one blow-up, a succession of additional blow-ups can be used to desingularise them and obtain (semi-)hyperbolic equilibria; see for example [48, 59]. In light of this, the blow-up technique can be summarised as follows:

Definition 2.17 ([99]). Let $X \subset \mathbb{R}^4$ be a vector field with a nilpotent or degenerate singularity $X(0) = 0$, and let $\tilde{X}$ be the result of local division of X. Then a *desingularisation* of X is a blow-up transformation $\Phi : B \to \mathbb{R}^4$ with blown-up locus $Z = \Phi^{-1}(0)$ and suitable weights $(\alpha, \beta, \gamma, \delta)$ such that for all local vector fields X_i induced by Φ and any point $p \in Z_i$ with $\tilde{X}_i(p) = 0$, the point p is a hyperbolic or semi-hyperbolic singularity of $\tilde{X}_i$.

Table 2.1 provides a summary of the weights used in the blow-up of several 3-dimensional normal forms, including the regular fold, folded node, folded saddle (see Sections 2.6 and 2.7.3–2.7.4) and different types of FSN singularities. Note that the FSN cases are degenerate and require additional parameters that need to be included in the blow-up transformation; this will become apparent in Sections 2.7.5–2.7.7.

3D Normal Form	Type of Blow-Up	Transformation/Weights
Regular Fold	Cylindrical	$(x, y, z, \varepsilon) = (\bar{r}^2\bar{x}, \bar{y}, \bar{r}\bar{z}, \bar{r}^3\bar{\varepsilon})$
Folded Node/Saddle	Spherical	$(x, y, z, \varepsilon) = (\bar{r}^2\bar{x}, \bar{r}\bar{y}, \bar{r}\bar{z}, \bar{r}^2\bar{\varepsilon})$
FSN I	Spherical	$(x, y, z, \varepsilon) = (\bar{r}^4\bar{x}, \bar{r}\bar{y}, \bar{r}^2\bar{z}, \bar{r}^4\bar{\varepsilon})$
FSN II	Spherical	$(x, y, z, \varepsilon) = (\bar{r}^2\bar{x}, \bar{r}\bar{y}, \bar{r}\bar{z}, \bar{r}^2\bar{\varepsilon})$
FSN III	Spherical	$(x, y, z, \varepsilon) = (\bar{r}^4\bar{x}, \bar{r}\bar{y}, \bar{r}^2\bar{z}, \bar{r}^4\bar{\varepsilon})$

Table 2.1: Blow-up weights used in the analysis of various three dimensional normal forms.

2.6 The Regular Fold

In Section 2.2 we defined three special structures of the reduced problem: regular singularities, regular fold points, and folded singularities. The latter led to the phenomenon of singular canards. Naturally, one might wonder if these special structures and solutions persist under small perturbations in ε. We first consider the flow past a regular fold for small $\varepsilon > 0$.

Consider a system with a two dimensional folded critical manifold, as per Definition 2.7. Then by the centre manifold reduction theorem 2.4, the local flow near the regular fold (denoted by L) is described by the three-dimensional canonical system

$$
\begin{aligned}
x' &= 1 + g_1(x, y, z, \varepsilon), \\
y' &= g_2(x, y, z, \varepsilon), \\
\varepsilon z' &= x + z^2 + \mathcal{O}(z^3, xyz, x^2z, \varepsilon),
\end{aligned}
\tag{2.32}
$$

where $g_i(0, y, 0, 0) = 0$ for $i = 1, 2$, and $0 < \varepsilon \ll 1$. The reduced flow of (2.32) is given by

$$
y' = g_2(x, y, z, \varepsilon),
\tag{2.33}
$$
$$
-2zz' = 1 + g_1(x, y, z, 0) + \mathcal{O}(xz, yz, x^2y, x^3, z^4).
\tag{2.34}
$$

Note that the 1 in the z' equation dictates that the reduced flow moves toward the fold (see Figure 2.4).

We now blow up a segment of the fold curve L in (2.32) to a cylinder $\mathbb{S}^2 \times I \times \mathbb{R}$, where $(\bar{x}, \bar{z}, \bar{\varepsilon}) \in \mathbb{S}^2$, $\bar{y} \in I$, and $\bar{r} \in \mathbb{R}$. The cylindrical blow-up transformation is given by $(x, y, z, \varepsilon) = (\bar{r}^2\bar{x}, \bar{y}, \bar{r}\bar{z}, \bar{r}^3\bar{\varepsilon})$. Specifically, the transformation in the rescaling chart $\kappa_2 : \bar{\varepsilon} = 1$ is given by

$$
x = \varepsilon^{2/3}x_2, \qquad y = y_2, \qquad z = \varepsilon^{1/3}z_2, \qquad \varepsilon = r_2^3.
\tag{2.35}
$$

Since ε is included in the blow-up transformation, we apply (2.35) to the extended system $\{(2.32), \varepsilon' = 0\}$ and desingularise by a factor of $\varepsilon^{1/3}\left(1 + \mathcal{O}(\varepsilon^{1/3})\right)$, which gives

$$
\begin{aligned}
x_2' &= 1, \\
y_2' &= \mathcal{O}(\varepsilon), \\
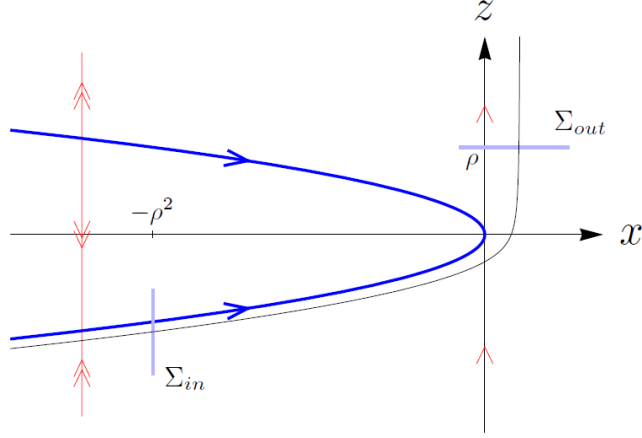z_2' &= x_2 + z_2^2 + \mathcal{O}(\varepsilon^{1/3}).
\end{aligned}
\tag{2.36}
$$

Figure 2.4: Projection of the critical manifold (dark blue) and sections. Fast fibres are indicated in red. Figure adapted from [76].

System (2.36) describes the flow on the cylinder in an $\mathcal{O}(\varepsilon^{1/3})$ neighbourhood of the fold L. Notice that the blow-up has transformed the original singularly perturbed system (2.32) into a regularly perturbed system (2.36). Setting $\varepsilon^{1/3} = 0$ in (2.36), restricted to (x_2, z_2), yields a Riccati equation which has a unique solution γ. This solution γ is asymptotic to the lower branch of the parabola $x_2 + z_2^2 = 0$ for $x_2 \to -\infty$, and asymptotic to $\Omega > 0$ for $z_2 \to \infty$ [100].

For small positive ρ and suitable rectangles $J_1, J_2 \in \mathbb{R}^2$, we define the sections

$$\Sigma^{in} := \{(-\rho^2, y, z) : (y, z) \in J_1\}, \qquad \Sigma^{out} := \{(x, y, \rho) : (x, y) \in J_2\}, \tag{2.37}$$

which are transverse to $\mathcal{S}_a$ and the fast fibres, respectively. The sections are shown in Figure 2.4. Let $\Pi_L : \Sigma^{in} \to \Sigma^{out}$ be the transition map for the flow of (2.32). Piecing together the dynamics in the rescaling chart, as well as an entry an exit chart, gives the following results:

Theorem 2.6 (Flow near a regular fold [100]; see also [64])**.** *For the regular fold in the canonical form (2.32), there exists a $\rho > 0$ and $\varepsilon_0 > 0$ such that for $\varepsilon \in (0, \varepsilon_0]$, the following holds:*

1. *There exists an interval I_{out} such that for $y \in I_{out}$, the slow manifold $\mathcal{S}_a^\varepsilon$ intersects Σ^{out} in a smooth curve, which is a graph, i.e. $x_{out} = h_{out}(y, \varepsilon)$.*

2. *The section Σ^{in} is mapped to an exponentially thin strip around $\mathcal{S}_a^\varepsilon \cap \Sigma^{out}$, i.e. its width in the x-direction is $\mathcal{O}(\exp(-c/\varepsilon))$, where c is a positive constant.*

3. *The map $\Pi_L : \Sigma^{in} \to \Sigma^{out}$ has the form*

$$\Pi_L \begin{pmatrix} y \\ z \end{pmatrix} = \begin{pmatrix} h_{out}(G_L(y, z, \varepsilon), \varepsilon) + \mathcal{O}(\exp(-c/\varepsilon)) \\ G_L(y, z, \varepsilon) \end{pmatrix}, \tag{2.38}$$

where $h_{out}(G_L(y, z, \varepsilon), \varepsilon) = \mathcal{O}(\varepsilon^{2/3})$ and $G_L(y, z, \varepsilon) = G_{L,0}(y) + \mathcal{O}(\varepsilon \ln \varepsilon)$. The function $G_{L,0}(y) = y + \mathcal{O}(\rho^3)$ is induced by the reduced flow on $\mathcal{S}_a$ from Σ^{out} to L.

25

Theorem 2.6 demonstrates that solutions, and hence the attracting and repelling slow manifolds, leave a neighbourhood of the regular fold L via the fast fibres $\mathcal{O}(\varepsilon^{2/3})$ close the weakly unstable fibre of the layer problem; see Figure 2.4. Since solutions leave the critical manifold in a neighbourhood of L, regular fold points are referred to as *jump points*.

2.7 Canard Theory

We now turn our attention to the persistence of singular canards away from the singular limit. Recall that by Fenichel's theorems, normally hyperbolic segments of $\mathcal{S}$ perturb to non-unique (but exponentially close) slow manifolds $\mathcal{S}^\varepsilon$, which inherit the same stability properties.

Definition 2.18. For a fixed choice of $\mathcal{S}^\varepsilon$, a *maximal canard* is a solution of the full system (2.1) which corresponds to the intersection between the attracting and repelling/saddle-type manifolds $\mathcal{S}_a^\varepsilon$ and $\mathcal{S}_r^\varepsilon/\mathcal{S}_s^\varepsilon$, extended by the flow of (2.1) into a neighbourhood of the folded singularity.

Remark 2.6. Since the slow manifolds are non-unique, it follows that each maximal canard is associated with a family of canards, which are exponentially close to the maximal canard. Moving to the singular limit, the family of canards collapses to a unique singular canard.

2.7.1 Planar canards

Recall that for $n = 1$ slow variables, folded singularities are degenerate. In such cases, we require the variation of at least one system parameter to observe the folded singularity. For planar singularly perturbed systems, we state the following classical result (for further details see [32, 33, 37, 65]):

Theorem 2.7 ([65]; see also [31]). *Suppose a planar slow/fast system*

$$x' = \varepsilon g(x, z, \varepsilon),$$
$$z' = f(x, z, I, \varepsilon),$$

has a generic fold point $p_* = (x_p, z_p) \in \mathcal{S}$, *i.e.*

$$f(p_*, I, 0) = 0, \quad f_z(p_*, I, 0) = 0, \quad f_{zz}(p_*, I, 0) \neq 0, \quad f_x(p_*, I, 0) \neq 0,$$

as per Definition 2.7. Assume that the critical manifold is locally attracting for $z < z_p$ *and locally repelling for* $z > z_p$, *and there exists a non-degenerate folded singularity for* $I = 0$ *at* p_*, *namely*

$$g(p_*, 0, 0) = 0, \quad g_x(p_*, 0, 0) \neq 0, \quad g_I(p_*, 0, 0) \neq 0.$$

Then a singular Andronov-Hopf bifurcation and a canard explosion occur at

$$I_{AH} = H_1 \varepsilon + \mathcal{O}(\varepsilon^{2/3}),$$
$$I_c = (H_1 + K_1)\varepsilon + \mathcal{O}(\varepsilon^{2/3}),$$

respectively. The coefficients H_1 *and* K_1 *can be calculated explicitly from normal form transformations, or by considering the the first Lyapunov coefficient of the Andronov-Hopf bifurcation [67].*
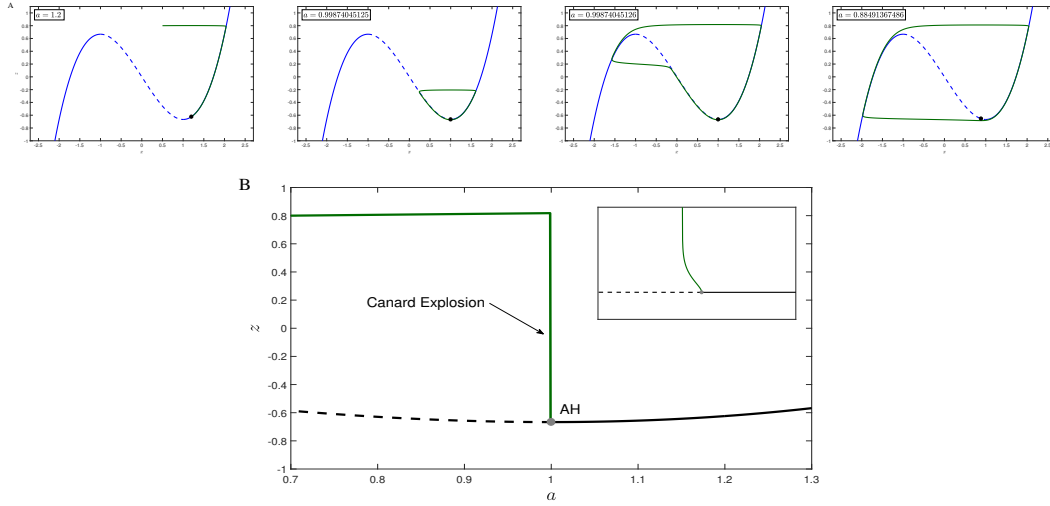
26

Figure 2.5: Canard explosion and singular Andronov-Hopf (AH) bifurcation of the VdP oscillator (2.39). *A:* Solutions of the full system (shown in green) for various values of a which are indicated on the diagram. The critical manifold is shown in blue, and the equilibrium of the full system is indicated by a black dot. *B:* Bifurcation diagram of the full system with respect to a. The singular AH bifurcation is indicated by a grey dot. The inset diagram shows the small amplitude oscillations near AH.

Remark 2.7 (see [31]). In the singular limit $I_{AH} = I_c$. For any $\varepsilon > 0$ and sufficiently small, the linearised system at the Andronov-Hopf bifurcation point has a pair of *singular eigenvalues*

$$\lambda(I; \varepsilon) = \alpha(I; \varepsilon) + i\beta(I; \varepsilon),$$

with $\alpha(I_{AH}; \varepsilon) = 0$, $\alpha_I(I_{AH}; \varepsilon) \neq 0$, and

(i) $\lim_{\varepsilon \to 0} \beta(I_{AH}; \varepsilon) = \infty$ on the slow time scale τ,

(ii) $\lim_{\varepsilon \to 0} \beta(I_{AH}; \varepsilon) = 0$ on the fast time scale t.

One of the most well-know examples of a planar canard explosion is the classic van der Pol (VdP) oscillator with constant forcing a [103], which is given by

$$\begin{aligned}
\varepsilon \dot{x} &= z - x^3/3 + x, \\
\dot{z} &= a - x.
\end{aligned} \tag{2.39}$$

Figure 2.5B shows the bifurcation diagram of the full VdP system with singular AH bifurcation (see inset) and canard explosion. Figure 2.5A shows the progression from quiescence to relaxation oscillations through various canard cycles. The second figure in row A shows a small amplitude oscillation near the singular AH, which is known as a 'canard without head'. The next figure shows the famous 'duck' shaped 'canard with head'. Notice that the canard cycles all occur in an exponentially small parameter window; this makes it very difficult to locate them numerically with initial value solvers. Thus these elusive duck shaped creatures were named 'canards' by the early French mathematicians who discovered them in studies of the VdP oscillator [7].

27

2.7.2 Folded node/saddle blow-up

Recall that system (2.24) is a normal form for both the folded node $(0 < \mu < 1)$ and folded saddle $(\mu < 0)$. By blowing up the folded singularity at the origin, we can prove the existence of canards for $\varepsilon \neq 0$ and study their properties for both cases. The spherical blow-up transformation for the folded node/saddle is given by $(x, y, z, \varepsilon) = (\bar{r}^2 \bar{x}, \bar{r}\bar{y}, \bar{r}\bar{z}, \bar{r}^2 \bar{\varepsilon})$, where $(\bar{x}, \bar{y}, \bar{z}, \bar{\varepsilon}) \in \mathbb{S}^3$. It suffices to study the dynamics in three directional charts: the entry chart κ_1, the rescaling chart κ_2, and the exit chart κ_3. The transformation in the rescaling chart $\kappa_2 : \bar{\varepsilon} = 1$ is given by

$$x = \varepsilon x_2, \qquad y = \varepsilon^{1/2} y_2, \qquad z = \varepsilon^{1/2} z_2, \qquad \varepsilon = r^2. \qquad (2.40)$$

Applying transformation (2.40) to system (2.24) gives

$$
\begin{aligned}
x_2' &= \frac{1}{2}\mu y_2 - (\mu + 1)z + \mathcal{O}(\sqrt{\varepsilon}), \\
y_2' &= 1, \\
z_2' &= x_2 + z_2^2 + \mathcal{O}(\sqrt{\varepsilon}).
\end{aligned}
\qquad (2.41)
$$

Similar to the regular fold case, the blow-up in the rescaling chart has transformed the original singularly perturbed system (2.24) into a regularly perturbed system (2.41). Setting $\sqrt{\varepsilon} = 0$ in (2.41) gives the unperturbed system, which has two explicit algebraic solutions:

$$
\begin{aligned}
\gamma_1(t) &= \left(-\frac{\mu^2}{4}t^2 + \frac{\mu}{2}, t, \frac{\mu}{2}t \right), \\
\gamma_2(t) &= \left(-\frac{1}{4}t^2 + \frac{1}{2}, t, \frac{1}{2}t \right).
\end{aligned}
$$

The special solutions γ_1 and γ_2 correspond to the eigenvalues $\lambda_1 = -\mu$ and $\lambda_2 = -1$, respectively. These solutions are important as they connect the attracting slow manifold (for $\bar{\varepsilon} > 0$) to the repelling slow manifold, and vice versa. Thus (γ_1, γ_2) can be viewed as extensions of the singular canards. Note that the unbounded branches of (γ_1, γ_2) connect to the singular canards of the reduced problem in chart κ_1.

2.7.3 Folded node canards

Consider system (2.24) in the case of a folded node with real eigenvalues $\lambda_1 \leq \lambda_2 < 0$. Again, let $\mu = \lambda_1/\lambda_2$ be the eigenvalue ratio of the folded singularity so that $0 < \mu < 1$.

Theorem 2.8 (Existence of maximal canards [16, 76, 99, 110, 111])**.** *Suppose system (2.24) has a folded node with eigenvalue ratio $0 < \mu < 1$. Then for sufficiently small $0 < \varepsilon \ll 1$ and μ bounded away from zero, we have the following results:*

(i) The singular strong canard perturbs to a maximal canard γ_s, called the primary strong canard.

(ii) For $\mu^{-1} \notin \mathbb{N}$, the singular weak canard perturbs to a maximal canard γ_w, called the primary weak canard.

(iii) *If $2k + 1 < \mu^{-1} < 2k + 3$, $k \in \mathbb{N}$ and $\mu^{-1} \neq 2k + 2$, then there exist k additional maximal canards γ_i, $i = 1, 2, \ldots, k$, called secondary canards. These k secondary canards, positioned between γ_s and γ_w, are $\mathcal{O}(\varepsilon^{(1-\mu)/2})$ close to γ_s at a distance $\mathcal{O}(1)$ from the fold curve $\mathcal{F}$.*

(iv) *For odd $\mu^{-1} \in \mathbb{N}$, the secondary canards bifurcate from γ_w in a transcritical bifurcation.*

(v) *For even $\mu^{-1} \in \mathbb{N}$, the secondary canards bifurcate from γ_w in a pitchfork bifurcation.*

Theorem 2.8 (i)–(ii) follows by extending the attracting and repelling slow manifolds along the strong and weak canards for μ^{-1}. Since they intersect transversally, the intersection will persist under small perturbations [99, 110]. Theorem 2.8 (iii)–(iv) was proven in [110] using an extension of Melnikov theory [109], and Theorem 2.8 (v) was postulated (but later formally proven in [76]).

Theorem 2.9 (Rotational properties of canards [16, 99, 110, 111])**.** *Suppose system (2.24) has a folded node with eigenvalue ratio $0 < \mu < 1$. Then for sufficiently small $0 < \varepsilon \ll 1$ and μ bounded away from zero with $2k + 1 < \mu^{-1} < 2k + 3$, $k \in \mathbb{N}$ and $\mu^{-1} \neq 2k + 2$, we have the following results:*

(i) *The primary strong canard γ_s twists once around the primary weak canard γ_w in an $\mathcal{O}(\sqrt{\varepsilon})$ neighbourhood of the folded node.*

(ii) *The jth secondary canard, $1 \leq j \leq k$, twists $2j + 1$ times around γ_w in an $\mathcal{O}(\sqrt{\varepsilon})$ neighbourhood of the folded node.*

Here a twist corresponds to half a rotation (180 degrees). Thus each maximal canard has a distinct rotation number.

Corollary 2.3 ([110])**.** Under the assumptions of Theorem 2.9, there exist $s_{max} - 1$ secondary canards, where

$$s_{max} := \left\lfloor \frac{1 + \mu}{2\mu} \right\rfloor,$$

and $\lfloor \cdot \rfloor$ is the floor function. The definition of s_{max} is valid away from resonances $\mu^{-1} \in \mathbb{N}$. The kth secondary canard γ_k, $k = 1, \ldots, s_{max} - 1$, makes k full rotations about γ_w. Furthermore, the number of oscillations, denoted by s, that solutions make in an $\mathcal{O}(\sqrt{\varepsilon})$ neighbourhood of the folded node is bounded above by s_{max}, i.e. $0 \leq s \leq s_{max}$.

From a geometric viewpoint, the primary weak canard γ_w acts as a local axis of rotation for the slow manifolds $\mathcal{S}_a^\varepsilon$ and $\mathcal{S}_r^\varepsilon$ (and hence also the strong canard and set of secondary canards contained therein). The strong canard forms the separatrix on $\mathcal{S}_a^\varepsilon$ that divides trajectories which oscillate from those which do not. The funnel region $\mathcal{S}_a^\varepsilon$ is split by the secondary canards into s_{max} subsectors I_k, $k = 1, \ldots, s_{max}$, with distinct rotational properties. Trajectories with initial conditions in I_k make $(2k + 1)/2$ twists (half-rotations) about γ_w. In the singular limit, the set of secondary canards collapses onto γ_s.

2.7.4 Folded saddle canards

Consider system (2.24) in the case of a folded saddle with real eigenvalues $\lambda_1 < 0 < \lambda_2$. Again, define the eigenvalue ratio $\mu = \lambda_1/\lambda_2$.

Theorem 2.10 (Existence of maximal true canard [99])**.** *Suppose system (2.24) has a folded saddle with eigenvalue ratio $\mu < 0$. Then for sufficiently small $0 < \varepsilon \ll 1$ and μ bounded away from zero, the singular true canard γ_t perturbs to a maximal canard called the* true canard*.*

Theorem 2.11 (Existence of faux canards [99])**.** *Suppose system (2.24) has a folded saddle with eigenvalue ratio $\mu < 0$. Then for sufficiently small $0 < \varepsilon \ll 1$ and μ bounded away from zero, a singular faux canard implies the existence of a 2-parameter family of faux canards.*

Until recently, Theorem 2.11 was the only result for faux canards. In [76, 78], the authors provide a comprehensive study of the folded saddle singularity and associated faux canards. In particular, they identify and classify different types of secondary faux canards, their rotational properties, as well as their bifurcations from the primary faux canard.

Theorem 2.12 (Existence and bifurcations of primary and secondary faux canards [76, 78])**.** *Suppose system (2.24) has a folded saddle with eigenvalue ratio $\mu < 0$. Then* secondary faux canards *are defined as faux canards which lie within the fast manifolds $W^{s/u}(\gamma_f)$ of the primary faux canard as $t \to \pm\infty$. For sufficiently small $0 < \varepsilon \ll 1$ and μ bounded away from zero, the following holds:*

(i) *There exist*

$$n_\alpha := 2 \cdot \max\left\{0, \left\lfloor -\frac{1}{2\mu} \right\rfloor - 1\right\} + 1,$$

secondary faux canards of type α (α-faux canards) for $\mu \in (-1,0)$. There are no secondary α-faux canards for $\mu \in (-\infty, -1)$.

(ii) *Secondary α-faux canards bifurcate from the primary faux canard in transcritical bifurcations for even $-\mu^{-1} \in \mathbb{N}$.*

(iii) *There exist no more than*

$$n_\beta := 2 \cdot \max\left\{0, \left\lfloor -\frac{\mu+1}{2\mu} \right\rfloor\right\} + 2 \cdot \max\left\{0, \left\lfloor -\frac{2\mu+1}{2\mu} \right\rfloor\right\} +$$
$$2 \cdot \max\left\{0, \left\lfloor -\frac{4\mu+1}{2\mu} \right\rfloor\right\} \left(\max\left\{0, \left\lfloor -\frac{4\mu+1}{2\mu} \right\rfloor\right\} + 1\right)$$

secondary faux canards of type β (β-faux canards) for $\mu \in (-1,0)$. There are no secondary β-faux canards $\mu \in (-\infty, -1)$.

(iv) *Secondary β-faux canards bifurcate from the primary faux canard in pitchfork bifurcations for odd $-\mu^{-1} \in \mathbb{N}$.*

Theorem 2.13 (Rotational properties of secondary faux canards [76, 78]). *Suppose system (2.24) has a folded saddle with eigenvalue ratio $\mu < 0$. Then for sufficiently small $0 < \varepsilon \ll 1$ and μ bounded away from zero, the following holds:*

(i) The set of secondary faux canards rotate about the primary faux canard in an $\mathcal{O}(\sqrt{\varepsilon})$ neighbourhood of the folded saddle.

(ii) The number of rotations that a secondary faux canard can make is bounded above by

$$s_{max} := \left\lfloor \frac{\mu - 1}{2\mu} \right\rfloor.$$

Remark 2.8. In [76, 78], the authors also proved the existence of *switching solutions*. These are trajectories which follow either γ_t or γ_f towards the folded saddle, switch near the folded singularity, and then follow the other canard away from the singularity. We refer the reader to [76, 78] for further details concerning switching solutions, their rotational properties and bifurcations.

2.7.5 Folded saddle-node type I canards

The following normal form [66]

$$
\begin{aligned}
\dot{x} &= -z + \delta(\alpha - y^2) + \mathcal{O}(x, y, yz, z^2, \varepsilon), \\
\dot{y} &= 1 + \mathcal{O}(x, y, z, \varepsilon), \\
\varepsilon \dot{z} &= x + z^2 + \mathcal{O}(z^3, xz^2, xyz, \varepsilon(x+y+z), \varepsilon^2),
\end{aligned}
\tag{2.42}
$$

with parameters $\alpha \in \mathbb{R}$, $\delta = \pm 1$, describes the local dynamics near a FSN I bifurcation. The additional higher order terms in (2.42) are required to explicitly generate a saddle-node bifurcation of folded singularities under the variation of the bifurcation parameter α. Note that system (2.42) can be transformed into system (2.24) by translating one of the folded singularities $(x, y, z) = (0, \pm\sqrt{\alpha}, 0)$ to the origin.

The blow-up transformation to the classical chart κ_2, which is simply an ε-dependent zoom near the FSN I, is given by

$$
x = \varepsilon x_2, \qquad y = \varepsilon^{1/4} y_2, \qquad z = \varepsilon^{1/2} z_2, \qquad \alpha = \varepsilon^{1/2} \alpha_2.
\tag{2.43}
$$

Notice that the parameter α is also rescaled such that $\lim_{\varepsilon \to 0} \alpha = 0$. Applying transformation (2.43) to system (2.42) yields

$$
\begin{aligned}
\dot{x}_2 &= -z_2 + \delta(\alpha_2 - y_2^2) + \mathcal{O}(\varepsilon^{1/4}), \\
\dot{y}_2 &= \varepsilon^{1/4} \left(1 + \mathcal{O}(\varepsilon^{1/4}) \right), \\
\dot{z}_2 &= x_2 + z_2^2 + \mathcal{O}(\varepsilon^{1/4}).
\end{aligned}
\tag{2.44}
$$

Thus the 1-fast/2-slow system (2.42) has been transformed into a 2-fast/1-slow system (2.44), which describes the dynamics in an $\mathcal{O}(\varepsilon^{1/4})$ neighbourhood of the FSN I singularity. In contrast, recall that the blow-up of the regular fold and folded node/saddle normal form

yielded a regularly perturbed system in chart κ_2. The layer problem of (2.44), which is given by

$$\dot{x}_2 = -z_2 + \delta(\alpha_2 - y_2^2),$$
$$\dot{z}_2 = x_2 + z_2^2,$$

(2.45)

has a one-dimensional critical manifold

$$CM := \left\{ (x_2, y_2, z_2) = \left(-\left(\alpha_2 - y_2^2\right)^2, y_2, \delta\left(\alpha_2 - y_2^2\right)\right), y \in \mathbb{R} \right\},$$

(2.46)

with two Andronov-Hopf bifurcations at $y_2 = \pm\sqrt{\alpha_2}$. The reduced flow of (2.44) simply describes the slow motion on CM, toward larger values of y_2. In particular, trajectories move slowly through the Andronov-Hopf bifurcations and experience a delayed loss of stability, i.e. trajectories follow CM_r for sometime before being repelled.

The critical manifold CM is a very important geometric object which connects the attracting and repelling manifolds $\mathcal{S}_a$ and $\mathcal{S}_r$ of (2.44) in the unperturbed case. It can be interpreted as the concatenation of the primary weak canard of the folded node and the primary faux canard of the folded saddle, i.e. the centre manifold W^C in Figure 2.3A. Away from CM, two explicit algebraic solutions of the layer problem (2.45) are known:

$$\gamma_\pm(t_2) = \left(-\frac{1}{4}t_2^2 + \frac{1}{2}, \pm\sqrt{\alpha_2}, \frac{1}{2}t_2 \right),$$

which are extensions of the strong canard of the folded node (at $y_2 = -\delta\sqrt{\alpha_2}$) and the true canard of the folded saddle (at $y_2 = \delta\sqrt{\alpha_2}$) of the reduced flow of (2.42).

Theorem 2.14 (Existence of primary maximal canards [66, 108]). *Consider system (2.42), with $\alpha_2 > 0$. For sufficiently small $0 < \varepsilon \ll 1$, the solutions $\gamma_\pm$ of (2.45) always perturb to a maximal strong canard associated with the folded node, and a maximal true canard associated with the folded saddle.*

Trajectories exponentially close to the maximal strong or true canard will cross the fold and follow the repelling slow manifold for $\mathcal{O}(1)$ times before falling off. All other trajectories are quickly attracted to CM.

Theorem 2.15 (Existence of canards and faux canards [108]). *Consider system (2.42), with $\alpha_2 > 0$, $\alpha_2 = \mathcal{O}(1)$ and $\delta = \pm 1$. Let $\mathcal{S}_a^{\varepsilon^{1/4}}$ and $\mathcal{S}_r^{\varepsilon^{1/4}}$ denote the attracting and repelling slow manifolds of (2.44). For sufficiently small $0 < \varepsilon \ll 1$, the following holds:*

(i) *There exists a canard solution $\mathcal{O}(\varepsilon^{1/4})$ close to CM, passing through a point in $\mathcal{S}_a^{\varepsilon^{1/4}}$, and continuing on to a point in $S_r^{\varepsilon^{1/4}}$.*

(ii) *There exists a faux canard solution $\mathcal{O}(\varepsilon^{1/4})$ close to CM, passing through a point in $\mathcal{S}_r^{\varepsilon^{1/4}}$, and continuing on to a point in $S_a^{\varepsilon^{1/4}}$.*

Theorem 2.16 (Number of canards and faux canards [108]). *Consider system (2.42), with $\alpha_2 > 0$ and $\delta = \pm 1$. Suppose that a (faux) canard solution exists. Then for sufficiently small $0 < \varepsilon \ll 1$, there are $\mathcal{O}(\varepsilon^{-1/4})$ (faux) canards.*

32

2.7.6 Folded saddle-node type II canards

The local dynamics near a FSN II singularity has been studied extensively in [25, 45, 66]. Near the FSN II singularity, there exists a full system singular Andronov-Hopf bifurcation whose periodic orbits can undergo secondary bifurcations and significantly impact the local dynamics. Guckenheimer [45] studied the periodic orbits and their bifurcations in the $\mu = \mathcal{O}(\varepsilon)$ regime. Krupa and Wechselberger *et al.* [66] added to this by studying the $\mu = \mathcal{O}(\sqrt{\varepsilon})$ regime, where the periodic orbits (and their associated bifurcations) can be ignored. Finally the transition between the two regimes was dealt with in [25]. Here we summarise the results of [66], in the $\mathcal{O}(\sqrt{\varepsilon})$ regime.

The local behaviour near an FSN II singularity is captured in the normal form [66]

$$
\begin{aligned}
\dot{x} &= y - (\mu + 1)z + \mathcal{O}(x, y^2, yz, z^2, \varepsilon), \\
\dot{y} &= \frac{1}{2}\mu + a_1 y + a_2 z + \mathcal{O}(x, y^2, yz, z^2, \varepsilon), \\
\varepsilon \dot{z} &= x + z^2 + \mathcal{O}(z^3, xz^2, xyz, \varepsilon(x+y+z), \varepsilon^2),
\end{aligned}
\tag{2.47}
$$

where the explicit higher order terms guarantee a transcritical bifurcation of a folded singularity and a regular equilibrium. We assume that $(a_1 + a_2) < 0$, which ensures that the ordinary singularity is a stable node on $\mathcal{S}_a$ for $\mu < 0$, and a saddle on $\mathcal{S}_r$ for $\mu > 0$.

The blow-up transformation to the classical chart κ_2 is given by

$$
x = \varepsilon x_2, \qquad y = \sqrt{\varepsilon} y_2, \qquad z = \sqrt{\varepsilon} z_2, \qquad \mu = \sqrt{\varepsilon} \mu_2,
\tag{2.48}
$$

where (similar to the FSN I case) the parameter μ must also be rescaled. The blow-up transformation once again converts a 1-fast/2-slow system (2.47) to a 2-fast/1-slow system

$$
\begin{aligned}
\dot{x}_2 &= y_2 - z_2 + \mathcal{O}(\sqrt{\varepsilon}), \\
\dot{y}_2 &= \sqrt{\varepsilon}\left(\frac{1}{2}\mu_2 + a_1 y_2 + a_2 z_2 + \mathcal{O}(\sqrt{\varepsilon})\right), \\
\dot{z}_2 &= x_2 + z_2^2 + \mathcal{O}(\sqrt{\varepsilon}),
\end{aligned}
\tag{2.49}
$$

which is singularly perturbed. The layer problem of (2.49), which is given by

$$
\begin{aligned}
\dot{x}_2 &= y_2 - z_2, \\
\dot{z}_2 &= x_2 + z_2^2,
\end{aligned}
\tag{2.50}
$$

has a one-dimensional critical manifold

$$
CM := \left\{ (x_2, y_2, z_2) = (-y_2^2, y_2, y_2),\ y \in \mathbb{R} \right\},
\tag{2.51}
$$

and an Andronov-Hopf bifurcation at the origin. The reduced flow of (2.49) on the manifold CM is given by

$$
\dot{y}_2 = \frac{1}{2}\mu_2 + (a_1 + a_2)y_2,
\tag{2.52}
$$

which has an attracting equilibrium $y_{2,p} = -\mu_2/2(a_1 + a_2)$. Similar to the FSN I case, the reduced flow (2.52), for $\mu_2 > 0$, moves solutions through the bifurcation at the origin and

they experience a delayed loss of stability. Away from CM, an explicit algebraic solution of the layer problem (2.50) is given by

$$\gamma_+(t_2) = \left(-\frac{1}{4}t_2^2 + \frac{1}{2}, 0, \frac{1}{2}t_2\right),$$

which for $\mu > 0$ ($\mu < 0$), is an extension of the singular canard γ_s (γ_t) of the folded node (folded saddle) of the reduced flow of (2.47).

Theorem 2.17 (Existence of Primary Maximal Canard [66]). *Consider system (2.47). For sufficiently small $0 < \varepsilon \ll 1$, the solution γ_+ of (2.45) always perturbs to a maximal strong canard associated with the folded node for $\mu > 0$, and a maximal true canard associated with the folded saddle for $\mu < 0$.*

Trajectories which are exponentially close to the maximal canard will cross the fold and follow the repelling slow manifold for $\mathcal{O}(1)$ times before falling off. All other trajectories between the maximal strong canard and the fold are quickly attracted to CM, which corresponds to the primary weak canard in the folded node case, i.e. W^C in Figure 2.3B.

Theorem 2.18 (Existence of Canards [66]). *Consider system (2.47), with $\mu = \mathcal{O}(\sqrt{\varepsilon})$. Let $\mathcal{S}_a^{\sqrt{\varepsilon}}$ and $\mathcal{S}_r^{\sqrt{\varepsilon}}$ denote the attracting and repelling slow manifolds of (2.49). Then for sufficiently small $0 < \varepsilon \ll 1$, there exists a canard solution $\mathcal{O}(\sqrt{\varepsilon})$ close to CM, passing through a point in $\mathcal{S}_a^{\sqrt{\varepsilon}}$, and continuing on to a point in $S_r^{\sqrt{\varepsilon}}$.*

Theorem 2.19 (Number of Canards [66]). *Consider system (2.47), with $\mu = \mathcal{O}(\sqrt{\varepsilon})$. Then for sufficiently small $0 < \varepsilon \ll 1$, there are $\mathcal{O}(\varepsilon^{-1/2})$ canards.*

2.7.7 Folded saddle-node type III canards

A canonical model of the FSN III bifurcation is given by

$$
\begin{aligned}
\dot{x} &= -z + \delta_1(\alpha - y^2) + \mathcal{O}(\varepsilon, x, z^2, zy^2, y^4) \\
\dot{y} &= \delta_2 y(1 + \mathcal{O}(\varepsilon, x, z, y^2)) \\
\varepsilon\dot{z} &= x - z^2 + \mathcal{O}(xz^2, z^3, \varepsilon(x+z), \varepsilon^2, \varepsilon y^2)
\end{aligned}
\tag{2.53}
$$

where $0 < \varepsilon \ll 1$, $\delta_1 = \delta_2 = \pm 1$. The higher order terms generate a pitchfork bifurcation of two folded singularities and an ordinary singularity, under the variation of the parameter α. In Chapter 7 of this thesis, we will employ techniques similar to those used in the analysis of the FSN I and II [66, 108] to unravel the dynamics of system (2.53). In particular, we will establish the existence of canards and faux canards and study the delayed loss of stability phenomenon.

Chapter 3

Averaging and Floquet Theory

Neural bursting behaviour consists of a quasi steady state on a slow time scale (the silent phase), interspersed with dramatic changes on the fast time scale (the active phase of rapid oscillations). Models of bursting phenomena are typically singularly perturbed, with a natural partitioning of variables into fast and slow. Combined with GSPT, averaging is a useful tool which approximates the motion of the slow variables over the active oscillatory phase of bursting. Essentially, the averaging technique involves 'averaging out' the fast oscillations to distil the slow motion on the fast subsystem oscillatory manifold. Most importantly, the technique allows us to identify familiar objects from canard theory (such as canards, folded singularities and FSN bifurcations), but in an averaged context. The averaged counterparts of canards and folded singularities are known as torus canards and toral folded singularities, respectively.

This chapter will be devoted to a review of averaging. The structure is as follows: In Section 3.1 we first discuss basic Floquet theory, the stability of periodic orbits and their bifurcations. We then move onto classical averaging in Section 3.2, where we state and prove several fundamental theorems. In Section 3.3 we discuss how the classical averaging theorems can be applied to generic singularly perturbed systems of the form (2.2), with hyperbolic periodic orbits. In Section 3.4 we tackle the more problematic non-hyperbolic case, which leads to averaged folded singularities (toral folded singularities) and torus canards. We conclude in Section 3.5 with a description of numerical techniques used to identify and continue averaged equilibria and folded singularities.

3.1   Floquet Theory

Before we begin a review of averaging, we first present some results from Floquet theory, which deals with the stability of periodic systems in continuous time. Consider an autonomous ordinary differential equation of the form

$$\dot{x} = f(x), \tag{3.1}$$

where $x \in \mathbb{R}^k$, $f : \mathbb{R}^k \to \mathbb{R}^k$, and we assume that (3.1) has a periodic solution $\Gamma(t)$ with period T. Applying the transformation $y(t) = x(t) - \Gamma(t)$ and expanding f in a Taylor

series along $\Gamma(t)$ gives

$$\dot{y} = A(t)y, \tag{3.2}$$

where $A(t) := D_x f|_{\Gamma(t)}$, and we have neglected the higher order terms. We refer to the above as the *linearised equation*, or the *variational equation* along the periodic orbit $\Gamma(t)$. The variable y represents a small perturbation away from $\Gamma(t)$. Note that since $\Gamma(t)$ is T-periodic, $A(t)$ is also T-periodic, i.e. $A(t+T) = A(t)$. Gaston Floquet [42, 52] developed the theory that describes solutions of periodic systems of the form (3.2). Before stating the main theorems, we establish some important definitions.

Definition 3.1 (Transition matrix [24, 74])**.** Let $Y(t)$ be any fundamental matrix of (3.2), i.e. the k columns of $Y(t)$ are comprised of k linearly independent solutions of (3.2). Then the *transition matrix* or *principal fundamental matrix solution* of system (3.2) is the matrix-valued function $\Phi(t, t_0) := Y(t)Y^{-1}(t_0)$, where $t > t_0$, which is the unique solution of the matrix initial value problem

$$\frac{d}{dt}\Phi = A(t)\Phi, \qquad \Phi(t_0, t_0) = I. \tag{3.3}$$

Additionally, we have the following results:

(i) Given $\Phi(t, t_0)$, the solution of (3.2) with initial value $y(t_0) = y_0$ is simply $y(t) = \Phi(t, t_0)y_0$.

(ii) Since $Y(t)$ is invertible, so is $\Phi(t, t_0)$ and its inverse is given by

$$\Phi^{-1}(t, t_0) = \left[Y(t)Y^{-1}(t_0)\right]^{-1} = Y(t_0)Y^{-1}(t) = \Phi(t_0, t). \tag{3.4}$$

(iii) Due to uniqueness, $\Phi(t, t_0)$ satisfies

$$\Phi(t, r) = \Phi(t, s)\Phi(s, r), \tag{3.5}$$

for all $t, s, r \in \mathbb{R}$.

Remark 3.1. When A is a constant matrix, $\Phi(t, t_0) = e^{(t-t_0)A}$, but this is not true in the non-autonomous case, i.e. when $A = A(t)$.

Lemma 3.1. *The transition matrix $\Phi(t, t_0)$ of the T-periodic linearised equation (3.2) satisfies*

$$\Phi(t + T, 0) = \Phi(t, 0)\Phi(T, 0), \tag{3.6}$$

for all $t \in \mathbb{R}$.

Proof. Both $\Phi(t + T, 0)$ and $\Phi(t, 0)\Phi(T, 0)$ satisfy equation (3.3). In particular, the two equations will coincide at $t = 0$, and equating the right hand sides gives

$$\Phi(t + T, 0)\big|_{t=0} = \Phi(t, 0)\Phi(T, 0)\big|_{t=0}. \tag{3.7}$$

But the solution to equation (3.3) must be unique. Thus (3.7) must hold for all $t \in \mathbb{R}$. $\quad\square$

The value of the transition matrix Φ at period one is known as the *monodromy matrix*; its structure and eigenvalues play an important role in characterizing periodic solutions of (3.2).

Definition 3.2 (Monodromy matrix [52, 74])**.** The *monodromy matrix* M is defined as the transition matrix at period one, i.e.

$$M := \Phi(T, 0). \tag{3.8}$$

Definition 3.3 (Floquet multipliers and exponents [52, 74])**.** The eigenvalues of the monodromy matrix M, denoted by μ_i, for $i = 1, \ldots, k$, are known as the *Floquet multipliers*. The exponents ρ_i, defined by $\mu_i = e^{\rho_i T}$, are called *Floquet exponents* or *Poincaré-Lyapunov exponents*.

Remark 3.2. Note that both the Floquet multipliers μ_i and exponents ρ_i may be complex for $i = 1, \ldots, k$. Furthermore, the Floquet exponents are not unique since $\mu_i = e^{\rho_i T} = e^{(\rho_i + 2\pi i j/T)T}$ for $j \in \mathbb{Z}$. On the other hand, the Floquet multipliers are unique and an intrinsic property of system (3.2).

To understand why the monodromy matrix is so important, consider the following argument. Given an initial condition $y(0) = y_0$, the solution to (3.2) at time T is $x(T) = My_0$. To extend the solution $y(t)$ beyond $t = T$, we solve a new initial value problem

$$\dot{y} = A(t)y, \qquad y(T) = My_0. \tag{3.9}$$

By defining the variable $\bar{\tau} = t - T$, system (3.9) can be transformed to system (3.2), with initial condition $y(0) = My_0$. Thus $y(2T) = M^2 y_0$, and by extension, $y(nT) = M^n y_0$. In other words, the long term behaviour of solutions is determined by M^n.

For systems of the form (3.2), where $A(t)$ is periodic, the monodromy matrix M always has one Floquet multiplier that is trivially equal to one.

Theorem 3.1. *The monodromy matrix M, associated with the variational equation (3.2) along the periodic solution $\Gamma(t)$, always has one trivial eigenvalue $\mu_1 = 1$. The corresponding eigenvector v_1 is given by*

$$v_1 = \dot{\Gamma}(0), \tag{3.10}$$

which is tangent to the periodic orbit $\Gamma(t)$ at the point $\Gamma(0)$.

Proof. Differentiating $\dot{\Gamma}(t)$ gives

$$\frac{d}{dt} \left[\dot{\Gamma}(t) = f(\Gamma(t)) \right] = D_x f \big|_{\Gamma(t)} \dot{\Gamma}(t) = A(t)\dot{\Gamma}(t), \tag{3.11}$$

which shows that $\dot{\Gamma}(t)$ is a solution of the variational equation (3.2). By Definition 3.1, we can write $\dot{\Gamma}(t) = \Phi(t, 0)\dot{\Gamma}(0)$. Since $\Gamma(t)$ is periodic, $\dot{\Gamma}(0) = \dot{\Gamma}(T)$ and

$$\dot{\Gamma}(0) = \Phi(T, 0)\dot{\Gamma}(0). \tag{3.12}$$

Thus $v_1 = \dot{\Gamma}(0)$ is an eigenvector of the monodromy matrix, with corresponding eigenvalue (Floquet multiplier) $\mu_1 = 1$. The eigenvector $v_1 = \dot{\Gamma}(0)$ is tangent to Γ at the point $\Gamma(0)$. $\square$

Consider the solution $y(t)$ of (3.2). Then by Definition 3.1 and Lemma 3.1, $y(t + T) = \Phi(t, 0)\Phi(T, 0)y_0$, where $y_0 = y(0)$. If y_0 is an eigenvector of the monodromy matrix M with associated non-trivial Floquet multiplier μ, then

$$
\begin{aligned}
y(t + T) &= \mu\Phi(t, 0)y_0, \\
&= \mu y(t).
\end{aligned}
\tag{3.13}
$$

After one period T, the solution $y(t)$ will either expand ($\mu > 1$) or contract ($\mu < 1$) in the direction of y_0. Intuitively, the magnitude of the Floquet multiplier μ determines the stability of periodic solutions.

Definition 3.4 (Stability of periodic orbits [74]). Suppose we have a periodic solution $\Gamma(t)$ of (3.1). Let μ_i, $k = 1, \ldots, k$, denote the Floquet multipliers of $\Gamma(t)$, and ρ_i the Floquet exponents. Without loss of generality, we assume that $\mu_1 = 1$ is the trivial Floquet multiplier equal to unity; note that there is a corresponding trivial exponent $\rho_1 = 0$. Then the periodic orbit $\Gamma(t)$ is *linearly stable* if $|\mu_i| \leq 1$ ($\text{Re}(\rho_i) \leq 0$), for $i = 1, \ldots, k$. On the other hand, the orbit is *linearly asymptotically stable* if $|\mu_i| < 1$ ($\text{Re}(\rho_i) < 0$), for $i = 2, \ldots, k$.

Definition 3.5 (Local bifurcations of periodic orbits). Suppose we have a periodic solution $\Gamma(t)$ of (3.1). Let μ_i, $k = 1, \ldots, k$, denote the Floquet multipliers of $\Gamma(t)$, and ρ_i the Floquet exponents. Without loss of generality, we assume that $\mu_1 = 1$ is the trivial Floquet multiplier equal to unity. Then we have the following results:

(i) A *saddle-node bifurcation of periodic orbits* (SNPO bifurcation) occurs when a real non-trivial Floquet multiplier crosses the unit circle at $+1$.

(ii) A *period doubling bifurcation* occurs when a real Floquet multiplier crosses the unit circle at -1.

(iii) A *torus bifurcation* occurs when a pair of complex conjugate Floquet multipliers cross the unit circle.

The following theorem establishes a relationship between the Floquet multipliers and the trace of the matrix $A(t)$:

Theorem 3.2 (Abel's Theorem [74]). *The determinant of the transition matrix is*

$$
\det(\Phi(t, t_0)) = \exp\left(\int_{t_0}^{t} \text{tr}(A(s))ds\right).
\tag{3.14}
$$

Since $\det(M) = \prod_i \mu_i$, we have the following relation for the product of the Floquet multipliers (or equivalently, the sum of the Floquet exponents):

$$
\begin{aligned}
\mu_1 \ldots \mu_k &= \exp\left(\int_0^T \text{tr}(A(s))ds\right), \\
\rho_1 + \ldots + \rho_k &= \frac{1}{T}\int_0^T \text{tr}(A(s))ds.
\end{aligned}
\tag{3.15}
$$

Theorem 3.2 implies that in the planar case ($k = 2$), the non-trivial Floquet multiplier of (3.2) is simply $\mu_2 = \exp\left(\int_0^T \text{tr}(A(s))ds\right)$.

In the remainder of this section, we state and prove Floquet's two main theorems. The first theorem provides an alternative formulation of the fundamental solution matrix:

Theorem 3.3 (Floquet [52, 74]). *Consider the T-periodic linear system (3.2) with Monodromy matrix M. Let $TK = \ln M$ denote the logarithm of M, where K is a constant matrix. Then there exists a T-periodic matrix $F(t)$ such that the transition matrix is*

$$\Phi(t,0) = F(t)e^{tK}. \tag{3.16}$$

Furthermore, $F(t)$ is nonsingular for all t and continuous.

Proof. Let $\Psi(t) = \Phi(t+T,0)$. Since $A(t)$ is T-periodic, Ψ satisfies (3.2), i.e.

$$\frac{d}{dt}\Psi = A(t)\Psi, \qquad \Psi(0) = M.$$

Because Φ is the transition matrix, all solutions Ψ can be written in the form $\Psi(t) = \Phi(t,0)\Psi(0) = \Phi(t,0)M$. By Lemma 3.1,

$$\Phi(t+T,0) = \Phi(t,0)M = \Phi(t,0)e^{TK}. \tag{3.17}$$

Define

$$F(t) = \Phi(t,0)e^{-tK}, \tag{3.18}$$

which is non-singular since Φ and e^{-tK} are non-singular. Using (3.17),

$$F(t+T) = \Phi(t+T,0)e^{-(t+T)K} = \Phi(t,0)e^{TK}e^{-(t+T)K} = F(t).$$

Thus the transition matrix of (3.2) is

$$\Phi(t,0) = F(t)e^{tK},$$

where $F(t)$ is non-singular and T-periodic. It is evident from (3.18) that $F(t)$ is continuous. $\square$

If $A(t)$ is real, then the transition matrix $\Phi(T,0)$ will also be real; however, K will generally be complex. Floquet's second theorem asserts that, at the cost of doubling the period, a real analogue of (3.16) can be found:

Theorem 3.4 (Floquet [52, 74]). *Consider the T-periodic linear system (3.2) with transition matrix $\Phi(t,t_0)$. Then*

$$\Phi(t,0) = \hat{F}(t)e^{t\hat{K}}, \tag{3.19}$$

where $\hat{F}(t)$ is a real $2T$-periodic matrix, and $\hat{K}$ is a real constant matrix. Furthermore, $\hat{F}(t)$ is non-singular for all t and continuous.

Proof. The proof is similar to Theorem 3.3. For any non-singular matrix M, there exists a real matrix $\hat{K}$ such that $M^2 = e^{T\hat{K}}$ [74]. Define

$$\hat{F}(t) = \Phi(t,0)e^{-t\hat{K}}, \tag{3.20}$$

and thus we have

$$\hat{F}(t+2T) = \Phi(t+2T,0)e^{-(t+2T)\hat{K}} = \Phi(t,0)M^2 M^{-2}e^{-t\hat{K}} = \hat{F}(t),$$

which proves that $\hat{F}(t)$ is $2T$-periodic. The remaining properties of $\hat{F}(t)$ follow from definition (3.20). $\qquad\square$

3.2 Classical Averaging

3.2.1 Notation

Classical averaging is concerned with systems of the form

$$\dot{x} = f(x,t,\varepsilon), \qquad x(t_0) = a, \tag{3.21}$$

where x, $a \in D \subset \mathbb{R}^n$, t, $t_0 \in [0,\infty)$, $\varepsilon \in (0,\varepsilon_0]$, and f is sufficiently smooth. The function f can be approximated by its Taylor polynomial of degree k about the point $\varepsilon = 0$:

$$f(x,t,\varepsilon) = f_0(x,t) + \varepsilon f_1(x,t) + \ldots + \varepsilon^k f_k(x,t) + \varepsilon^{k+1} f_{[k+1]}(x,t,\varepsilon),$$

with remainder term $R_{k+1}(x,t,\varepsilon) =: \varepsilon^{k+1} f_{[k+1]}(x,t,\varepsilon)$. Employing a notation similar to [92], the coefficients of the polynomial terms $P_k(x,t,\varepsilon)$ are given by

$$f_k(x,t) := \frac{f^{(k)}(x,t,0)}{k!},$$

and the coefficient of the remainder term is

$$f_{[k+1]}(x,t,\varepsilon) := \frac{f^{(k+1)}(x,t,\varepsilon)}{(k+1)!}, \qquad 0 < \varepsilon < x.$$

Thus the square brackets are used to differentiate the remainder term from a regular Taylor polynomial term.

3.2.2 Periodic averaging

Although averaging can be applied to quasi-periodic and even aperiodic systems, we restrict our attention to the periodic case. The goal of classical periodic averaging is to solve a perturbation problem (3.21) in so-called *standard form*,

$$\dot{x} = \varepsilon f_1(x,t) + \varepsilon^2 f_{[2]}(x,t,\varepsilon), \qquad x(0) = a, \tag{3.22}$$

where f_1 and $f_{[2]}$ are T-periodic functions of time t. We also assume that f_1 is Lipschitz on the domain $\overline{D}$, with Lipschitz constant L_{f_1}.

Definition 3.6. Given system (3.22), the *truncated averaged equation* is defined as

$$\dot{z} = \varepsilon \bar{f}_1(z), \qquad z(0) = a, \tag{3.23}$$

where

$$\bar{f}_1(z) = \frac{1}{T} \int_0^T f_1(z, s) ds. \tag{3.24}$$

Note that z is fixed in the above integration.

Does the solution $z(t)$ of (3.23) provide a good approximation to the solution $x(t)$ of the original system (3.22)? In short, the main averaging theorem establishes that, under appropriate conditions, $z(t)$ remains $\mathcal{O}(\varepsilon)$ close to $x(t)$ for times that are $\mathcal{O}(1/\varepsilon)$. In the remainder of this section we will state the averaging theorems from [92], and associated lemmas needed to prove them. Note that there are different proofs of the averaging theorems. We will focus on the classical proof which utilises near-identity transformations, as this will become useful in subsequent sections of this thesis.

Definition 3.7 (Near-identity transformation [92])**.** A near identity transformation is a family of transformations, which depend on ε, and reduce to the identity when $\varepsilon = 0$. In the context of averaging, a near-identity transformation for (3.22) is given by

$$x = y + \varepsilon u_1(y, t, \varepsilon) =: U(y, t, \varepsilon), \tag{3.25}$$

where u_1 is T-periodic function of time.

The following lemmas and theorems will deal with proving that an appropriate function u_1 exists, such that (3.25) transforms the original system (3.22) into what is called the full averaged equation.

Definition 3.8. For an appropriate function u_1, the near-identity transformation (3.25) transforms the original system (3.22) into the *full averaged equation*

$$\dot{y} = \varepsilon \bar{f}_1(y) + \varepsilon^2 f_{[2]}^*(y, t, \varepsilon), \tag{3.26}$$

for some T-periodic function $f_{[2]}^*$ generated by (3.25). Notice that the truncated averaged equation (3.23) is obtained by neglecting the $\mathcal{O}(\varepsilon^2)$ term in (3.26).

Lemma 3.2 ([92])**.** *Consider the near-identity transformation (3.25) as a smooth mapping $y \mapsto U(y, t, \varepsilon)$, $y \in D$, which depends on t and ε. For any bounded and connected open set $D \subset \mathbb{R}^n$ there exists an ε_0 such that for all $t \in \mathbb{R}$ and all $0 \leq \varepsilon \leq \varepsilon_0$, the mapping is injective (one-to-one). The inverse mapping is given by*

$$y = x + \varepsilon v_1(x, t, \varepsilon) =: V(x, t, \varepsilon), \tag{3.27}$$

and is smooth in (x, t, ε).

41

Remark 3.3. The proof below makes use of the fact if f_1 is Lipschitz on D with constant L_{f_1}, then u_1 is Lipschitz on D with constant $2TL_{f_1}$, where T is the period. This is formally proved in Lemma 3.3.

Proof. Suppose $U(y_1, t, \varepsilon) = U(y_2, t, \varepsilon)$. Then $y_1 + \varepsilon u_1(y_1, t, \varepsilon) = y_2 + \varepsilon u_1(y_2, t, \varepsilon)$ and

$$
\begin{aligned}
\|y_2 - y_1\| &= \varepsilon \|u_1(y_1, t, \varepsilon) - u_1(y_2, t, \varepsilon)\|, \\
&\leq \varepsilon L_{u_1} \|y_1 - y_2\|.
\end{aligned}
$$

If $L_{u_1}\varepsilon < 1$, we have shown that unless $\|y_2 - y_1\|$ vanishes, it is less than itself. Thus for sufficiently small $0 \leq \varepsilon \leq 1/L_{u_1}$, we have a contradiction, and U must be injective. Hence U maps D invertibly onto $U(D, t, \varepsilon)$, and the inverse V exists. Now we check the form of the inverse and its smoothness.

Since $D_y U(y, t, 0) = I_n$, we can use the implicit function theorem to prove that $x = U(y, t, \varepsilon)$ has a locally smooth inverse. Each $y_0 \in D \subset \mathbb{R}^n$ has a neighbourhood on which U is invertible for ε in some interval which depends on y_0. Since the closure of D is compact, it can be covered by a finite number k of these neighbourhoods, with bounds $\varepsilon_1, \ldots, \varepsilon_k$ on ε. If we define $\varepsilon_0 := \min\{1/L_{u_1}, \varepsilon_1, \ldots, \varepsilon_k\}$, then the local inverses (which are smooth and have the form (3.27)) exist and must coincide with the global inverse V. $\qquad\square$

Lemma 3.3 ([92]). *There exist non-unique mappings U such that (3.25) transforms (3.22) to (3.26). In particular, u_1 may be taken to have Lipschitz constant $2TL_{f_1}$, where T is the period.*

Proof. First assume that the desired u_1 exists, and that equations (3.22) and (3.26) are related by the coordinate transformation $x = U(y, t, \varepsilon)$. Then by the chain rule

$$
\begin{aligned}
\dot{x} &= \dot{U}(y, t, \varepsilon) + D_y U(y, t, \varepsilon)\dot{y}, \\
&= \varepsilon \dot{u}_1(y, t, \varepsilon) + [I + \varepsilon D_y u_1(y, t, \varepsilon)] \left[\varepsilon \bar{f}_1(y) + \varepsilon^2 f_{[2]}^*(y, t, \varepsilon) \right].
\end{aligned}
$$

Taylor expanding $f_1(U(y, t, \varepsilon), t)$ about $\varepsilon = 0$ yields

$$
\varepsilon f_1(y, t) + \mathcal{O}(\varepsilon^2) = \varepsilon \dot{u}_1(y, t, \varepsilon) + \varepsilon \bar{f}_1(y) + \mathcal{O}(\varepsilon^2),
$$

and extracting leading order term in ε gives

$$
\dot{u}_1(y, t, \varepsilon) = f_1(y, t) - \bar{f}_1(y), \tag{3.28}
$$

which is known as the *homological equation* of averaging theory. Integrating (3.28), we obtain the solution

$$
u_1(y, t, \varepsilon) = \int_0^t \left[f_1(y, s) - \bar{f}_1(y) \right] ds + \kappa_1(y, \varepsilon). \tag{3.29}
$$

Notice that the right hand side of (3.28) has zero mean (when integrating over the period T). It follows that (3.29) will be T-periodic in time for any choice of the function κ_1.

42

To formally prove the lemma, we simply reverse our steps. Given equation (3.22) and taking u_1 as in (3.29), we seek an equation for $\dot{y}$. If follows that the equation in $\dot{y}$ must have the form (3.26) for some $f_{[2]}^*$. Finally we prove that if $\kappa_1(y,\varepsilon) = 0$, then u_1 is Lipschitz with constant $2TL_{f_1}$. It can be easily shown that $\bar{f}_1$ has the same Lipschitz constant as f_1. Since u_1 is periodic, for each t there exists a $\tilde{t} \in [0, T]$ such that $u_1(y, t, \varepsilon) = u_1(y, \tilde{t}, \varepsilon)$. Thus

$$
\begin{aligned}
\left\| u_1(y_1, t, \varepsilon) - u_1(y_2, t, \varepsilon) \right\| &= \left\| u_1(y_1, \tilde{t}, \varepsilon) - u_1(y_2, \tilde{t}, \varepsilon) \right\|, \\
&\leq \int_0^{\tilde{t}} \left(\left\| f_1(y_1, s) - f_1(y_2, s) \right\| + \left\| \bar{f}_1(y_1) - \bar{f}_1(y_2) \right\| \right) ds, \\
&\leq \int_0^{\tilde{t}} 2L_{f_1} \left\| y_1 - y_2 \right\| = 2L_{f_1} \tilde{t} \left\| y_1 - y_2 \right\|, \\
&\leq 2L_{f_1} T \left\| y_1 - y_2 \right\|,
\end{aligned}
$$

which finishes the proof of the lemma. $\qquad \square$

Remark 3.4. Taking $\kappa_1(y, \varepsilon) = 0$ is advantageous since $U(y, 0, \varepsilon) = y$. In other words, initial conditions at time $t = 0$ don't need to be transformed when changing coordinates from x to y. Due to the periodicity of u_1, $U(y, mT, \varepsilon) = y$ at each *stroboscopic time* mT, $m \in \mathbb{Z}$. Thus choosing $\kappa_1(y, \varepsilon) = 0$ is known as *stroboscopic averaging*.

Lemma 3.4 ([92]). *Let $x(t, \varepsilon)$ denote the solution of (3.22) with initial condition $x(0, \varepsilon) = a$, let $y(t, \varepsilon)$ denote the solution of the full averaged equation (3.26) with initial condition $y(0, \varepsilon) = V(a, 0, \varepsilon) = a + \varepsilon v_1(a, 0, \varepsilon)$, and let $z(t, \varepsilon)$ denote the solution of the truncated averaged equation (3.23) with $z(t, 0) = a$. Then $y(t, \varepsilon)$ and $z(t, \varepsilon)$ satisfy*

$$
\|y(t, \varepsilon) - z(t, \varepsilon)\| = \mathcal{O}(\varepsilon), \tag{3.30}
$$

for time $\mathcal{O}(1/\varepsilon)$. The solution $z(t, \varepsilon)$ is called the first approximation *to $x(t, \varepsilon)$.*

Proof. Writing $y(0, \varepsilon) = a + \varepsilon v_1(a, 0, \varepsilon) = a + \varepsilon b(\varepsilon)$, the solutions $y(t, \varepsilon)$ and $z(t, \varepsilon)$ are given by

$$
y(t, \varepsilon) = a + \varepsilon b_1(\varepsilon) + \int_0^t \left(\varepsilon \bar{f}_1(y(s, \varepsilon), s) + \varepsilon^2 f_{[2]}^*(y(s, \varepsilon), s, \varepsilon) \right) ds,
$$

$$
z(t, \varepsilon) = a + \int_0^t \varepsilon \bar{f}_1(z(s, \varepsilon)) ds.
$$

Define $E(t, \varepsilon) = y(t, \varepsilon) - z(t, \varepsilon)$. Since f_1 is Lipschitz on D with constant L_{f_1} (and $\bar{f}_1$ has the same Lipschitz constant), we have

$$
\|E(t, \varepsilon)\| \leq \varepsilon \|b(\varepsilon)\| + \varepsilon L_{f_1} \int_0^t \|E(s, \varepsilon)\| ds + \varepsilon^2 M t, \tag{3.31}
$$

where M is the bound for $f_{[2]}^*$ on $\bar{D}$. The result follows by applying the specific Gronwall inequality from Lemma 3.6 in Section 3.6. $\qquad \square$

Building on the above Lemma, we can finally prove the classical averaging theorem.

Theorem 3.5 (Classical averaging theorem [92]; see also [47]). *Let $x(t, \varepsilon)$ denote the solution of (3.22) with initial condition $x(0, \varepsilon) = a$, and let $z(t, \varepsilon)$ denote the solution of (3.23) with $z(t, 0) = a$. Then the solutions $x(t, \varepsilon)$ and $z(t, \varepsilon)$ satisfy the estimate*

$$\|x(t, \varepsilon) - z(t, \varepsilon)\| = \mathcal{O}(\varepsilon),$$

for time $\mathcal{O}(1/\varepsilon)$.

Proof. By the triangle inequality,

$$\|x(t, \varepsilon) - z(t, \varepsilon)\| \le \|x(t, \varepsilon) - y(t, \varepsilon)\| + \|y(t, \varepsilon) - z(t, \varepsilon)\|.$$

The second term is $\mathcal{O}(\varepsilon)$ for time $\mathcal{O}(1/\varepsilon)$ by Lemma 3.4. Since $x(t, \varepsilon) = U(y(t, \varepsilon), t, \varepsilon)$, the first term is $\mathcal{O}(\varepsilon)$ for all time. $\qquad\square$

3.3 Averaging in a Slow/Fast Context

Recall the generic singularly perturbed system (2.2)

$$\begin{aligned} x' &= \varepsilon g(x, z, \varepsilon), \\ z' &= f(x, z, \varepsilon), \end{aligned}$$

from Section 2.1. Even though (2.2) is not in the so-called standard form (3.22) to which classical averaging might be applied, averaging is still a very useful tool in understanding the slow dynamics near a family of layer problem periodic orbits. We assume that the layer problem of (2.2), which is given by

$$z' = \frac{dz}{dt} = f(x, z, 0), \tag{3.32}$$

has periodic solutions $z(t, x) = \gamma(t, x)$ with period $T(x)$, which depend on x. We assume that the set of all periodic solutions forms a continuous family or manifold, parametrised by the slow variable x,

$$\mathcal{P} := \left\{ (x, z) \in \mathbb{R}^{n+m} : z = \gamma(t; x), \ \gamma'(t; x) = f(x, \gamma(t; x), 0), \ \gamma(t; x) = \gamma(t + T; x) \right\}, \tag{3.33}$$

where the period $T(x)$ is finite and non-zero, i.e. $T(x)$ is bounded above and below by some constants T_L and T_U. We assume that each orbit $\gamma(t, x)$ is hyperbolic (with all non-trivial Floquet multipliers $|\mu| \ne 1$); in other words, each orbit is asymptotically stable, unstable or of saddle type, and there are no bifurcations such as a SNPO.

Now we may substitute $z(t, x) = \gamma(t, x)$ into the equation for $\dot{x}$ in the reduced problem (2.3), and integrate (or average) over the period $T(y)$,

$$\dot{X} = \frac{1}{T(X)} \int_0^{T(X)} g(X, \gamma(s, X), 0) ds =: \bar{g}(X). \tag{3.34}$$

We refer to (3.34) as the *averaged reduced problem*. Intuitively, the averaging procedure 'averages out' the fast rotations of γ to distil out the slow dynamics (3.34) near the manifold of periodic orbits $\mathcal{P}$.

3.3.1 Two fast variables

In this section we will prove the classical averaging theorem [83] for singularly perturbed systems with $z \in \mathbb{R}^2$. Note that [83] and other frequently cited literature [8, 68] apply a change of variables $t = T(X)\theta$ to (3.34). While convenient in other settings (e.g. adding stochastic forcing), it is not essential and we omit this step in the theorem and subsequent proof. The pertinent aspect of the theorem is that z and x remain $\mathcal{O}(\varepsilon)$ close to γ and X, respectively.

Theorem 3.6 ([83]; see also [8, 68])**.** *Consider a singularly perturbed system of form (2.2) with $z \in \mathbb{R}^2$. Assume that the layer problem (3.32) has a family of periodic orbits (3.33), which are stable. Assume that the solution $x(\tau)$ on the slow time scale, with initial condition $x(0) = x_0$, stays inside D_0 for $0 \leq \tau \leq \tau_1$. Let z_0 be sufficiently close to $\gamma(\theta_0, x_0)$ for some θ_0. Then the following estimates hold:*

$$x(\tau) = X(\tau) + \mathcal{O}(\varepsilon),$$
$$z(\tau) = \gamma(\theta(\tau), X(\tau)) + \mathcal{O}(\varepsilon), \tag{3.35}$$

for $\varepsilon|\log \varepsilon| \leq \tau \leq \tau_1$.

Remark 3.5. Much of this proof is adapted from [104], which deals with averaging near an SNPO bifurcation. This case will be addressed later in Section 3.4.

Proof. Define the unit tangent $p(t, x) \in \mathbb{R}^2$ and unit normal $n(t, x) \in \mathbb{R}^2$ vectors to the periodic orbit $z = \gamma(t, x)$ as follows:

$$p(t, x) = \frac{f(x, \gamma(t, x), 0)}{\|f(x, \gamma(t, x), 0)\|}, \qquad n(t, x) = Jp(t, x), \tag{3.36}$$

where J is the skew-symmetric matrix

$$J = \begin{pmatrix} 0 & 1 \\ -1 & 0 \end{pmatrix}.$$

We begin with the coordinate transformation

$$z = \gamma(t, x) + rn(t, x), \tag{3.37}$$

where $r \in \mathbb{R}$ represents a small radial perturbation away from the periodic orbit $\gamma(t, x)$, in the direction of the unit normal vector $n(t, x)$. Differentiating (3.37) gives

$$z' = f(x, \gamma, 0) + r'n + rn', \tag{3.38}$$

since γ satisfies (3.32), i.e. $\gamma' = f(x, \gamma, 0)$. Using (3.38) and Taylor expanding $f(x, z, \varepsilon)$ and $g(x, z, \varepsilon)$ in (2.2) about $(z, \varepsilon) = (\gamma, 0)$ yields the following system:

$$x' = \varepsilon \left(g(x, \gamma, 0) + D_z g(x, \gamma, 0)nr + \mathcal{O}\left(\varepsilon, r^2\right) \right),$$
$$r'n + rn' = D_z f(x, \gamma, 0)nr + \mathcal{O}\left(\varepsilon, r^2\right). \tag{3.39}$$

Notice that since $n \cdot n = 1$, it follows that $n \cdot n' = 0$. Thus to eliminate n' we project the fast variables onto the unit normal vector, i.e. left multiply the equation in r' and n' by n^T, which gives

$$
\begin{aligned}
x' &= \varepsilon \left(g(x, \gamma, 0) + D_z g(x, \gamma, 0) nr + \mathcal{O}\left(\varepsilon, r^2\right) \right), \\
r' &= n^T D_z f(x, \gamma, 0) nr + \mathcal{O}\left(\varepsilon, r^2\right).
\end{aligned}
\tag{3.40}
$$

For ease of notation, we define the coefficients

$$
\begin{aligned}
a(t; x) &= n^T D_z f(x, \gamma, 0) n, \\
\tilde{b}(t; x) &= D_z g(x, \gamma, 0) n.
\end{aligned}
$$

Now we average the fast radial motion in (3.40) over the period $T(x)$. Formally, there exists a near-identity coordinate transformation of the form

$$
r = \alpha(t; x) R + \mathcal{O}(R^2), \qquad \alpha \in \mathbb{R},
$$

where R is small, which transforms (3.40) to

$$
\begin{aligned}
x' &= \varepsilon \left(g(x, \gamma, 0) + \tilde{b}\alpha R + \mathcal{O}\left(\varepsilon, R^2\right) \right), \\
R' &= \bar{a} R + \mathcal{O}\left(\varepsilon, R^2\right),
\end{aligned}
\tag{3.41}
$$

where $\bar{a}(x)$ is the average of $a(t; x)$ over the period $T(x)$. The coefficient α is chosen so that

$$
\frac{1}{\alpha} \frac{d\alpha}{dt} = a(t; x) - \frac{1}{T(x)} \int_0^{T(x)} a(t; x) dt, \qquad \alpha(0) = 1.
$$

Let $b := \tilde{b}\alpha$. We average the slow motion by introducing the near-identity coordinate transformation

$$
x = u + \varepsilon w(t, R, u).
\tag{3.42}
$$

In a similar fashion to the radial averaging, the function w can be expanded as a power series in R, and the coefficients chosen such that (3.43) transforms (3.41) to

$$
\begin{aligned}
u' &= \varepsilon \left(\bar{g} + \bar{b} R + \mathcal{O}\left(\varepsilon, R^2\right) \right), \\
R' &= \bar{a} R + \mathcal{O}\left(\varepsilon, R^2\right).
\end{aligned}
\tag{3.43}
$$

Specifically, the components of w are chosen such that

$$
\frac{dw_j}{dt} = g_j - \bar{g} + (b_j - \bar{b}_j) R + \mathcal{O}(\varepsilon, R^2), \qquad j = 1, 2.
$$

The averaging procedure has produced a slow/fast system (3.43) with critical manifold $\mathcal{S} := \{R = 0\}$. If follows from Lemma 3.7 that $\bar{a} = \rho_2$, the non-trivial Floquet exponent. We assume that $\rho_2 \neq 0$, i.e. $\mathcal{P}$ is not folded. Since we assumed that the periodic orbit γ is stable, $\rho_2 < 0$ and the critical manifold is attracting. Fenichel theory guarantees the existence of a slow manifold $\mathcal{O}(\varepsilon)$ close to $\mathcal{S}$. Thus in an $\mathcal{O}(\varepsilon)$ neighbourhood of the critical manifold, the classical averaging theorem applies (see Theorem 3.5) and the estimates follow.

Remark 3.6. When the periodic orbit γ is unstable, the proof can be similarly constructed, except in reverse time. Thus trajectories will approach the critical manifold $R = 0$, and the classical averaging estimates still hold.

When γ is of saddle type, the statement of Theorem 3.6 needs to be modified slightly. Instead of the initial condition z_0 being sufficiently close to $\gamma(\theta_0, x_0)$, the trajectory $(x, \gamma(t; x))$ must be contained in the fibers of the stable or unstable manifold of $\mathcal{P}$. In other words, let $(x, \gamma(t; x)) \in W^s(\mathcal{P})$ or $(x, \gamma(t; x)) \in W^u(\mathcal{P})$. With that minor modification, the proof follows. Note that in the case $(x, \gamma(t; x)) \in W^u(\mathcal{P})$, time needs to be reversed as discussed above.

$\square$

3.4   Averaging in the Non-Hyperbolic Case

The averaging procedure outlined in Section 3.3.1 relies on the fact that the periodic orbit γ is hyperbolic. Clearly this breaks down at an SNPO bifurcation, i.e. when $\mathcal{P}$ is folded. In a recent study, Vo [104] (see also [107]) addressed this issue for $m = 2$ fast variables and any number of slow variables $n \in \mathbb{N}$. Here we provide a summary of the essential results.

Consider system (2.1) with $m = 2$ fast variables. We make the following assumptions:

(i) Assume that the layer problem (2.3) has a manifold of limit cycles $\mathcal{P}$, as defined by (3.33), with finite non-zero period T.

(ii) Assume that $\mathcal{P}$ is folded, i.e. possess a manifold of SNPOs,

$$\mathcal{P}_F := \{(x, z) \in \mathcal{P} : \rho_2 = 0\},$$

where ρ_2 is the non-trivial Floquet exponent. Furthermore, assume that $\mathcal{P}$ is non-degenerate, and can be partitioned into attracting ($\rho_2 < 0$) and repelling ($\rho_2 > 0$) subsets (separated by $\mathcal{P}_F$), i.e. $\mathcal{P} = \mathcal{P}_a \cup \mathcal{P}_F \cup \mathcal{P}_r$.

(iii) Assume that the critical manifold $\mathcal{S}$ of (2.3) and $\mathcal{P}$ are disjoint.

Theorem 3.7 ([104]). *Consider system (2.2), with $n = 2$ slow variables, under assumptions (i)–(iii). Let $(x, \gamma(t; x)) \in \mathcal{P}_F$. Then there exists sequence of near-identity transformations which, in a neighbourhood of $(x, \gamma(t; x))$, transform (2.2) to the $(n+1)$-dimensional slow/fast system*

$$\begin{aligned}
u' &= \varepsilon \left(\bar{g} + \bar{d}R + \bar{e}u + \mathcal{O}\left(\varepsilon, R^2, Ru, u^2\right) \right) =: G(R, u, \varepsilon), \\
R' &= \bar{a}^T u + \bar{b}R^2 + \bar{c}^T Ru + \mathcal{O}\left(\varepsilon, R^3, R^2u, u^2\right) =: F(R, u, \varepsilon).
\end{aligned} \tag{3.44}$$

Proof. The proof is similar to the hyperbolic case in Theorem 3.6, which we have already proven in detail. We give a short outline:

As in the hyperbolic case, the idea is to make a coordinate transformation (3.37) to switch to a coordinate frame that moves with the limit cycle γ, and Taylor expand f and g about $(x, z, \varepsilon) = (0, \gamma, 0)$. It follows from Lemma 3.7 that the average of the linear radial term is zero, and it can be removed via another coordinate transformation. Finally, the fast oscillations are averaged out via a series of near-identity coordinate transformations. We refer the reader to [104] for further details. $\square$

As a result of Theorem 3.7, we can study the properties of the averaged radial system (3.44) using Fenichel theory and other familiar techniques from Chapter 2. Objects such as the critical manifold $\mathcal{S}$ and the manifold of fold bifurcations $\mathcal{F}$ are defined in the usual manner:

$$\mathcal{S} := \left\{ (R, u) \in \mathbb{R}^{1+m} : F(R, u, 0) = 0 \right\},$$
$$\mathcal{F} := \{ (R, u) \in \mathcal{S} : F_R(R, u, 0) = 0 \}.$$

Definition 3.9 (Toral folded singularities [104])**.** The set of folded singularities $\mathcal{M}$ of (3.44) is defined as

$$\mathcal{M} := \{ (R, u) \in \mathcal{F} : (D_u F)G = 0 \}.$$

Thus the original system (2.2) possess a *folded singularity of periodic orbits* or *toral folded singularity*, if it has a periodic orbit $(x, \gamma(t; x)) \in \mathcal{P}_F$ such that

$$\bar{a} \cdot \bar{g} = 0, \tag{3.45}$$

where $\bar{a}$ and $\bar{g}$ are the averaged coefficients in (3.44).

In the same manner as folded singularities, toral folded singularities are classified based on the two non-zero eigenvalues of the desingularised flow of (3.44); see Definition 2.10.

Condition (3.45) is the averaged analogue of the violation of transversality (2.19): the projection of the averaged flow along $\mathcal{P}$ onto the averaged slow variable subspace is tangent to the projection of $\mathcal{P}_F$. The toral folded singularity allows the averaged radial flow to cross the fold, just like a folded singularity. This leads to the definition of singular torus canards.

Definition 3.10 (Singular torus canards [104])**.** Suppose system (2.2), under Assumptions (i)–(ii), possess a toral folded singularity. A *singular (faux) torus canard* is a singular (faux) canard solution of the averaged radial system (3.44).

While the results of [104] are an important theoretical step forward in the extension of canard theory to the torus canard case, many open problems remain. Most notable is the fact that the proof of Theorem 3.7 breaks down for systems with more than two fast variables.

3.5 Numerics: Averaging in slow/fast systems

The averaging procedure outlined in Theorem 3.7 produced an explicit averaged reduced normal form (3.44), which is an essential step needed in the proof of the theorem. From this normal form, toral folded singularities are easily defined (see Definition 3.9). However, computing the averaged coefficients of (3.44) can prove cumbersome and tedious (though it has been done for a selection of models [104]). In light of this, we return to the original definition of the averaged reduced system given in (3.34). In an effort to find a more simple and robust numerical implementation of averaging, we focus on directly simulating the averaged slow vector field. Numerical continuation facilitates the computation of averaged nullclines and equilibria as zeros of the averaged vector field. Since we are not computing

the averaged coefficients in (3.45), the definition of toral folded singularities needs to be tweaked before we can detect them.

Consider a standard singularly perturbed system of the form (2.1), with slow variable $x \in \mathbb{R}^2$, and fast variable $z \in \mathbb{R}^m$. Assume that the layer problem has a family of periodic orbits (3.33).

3.5.1 Averaged nullclines

The averaged nullclines can be computed by reformulating the layer problem of (2.1) as a boundary value problem (BVP), with m periodic boundary conditions,

$$\dot{z} = T \cdot f(x, z, 0), \qquad z(0) = z(1), \tag{3.46}$$

where $t \in [0, 1]$. Since the interval of periodicity is rescaled to the unit interval, the period T becomes an explicit parameter in (3.46). To guarantee uniqueness and fix the phase of a periodic solution, we impose the integral phase condition

$$\int_0^1 (z(t; x) - \tilde{z}(t; x))^T \tilde{z}_t(t; x) dt = 0, \tag{3.47}$$

where $\tilde{z}(t; x)$ refers to the layer problem solution at the previous continuation step. Finally, we impose one of the following integral constraints:

$$\int_0^1 g_1(x_1, x_2, z(t; x_1, x_2), 0) \, dt = C_1, \tag{3.48}$$

$$\int_0^1 g_2(x_1, x_2, z(t; x_1, x_2), 0) \, dt = C_2, \tag{3.49}$$

where $C_{1,2} = 0$. System (3.46), subject to constraints (3.47)–(3.48) with $C_1 = 0$, defines the x_1 averaged nullcline, in the slow (x_1, x_2)-plane. The problem is easily implemented in the software package AUTO [34] as a two-point BVP, with three free continuation parameters $\{T, x_1, x_2\}$. The x_2 averaged nullcline is computed by swapping constraint (3.48) for (3.49), with $C_2 = 0$.

3.5.2 Averaged equilibria

In any phase plane analysis, the intersection of nullclines naturally define equilibria of the system. The same is true in this case with regard to the averaged nullclines – their intersections give averaged equilibria. Using a similar boundary value set up as in the previous section, we can easily identify and continue the averaged equilibria with respect to a system parameter.

Consider the BVP defined by equations (3.46) and (3.47), subject to integral constraints (3.48) and (3.49), with $C_{1,2} = 0$. Appropriate starting data can be obtained by identifying an intersection of the averaged nullclines and sampling a solution from AUTO (or continuing until $C_{1,2} = 0$). The implementation described above naturally facilitates the continuation of any averaged equilibria with respect to a system parameter λ; the active continuation parameters would be $\{T, x_{1,2}, \lambda\}$. Any additional bifurcations flagged by AUTO while continuing in λ can easily be continued with respect to a second system parameter, thus enabling the construction of two-parameter bifurcation diagrams.

3.5.3 Toral folded singularities

Computing the averaged (toral) folded singularities is more complicated. For manifolds of equilibria, we know that at a folded singularity the transversality condition (2.19) is violated. Recall that violation of transversality is geometrically equivalent to a tangency of the reduced flow and the fold (projected onto the slow subspace); see Section 2.3. The averaged version of this tangency condition is given by (3.45) – although this only formally holds for $m = 2$ fast variables. We adapt the geometric interpretation of (toral) folded singularities to facilitate their detection in AUTO. Note that the method described below only works for $n = 2$ slow variables.

Let $\hat{\boldsymbol{n}}(x_1, x_2)$ be the unit normal vector to $\mathcal{P}_F$, the SNPO curve from the layer problem, projected onto the slow (x_1, x_2)-plane. Let $\boldsymbol{a}(x_1, x_2) := (a_1(x_1, x_2), a_2(x_1, x_2))^T$ denote the averaged slow vector field (3.48)–(3.49), and $\hat{\boldsymbol{a}}$ the normalised vector. Then, using a dot product condition, we define the set of averaged (toral) folded singularities as

$$\mathcal{M} := \{(x_1, x_2, z) \in \mathcal{P}_F \,\big|\, \mathcal{D} := \hat{\boldsymbol{n}}(h_1, h_2)^T \hat{\boldsymbol{a}}(h_1, h_2) = 0\}, \tag{3.50}$$

where $\mathcal{D} : \mathbb{R}^2 \to \mathbb{R}$. For $n = 2$ slow variables, $\mathcal{P}_F$ is a one-dimensional manifold, and projected onto the slow subspace it is simply a curve in the (x_1, x_2)-plane. Thus the normal vector can be written as

$$\boldsymbol{n}(x_1, x_2) = \begin{pmatrix} dx_2 \\ -dx_1 \end{pmatrix}.$$

To identify a toral folded singularity, we implement system (3.46) extended by

$$\begin{aligned} y_1' &= 0, \\ y_2' &= 0, \end{aligned} \tag{3.51}$$

where y_1 and y_2 act as dummy variables. Once again we impose the integral phase condition (3.47), and the integral constraints (3.48)–(3.49), which keep track of the averaged slow vector field. Using two integral constraints, we assign the value of x_1 and x_2 to the dummy variables y_1 and y_2:

$$\int_0^1 y_1 \, dt = x_1, \qquad \int_0^1 y_2 \, dt = x_2, \tag{3.52}$$

which alternatively could be achieved using boundary conditions. Finally we implement the dot product condition (3.50) via the integral constraint

$$\int_0^1 ((y_2 - \tilde{y}_2)C_1 - (y_1 - \tilde{y}_1)C_2) \, dt = \tilde{C}, \tag{3.53}$$

where $\tilde{y}$ denotes the solution y (i.e. x) at the previous continuation step. Note that for a sufficiently small step size, $(y - \tilde{y}) \approx dx$. We refer to $\{(3.46) - (3.49), (3.51) - (3.53)\}$ as the *extended system*.

In AUTO, we first identify the fold in the BVP $\{(3.46) - (3.49)\}$, which corresponds to the SNPO of (2.3). This fold curve is continued in (x_1, x_2) under the extended system, with

active continuation parameters $\{T, \tilde{C}, C_{1,2}, x_{1,2}\}$. A toral folded singularity is flagged when $\tilde{C} = 0$. The above implementation provides a quick and easy way to locate a toral folded singularity for a fixed set of system parameters. However, the toral folded singularities do not form solutions of the zero problem and thus it is not possible to continue them with respect to a system parameter in AUTO. Alternatively, we can set up a grid in parameter space, locate the toral folded singularity at each grid point, and then interpolate to produce a smooth 'bifurcation curve'. This is not ideal for toral folded singularity continuation, and we turn our attention to formulating a better numerical continuation method.

3.5.4 Continuation of toral folded singularities

The basic approach to toral folded singularity continuation is to set up two copies of the layer problem period orbit $\gamma(t; x)$, with a fixed (small) distance between them. This allows for the computation of the normal vector $\boldsymbol{n}$ while continuing along the SNPO curve. However, simultaneously continuing two periodic orbits requires an explicit implementation of an SNPO condition for both orbits in AUTO. To resolve this issue, we first implement the variational equation and compute the Floquet multipliers (and eigenvectors).

Recall that any solution $y(t)$ of the variational equation (3.2) satisfies $y(T) = My(0)$, and a multiplier (eigenvalue) μ of M satisfies $u(T) = \mu u(0)$. Let μ_i be the ith Floquet multiplier associated with $\gamma(t; x)$, and let $u_i \in \mathbb{R}^m$ be the associated eigendirection of the monodromy matrix. Then it follows that (μ_i, u_i) is a solution of the following BVP:

$$\begin{aligned}
\dot{u}(t) &= T(x)D_z f(x, z(t; x), 0)u(t), \\
u(1) &= \mu u(0), \\
u(0)^T u(0) &= h,
\end{aligned} \tag{3.54}$$

where $t \in [0, 1]$, and $z(t; x)$ is the periodic orbit segment generated by implementing $\{(3.46), (3.47)\}$.

Setting $\mu_i = e^{\rho_i}$ and $w_i(t) = e^{\rho_i t}u_i(t)$ transforms (3.54) to the equivalent BVP

$$\begin{aligned}
\dot{w}(t) &= T(x)D_z f(x, z(t; x), 0)w(t) + \ln|\mu|w(t), \\
w(1) &= \text{sgn}(\mu)w(0), \\
w(0)^T w(0) &= h,
\end{aligned} \tag{3.55}$$

which improves the numerical stability of the computation. The above BVP has a trivial solution $(\mu, w) = (0, 0)$ for $h = 0$, which forms the starting point. As μ is continued, Floquet multipliers μ_i are flagged as branch points, from which emanate secondary solution families (μ_i, w) with $h \neq 0$. For this particular problem, we continue until μ_2, the non-trivial Floquet multiplier closest to the unit circle, is flagged. The normalization $h = 1$ uniquely determines the solution (μ_2, w_2). The method described above is utilised in the continuation of point-to-cycle connections; we refer the reader to [35, 61] for further details.

After normalization, we continue in μ_2 until we reach the SNPO, which is defined by $\ln|\mu_2| = 0$. We then extend system $\{(3.46), (3.47), (3.55)\}$ and create a 'second copy' of the

problem,

$$\dot{z}_c = T_c(x_c)f(x_c, z_c, 0),$$
$$z_c(0) = z_c(1),$$
$$\int_0^1 (z_c(t; x_c) - \tilde{z}_c(t; x_c))^T \tilde{z}_{c_t}(t; x_c) dt = 0,$$
$$\dot{w}_c(t) = T_c(x_c)D_{z_c}f(x_c, z_c(t; x_c), 0)w_c(t) + \ln|\mu_2|w_c(t),$$
$$w_c(1) = \text{sgn}(\mu_2)w_c(0),$$
$$w_c(0)^T w_c(0) = h,$$

$$(3.56)$$

with the additional boundary condition

$$d_x = \|(x - x_c)\|^2. \tag{3.57}$$

A periodic orbit sampled from system $\{(3.46),(3.47),(3.55)\}$ is used as starting data for the extended system, with $d_x = 0$. Note that d_x represents the distance in x between the two solutions of our problem. Since $\mu_2 = 0$, $h = 1$ will remain fixed for both solutions in future continuations (i.e. both solutions will be constrained to the SNPO curve), we do not create copies of those parameters. Next, we grow the two copies apart by continuing in d_x until we reach a suitable small, non-zero value. By fixing $d_x \neq 0$ in $\{(3.46),(3.47),(3.55),(3.56)\}$, we essentially create a 'trailing' periodic orbit, restricted to the SNPO curve. Using the difference $(x - x_c)$, we can approximate the normal vector $\boldsymbol{n}$ to the SNPO curve in the x-plane. We extend our system once again by implementing the slow averaged vector field and the dot product condition

$$\int_0^1 g\left(x, z(t; x), 0\right) dt = C,$$
$$\int_0^1 \hat{\boldsymbol{n}}^T C \, dt = \tilde{C},$$

$$(3.58)$$

where $C, x, x_c \in \mathbb{R}^2$. The final extended system defined by $\{(3.46),(3.47),(3.55) - (3.58)\}$ consists of $4m$ differential equations, $(4m+3)$ boundary conditions, and 5 integral constraints. Thus we require 9 active continuation parameters. Next, we continue in $\{T, T_c, x, x_c, C, \tilde{C}\}$ until we reach the toral folded singularity at $\tilde{C} = 0$. Finally, with $\tilde{C}$ fixed, we continue in an additional system parameter to generate the toral folded singularity bifurcation curve.

Remark 3.7. For one slow variable, the above numerical implementation can be greatly simplified. Similar to folded singularities with one slow variable (see Section 2.3.1), toral folded singularities occur when the averaged nullcline intersects the SNPO. In this case, toral folded singularities can be identified in the BVP $\{(3.46),(3.47)\}$, while continuing along the SNPO curve, coupled with the condition $\int_0^1 g(x, z) dt = 0$. In other words, a toral folded singularity is flagged as an equilibrium of the system and can be easily continued with respect to a system parameter.

3.6 Appendix

Lemma 3.5 (General Grönwall Lemma [92]). *Suppose that for $t_0 \leq t \leq t_0 + T$ we have*

$$\varphi(t) \leq \alpha + \int_{t_0}^{t} \beta(s)\varphi(s)ds, \tag{3.59}$$

where φ and β are continuous and $\beta(t) > 0$. Then

$$\varphi(t) \leq \alpha \exp \int_{t_0}^{t} \beta(s)ds,$$

for $t_0 \leq t \leq t_0 + T$.

Proof. Define

$$\Phi(t) = \alpha + \int_{t_0}^{t} \beta(s)\varphi(s)ds.$$

Then $\varphi(t) \leq \Phi(t)$, and $\dot{\Phi}(t) = \beta(t)\varphi(t)$. Since $\beta(t) > 0$, we have

$$\dot{\Phi}(t) - \beta(t)\Phi(t) \leq 0.$$

Using an integrating factor, the above differential inequality can be rewritten as

$$\frac{d}{dt}\left(\Phi(t)\exp\left(-\int_{t_0}^{t}\beta(s)ds\right)\right) \leq 0,$$

and integrated to obtain

$$\Phi(t)\exp\left(-\int_{t_0}^{t}\beta(s)ds\right) - \alpha \leq 0, \tag{3.60}$$

where $\alpha = \Phi(t_0)$. Rearranging (3.60) gives the required result. $\square$

Lemma 3.6 (Specific Grönwall Lemma [92]). *Suppose that for $t_0 \leq t \leq t_0 + T$ we have*

$$\varphi(t) \leq \delta_2(t - t_0) + \delta_1 \int_{t_0}^{t} \varphi(s)ds + \delta_3, \tag{3.61}$$

with φ continuous for $t_0 \leq t \leq t_0 + T$, and constants $\delta_1 > 0$, $\delta_2 \geq 0$, $\delta_3 \geq 0$. Then

$$\varphi(t) \leq \left(\frac{\delta_2}{\delta_1} + \delta_3\right)e^{\delta_1(t-t_0)} - \frac{\delta_2}{\delta_1},$$

for $t_0 \leq t \leq t_0 + T$.

Proof. Rearranging equation (3.61) gives

$$\varphi(t) + \frac{\delta_2}{\delta_1} \leq \delta_1 \int_{t_0}^{t} \left(\varphi(s) + \frac{\delta_2}{\delta_1} \right) ds + \delta_3 + \frac{\delta_2}{\delta_1},$$

which is of the same form as (3.59), i.e.

$$\hat{\varphi}(t) \leq \hat{\alpha} + \int_{t_0}^{t} \hat{\beta}\hat{\varphi}(s) ds,$$

where $\hat{\varphi}(t) = \varphi(t) + \delta_2/\delta_1$, $\hat{\alpha} = \delta_3 + \delta_2/\delta_1$, and $\hat{\beta} = \delta_1$. Applying the general form of Grönwall's Lemma and rearranging gives the desired result. $\square$

Lemma 3.7 (see [104]). *Let $(x, \gamma(t,x)) \in \mathcal{P}$, and let $n(t,x)$ denote the unit normal vector to the periodic orbit $\gamma(t,x)$. Then*

$$\frac{1}{T(x)} \int_{0}^{T(x)} n^T (D_z f) n \, ds = \frac{1}{T(x)} \int_{0}^{T(x)} \left(\mathrm{tr} D_z f - \frac{f^T (D_z f) f}{\|f\|^2} \right) ds = \rho_2,$$

where f and its derivatives are evaluated along $(x, \gamma(t,x), 0)$, and ρ_2 is the non-trivial Floquet exponent. When $(x, \gamma(t,x)) \in \mathcal{P}_F$, we have

$$\frac{1}{T(x)} \int_{0}^{T(x)} n^T (D_z f) n \, ds = 0.$$

Proof. A simple calculation shows that

$$\begin{aligned}
n^T (D_z f) n &= \frac{1}{\|f\|^2} \begin{pmatrix} f_2 \\ -f_1 \end{pmatrix}^T \begin{pmatrix} f_{1_{x_1}} & f_{1_{x_2}} \\ f_{2_{x_1}} & f_{2_{x_2}} \end{pmatrix} \begin{pmatrix} f_2 \\ -f_1 \end{pmatrix}, \\
&= \frac{1}{\|f\|^2} \begin{pmatrix} f_1 \\ f_2 \end{pmatrix}^T \begin{pmatrix} f_{2_{x_2}} & -f_{1_{x_2}} \\ -f_{2_{x_1}} & f_{1_{x_1}} \end{pmatrix} \begin{pmatrix} f_1 \\ f_2 \end{pmatrix}, \\
&= \frac{1}{\|f\|^2} f^T \mathrm{adj}(D_z f) f,
\end{aligned}$$

where adj denotes the classical adjoint or adjugate matrix. Since $D_z f$ is invertible along γ, the adjoint matrix can be rewritten as

$$\mathrm{adj}(D_z f) = \det(D_z f) \cdot (D_z f)^{-1}. \tag{3.62}$$

The Cayley-Hamilton theorem states that any $n \times n$ invertible matrix A satisfies its own characteristic equation, that is

$$A^n + c_{n-1} A^{n-1} + \ldots + c_1 A + (-1)^n \det(A) I_n = 0.$$

Rearranging the above equation gives an expression for the inverse of A:

$$A^{-1} = \frac{(-1)^{n-1}}{\det(A)} \left(A^{n-1} + c_{n-1} + \ldots + c_1 I_n \right).$$

54

For a 2×2 matrix, the coefficient $c_1 = -\mathrm{tr}(A)$. Applying the Cayley-Hamilton theorem to (3.62) gives

$$\mathrm{adj}(D_z f) = \mathrm{tr}(D_z f) I_2 - A,$$

and thus

$$n^T (D_z f) n = \mathrm{tr}(D_z f) - \frac{f^T (D_z f) f}{\|f\|^2}. \tag{3.63}$$

Averaging the first term over the period $T(x)$ gives the sum of the Floquet exponents; since $z \in \mathbb{R}^2$, the sum is simply ρ_2, the non-trivial exponent. The average of the second term is zero since

$$\frac{f^T (D_z f) f}{\|f\|^2} = \frac{1}{2} \frac{d}{dt} \left(\ln \left(\frac{1}{2} f^T f \right) \right),$$

and f is $T(x)$-periodic. $\qquad \square$

Chapter 4

Torus Canards in the Wilson-Cowan-Izhikevich Model

In this chapter we present a brief study of the Wilson-Cowan-Izhikevich (WCI) model, a minimal neural bursting model which is known to posses torus canards [18, 104]. The aim of this chapter is to demonstrate how the tools and techniques outlined in Chapters 2 and 3 are utilised to dissect the phenomenon of torus canards. The extended version of the Wilson-Cowan model [113], first proposed by Izhikevich [54], is given by the set of ordinary differential equations

$$
\begin{aligned}
\dot{x} &= -x + S(r_x + ax - by + u) =: f_1(x, y, u), \\
\dot{y} &= -y + S(r_y + cx - dy + fu) =: f_2(x, y, u), \\
\dot{u} &= \varepsilon(k - x) =: \varepsilon g(x),
\end{aligned}
\tag{4.1}
$$

where $S(z) = 1/(1 + \exp(-z))$ and $0 < \varepsilon \ll 1$. System (4.1) is known as the WCI model. The small parameter ε creates a timescale separation, and $(x, y) \in \mathbb{R}^2$ are fast while $u \in \mathbb{R}$ is slow. Wilson and Cowan [113] originally used a mean-field approach to construct a two-dimensional ODE system describing the dynamics and interactions of simple excitatory and inhibitory model neurons. The variable $x(t)$ represents the proportion of excitatory cells firing per unit time (at time t), while $y(t)$ represents the proportion of inhibitory cells. The sigmoid function $S(x)$ is the firing rate or response function, which gives the expected proportions of the subpopulations receiving at least threshold excitation. Izhikevich [54] extended the Wilson-Cowan model by adding a slow sub-system $\dot{u} = \varepsilon g(x)$. This addition creates bistability and thus allows for bursting behaviour, which is not possible in the original model. Following [18], we set $g(x) = k - x$ and treat k and r_x as the primary and secondary bifurcation parameters, respectively. Unless otherwise stated, the values of the remaining parameters are given in Table 4.1.

4.1 Full System Bifurcation Analysis

Before we present a GSPT analysis of the WCI model, we briefly review the full system bifurcation structure. Figure 4.1 shows the bifurcation diagram of (4.1), with respect to the parameter k. For large values of k we have a stable branch of equilibria which loses

Parameter	Value	Parameter	Value
a	10.5	f	0.3
b	10	r_y	-9.7
c	10	ε	0.03
d	-2		

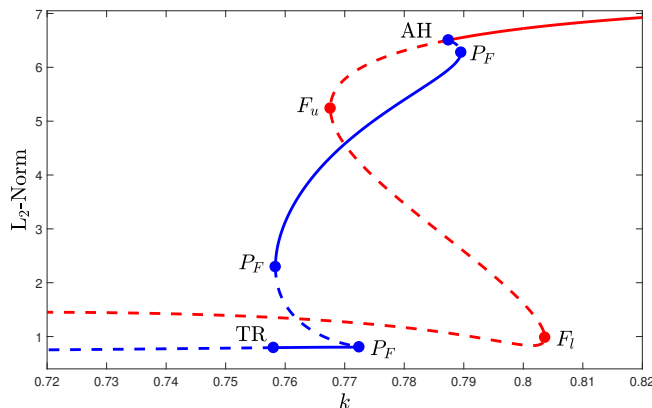**Table 4.1:** Parameter values of the WCI model 4.1, as in [18].

Figure 4.1: Bifurcation analysis of the full system (4.1), with respect to k, for $r_x = -4.76$.

stability at a subcritical Andronov-Hopf bifurcation (AH). The periodic orbits emanating from AH are split into four branches, separated by three SNPO bifurcations (labelled P_F). The second and fourth branches are stable. These stable branches of periodics correspond to the two spiking solutions of the model; see Figure 4.7C. As k is decreased, the lower fourth branch loses stability at a supercritical torus bifurcation (TR) where a phase space torus is born (see [82, 69, 53] for more examples of torus bifurcations in slow/fast systems). Notice that the model exhibits bistability for values of k between the two lower P_F bifurcations. As k is decreased below TR, the torus grows in amplitude. The torus structure can be seen in the Poincaré map in Figure 4.2A. The return map is constructed by setting up a Poincaré section ($y = constant$), and recording when the flow of (4.1) crosses the section transversally. The value of x is then plotted versus its value at the previous crossing to produce the map. In Figure 4.2B, we see that the torus quickly begins to break down as k is decreased, and the full system transitions to bursting (see Figure 4.3C).

From the full system bifurcation analysis, it is not obvious why the full system transitions

Torus breakdown is a complex phenomenon which can generate chaos. The breakdown is preceded by a loss of smoothness [41] and the torus becoming resonant [1], which leads to the disintegration of the torus in a number of different ways. Some of these pathways include homoclinic tangencies, a SNPO bifurcation where the unstable set of the saddle-node periodic orbit forms a non-smooth manifold homeomorphic to the torus, period doubling bifurcations, and other bifurcations involving periodic orbits (see [2] for further details). The complexities and mode of torus breakdown in the WCI model (and the Butera model studied later in Chapter 5) are left for future analysis.

From the full system bifurcation analysis, it is not obvious why the full system transitions
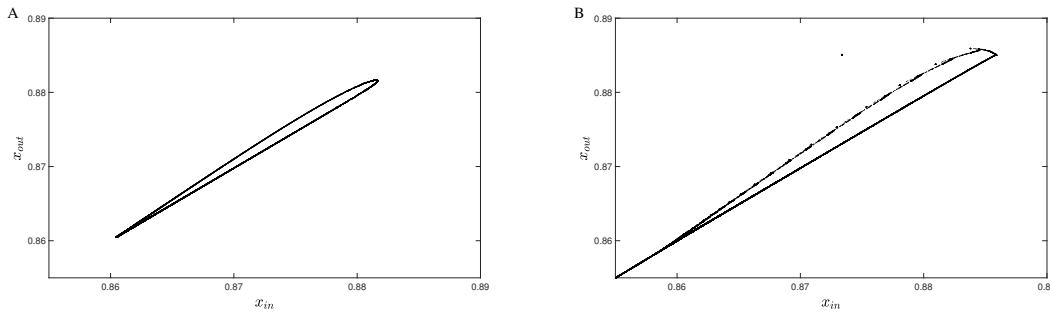
Figure 4.2: Poincaré return maps of the full system for $r_x = -4.76$ and *A: $k = 0.7574$, and B: $k = 0.75738145407$.*

from spiking to bursting. We see that TR is correlated with this transition, but that is all we can glean. To better understand this transition, and the genesis of the spiking and bursting patterns, we switch to a GSPT/averaging approach, as outlined in Chapters 2 and 3.

4.2 The Layer Problem

Setting $\varepsilon = 0$ in system (4.1) yields the layer problem

$$
\begin{aligned}
x' &= f_1(x, y, u), \\
y' &= f_2(x, y, u),
\end{aligned}
\tag{4.2}
$$

where the slow variable u is treated as a parameter. The Jacobian of (4.2) is given by

$$
A(x, y; u) = \begin{pmatrix} -1 + a\bar{S}(r_x + ax - by + u) & -b\bar{S}(r_x + ax - by + u) \\ c\bar{S}(r_y + cx - dy + fu) & -1 - d\bar{S}(r_y + cx - dy + fu) \end{pmatrix},
\tag{4.3}
$$

where $\bar{S}(z) = \exp(-z)/(1 + \exp(-z))^2$. The set of equilibria of (4.2) form the critical manifold

$$
\mathcal{S} := \{(x, y, u) \in \mathbb{R}^3 : f_1 = f_2 = 0\},
$$

which, since we only have one slow variable, is a one-dimensional manifold embedded in $\mathbb{R}^3$. A projection of $\mathcal{S}$ into the (x, u)-plane is shown in Figure 4.3A in red. The stability of $\mathcal{S}$ would typically be determined by linearising about $\mathcal{S}$ (evaluating the Jacobian $A|_{\mathcal{S}}$) and examining the eigenvalue structure. However, $f_1 = f_2 = 0$ cannot be solved explicitly and so we use numerical software to determine the stability and identify any bifurcations of $\mathcal{S}$.

The critical manifold is partitioned by two fold bifurcations (labelled F_u and F_l) into three branches. The lower branch is attracting and the middle branch is of saddle type. For large u, the upper branch is attracting, but as u is decreased the branch loses stability at a supercritical Andronov-Hopf bifurcation (labelled AH), from which we see the emergence of periodic orbits. Let $\gamma(t; u)$ denote a particular periodic orbit of the layer problem (4.2),
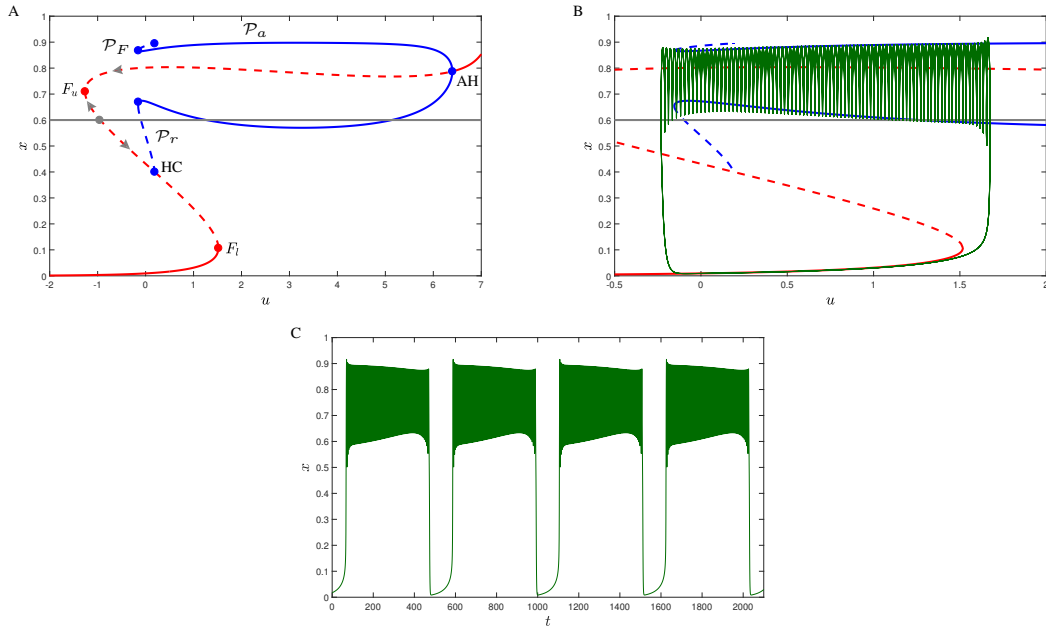
Figure 4.3: *A:* Bifurcation analysis of the layer problem (4.2) with (respect to u) for $k = 0.6$ and $r_x = -4.76$. The critical manifold is shown in red, while branches of periodic orbits are shown in blue. Solid lines denote stable branches and dashed lines denote unstable branches. The u-nullcline $x = k$ is shown in grey. The grey arrows indicate the direction of the reduced flow (4.4). *B:* Bifurcation analysis of the layer problem with a trajectory of the full system (4.1) overlayed in green. *C:* Time trace of the bursting trajectory.

with period $T(u)$. As in Sections 3.3 and 3.4, let $\mathcal{P}$ denote the family of all periodic orbits γ, i.e.

$$\mathcal{P} := \{(x, y, u) \in \mathbb{R}^3 : (x, y) = \gamma(t; u), \ \dot{\gamma}(t; u) = f(\gamma(t; u), u), \ \gamma(t; u) = \gamma(t + T(u); u)\},$$

and let $\mathcal{P}_a$ ($\mathcal{P}_r$) denote the attracting (repelling) branches, respectively. Let $\mathcal{P}_F$ denote a SNPO bifurcation. Returning to Figure 4.3, the periodic branch emanating from AH is initially stable, but coalesces with a second unstable branch at a SNPO bifurcation (labelled $\mathcal{P}_F$). The unstable branch of periodics terminates in homoclinic bifurcation (labelled HC) on the middle branch of $\mathcal{S}$.

Notice that the layer problem (which corresponds to the original WC model) exhibits bistability of equilibrium and periodic solutions. In the interval $(\mathcal{P}_F, F_l)$, the lower branch of equilibria (i.e. $\mathcal{S}$) and the manifold of periodic orbits $\mathcal{P}_a$ are both attracting. Izhikevich's extension of the original WC model allows for the slow variation of u, and thus the possibility of fold/fold-cycle bursting.

4.3 The Reduced Problem

Switching to the slow timescale $\tau = \varepsilon t$ and setting $\varepsilon = 0$ in (4.1) yields the reduced problem

$$
\begin{aligned}
0 &= f_1(x, y, u), \\
0 &= f_2(x, y, u), \\
\dot{u} &= g(x, y, u),
\end{aligned}
\tag{4.4}
$$

which approximates the slow flow along the critical manifold $\mathcal{S}$. Let $\boldsymbol{z} = (x, y)^T$ and $\boldsymbol{f} = (f_1, f_2)^T$. As outlined in Section 2.2, we can reformulate the reduced problem by taking the total time derivative of $\boldsymbol{f} = 0$ and multiplying by $\mathrm{adj}(D_{\boldsymbol{z}}\boldsymbol{f})$. After desingularisation, we obtain the desingularised reduced system which is given by

$$
\begin{aligned}
\dot{u} &= -\det(D_{\boldsymbol{z}}\boldsymbol{f}) \cdot g(\boldsymbol{z}, u), \\
\dot{\boldsymbol{z}} &= \mathrm{adj}(D_{\boldsymbol{z}}\boldsymbol{f}) \cdot D_u\boldsymbol{f} \cdot g(\boldsymbol{z}, u),
\end{aligned}
\tag{4.5}
$$

where $\boldsymbol{z} \in \mathcal{S}$. As defined in (2.18), equilibria or regular singularities of (4.5) are given by $g(\boldsymbol{z}, u) = 0$ for all $\boldsymbol{z} \in \mathcal{S} \setminus \mathcal{F}$. Visually, we can identify any equilibria by plotting the g-nullcline $x = k$ and looking for it's intersections with $\mathcal{S}$. In Figure 4.3A, there is a single unstable equilibrium on the middle branch of $\mathcal{S}$ at $x = 0.6$.

In a typical GSPT analysis, the reduced flow is often calculated from the desingularised reduced system in an appropriate coordinate chart. However, since we only have one slow variable, it is easiest to calculate the reduced flow from (4.4) directly. This can be done by considering where points along $\mathcal{S}$ lie in relation to the u-nullcline $x = k$. Above the nullcline, the reduced flow is decreasing in u, while below the nullcline, the reduced flow is increasing in u. Thus in Figure 4.3A, the reduced flow along $\mathcal{S}$ moves toward both F_l and F_u. Note that as k is increased, the u-nullcline moves to higher values of x while $\mathcal{S}$ remains fixed (as it is independent of k).

The two fold points F_l and F_u numerically identified in Section 4.2 are jump (or regular fold) points if they satisfy the transversality condition

$$
\mathrm{adj}(D_{\boldsymbol{z}}\boldsymbol{f}) \cdot D_u\boldsymbol{f} \cdot g \neq 0,
\tag{4.6}
$$

from Definition 2.7 in Section 2.3. By Remark 2.3, the rows of the adjoint matrix $\mathrm{adj}(D_{\boldsymbol{z}}\boldsymbol{f})$ consist of either the zero vector or l, the left nullvector of $D_{\boldsymbol{z}}\boldsymbol{f}$. Furthermore, from Definition 2.5, we know that $l \cdot D_u\boldsymbol{f} \neq 0$ at the fold points. Since $u, g \in \mathbb{R}$, the transversality condition (4.6) is satisfied when $g \neq 0$. Geometrically speaking, condition (4.6) is satisfied if the u-nullcline does not intersect F_l and F_u. This is the case in Figure 4.3 for $k = 0.6$, and hence both folds are jump points.

Examining Figure 4.3B more closely, we observe that for small values of u, trajectories of the full system converge to the lower attracting branch of $\mathcal{S}$. Below the u-nullcline, trajectories move toward F_l (which is a jump point; see Section 2.6) where they fall off and converge to the attracting branch of periodics $\mathcal{P}_a$. Based on Figure 4.3B, one might argue that trajectories oscillating near $\mathcal{P}_a$ move slowly left as $\mathcal{P}_a$ is (almost) always above the u-nullcline. As a result, oscillating trajectories move slowly left until they reach $\mathcal{P}_F$; here trajectories fall down to the lower attracting branch of $\mathcal{S}$ and the cycle repeats. Thus we see
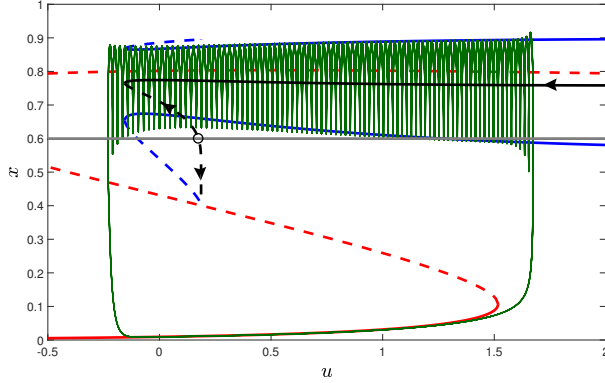
Figure 4.4: Bifurcation analysis of the layer problem (4.2), with slow averaged dynamics, for $(k, r_x) = (0.6, -4.76)$, the same parameter values as in Figure 4.3. The u-nullcline is plotted in grey, while the curve $(u, \langle x \rangle)$ is plotted in black. The unstable equilibrium of the averaged reduced system (4.8) is denoted by an open black circle. The black arrows indicate the direction of the averaged slow motion.

a fold/fold-cycle (or top-hat) bursting pattern; see Figure 4.3C. However, as k is increased the u-nullcline moves further up into the middle of $\mathcal{P}_a$, and it is no longer immediately obvious what the slow u dynamics are. In such cases we employ the averaging technique to approximate the slow motion in u over a periodic orbit of the layer problem. Note that for systems with more than one slow variable, it becomes impossible to estimate the slow motion based on the positioning of nullclines.

4.4 Averaged Reduced System

As in Sections 3.3 and 3.4, we approximate the slow motion in u over a periodic orbit γ of the layer problem by averaging the slow equation in (4.1). Formally, there exists a near-identity coordinate transformation which transforms (4.1) to

$$\dot{U} = \frac{\varepsilon}{T(U)} \int_0^{T(U)} g(\gamma(t; u), u) \, dt, \tag{4.7}$$

where we assume $(\gamma(t; u), u) \in \mathcal{P}$. We refer to (4.7) as the *averaged reduced system*. Since g is a simple linear function in x, equation (4.7) simplifies to

$$\dot{U} = \varepsilon(k - \langle x \rangle) =: \varepsilon G(\langle x \rangle, k), \tag{4.8}$$

where $\langle x \rangle$ denotes the time average of x over the course of a periodic orbit, i.e. $\langle x \rangle = \left(\int_0^T x \, dt \right) / T$. Setting the right hand side of (4.8) to zero yields averaged equilibria, whose stability is determined by the sign of the function $G(\langle x \rangle, k)$. Formally, the averaged nullcline is defined as the curve $(G(\langle x \rangle, k), \langle x \rangle)$. However, we do not plot this curve as it is easier to visualise the averaged equilibria as intersections of the curve $(u, \langle x \rangle)$ and the line $u = k$ (i.e. the u-nullcline). Below the equilibrium $(\langle x \rangle < k)$ U increases, and above the equilibrium $(\langle x \rangle > k)$ U decreases.
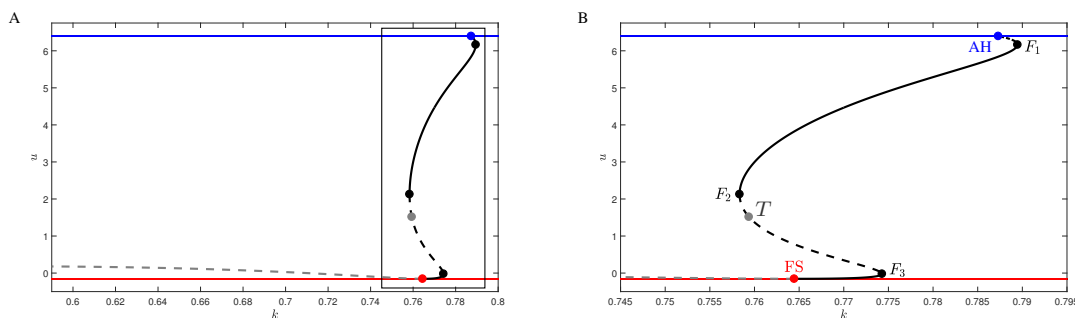
61

Figure 4.5: Bifurcation diagram of the averaged reduced problem (4.8), with respect to the parameter k, for $r_x = -4.76$. *A:* Branches of equilibria are shown in black and grey, where solid (dashed) branches are stable (unstable), respectively. Black (grey) branches indicate that the averaged equilibria lie on $\mathcal{P}_a$ ($\mathcal{P}_r$), the attracting (repelling) branch of layer problem periodic orbits. The continuation of the Andronov-Hopf and SNPO ($\mathcal{P}_F$) bifurcations of the layer problem (4.2) are shown in blue and red, respectively. The upper unstable branch of averaged equilibria terminate at the point labelled AH, beyond which there are no periodic orbits in (4.2). *B:* Zoom near the black box in panel A. Various saddle-node or fold bifurcations are denoted by F. The lower (grey) unstable branch of equilibria intersects the $\mathcal{P}_F$ branch at the point FS, which is a (toral) folded singularity. The solid grey circle T marks the point where the unstable periodic orbit (of saddle type) aligns with the fold of equilibria F_l.

The linear structure of the slow equation $\dot{u} = \varepsilon g$ facilitates a simplified averaged reduced system (4.8), which can be easily implemented in a variety of software packages to identify averaged equilibria. A similar method is used in a study of the Hindmarsh-Rose model [94], which also has a linear slow equation.

Remark 4.1. For systems with more complicated non-linear slow equations, we implement the averaging procedure in the software package AUTO, as outlined in Section 3.5.2. There are many other studies of neural models with one slow variable which make use of averaging [19, 26, 93], including the WCI model [104]. For systems with two slow variables, averaging becomes more complex to implement numerically (see Section 3.5). In Section 5 we will study a coupled neuron model with two slow variables.

Figure 4.4 shows a plot of the averaged slow motion for $k = 0.6$ (the same parameter value as Figure in 4.3). The curve $(u, \langle x \rangle)$ is plotted in black; its intersection with the g-nullcline (shown in grey) corresponds to the equilibrium of (4.8), which in this case is unstable. Notice that the averaged equilibrium lies on the unstable branch of $\mathcal{P}$. The slow averaged motion is indicated along $(u, \langle x \rangle)$ by black arrows. Utilising information from the averaged reduced problem (4.8), we can immediately justify the bursting pattern seen in Figures 4.3B and 4.3C: during the active phase of bursting (near the attracting branch of $\mathcal{P}$, between F_l and $\mathcal{P}_F$), the averaged slow motion is always decreasing.

What happens as k is increased or decreased? Using the numerical technique outlined in Section 3.5.2, we continue the averaged equilibria and construct an 'averaged bifurcation diagram' – see Figure 4.5. Our numerical implementation distinguishes between equilibria which lie on $\mathcal{P}_a$ (shown in black) and $\mathcal{P}_r$ (grey). However, we can only infer the stability of equilibria from the structure of the bifurcations and simulations of the full system. As k is increased from 0.6, two branches of equilibria emerge from a saddle-node bifurcation
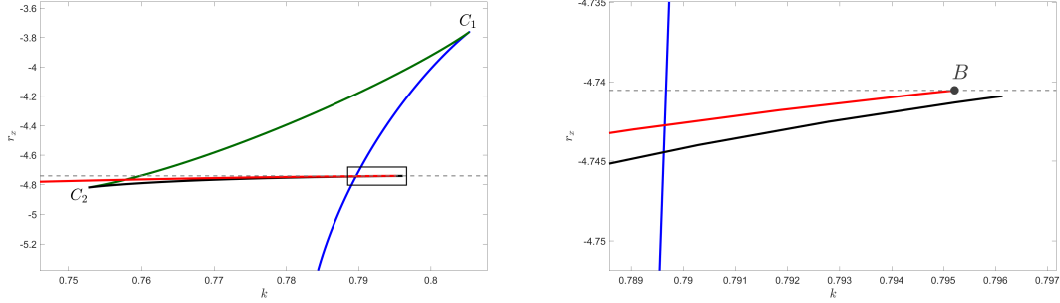
Figure 4.6: Two-parameter bifurcation diagram of the averaged reduced problem (4.8), projected into the (k, r_x)-plane. The continuation of the three fold bifurcations F_1, F_2 and F_3 are shown in blue, green and black, respectively. The toral folded singularity branch is shown in red. The grey dashed line $r_x \approx -4.7406$ indicates the value at which a Bautin bifurcation occurs in the layer problem. *A:* The fold bifurcation curves meet at two cusp bifurcations, labelled C_1 and C_2. *B:* Zoom near the black box in panel A. The toral folded singularity branch terminates at a Bautin bifurcation (labelled B). For values of r_x greater than B, the layer problem SNPO vanishes and the system no longer exhibits fold/fold-cycle bursting. Note that although the red and black branches both cross the blue branch, these crossings are not bifurcations. They simply indicate that the bifurcations occur at the same value of k, but they do not intersect.

labelled F_2, the upper (lower) branch being stable (unstable), respectively. As k is further increased, the lower (grey) unstable branch of equilibria intersects the branch of layer problem $\mathcal{P}_F$ bifurcations at FS. The unstable equilibria move from $\mathcal{P}_r$ to $\mathcal{P}_a$, through $\mathcal{P}_F$, and become stable. Recall from Section 2.3.1 that for singularly perturbed systems with one slow variable, folded singularities are degenerate and require the variation of a system parameter to detect. Furthermore, folded singularities are in fact points where ordinary singularities interact with the fold. The same is true for toral folded singularities. At $k = 0.7644$, the lower branch of averaged equilibria collide with $\mathcal{P}_F$ at a toral folded singularity FS. As k is increased past FS, the two lower branches of equilibria collide in another saddle-node bifurcation (labelled F_3). Beyond F_3, an unstable branch of equilibria emerge from the layer problem Andronov-Hopf bifurcation (labelled AH). Finally, the two upper branches of equilibria collide in a saddle-node bifurcation (F_1).

4.4.1 Two-parameter continuation

Using the numerical methods outlined in Section 3.5.4 and 3.5.2, we can continue the toral folded singularity and the fold bifurcations of the averaged reduced system with respect to an additional system parameter. Figure 4.6 shows a bifurcation diagram of the averaged reduced system projected into the (k, r_x)-plane. The F_1 and F_2 branches coalesce in a cusp bifurcation C_1, and the F_2 and F_3 branches coalesce at a second cusp bifurcation C_2. The grey dashed line $r_x \approx -4.7406$ is the continuation of a Bautin bifurcation B of the layer problem (recall that the layer problem is independent of k). There the SNPO collides with AH and is annihilated. Naturally, the red toral folded singularity branch terminates at B. Moving in the direction of decreasing k, the toral folded singularity branch eventually terminates at an $SNPO\text{-}HC$ bifurcation of the layer problem (not shown). At
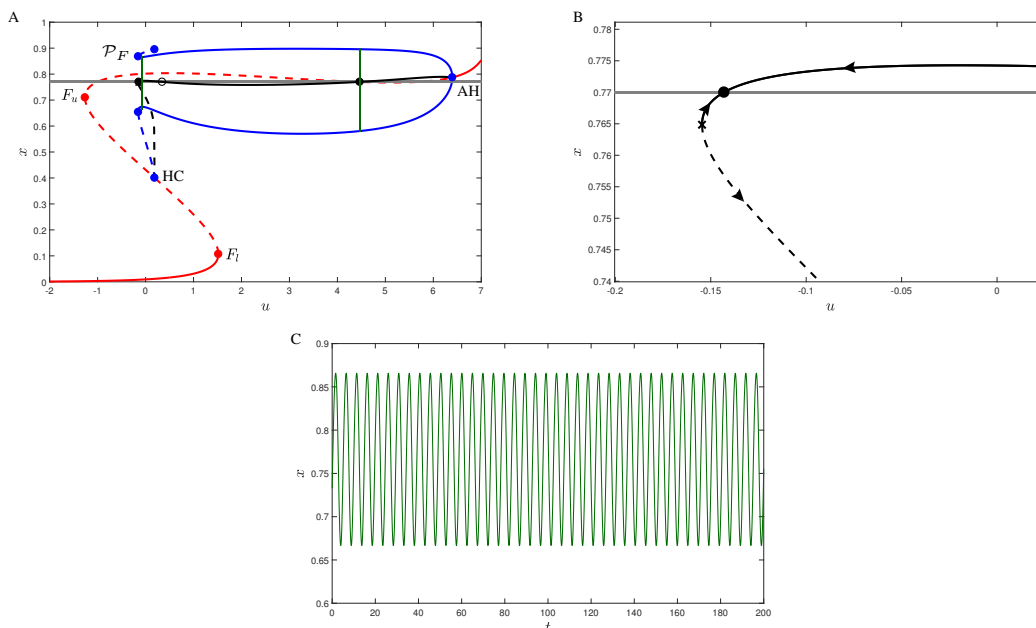
Figure 4.7: Bifurcation analysis of the layer problem (4.2), with slow averaged dynamics, for $(k, r_x) = (0.77, -4.76)$. *A:* Bifurcation diagram of the layer problem; the labelling of the bifurcations follows the conventions of Figure 4.3A. The curve $(u, \langle x \rangle)$ is plotted in black. The intersections of the black curve and the u-nullcline (grey) are equilibria of (4.8). Open black circles indicate unstable equilibria, while closed black circles are stable. Note that the full system exhibits bistability: the two spiking trajectories are shown in green. *B:* Zoom of the averaged reduced dynamics on $(u, \langle x \rangle)$ near the SNPO bifurcation (which is indicated by a black cross). *C:* Time trace of the spiking solution at $u \approx -0.143$, near $\mathcal{P}_F$.

this bifurcation, the SNPO and homoclinic bifurcations collide and the SNPO disappears. The region enclosed by $SNPO\text{-}HC$ and B is where the WCI model exhibits fold/fold-cycle bursting. Beyond this region, the full system can exhibit fold/homoclinic, fold/hopf and other complex bursting patterns [18, 30]. An analysis of these regions using averaging techniques is left for future work.

4.5   Torus Canards

Consider the transition from spiking to bursting, as k is decreased through TR, which occurs at $k = 0.758034$. Figures 4.7A and 4.7B show the structure of the layer problem, as well as the averaged reduced dynamics, for $k = 0.77$. We see three averaged equilibria, two of which are stable. The two stable equilibria correspond to stable spiking solutions of the full system. Note that one of the stable equilibria lies very close to $\mathcal{P}_F$.

As k is decreased to 0.7574, we move through several singular limit bifurcations. Firstly, the equilibrium closest to $\mathcal{P}_F$ moves through it (at the folded singularity FS) and onto the lower repelling branch $\mathcal{P}_r$; see Figure 4.8A. Note that for $k \in (T, FS)$, from a singular limit perspective, the system cannot exhibit bursting. This is due to the fact that the unstable periodic orbit still lies at values of u which are less than F_l. As a result, when trajectories
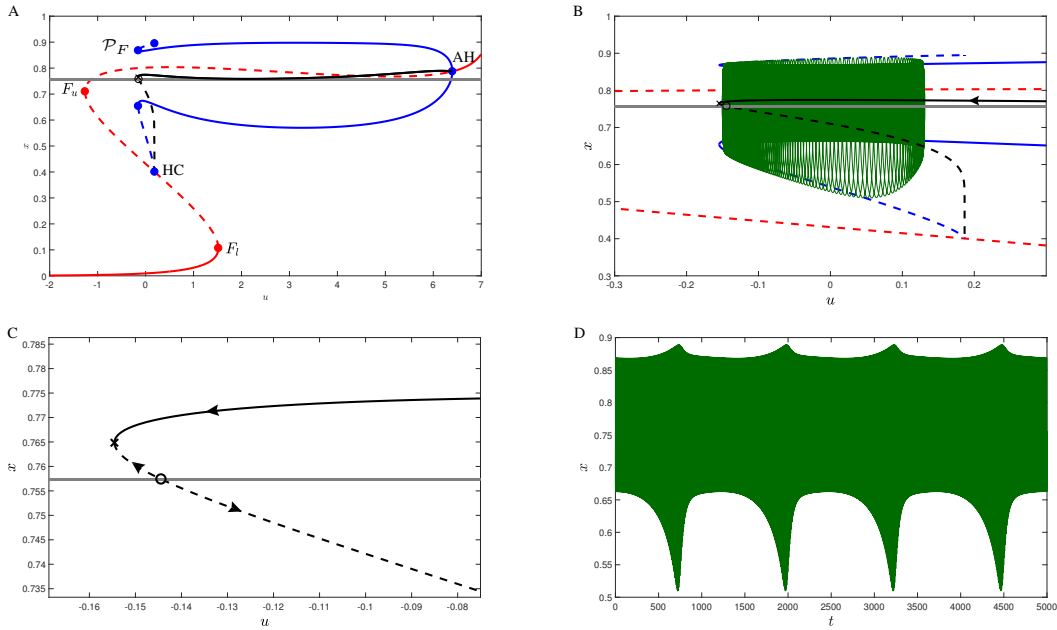
Figure 4.8: Bifurcation analysis of the layer problem (4.2), with slow averaged dynamics, for $(k, r_x) = (0.7574, -4.76)$. Figure follows the same conventions as Figure 4.7. Notice the amplitude modulated spiking (AMS) pattern in panel D.

jump off $\mathcal{S}$ near F_l and transition to $\mathcal{P}_a$, the averaged reduced flow moves trajectories to the right towards the stable periodic orbit. Past the global bifurcation labelled T in Figure 4.5B, the unstable periodic orbit lies at values of u which are greater than F_l. Finally, the two averaged equilibria furthest away from $\mathcal{P}_F$ collide and disappear in a saddle-node bifurcation F_2; see Figure 4.8C. As a result of these three bifurcations, the full system has transitioned from a bistable spiking state to an amplitude modulated spiking (AMS) pattern, which can be seen in Figure 4.8D. In (x, u) phase space (see Figure 4.8B), we see that the AMS trajectory traverses both the attracting and repelling branches $\mathcal{P}_a$ and $\mathcal{P}_r$ in a canard-like fashion.

Remark 4.2. While bursting is theoretically possible for $k < T$ from the singular limit structure, it is not observed in the full system until k is further decreased. This is due to the canard dynamics, resulting from the phase space torus born out of TR, which give rise to AMS. Once the torus begins to break down (see Figure 4.2B – breakdown begins near $k \approx 0.75738$), the system transitions to a bursting pattern.

As k is decreased a little further to 0.757, the system transitions to a bursting pattern, with a very long active phase, which can be seen in Figure 4.9D. The slow averaged dynamics are almost identical as k has hardly changed (cf. Figures 4.8C and 4.9C). Notice that the bursting trajectory in Figure 4.9B also exhibits canard behaviour as it traverses the repelling branch $\mathcal{P}_r$ for a significant amount of time.
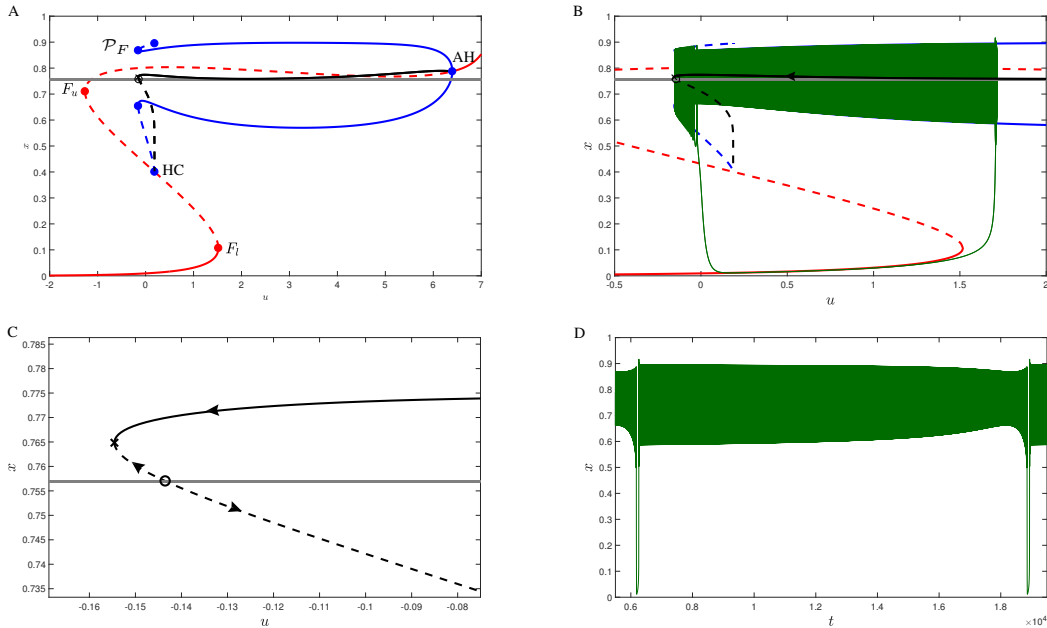
Figure 4.9: Bifurcation analysis of the layer problem (4.2), with slow averaged dynamics, for $(k, r_x) = (0.757, -4.76)$. Figure follows the same conventions as Figure 4.7.

4.6 Discussion

In this chapter, we studied the Wilson-Cowan-Izhikevich (WCI) model using a combination of full system bifurcation analysis and GSPT/averaging. In particular, we examined the transition from spiking to bursting, which occurs near a full system singular torus bifurcation.

We showed that the transition from spiking to bursting is reminiscent of the transition from quiescence to relaxation oscillations in the van der Pol oscillator (VdP); see Section 2.7.1. There the transition occurs via a canard explosion: In an exponentially small parameter window we see the rapid increase in amplitude of small amplitude oscillations ('canards without head') to duck shaped 'canards with head'. Nearby in the full system there is a singular Andronov-Hopf bifurcation. In the WCI model, the amplitude modulated spiking solutions resemble canards without head, and bursting trajectories which follow the repelling branch $\mathcal{P}_r$ resemble canards with head. These solutions which track the repelling branch of periodic orbits are called torus canards, aptly named due to the nearby torus bifurcation in the full system. In a similar manner to the VdP oscillator, the transition from spiking to bursting occurs in a small parameter window, via a *torus canard explosion* [18].

To aid our understanding of the observed torus canards, we constructed an averaged reduced system, which approximates the slow motion near the layer problem manifold of periodic orbits $\mathcal{P}$. We showed that the singular torus bifurcation in the full system corresponds to a degenerate folded singularity of the averaged reduced system, wherein the averaged nullcline collides with the fold of periodic orbits. Using an averaged normal form,

Vo [104] numerically continued the (toral) folded singularity in two-parameter space, thereby demarcating the singular limit bursting and spiking regions. In a similar manner to [104], we continued the folded singularity in two parameters. However, we improved upon past work by also continuing the averaged equilibria, and providing a complete two-parameter continuation of the averaged reduced structures in the WCI model.

Torus canards were first discovered in a model for neuronal activity in cerebellar Purkinje cells [60]. Following their discovery, they have been observed in many other neural models such as the Politi-Höfer model [104], an elliptic burster known as the FitzHugh-Nagumo-Rinzel model [114], the Morris-Lecar-Terman and Hindmarsh-Rose models [18], where they mark the transition from spiking to bursting. Other examples include a rotated planar van der Pol system with symmetry breaking [6] and a chemical oscillator [98]. In [30], the authors show that the WCI model also exhibits complex canard dynamics, known as canards of mixed type (CMT), which involve torus canard behaviour. The numerical averaging methods we employed in this chapter could provide additional insights into CMTs, as well as other oscillatory solutions in neural models. We show in Chapter 5 that torus canards also occur in the Butera model, a coupled neuron model, near the transition from spiking to bursting. However, the Butera model has two slow variables, and this naturally leads to the possibility of generic toral folded singularities and torus canards which exist on open parameter intervals.

Chapter 5

Torus Canards in the Butera Model

Author's Contributions: The majority of this chapter is published in [87]. The numerical analysis was performed KR, and all figures were produced by KR. The manuscript was written and edited by all authors. The numerical identification and continuation of toral folded singularities, which was not published, was later contributed by KR.

5.1 Introduction

Rhythmic breathing patterns in mammals are generated by networks of neurons in the lower brain stem. In particular, experiments have shown that neurons in a region of the medulla known as the pre-Bötzinger complex (pre-BötC) play a vital role in respiration [43, 84, 95]. Butera and colleagues presented a model for two synaptically coupled pre-BötC neurons in [20, 21]. The model is conductance based, where each neuron is described by four non-linear ODEs,

$$
\begin{aligned}
v_i' &= (-I_{NaP} - I_{Na} - I_K - I_L - I_{tonic-e} - I_{syn-e})/C =: f_1(v_i, n_i, h_i, s_i), \\
n_i' &= (n_\infty(v_i) - n_i)/\tau_n(v_i) =: f_2(v_i, n_i), \\
h_i' &= \varepsilon(h_\infty(v_i) - h_i)/\tau_h(v_i) =: g(v_i, h_i), \\
s_i' &= \alpha_s(1 - s_i)s_\infty(v_i) - s_i/\tau_s =: f_3(v_i, s_i),
\end{aligned}
\tag{5.1}
$$

where $i = 1, 2$, and $0 < \varepsilon \ll 1$. The first equation in (5.1) describes the evolution of the membrane potential v_i, which depends on various ionic currents (see Table 5.1 for a description of each current). The steady-state voltage dependent (in)activation function of x is given by $x_\infty(v) = (1 + \exp((v - \theta_x)/\sigma_x))^{-1}$ for each $x \in \{h_i, m, m_P, n_i, s_i\}$. The voltage-dependent time constant $\tau_x(v) = \bar{\tau}_x/\cosh((v - \theta_x)/(2\sigma_x))$ for $x \in \{h_i, n_i\}$, is a sigmoid with a half (in)activation at $v = \theta_x$ and a slope proportional to $1/\sigma_x(v)$. Model parameter values, taken from [20, 21] and also used in [11, 87], are listed in Table 5.2.

Each neuron receives sustained excitation in the form of a background tonic drive $I_{tonic-e} = g_{ton}(v_i - E_{syn})$, as well as an excitatory synaptic current $I_{syn-e} = g_{syn}s_j(v_i - E_{syn})$. The parameters g_{ton} and g_{syn}, which represent the mean conductance of the respective currents, play an important role in determining the type of activity patterns observed.

Current	Description	Equation
I_{Na}	Sodium current	$g_{Na}m_\infty(v_i)(1-n)(v_i - E_{Na})$
I_{NaP}	Persistent sodium current	$g_{NaP}m_{P,\infty}(v_i)h_i(v_i - E_{Na})$
I_K	Potassium current	$g_K n_i^4(v_i - E_K)$
I_L	Leak current	$g_L(v_i - E_L)$
$I_{tonic-e}$	Background tonic drive	$g_{ton}(v_i - E_{syn})$
I_{syn-e}	Excitatory synaptic current	$g_{syn}s_j(v_i - E_{syn})$

Table 5.1: Currents in the Butera model 5.1, where $i = 1, 2$ and $j = 3-i$.

Parameter	Value	Parameter	Value	Parameter	Value	Parameter	Value
g_{NaP}	2.8 nS	E_{Na}	50.0 mV	$\theta_{m,P}$	-40 mV	$\sigma_{m,P}$	-6 mV
		$\bar{\tau}_h/\epsilon$	10000 msec	θ_h	-48 mV	σ_h	6 mV
g_{Na}	28 nS			θ_m	-34 mV	σ_m	-5 mV
g_K	11.2 nS	E_K	-85.0 mV				
		$\bar{\tau}_n$	10 msec	θ_n	-29 mV	σ_n	-4 mV
g_L	2.8 nS	E_L	-65.0 mV	C	21 pF	E_{syn-e}	0 mV
α_s	0.2 msec^{-1}	τ_s	5 msec	θ_s	-10.0 mV	σ_s	-5 mV

Table 5.2: Parameter values used in the Butera model 5.1.

Model (5.1) can exhibit quiescence, periodic (or tonic) spiking, and bursting; see Figure 5.2. The single-neuron version of (5.1) exhibits square-wave, or fold/homoclinic bursting according to Izhikevich's bursting classification scheme, where the active phase of bursting terminates at a homoclinic bifurcation of the layer problem of (5.1). In contrast, the active phase of bursting in the two-neuron model (5.1) may terminate at a SNPO bifurcation of the layer problem, resulting in top-hat [11] or fold/fold cycle bursting. The SNPO bifurcation will play a crucial role in our subsequent analysis since it can lead to toral folded singularities and hence generate complex torus canard behaviour

In this chapter, we consider issues that are associated with transitions between various activity patterns in the Butera model. Our work identifies torus canards as playing a key role in the bifurcations underlying the bursting to spiking transition in the model neuron pair. Unlike the 1-slow/2-fast WCI model studied in Chapter 4, the torus canard behaviour observed in the 2-slow/6-fast Butera model occurs on open parameter intervals. The addition of a second slow variable in the Butera model unfolds the torus canard phenomenon, making it robust and generic [104]. We employ the technique of averaging to study a two-dimensional averaged reduced system, which approximates the slow dynamics near periodic solutions of the layer problem. We identify toral folded node and saddle singularities, the averaged counterparts of folded singularities that are typically associated with the canard structure in singularly perturbed systems with two or more slow variables. Codimension-one bifurcations of the generic folded singularities (i.e. FSN bifurcations) in the averaged reduced problem turn out to be closely related to the observed transitions between activity patterns. In particular, we find three different kinds of FSN bifurcations: FSN II and III (which are both associated with singular torus bifurcations in the full system), and FSN
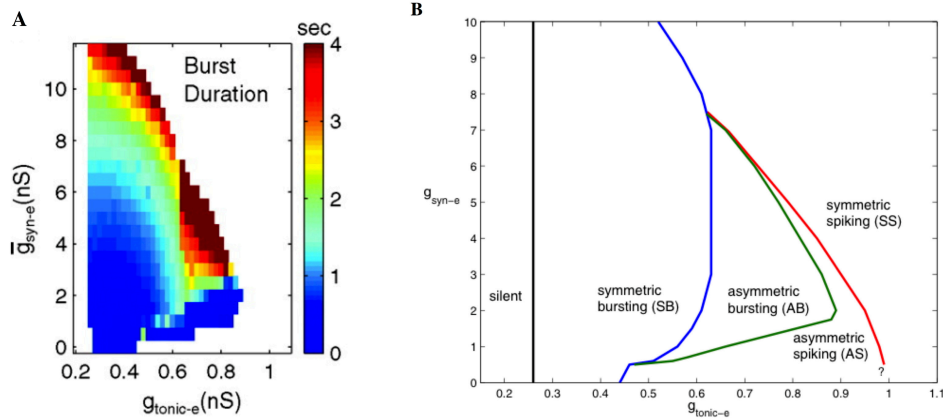
Figure 5.1: Boundaries of activity regimes for model (5.1). *A:* Bursting region in (g_{ton}, g_{syn}) parameter space, as identified by Butera et al., colour-coded by burst duration; figure adapted from [20]. *B:* The bursting and spiking regions identified by Best et al.; figure adapted from [11].

I. The FSN III bifurcation, which arises as a consequence of the symmetry induced by coupling a pair of identical neurons, is novel and studied for the first time in this work.

The remainder of this chapter is organised as follows. In Section 5.1, we briefly describe the model (5.1) and associated structures that play a role in our analysis and we concisely review the main findings of the earlier analysis of activity patterns in the two-neuron case [11]. In Section 5.2, we consider the bifurcation structure of the full two-neuron model system as particular parameters, also considered in past work, are varied. Identified bifurcations are observed to correspond to changes in model dynamics, and several bifurcation curves are found to coalesce at an organising centre. To better understand the source of the emergent dynamics, in Section 5.3 we use a geometric singular perturbation approach and explore the parameter dependence of equilibria, folded singularities, and their bifurcations in an averaged reduced problem via numerical continuation. Finally, we close with a discussion in Section 5.4.

5.2 Full System Bifurcation Analysis

5.2.1 One parameter diagrams and associated activity patterns

Butera et al. [20] used simulations on a grid in (g_{ton}, g_{syn}) parameter space to approximate the boundaries of the bursting regime (see Figure 5.1A). Through additional numerical simulations, Best et al. [11] refined the diagram and added additional boundaries (see Figure 5.1B) that distinguished between two different types of bursting and spiking: symmetric and asymmetric. The time traces of the different activity patterns from 5.1B are shown in Figure 5.2. In both bursting regimes, the bursts are synchronised but the neurons fire out of phase; in the spiking regimes, the spikes are also out of phase. The classification of symmetric versus asymmetric is based on the dynamics of the slow variables: in symmetric regimes, the slow variables evolve in a similar manner, while in asymmetric regimes they are noticeably different. Our first goal is to identify full system bifurcation structures of
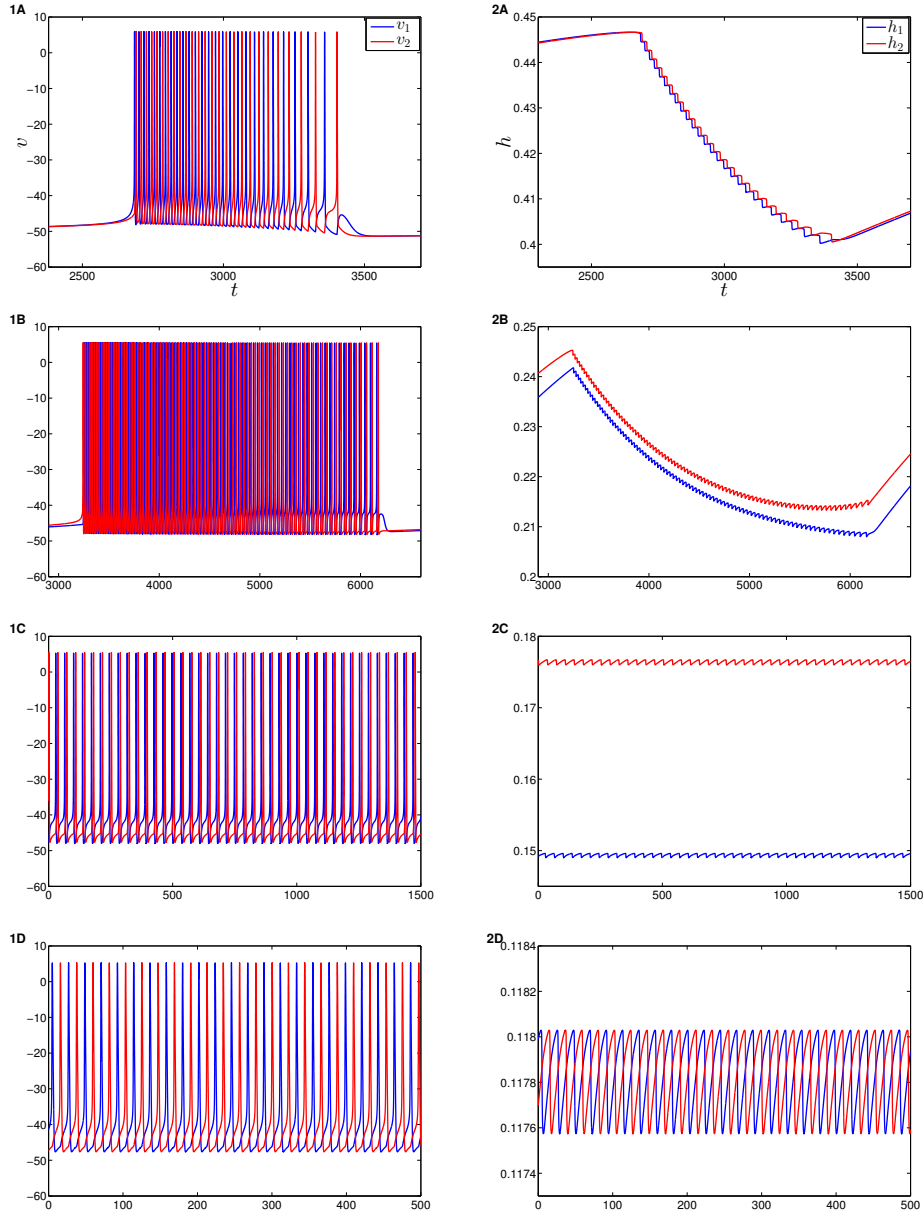
Figure 5.2: Activity patterns of model (5.1) with $g_{syn} = 3.0$. *1A-1D:* Time traces of v_1 (blue) and v_2 (red) for symmetric bursting ($g_{ton} = 0.45$), asymmetric bursting ($g_{ton} = 0.75$), asymmetric spiking ($g_{ton} = 0.877$) and symmetric spiking ($g_{ton} = 0.99$). In the bursting cases, only a single burst is shown. *2A-2D:* Time traces of the slow variables h_1 (blue) and h_2 (red) for the same values of g_{ton} as in 1A-1D.

(5.1) that are associated with the transitions between different activity patterns.

The bifurcation structure of the full Butera model (5.1) is very complex; we only focus on the bifurcations that play a role in the transitions between activity patterns. Figure 5.3 shows the bifurcation diagram with respect to g_{ton}, for fixed $g_{syn} = 3$. For large values of
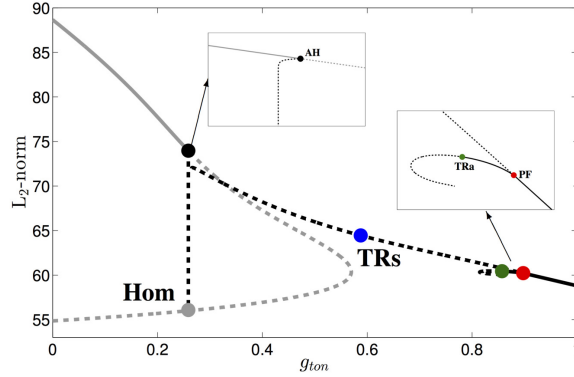
Figure 5.3: One parameter bifurcation diagram (with respect to g_{ton}) of the full system (5.1) for $g_{syn} = 3$. Equilibria are indicated with grey lines and periodic orbits with black ones (solid for stable, dashed for unstable). For low g_{ton}, the branch of equilibria loses stability in a subcritical singular AH bifurcation (black dot) and subsequently goes through an incomplete canard explosion terminating in a homoclinic (Hom, grey dot). Further on, the equilibrium branch goes through two saddle-node bifurcations (only one shown here) and for large g_{ton} another subcritical AH bifurcation arises (also not shown). The emanating unstable branch of periodic orbits goes through a SNPO bifurcation and finally stabilises in a pitchfork bifurcation. The resulting primary stable family of periodic orbits (SS) is the one shown for $g_{ton} \approx 1$. Bifurcations of this branch of periodic orbits are described in the text (red dot: PF, supercritical pitchfork bifurcation; green dot: TR$_a$, torus bifurcation; blue dot: TR$_s$, torus bifurcation). Note there are other bifurcations past TR$_a$ along the asymmetric branch as well as after the TR$_s$ along the symmetric branch and eventually both branches terminate (with the primary periodic orbit branch terminating in a homoclinic bifurcation quite close to the black dot), but these bifurcations are not relevant in our analysis. *Insets:* Zoomed views near PF/TR$_a$ and HB.

g_{ton}, we are able to identify a family of stable periodic orbits, which corresponds to the symmetric spiking patterns observed in the model (see Figure 5.2, $g_{ton} = 0.99$, panels 1D and 2D); let SS denote this branch of solutions. As g_{ton} is decreased, the SS branch loses stability at a supercritical pitchfork bifurcation (PF). The secondary stable branches of periodic orbits bifurcating from PF correspond to the asymmetric spiking (AS) patterns, and PF marks the transition from symmetric spiking to asymmetric spiking (SS to AS). We only continue one of the branches that bifurcate from PF since the second branch is identical, i.e. has the same L_2-norm, due to the symmetry in system (5.1) arising from coupling two identical cells. Figure 5.2 ($g_{ton} = 0.877$, panels 1C and 2C) shows one realisation of the AS pattern. By symmetry, the second realisation is obtained by switching the colours.

As g_{ton} is decreased further, the AS branch loses stability in a supercritical torus bifurcation (TR$_a$), where an attracting torus in phase space is created. The AS solutions shown in Figure 5.4 bifurcate to an amplitude modulated spiking (AMS) pattern shown in Figure 5.5 as trajectories switch to the new torus attractor. The torus structure can be clearly identified in the return map shown in Figure 5.6A. The return map is constructed by setting up a Poincaré section and recording when the flow crosses the section. In phase space, this section is a codimension-one (codim-1) surface through the torus attractor constructed by
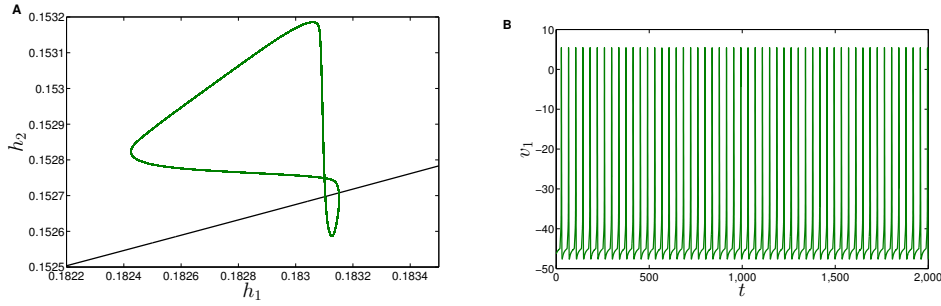
Figure 5.4: Trajectory of the full system (green) for $(g_{ton}, g_{syn}) = (0.87, 3)$, just before TR_a occurs. For this particular choice of parameters, the full system exhibits asymmetric spiking. *A:* Trajectory of the full system projected into the slow phase plane. The black curve is the continuation of the SNPO bifurcation of the layer problem (see Section 5.3). *B:* Voltage time trace of one of the cells; we observe asymmetric spiking, with voltage spikes of the other cell occurring in anti-phase with these (not shown).
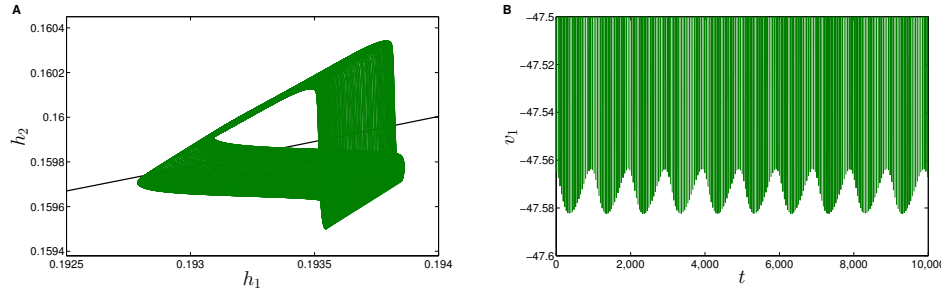
Figure 5.5: Trajectory of the full system (green) for $(g_{ton}, g_{syn}) = (0.85679, 3)$, with g_{ton} just below TR_a (as also shown in Figure 5.6A). For this particular choice of parameters, the full system exhibits amplitude modulated spiking (AMS). *A:* Trajectory of the full system projected into the slow phase plane along with the layer problem SNPO bifurcation curve (black). *B:* Voltage time trace of trajectory, zoomed to focus on spike troughs. As a result of the phase space torus, we see an AMS pattern in the voltage.

fixing one variable of (5.1). We evolve the full system and, after a suitable transient time, record when trajectories cross the Poincaré section transversally. The Poincaré map itself is constructed by plotting the value of one variable, which is not constant on the Poincaré section, at one crossing versus that variable's value at the previous crossing.

As g_{ton} is decreased further still, the torus quickly breaks down; see Figure 5.6B-D. Complex firing patterns are observed (see Figures 5.7-5.8), which mark the transition from asymmetric spiking to asymmetric bursting (AS to AB). For small enough g_{ton}, the AB patterns become more regular; see Figures 5.2 (panels 1B and 2B) and 5.9 for $g_{ton} = 0.75$. There is a delay between the TR_a bifurcation and the onset of AB due to the AMS patterns before the torus is destroyed. The breakdown of the torus clearly corresponds to the AS to AB transition, and hence the associated TR_a bifurcation is closely related to the AS/AB boundary.

The AB patterns observed (e.g., Figure 5.9) are not actually periodic and we are not able to continue these bursting solutions in continuation software packages such as AUTO
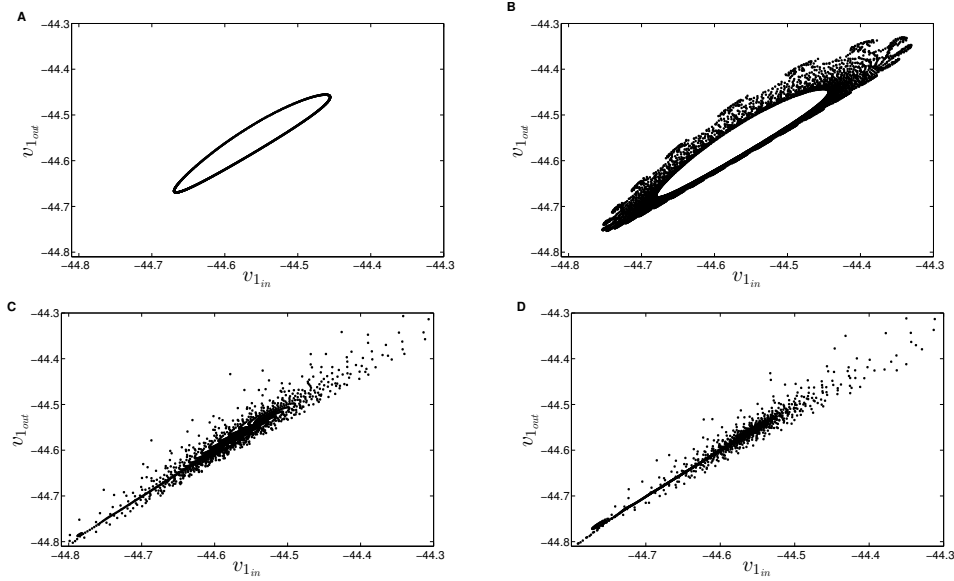
Figure 5.6: Return maps of the flow of the full system (5.1). *A:* $(g_{ton}, g_{syn}) = (0.85679, 3)$. The full system exhibits AMS; see Figure 5.5. We can clearly see the formation of a torus. *B:* $(g_{ton}, g_{syn}) = (0.856765, 3)$. The torus begins to break down. *C:* $(g_{ton}, g_{syn}) = (0.85676, 3)$, just after the torus begins to break down. *D:* $(g_{ton}, g_{syn}) = (0.8565, 3)$. For panels C and D, the full system exhibits complex bursting patterns.
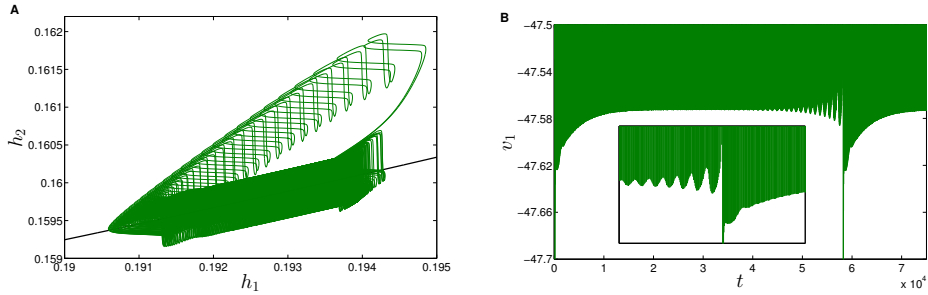

Figure 5.7: Trajectory of the full system (green) for $(g_{ton}, g_{syn}) = (0.8565, 3)$, for g_{ton} just below TR_a (as also shown in Figure 5.6D). *A:* Trajectory of the full system projected into the slow phase plane along with the layer problem SNPO bifurcation curve (black). *B:* Voltage time trace of trajectory, zoomed in to focus on spike troughs. We observe a complicated pattern in which amplitude modulation occurs towards the end of each burst.

[34]. Nonetheless we are able to identify a bifurcation structure that is closely related to the transition from asymmetric bursting to symmetric bursting (AB to SB). Recall the unstable symmetric spiking (SS) pattern created in the PF bifurcation. As we continue this unstable SS branch in the direction of decreasing g_{ton}, it undergoes a torus bifurcation (TR_s) as well (see Figure 5.3). This bifurcation occurs in close proximity to where we numerically observe the AB to SB transition. Since two Floquet multipliers destabilise as we decrease g_{ton} through the TR_s bifurcation, and the numerically observed transition from SB to AB happens close by but for a larger g_{ton} value than the TR_s bifurcation, we conjecture that
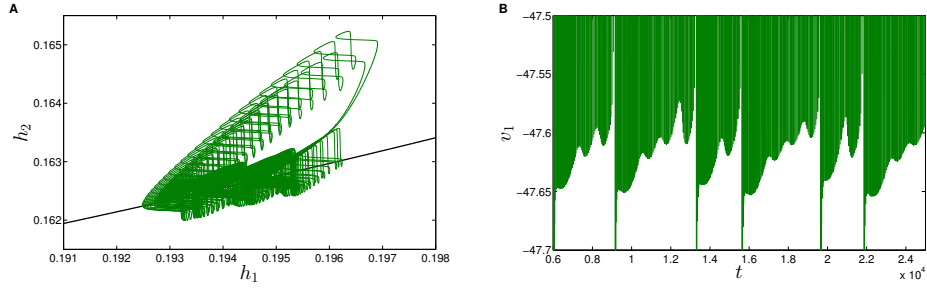
Figure 5.8: Trajectory of the full system (green) for $(g_{ton}, g_{syn}) = (0.85, 3)$, below the TR_a bifurcation. *A:* Trajectory of the full system projected into the slow phase plane along with the layer problem SNPO bifurcation curve (black). Note that the true attractor is quite chaotic, and we only show a portion of it here. *B:* Voltage time trace of trajectory, zoomed to focus on spike troughs.
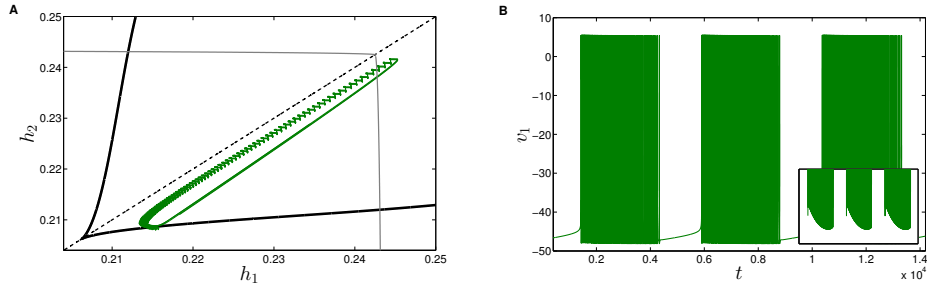

Figure 5.9: Trajectory of the full system (green) for $(g_{ton}, g_{syn}) = (0.75, 3)$ where the model shows a typical AB pattern. *A:* Trajectory of the full system projected into the slow phase plane along with the layer problem SNPO bifurcation curve (black). The $h_1 = h_2$ symmetry axis is indicated by the black dashed line. The thin grey line is the continuation of F_l (the fold of equilibria from the layer problem; see Section 5.4.1) in (h_1, h_2), which approximates the end of the silent phase. *B:* Voltage time trace of trajectory. The inset diagram in the bottom right corner shows a zoom of the bottom region.

the TR_s bifurcation contributes to the transition and is subcritical. Similarly as before, we expect a torus breakdown nearby (although the torus is unstable and we cannot observe this breakdown as we did near TR_a), which would then be involved in the emergence of an unstable symmetric AMS pattern as well as the stable SB pattern, as suggested by our numerical observations. The relationship between the TR_a bifurcation and the AS/AB transition will become much clearer in Section 5.3, where we identify corresponding bifurcations in the context of GSPT.

Decreasing g_{ton} further, we observe the final transition from SB to quiescence. As we approach the transition, numerics indicate that the silent phase of the SB pattern becomes longer and longer, which suggests that the termination involves a homoclinic bifurcation. On the other hand, for very low g_{ton} there is a stable branch of equilibria that correspond to the quiescent state of the Butera model. For increasing g_{ton}, the stable equilibrium loses stability in a (subcritical) AH bifurcation (see Figure 5.3). The emerging small amplitude oscillations quickly bifurcate through an incomplete canard explosion that terminates in a homoclinic.

This type of progression is indicative of the singular nature of the AH bifurcation, and creates a small window of bistability (which we observe numerically) between the SB and quiescent states. The exact bifurcation sequence towards the stable, highly irregular SB pattern is unknown.

In summary, we have identified four important bifurcations (AH, TR_a, TR_s, PF) that can be related to the boundaries of the five observed activity patterns in Figure 5.1B (quiescent, SB, AB, AS, SS). Figure 5.10A shows a continuation of the four codim-1 bifurcations in (g_{ton}, g_{syn}) parameter space, which was completed using AUTO. A first comparison between Figures 5.1B and 5.10A shows good agreement, except for low g_{syn} values. Discrepancies arise because of the different techniques used to find the boundaries between the various regions of activity. The boundaries in Figure 5.10A are based upon a full system bifurcation analysis, while those in Figure 5.1B were generated from brute force simulations, leading to difficulties in distinguishing between bursting and spiking for low g_{syn}. In Section 5.3, we present a GSPT analysis in the context of averaging and further discuss where our results break down and how this could lead to discrepancies between Figures 5.1B and 5.10A. Furthermore, we emphasise that while the PF bifurcation curve in Figure 5.10A clearly marks the transition from symmetric spiking to asymmetric spiking, the torus bifurcation curves serve only as proxies that are close to transitions between the other activity patterns.

5.2.2 Two parameter continuation

Having identified the relevant bifurcations in a one parameter continuation, we now turn our attention to a two-parameter continuation in (g_{ton}, g_{syn}) parameter space. Certain codim-2 bifurcations naturally partition (g_{ton}, g_{syn}) space into six distinct Cases (see Figure 5.12). In this section we identify the codim-2 bifurcations associated with the boundaries and discuss the transition between the different Cases.

There is additional bifurcation structure in the Butera model that has not been previously identified. As we continue the PF branch in (g_{ton}, g_{syn}) towards larger values of g_{syn} (starting from Case 1 in Figure 5.11), we observe a codim-2 bifurcation (a degenerate pitchfork bifurcation) where the PF changes its criticality from supercritical to subcritical (see also Figure 5.10C). At this codim-2 point, which marks the boundary between Cases 1 and 2, a branch of codim-1 SNPO bifurcations emerge. The numerically generated bifurcation curves (see Figure 5.10C) are difficult to distinguish due to their proximity, and a qualitative sketch of their positioning is shown in Figure 5.11 (SNPO shown in black). Figure 5.12 shows the corresponding one-parameter bifurcation diagram for fixed $g_{syn} = 6$, where the PF bifurcation has switched to subcritical and we see the associated SNPO bifurcation; compare with the supercritical case in Figure 5.3. This SNPO bifurcation was not identified in the initial analysis of Best et al. [11] and it has some important implications. In particular, for a fixed value of g_{syn} above the degenerate PF, there exists a small interval of g_{ton} values for which the SS and AS branches coexist. Thus the model exhibits bistability of the symmetric and asymmetric spiking patterns (see Figure 5.12) for large enough g_{syn}.

As g_{syn} is increased, the TR_a branch exchanges position with the PF branch. Note that this is not a codim-2 bifurcation as TR_a and PF do not collide, but it nonetheless marks the transition from Case 2 to 3 in Figure 5.11. Further increasing g_{syn} leads to the collision of the TR_a and SNPO branches in another codim-2 bifurcation, a fold-torus
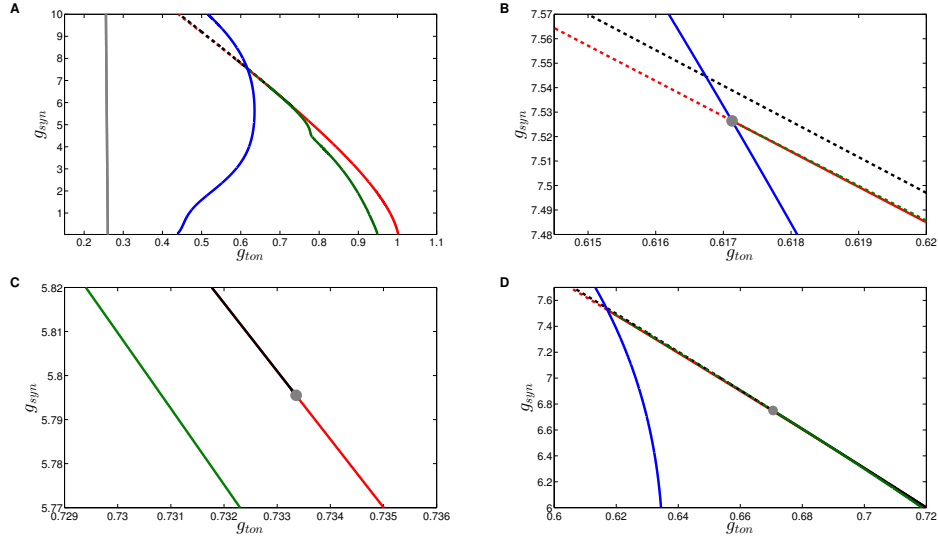
Figure 5.10: Continuation results for the full system. Panels A to D show two-parameter bifurcation diagrams of the full system (5.1) for $\epsilon/\bar{\tau}_h = 10^{-5}$. Different colours indicate different bifurcations (blue, TR_s; green, TR_a; red, PF; black, SNPO; grey, AH). *A:* Bifurcation curves over the full range of parameter values considered. *B:* Zoom near the organising centre (marked with a grey circle), where the TR_s, TR_a and SNPO curves collide. *C:* Zoom showing the change in criticality of the PF bifurcation. We see the SNPO branch emerging from the co-dimension two bifurcation (marked with a grey circle). Unfortunately, the angle between the red and the black curves is so small that one cannot distinguish the curves by eye (compare with the sketch in Figure 5.11). *D:* Zoom near codimension-two TR_a-SNPO bifurcation. Again, the angle between the green and the black curves is so small that one cannot distinguish the curves by eye although one might be convinced that the curves get closer around $g_{ton} \approx 0.67$ (compare with the sketch in Figure 5.11). In all panels, the red and black dashed lines indicate regions where the SNPO and PF bifurcation curves have no impact on the observed activity patterns.

bifurcation (TR_a-SNPO). This codim-2 bifurcation marks the boundary between Cases 3 and 4. Again, the numerically generated bifurcation curves (Figure 5.10A,D) are difficult to distinguish due to their proximity. On the other hand, Figure 5.13 (a one-parameter bifurcation diagram for fixed $g_{syn} = 7$) clearly shows that the TR_a bifurcation has passed through the SNPO bifurcation (compare with Figure 5.12). After this bifurcation, the AS family becomes completely unstable, and hence the switch from solid to dashed green in Figure 5.11. The one-parameter bifurcation diagrams associated with the TR_a and the SNPO branches no longer involve any stable oscillations (see Figure 5.13). Hence, we show these two branches as dashed in Figure 5.11 above the codim-2 point.

We observe another codim-2 bifurcation (which forms the boundary of Cases 4 and 5) where the TR_s and PF branches cross and the TR_a branch terminates (a pitchfork-torus bifurcation). This bifurcation can also be observed in the numerically generated bifurcation curves (Figure 5.10B). Note that the PF branch remains subcritical on both sides of this codim-2 point; the switch from solid to dashed indicates that there are no stable oscillations associated with the PF bifurcation. Similar to the transition diagram produced by Best et al. (see Figure 5.1B), our identified codim-1 bifurcation curves appear
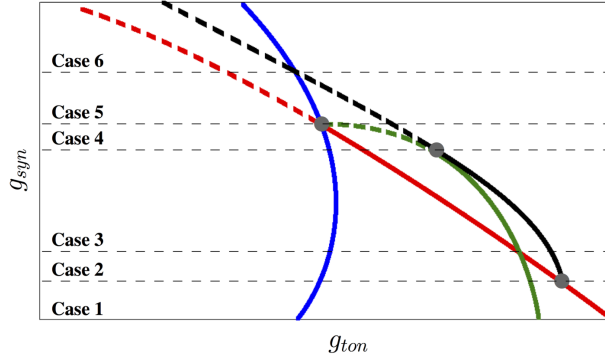
Figure 5.11: Schematic zoom of Figure 5.10 highlighting the codim-2 points (grey circles) and the structure near the organising centre. See Figure 5.10 for a description of the bifurcations. The red and black dashed lines indicate regions where the SNPO and PF bifurcation curves have no impact on the observed activity patterns, while the dashed green is used to show where no stable solution is involved in the TR_a bifurcation. The PF changes criticality where the SNPO and PF curves meet. Thin black dashed lines indicate the boundaries between six different cases, discussed in detail in Section 5.3.

to coalesce near $g_{syn} \approx 7.5$ at an *organising centre*, which is the codim-2 pitchfork-torus bifurcation point. The organising centre obviously plays a central role in regulating the dynamics of the model in (g_{ton}, g_{syn}) parameter space, in particular whether we observe symmetric or asymmetric activity patterns. As g_{syn} is further increased, the PF and TR_a bifurcation exchange positions. Once again, this point is not a bifurcation, but it does form the boundary of Cases 5 and 6.

In the next section we shift our focus to a GSPT framework and identify for each of the codim-1 bifurcations (TR_s, TR_a, PF, SNPO) a corresponding singular limit bifurcation, that expands our explanation of how the changes observed in bursting/spiking patterns (SB, AB, AS, SS) occur. The singular limit bifurcations will involve both regular and folded singularities of an averaged system, i.e. our work links to the concept of toral folded singularities and torus canards.

5.3   Averaging in the Context of GSPT

While the full system bifurcation analysis is useful, such an analysis does not shed much light on the genesis of the complex bursting and spiking patterns that arise in the model. Although we do not present a thorough dimensional analysis here, the small size of $\epsilon/\bar{\tau}_h$ leads to a significant separation between the rates of change of h_1, h_2 and those of the other variables in model (5.1). Thus the Butera model (5.1) can be treated as slow/fast system, with a six-dimensional layer problem consisting of the equations for v_i, n_i, s_i with both h_i fixed. Given the time scale separation in the model, it is useful to consider the complex patterns and the bifurcations observed in the full model from a GSPT standpoint.
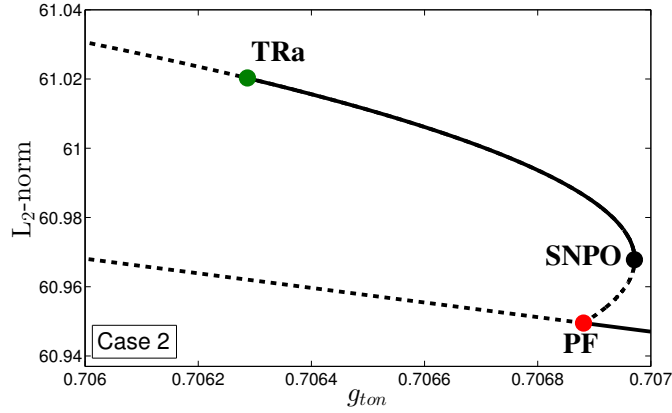
Figure 5.12: One parameter bifurcation (with respect to g_{ton}) of the full system for $g_{syn} = 6$, Case 2. Stable families of periodic orbits are indicated with solid black lines, while unstable families are indicated with dashed lines. For large g_{ton}, we see the primary stable family of periodic orbits (SS) that emanate from a subcritical AH bifurcation (not shown). The pitchfork bifurcation (PF) is now subcritical and an unstable family of periodic orbits emerge from the bifurcation. These orbits coalesce with a stable family (corresponding to AS) at an SNPO bifurcation, yielding bistability for an interval of g_{ton} values above the PF. As g_{ton} is decreased, the AS branch loses stability at TR_a.
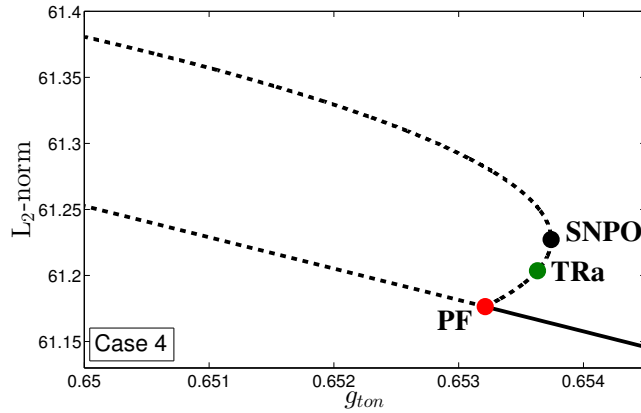

Figure 5.13: One parameter bifurcation diagram (with respect to g_{ton}) of the full system for $g_{syn} = 7$, Case 4. A stable family of periodic orbits is indicated with a solid black line, while unstable families are indicated with dashed lines. For large g_{ton}, we see the primary stable family of periodic orbits (SS) that emanate from a subcritical AH bifurcation (not shown). There is a subcritical PF, and two unstable branches of periodic orbits merge at an SNPO. Notice that in this case, TR_a occurs on the lower branch of periodic orbits emanating from PF. Consequently, all solutions other than SS are unstable.

5.3.1 The layer problem

As is the standard approach in GSPT, we study first the *layer problem*, which is given by setting $\epsilon = 0$ in (5.1):

$$v_i' = f_1(v_i, n_i, h_i, s_i),$$
$$n_i' = f_2(v_i, n_i), \tag{5.2}$$
$$s_i' = f_3(v_i, s_i).$$

The set of critical points of the layer problem forms the two-dimensional critical manifold

$$\mathcal{S} := \{(v_i, n_i, h_i, s_i) : f_1 = f_2 = f_3 = 0\}, \tag{5.3}$$

which is embedded in $\mathbb{R}^8$. Figure 5.14 shows a bifurcation diagram of the layer problem, with $h_1 = h_2 = h$ as the bifurcation parameter, projected into the (v_1, h) plane. The critical manifold consists of three branches, $\mathcal{S}_u$, $\mathcal{S}_m$ and $\mathcal{S}_l$, separated by two saddle-node or fold bifurcations (F_l and F_u). The upper branch $\mathcal{S}_u$ is stable for large h, but loses stability as h is decreased through an AH bifurcation. The periodic orbits emanating from AH correspond to in-phase solutions (labelled IP), which are always unstable, and hence we ignore them. Close to the first AH, a second AH bifurcation occurs, from which a family of anti-phase periodic orbits (AP) emerges. Initially, the branch of periodic orbits emanating from this second AH bifurcation is unstable, but this branch coalesces with a second stable branch ($\mathcal{P}_s$) at a saddle-node of periodic orbits bifurcation. As h is decreased, $\mathcal{P}_s$ undergoes another saddle-node of periodic orbits bifurcation (labelled SNPO) where it merges with a third branch of unstable periodic orbits ($\mathcal{P}_u$). This unstable branch $\mathcal{P}_u$ terminates in a homoclinic bifurcation on $\mathcal{S}_m$. This middle branch is of saddle type and has, by symmetry, a pair of unstable and two pairs of stable eigenvalues (at the homoclinic, the unstable pair has larger magnitude than the leading pair of stable eigenvalues). The lower branch $\mathcal{S}_l$ is stable. Hence, between the lower fold of equilibria (F_l) and the fold of periodics (SNPO), we have bistability. Such bistability and the fold of periodics are key ingredients for fold/fold cycle (or top hat) bursting (see Figure 5.14B). We continue these codim-1 bifurcations, SNPO and F_l, away from the symmetry axis $h_1 = h_2$ into (h_1, h_2)-space. Both continuations can be seen, e.g., in Figure 5.9, while segments of the SNPO continuation also appear in several earlier figures.

5.3.2 The (averaged) reduced problem

Switching to the slow timescale $t = \tau/\epsilon$ in (5.1) and then setting $\epsilon = 0$ gives the *reduced problem*,

$$0 = f_1(v_i, n_i, h_i, s_i),$$
$$0 = f_2(v_i, n_i),$$
$$\dot{h} = (h_\infty(v_i) - h_i)/\tau_h(v_i), \tag{5.4}$$
$$0 = f_3(v_i, s_i).$$

The flow of the reduced problem is restricted to the double-folded critical manifold $\mathcal{S}$, the set of critical points of the layer problem. For low g_{ton} values, there exists a stable equilibrium on the lower attracting branch S_l (almost) independent of g_{syn}, which defines the resting membrane potential of the neuron. As g_{ton} increases, this stable equilibrium bifurcates via the lower fold F_l to the unstable middle branch S_m. Solutions transition from the silent phase near S_l to the active phase near S_u, creating a bursting pattern. Normal hyperbolicity
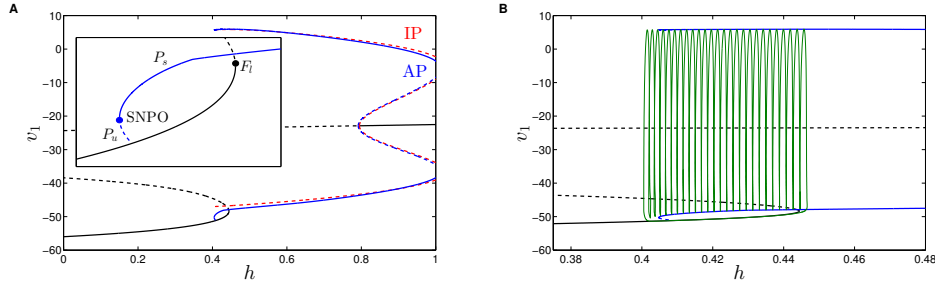
Figure 5.14: One parameter bifurcation diagram (with respect to $h_1 = h_2 = h$) of the layer problem for $(g_{ton}, g_{syn}) = (0.45, 3)$. *A:* Bifurcation structures. The critical manifold is shown in black. Two families of periodic orbits emerge from two AH bifurcations (not labelled) - the anti-phase (AP) family is shown in blue while the unstable in-phase (IP) family is shown in red. Stable (unstable) families of periodic orbits and equilibria are indicated with solid (dashed) lines, respectively. The inset diagram shows the interval of bistability bounded by the fold of periodics (SNPO) and fold of equilibria (F_l). *B:* Zoomed view including the projection of a symmetric bursting solution (green).

is lost at F_l where solutions leave $\mathcal{S}$ in a neighbourhood of F_l, and jump to the active phase. The lower fold F_l is a *jump point* where solutions switch from the slow to the fast time scale via an intermediate time scale; see Section 2.6 and [65, 100] for further details.

On the other hand, during the active phase of bursting, solutions oscillate in the vicinity of $\mathcal{S}$. This oscillatory motion is restricted closely to the manifold of periodic orbits $\mathcal{P}_s$ of the layer problem. The fast oscillations are accompanied by a slow drift in (h_1, h_2)-space. The slow motion near $\mathcal{P}_s$ is crucial in distinguishing between bursting and spiking behaviour, and we employ the technique of averaging to study it.

As in past work [11], we use the technique of averaging (see Section 3.3) to obtain an *averaged reduced system*

$$
\begin{aligned}
\langle \dot{h_1} \rangle &\equiv \frac{1}{T(h_1, h_2)} \int_0^{T(h_1,h_2)} g(v_{1_p}(h_1, h_2; t), h_1)\, dt \ =: a_1(h_1, h_2), \\
\langle \dot{h_2} \rangle &\equiv \frac{1}{T(h_1, h_2)} \int_0^{T(h_1,h_2)} g(v_{2_p}(h_1, h_2; t), h_2)\, dt \ =: a_2(h_1, h_2),
\end{aligned}
\tag{5.5}
$$

where $T(h_1, h_2)$ denotes the period of the layer problem periodic orbit that exists at (h_1, h_2), and v_{1_p}, v_{2_p} are the time courses of v_1, v_2 around this orbit. The averaged reduced system gives a first-order approximation of the slow (h_1, h_2) dynamics of trajectories of the full system near $\mathcal{P}_s$. Specifically, we focus on the so-called *averaged nullclines* of (5.5) given by

$$
\begin{aligned}
\mathcal{A}_1 &:= \{(h_1, h_2) : a_1(h_1, h_2) = 0\}, \\
\mathcal{A}_2 &:= \{(h_1, h_2) : a_2(h_1, h_2) = 0\}.
\end{aligned}
\tag{5.6}
$$

The intersections of $\mathcal{A}_1$ and $\mathcal{A}_2$ yield *averaged equilibria*. If an averaged equilibrium is a hyperbolic fixed point of (5.5), then for $\varepsilon > 0$ but sufficiently small, there exists a unique hyperbolic periodic orbit in the full system (5.1). The stability type of this periodic orbit, with respect to the slow variables (h_1, h_2), is given by the stability of the averaged equilibrium in the context of the averaged reduced system, while stability in the fast directions is determined by the stability of the corresponding periodic orbit of the layer problem [83, 26].

We also identify special structures of the averaged reduced system (5.5), which live on the SNPO, called *averaged folded singularities* or *toral folded singularities*. Recall the geometric condition for a toral folded singularity from Section 3.4: in the averaged slow variable $(\langle h_1 \rangle, \langle h_2 \rangle)$ subspace, the projection of the averaged slow flow (5.5) is tangent to the projection of the SNPO. Note that we assume that this condition holds for $m > 2$ fast variables; see Section 3.4 for further details. In a similar fashion to regular folded singularities, toral folded singularities allow the averaged reduced flow (5.5) to cross the SNPO. This naturally leads to torus canards: solutions which cross the SNPO and track the repelling branch of periodics $\mathcal{P}_u$ for $\mathcal{O}(1)$ time before being repelled.

We utilise the software package AUTO [34] to compute the average nullclines by continuation, continue the averaged equilibria and toral folded singularities with respect to the parameters g_{ton} and g_{syn} (see Sections 3.5.1–3.5.3 for a description of the numerical implementation). Our numerical implementation of the averaged equilibria and toral folded singularities facilitates the detection of bifurcations of the averaged reduced problem, which is central to our analysis. In the past, numerical averaging methods for fast-slow systems have mainly been implemented for systems with a single slow variable [26, 93], with a few exceptions [23, 96, 11]. We extend the standard averaging techniques, particularly with the continuation of averaged equilibria and detection of their bifurcations.

Key to our analysis of the averaged reduced problem is the existence of the folded structure of periodic orbits in the layer problem (SNPO in Figure 5.14), which forms the boundary of the active oscillatory phase for g_{syn} away from zero. We denote the continuation of this boundary in (h_1, h_2)-space by $\mathcal{B}$. Best et al. [11] approximated $\mathcal{B}$ numerically through simulations. Furthermore, they restricted their analysis of the averaged nullclines to the domain $\mathcal{O}$ in the (h_1, h_2) plane, in which the layer problem exhibits stable periodic oscillations, i.e. to the stable branch $\mathcal{P}_s$. We also take the unstable oscillation branch $\mathcal{P}_u$ into account, which is crucial for understanding the bifurcations responsible for the observed transitions between activity patterns.

Remark 5.1. It is a striking result that coupling two tonically spiking model neurons with $g_{syn} > 0$ can cause bursting to emerge in the neuron pair. While such bursting can already arise for quite weak g_{syn}, bifurcation structures may start to break down for small g_{syn}; for example, the SNPO of the layer problem will not persist for sufficiently low g_{syn} since in the uncoupled case we have a pair of fold/homoclinic (square wave) bursters, as detailed in [11]. Hence we avoid the weak coupling limit and restrict our analysis to $g_{syn} \geq 1$, where the distinction between bursting and tonic spiking is clearer as the neurons affect each other more significantly. Furthermore, for $g_{syn} \geq 1$, the folded structure of the layer problem manifold of periodic orbits (i.e. the SNPO) exists for all relevant values of g_{ton}.

5.3.3   Bifurcation analysis of the averaged reduced problem

In Figure 5.15 we see a bifurcation diagram of the averaged reduced problem, with respect to the parameter g_{ton}, for fixed g_{syn}=5.5. We refer to this as Case 1 (see also Figure 5.10B for this and other cases discussed below). We identify four bifurcations: a pitchfork bifurcation (PF), two folded saddle-node type I (FSN I) bifurcations, two folded saddle-node type II (FSN II) bifurcations and a folded saddle-node type III (FSN III) bifurcation. Recall from Section 2.3.2 that there is a well known singularity structure associated with
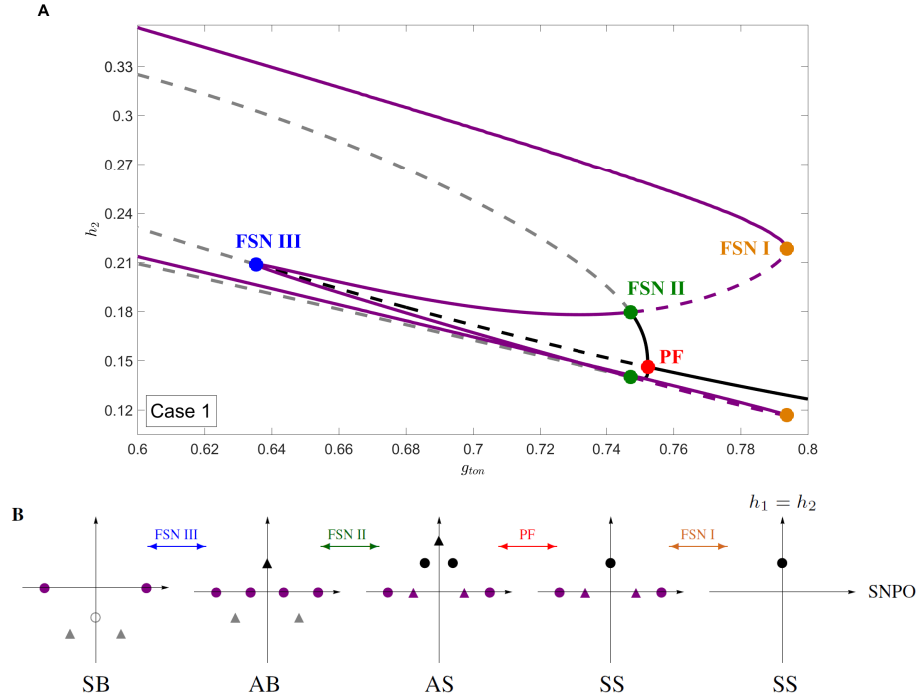
Figure 5.15: *A:* Continuation of averaged equilibria (black/grey) and folded singularities (purple) for $g_{syn} = 5.5$, Case 1, projected into the (g_{ton}, h_2) plane. Bifurcations of average equilibria are labelled in the diagram and stable (unstable) equilibria are indicated by solid (dashed) lines, respectively. Branches coloured black (grey) indicate that the branch of equilibria lie on $\mathcal{P}_s$ ($\mathcal{P}_u$), respectively. Solid purple branches denote averaged folded node singularities, while the purple dashed denote folded saddles. *B:* Summary of all the averaged equilibria (black/grey) and folded singularities (purple) in Case 1. Each panel shows the structure of the averaged reduced system for (in order of increasing g_{ton}): symmetric bursting (SB), asymmetric bursting (AB), asymmetric spiking (AS) and symmetric spiking (SS). Averaged equilibria are coloured black/grey while folded singularities are purple. Closed (open) circles are stable (unstable) nodes while the triangle indicates a saddle equilibrium. The purple circles and triangles are folded node and folded saddle singularities, respectively. The horizontal axis represents the fold or SNPO curve in the (h_1, h_2) plane, while the vertical axis represents the symmetry axis $h_1 = h_2$.

folds, known as folded singularities. The FSN I bifurcation is a saddle-node bifurcation of folded singularities (one folded saddle and one folded node). The FSN II bifurcation is a transcritical bifurcation of a folded singularity and a regular equilibrium of the reduced problem. See Sections 2.4.1 and 2.7.5–2.7.6 for further details regarding FSN bifurcations. The FSN III bifurcation, which is novel and will be analysed in greater detail in Chapter 7, is a pitchfork bifurcation of two folded singularities and one equilibrium of the averaged reduced problem. Note that we infer the type/stability of the numerically identified toral folded singularities based on the constraint of achieving consistency across scenarios and perform numerical simulations that show results consistent with our inferences. In Section 6, we present an analysis of a canonical system that encompasses exactly the collection of structures and interactions inferred here.
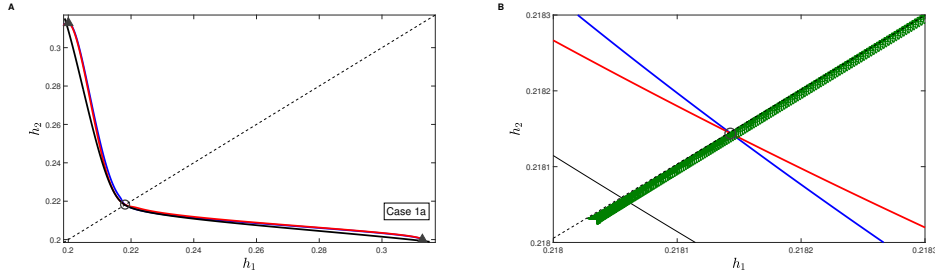
Figure 5.16: Phase plane for the averaged reduced system (5.5) for $(g_{ton}, g_{syn}) = (5.5, 0.62)$, Case 1a, where the full system exhibits symmetric bursting. *A:* Average nullcline configuration; the average nullclines $\mathcal{A}_1$ and $\mathcal{A}_2$ are shown in blue and red respectively. The continuation of the SNPO (the boundary curve $\mathcal{B}$) is shown in solid black while the symmetry axis $h_1 = h_2$ is shown in dashed black. $\mathcal{A}_1$ and $\mathcal{A}_2$ intersect along the symmetric axis resulting in an unstable node equilibrium, indicated by an open grey circle. There are also two asymmetric saddle equilibria, indicated with solid black triangles. Note that there are two outer folded node singularities, which lie outside the range of the diagram (see Figure 5.15). *B:* Zoom near the unstable node. The full system trajectory (green) approaches the SNPO from the upper right along the symmetry axis, exhibiting a path with small wiggles reflecting the active phase of the burst. Notice that the trajectory appears to pass straight through the node, unaffected. This is in fact a result of the projection onto the slow phase plane - the node lies on the unstable manifold of periodic orbits $(\mathcal{P}_u)$, while the trajectory of the full system oscillates near the stable manifold of periodic orbits $(\mathcal{P}_s)$. Their apparent crossing is an artefact of the projection (see Figure 5.17). As the trajectory crosses the SNPO curve (black), it leaves the active phase of the burst and enters the silent phase where it returns back towards the upper right (without wiggles; not visible here since the ranges of h_1, h_2 values traversed in the active and silent phases are the same).

With g_{syn} fixed, the identified bifurcations partition the g_{ton} axis into four intervals or subcases, which we refer to as Cases 1a through d. Utilising the average nullclines and resulting equilibria, we now present an analysis of each subcase for $g_{syn} = 5.5$ to elucidate the genesis of observed activity patterns. A summary of the averaged equilibrium structure and folded singularities for each subcase is provided in Figure 5.15B. Again, note that the properties of folded singularities are inferred here and corroborated in a canonical system in Section 6.

In Figure 5.16 we see the structure of the averaged reduced problem for $g_{syn} = 5.5$ and $g_{ton} = 0.62$ (Case 1a). For these parameter values, the full system exhibits symmetric bursting. Previously, Best et al. [11] characterised the symmetric bursting regime by $\langle \dot{h_1} \rangle, \langle \dot{h_2} \rangle < 0$, i.e. the absence of any averaged nullclines in $\mathcal{O}$. As can be seen in Figure 5.16, the averaged nullclines clearly exist within $\mathcal{O}$ for this particular case, and we find three averaged equilibria: a symmetric (i.e. $h_1 = h_2$) node, which is unstable, and two asymmetric saddles. Another interesting observation is the fact that bursting trajectories of the full system appear to pass straight through the node, unaffected. Careful consideration of our projection onto the (h_1, h_2) plane will help clarify theses nuances.

Recall that in the layer subsystem, there exists a stable manifold of periodic orbits $(\mathcal{P}_s)$ that coalesces with an unstable manifold of periodic orbits $(\mathcal{P}_u)$ at an SNPO bifurcation. It is the continuation of the SNPO, projected into the slow phase plane, which forms the boundary of the oscillatory region. A complication arising in this projection is that the
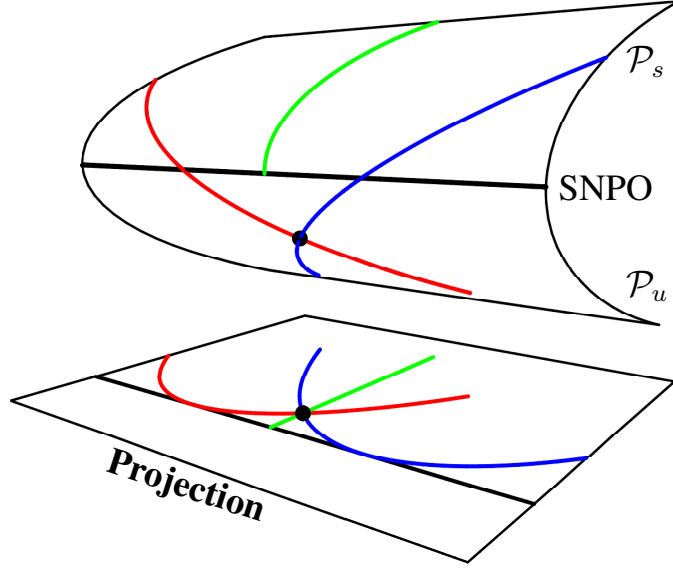
Figure 5.17: Illustration of how projecting from higher dimensions into the slow phase plane can be misleading. Illustrative average nullclines are shown in blue and red and their intersection (i.e. averaged equilibrium) is indicated with a black dot. Any trajectory travelling near $\mathcal{P}_s$ toward the SNPO curve (illustrated in green) will appear to cross the averaged equilibrium in the projection.

regions in (h_1, h_2) corresponding to $\mathcal{P}_s$ and $\mathcal{P}_u$ overlap. The unstable node found in the symmetric bursting regime actually lies on $\mathcal{P}_u$, while the bursting trajectory of the full system (5.1) passes along $\mathcal{P}_s$ (see also Figure 5.17). The projection onto the slow phase plane causes the two to seemingly overlap, but in reality they do not. Best et al. [11] computed the average nullclines via numerical simulations and did so only along $\mathcal{P}_s$, not $\mathcal{P}_u$. This explains why no averaged nullclines or equilibria were previously found for the symmetric bursting regime in Case 1.

If g_{ton} is increased to $g_{ton} = 0.7$, then the full system switches to an asymmetric bursting pattern, which we call Case 1b. The average nullcline structure for this case can be seen in Figure 5.18. In addition to the two outer folded singularities from Case 1a, we find an additional pair of folded singularities along the SNPO curve. The two asymmetric saddle equilibria from Case 1a persist, and we see the appearance of a symmetric saddle equilibrium on $\mathcal{P}_s$. As a result, trajectories of the full system now turn away from the symmetry axis near the saddle equilibrium and continue to burst until crossing the boundary. This regime is characterised by a much longer burst duration compared to Case 1a, which is caused by the long excursion away from the symmetry axis during the active phase (see also Figure 5.1A and [11]).

Note that the symmetric equilibrium has bifurcated from $\mathcal{P}_u$ via the SNPO curve to $\mathcal{P}_s$, and in doing so it must have exchanged its stability with a folded singularity. Due to the symmetry of our system (and the presence of two inner folded singularities), we infer the occurrence of a pitchfork bifurcation of folded and ordinary singularities, namely the FSN III that we mentioned earlier (also see Section 6). Based on the structure of the FSN
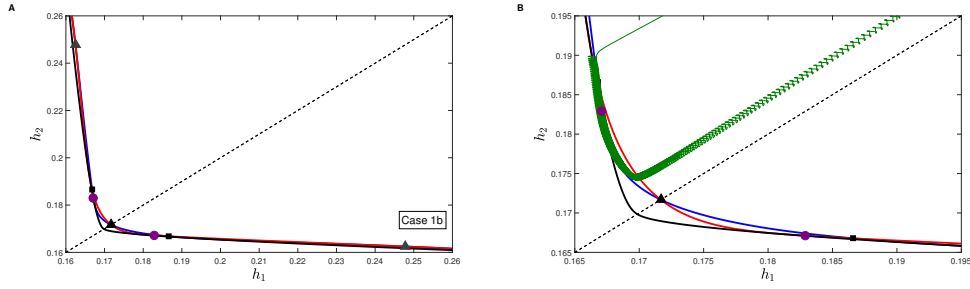
Figure 5.18: Phase plane for the averaged reduced system (5.5) for $(g_{ton}, g_{syn}) = (0.7, 5.5)$, Case 1b. *A*: Nullcline configuration, with the h_1-average nullcline in blue and the h_2-average nullcline in red. The symmetry axis $h_1 = h_2$ is indicated by a black dashed line. The solid black line is the continuation of the layer problem SNPO projected into the slow phase plane. The symmetric saddle equilibrium is denoted by a solid black triangle, while the two outer saddles are denoted by solid grey triangles. The solid squares mark meeting points of the projections of the average nullclines to the slow phase plane that are not true equilibria of averaged slow subsystem. Along the SNPO, there are two folded node singularities, marked by purple circles. Once again, there are two outer folded node singularities, which lie outside the range of the diagram (see Figure 5.15). *B*: Zoom near the symmetric saddle equilibrium point for Case 1b. An asymmetric bursting trajectory of the full system is shown in green. The two phases of the bursting solution are clearly visible: the segment of the trajectory with small wiggles indicates the active phase while the segment without wiggles the silent phase. Note the apparent crossing of the averaged nullclines at the solid squares, which is a 'fake intersection' of the nullclines (see Figure 5.20).
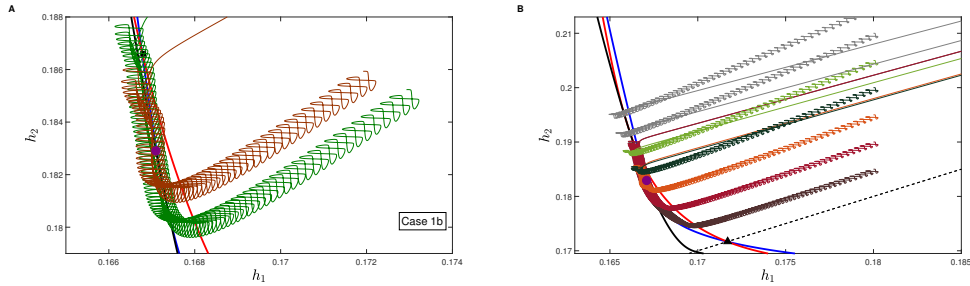

Figure 5.19: Transient behaviour for Case 1b, $(g_{ton}, g_{syn}) = (0.7, 5.5)$, near a folded node singularity. As in previous figures, the red and blue curves are averaged nullclines and the solid black curve is the continuation of the layer problem SNPO, while the dashed black curve is the symmetry axis. *A:* Segments of trajectories of the full system are shown in purple and brown. The two phases of these bursting solutions are clearly visible: segments of trajectories with small oscillations or wiggles correspond to the active phase, while segments without wiggles correspond to the silent phase. The small amplitude oscillations near the fold (SNPO) in the active phase of the burst provide further numerical evidence of the existence of the nearby folded node. *B:* Due to the folded node, transients in different regions of the slow phase plane have different rotational properties. Transients in grey show no small amplitude oscillations in the active phase, while those in other colours make an excursion along the fold and exhibit small amplitude oscillations (as shown in Panel A).

III bifurcation, we also infer that the pair of inner folded singularities must be folded node singularities. Past work attributed the SB/AB transition to the abrupt appearance of the saddle equilibrium in the oscillatory region $\mathcal{O}$. We now understand the true genesis of
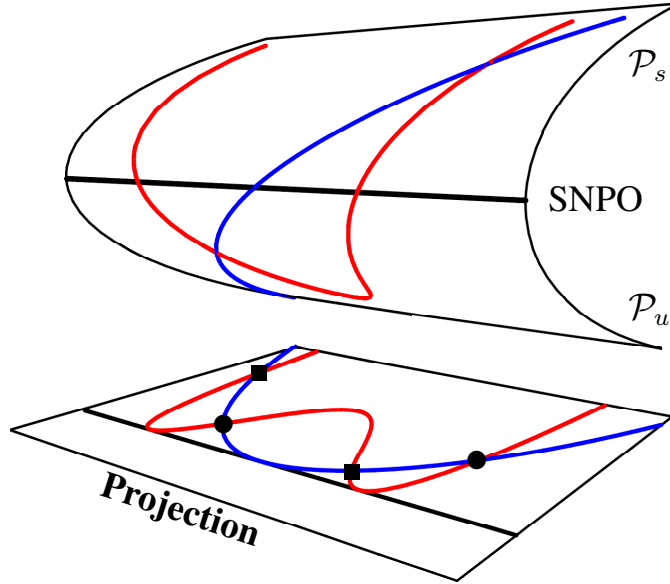
86

Figure 5.20: Illustration of how projecting from higher dimensions into the slow phase plane can lead to fake intersections of the average nullclines. Schematic average nullclines are shown in blue and red and their true intersections (i.e. averaged equilibria) are marked with black circles in the projection. Note that when the average nullclines are equidistant from the fold curve, but on opposite sheets of the fold, the average nullclines appear to intersect in the projection. These fake intersections are marked with solid squares.

the transition: an equilibrium always existed in the symmetric bursting regime, but as an unstable node on $\mathcal{P}_u$, and this node crosses the fold onto $\mathcal{P}_s$ through a FSN III bifurcation as we transition to asymmetric bursting. Note that we are actually able to locate the FSN type III singularity via continuation of the averaged equilibria by monitoring Floquet multipliers, i.e. we are able to identify when the averaged equilibria cross the SNPO (see Figure 5.15).

In the FSN III bifurcation, two folded node singularities are born on the symmetry axis concurrently with the change of stability of the symmetric equilibrium. As g_{ton} is increased, these folded nodes move along the SNPO, away from the symmetry axis. Apart from the numerical techniques used to identify the toral folded singularities (see Section 3.5.3), we find further evidence of their existence in the behaviour of nearby transient trajectories. Figure 5.19 shows transient small amplitude oscillations near the toral folded node, which are a hallmark of a regular folded node singularity [99, 110]. Typically, a folded node forms several separatrices through canards that partition the phase space into regions with various rotational properties. The closer trajectories lie to the axis of rotation formed by the weak canard, the smaller the amplitude of the oscillations they exhibit. Furthermore, outside of the funnel, trajectories undergo no rotations. Examples of trajectories outside the funnel are given by the grey orbits in Figure 5.19B, which immediately reverse direction upon reaching the SNPO curve, rather than experiencing an excursion along the curve, as the coloured trajectories within the funnel do. Note that due to the symmetry properties of the
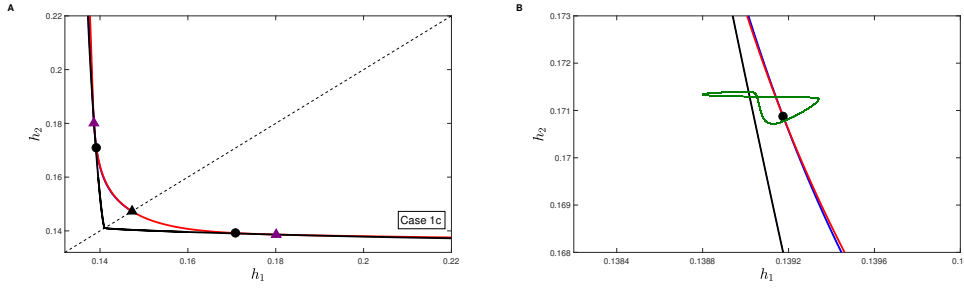
Figure 5.21: Average nullcline configuration for $(g_{ton}, g_{syn}) = (0.74985, 5.5)$, Case 1c. *A*: The h_1 and h_2-average nullclines are shown in blue and red, respectively. Note that the nullclines are nearly identical and it is very difficult to distinguish them. In this case the system has a symmetric saddle equilibrium on the symmetry axis (indicated by a solid black triangle) as well as two asymmetric stable node equilibria (solid black circles). There are also two folded saddle singularities (solid purple triangles) and two folded node singularities (not shown in this diagram). *B*: Zoom near the left asymmetric stable node. The stable spiking solution trajectory of the full system is shown in green. This pattern of spiking is called asymmetric, because the solution converges to the asymmetric stable node, away from the $h_1 = h_2$ symmetry axis in the slow phase plane.

system, we find similar small amplitude oscillations on the other side of the symmetry axis as well (not shown).

Remark 5.2. In the context of averaging, Vo [104] formally proved that some well known results of canard theory (such as the rotational properties of folded node canards and the existence of maximal canards) carry over to toral folded singularities. However, some results (such as the dynamics of faux toral saddle canards) were left for future work. Furthermore, Vo's results only hold for systems with $m = 2$ fast variables. As the Butera model has $m = 6$ fast variables, our numerics suggests that the results of [104] should extend naturally to higher dimensions, but it remains to formally justify this.

Upon closer examination of Figure 5.18A, we find another artefact of the projection: it appears that we have 5 intersections of the averaged nullclines, i.e. two more than in the previous case. As in the Case 1a, we see that the asymmetric bursting trajectory appears to pass through one of these (new) intersections (see Figure 5.18B). This time, the projection onto the slow phase space provides yet another deceptive view, because in fact, the nullclines do not intersect at all. Nullclines which are equidistant from the SNPO curve, but on opposite sheets of $\mathcal{P}$, appear to intersect in the projection; see the sketch in Figure 5.20. Thus we refer to these intersections in the projection only as '*fake intersections*'.

Increasing g_{ton} to 0.74985 (Case 1c), the system transitions to asymmetric spiking. This activity pattern is characterised by the appearance of a pair of stable, asymmetric node equilibria along $\mathcal{P}_s$, while the symmetric saddle equilibrium (also on $\mathcal{P}_s$) from Case 1b persists (Figure 5.21). Additionally, the pair of inner folded node singularities from the previous case have switched to saddle type, while the outer pair of folded node singularities persist. The full system exhibits asymmetric spiking, as trajectories are quickly attracted to one of the asymmetric stable nodes on $\mathcal{P}_2$, where they remain. The asymmetric node equilibria have bifurcated from $\mathcal{P}_u$ via the SNPO curve to $\mathcal{P}_s$, and exchanged stability with a pair of folded singularities singularities in a FSN bifurcation. As seen in Figure 5.15, the
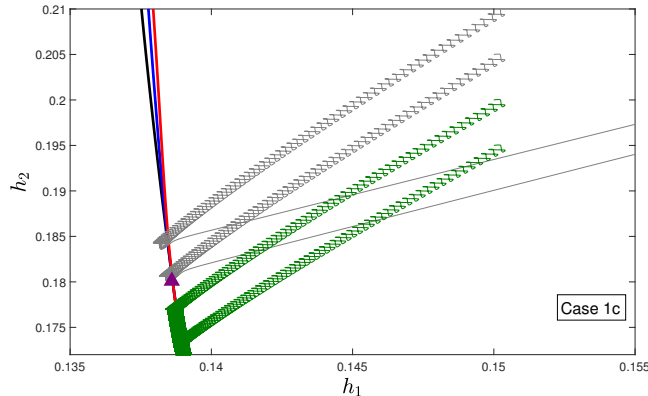
Figure 5.22: Transient trajectories near a folded saddle singularity (solid purple triangle) for Case 1c (asymmetric spiking), $g_{ton} = 0.74985$. Trajectories clearly show the existence of a separatrix, a hallmark of a folded saddle, which partitions the slow phase plane. Trajectories (grey) above the folded saddle burst until reaching the SNPO, fall off $\mathcal{P}_s$, and then enter the silent phase. Trajectories (green) below the folded saddle instead turn at the fold and converge to the stable node equilibrium (not shown), in the direction of decreasing h_2.

transition can be attributed to a transcritical bifurcation of folded and ordinary singularities, a FSN type II bifurcation (and thus we infer that the inner folded singularities must be of saddle type). This bifurcation, which was reviewed in Section 2.7.6, has been studied in other work [45, 66] and is well understood (in the context of equilibrium manifolds).

While toral folded node singularities existed in Case 1b, we found toral folded saddle singularities in Case 1c. One of the distinctive features of a regular folded saddle is the formation of a separatrix (canard), which partitions the phase space into two different regions. Trajectories in these two regions may exhibit very different behaviour. For example, Figure 5.22 shows transient trajectories with two distinctive behaviours. Grey trajectories burst until crossing the SNPO, after which they enter the silent phase. On the other hand, green trajectories burst while moving towards the SNPO, but make a sharp turn close to the SNPO and then converge to an asymmetric stable node equilibrium (not shown). This motion towards the stable equilibrium near the SNPO can be attributed to the presence of a faux that prevents the cell from reaching the SNPO and hence from leaving the active phase. Once again, our numerical simulations provide further evidence of the existence of a toral folded saddle, resulting in a separatrix that partitions the (h_1, h_2) plane (again, due to symmetry, the same structure is present near the second folded saddle). The role of folded saddle canards (in an equilibrium context) has been highlighted in a neural model study of observed paradoxical excitation due to propofol anaesthesia [77] as well as in modelling neural excitability in general [112].

Increasing g_{ton} to 0.785 (Case 1d), the system transitions to symmetric spiking. This activity pattern is characterised by the presence of a single stable, symmetric node equilibrium along $\mathcal{P}_s$ (Figure 5.24). Here, the symmetric equilibrium has bifurcated via a supercritical PF bifurcation of the symmetric saddle equilibrium and the pair of stable asymmetric equilibria. This transition has been described in detail in [11]. Notice that the inner pair of folded saddle singularities and the outer pair of folded node singularities from the previous
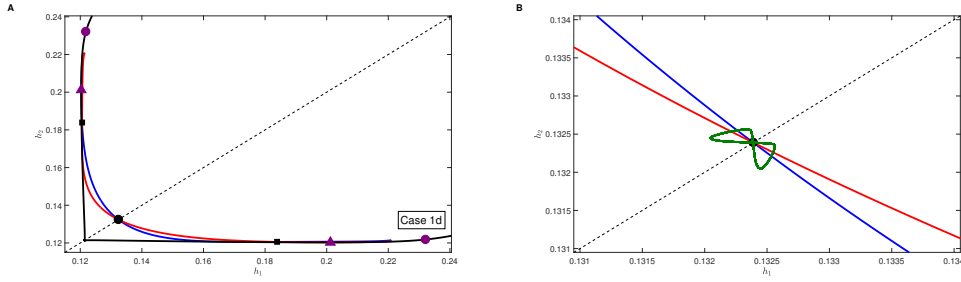
Figure 5.23: Average nullcline configuration for $(g_{ton}, g_{syn}) = (0.785, 5.5)$, Case 1d. *A*: The h_1-average nullcline is shown in blue while the h_2-average nullcline is shown in red. The symmetry axis $h_1 = h_2$ is indicated by a black dashed line, while the solid black line is the continuation of the layer problem SNPO projected into the slow phase plane. The symmetric stable node is indicated by a solid black circle, and the two pairs of folded singularities, are indicated by purple circles (folded node) and triangles (folded saddle). Once again, the solid black squares mark intersections of the average nullclines in the projection to the slow phase plane, which are not true intersections. Note that due to numerical difficulties, the continuation of the averaged nullclines terminates near $(h_1, h_2) = (0.121, 0.22)$, $(0.22, 0.121)$. *B*: Zoom near the symmetric stable node equilibrium for Case 1d. A stable periodic orbit of the full system, corresponding to symmetric spiking, is shown in green.

case persist.

Finally, increasing g_{ton} to 0.8 (Case 1e), we see that the system still exhibits symmetric spiking. While there has been no transition in activity patterns, the two pairs of folded singularities from the previous case have disappeared, while the symmetric node equilibrium on $\mathcal{P}_s$ persists; see Figure 5.23. The folded singularities have collided in two saddle-node bifurcations and annihilated each other. Thus the transition to Case 1d is marked by a FSN I bifurcation. We emphasise that there is no change in the stable attractor (i.e. the symmetric spiking state) of the model, however, the behaviour of transient trajectories could differ between Cases 1d and 1e.

5.3.4 Continuation for Cases 2 through 6

Next, we present continuations in g_{ton} for other cases corresponding to increasing values of g_{syn}. If g_{syn} is increased to $g_{syn} = 6$ (Case 2, see Figure 5.25), the bifurcation diagram of the averaged equilibria and folded singularities remains much the same as in Case 1, except for the appearance of two saddle node bifurcations (SN) and a change in criticality of the pitchfork, which occur together as g_{syn} increases. Now each branch of asymmetric equilibria that emerges at PF is unstable and coalesces with a second, stable, outer asymmetric branch at an SN, with one SN on each side of the symmetry axis. As g_{syn} is further increased, we move through the additional Cases 3-6. These cases are distinguished by the relative positions of the FSN II, PF, SN, and FSN III bifurcations. For example, in Case 3 (see Figure 5.26), FSN II lies between PF and SN along the outer branch of asymmetric equilibria. Also notice that FSN III and PF move closer together, compared to Case 2. As we transition to Case 4 (see Figure 5.27), FSN II moves over SN onto the inner branch of asymmetric equilibria. If we further increase g_{syn}, the FSN II collides with PF and is annihilated while FSN III moves through PF; these bifurcations arise together at the codimension-two
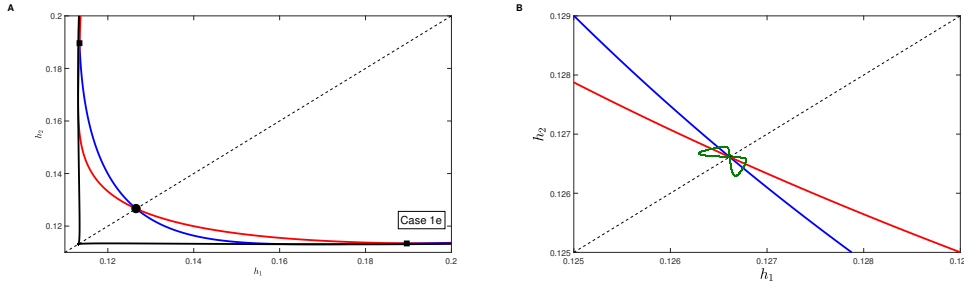
Figure 5.24: Average nullcline configuration for $(g_{ton}, g_{syn}) = (0.8, 5.5)$, Case 1e. *A*: The h_1-average nullcline is shown in blue while the h_2-average nullcline is shown in red. The symmetry axis $h_1 = h_2$ is indicated by a black dashed line, while the solid black line is the continuation of the layer problem SNPO projected into the slow phase plane. The symmetric stable node is indicated by a solid black circle, and the solid black squares mark intersections of the average nullclines in the projection to the slow phase plane. The nullclines do not actually intersect at these latter points, however, which result from the projection. *B*: Zoom near the symmetric stable node equilibrium for Case 1d. A stable periodic orbit of the full system, corresponding to symmetric spiking, is shown in green.

organising centre. The only difference between Case 5 and 6 (see Figures 5.28 and 5.29) is the position of FSN III relative to SN. In Case 5, FSN III lies between PF and SN, while in Case 6 it occurs at values of g_{ton} larger than SN.

Note that FSN II and III bifurcations in this singular limit approximation correspond to the torus bifurcations identified in the full system. It is well known that the FSN II singularity is the dynamic unfolding of the 2D singular Andronov-Hopf bifurcation, i.e. the FSN II indicates a singular AH bifurcation in the full system [31, 45]. We show in Section 6 that the same is true for a FSN III bifurcation. Unlike the FSN II and III, the FSN I bifurcation has no full system AH bifurcation [108]. In the context of the averaged reduced problem, the bifurcating 'equilibrium' state is actually a periodic orbit, and each AH bifurcation implies the creation of a torus. Thus Vo conjectures (and provides numerical evidence) in [104] that the FSN II bifurcation of the averaged reduced problem unfolds (in ε) to a singular torus bifurcation of the full system; we conjecture that the same is true for the FSN III. In classical planar singularly perturbed problems, the singular AH is always accompanied by a canard explosion [37, 65], an explosive growth in amplitude along a family of periodic orbits within an exponentially small parameter interval, which facilitates the rapid transition from small amplitude oscillations to relaxation oscillations. In the averaged setting that we consider, these singular bifurcations indicate the breakdown of a torus, as discussed in Section 5.2, and rapid transitions between the observed bursting patterns (SB, AB).

In the transitions between certain cases, we observe three codim-2 bifurcations in the averaged reduced problem, which are strongly related to the codim-2 bifurcations identified in the full system bifurcation analysis (see Figure 5.12). At the transition from Case 1 to 2, we see that PF changes its criticality from supercritical to subcritical and SN bifurcations emerge as g_{syn} is increased. This bifurcation corresponds to the degenerate PF observed in the full system, except that there a SNPO bifurcation emerged as g_{syn} was increased, since we were dealing with periodic orbits. As we move from Case 3 to Case 4, the FSN
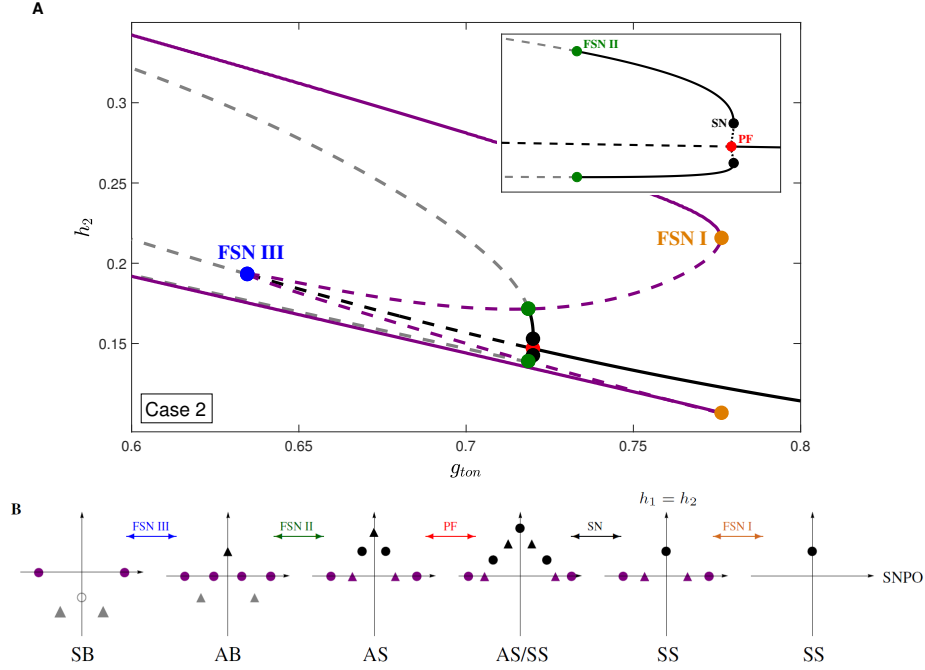
Figure 5.25: Bifurcations for $g_{syn} = 6$, Case 2. *A:* Continuation of averaged equilibria (black/grey) and folded singularities (purple), projected into the (g_{ton}, h_2) plane. Bifurcations of averaged equilibria are labelled in the diagram and stable (unstable) equilibria are indicated by solid (dashed) lines, respectively. Branches coloured black (grey) indicate equilibria that lie on $\mathcal{P}_s$ ($\mathcal{P}_u$), respectively. Solid purple branches denote averaged folded node singularities, while the purple dashed denote folded saddles. The inset diagram shows a zoom near the PF bifurcation. *B:* Summary of all the averaged equilibria and folded singularities of Case 2. Averaged equilibria are coloured black/grey while folded singularities are purple. Closed (open) circles are stable (unstable) nodes while the triangle indicates a saddle equilibrium. The purple circles and triangles are folded node and saddle singularities, respectively. The horizontal axis represents the fold or SNPO curve in the (h_1, h_2) plane, while the vertical axis represents the symmetry axis $h_1 = h_2$.

II and SN bifurcations coalesce at a second codim-2 bifurcation, similar to the collision of TR_a and SNPO (fold-torus bifurcation, TR_a-SNPO) in the full system. The final codim-2 bifurcation occurs at the organising centre between Cases 4 and 5, where FSN II, FSN III and PF collide. This bifurcation is similar to the pitchfork-torus bifurcation (PF-TR_a-TR_s) observed at the organising centre in the full system.

5.4   Discussion

In this work, we studied activity patterns, and transitions between them, in a model for an identical pair of respiratory neurons coupled with synaptic excitation. This model was originally introduced by Butera et al. [20, 21, 22] and it describes neurons in the pre-Btzinger complex, a brain stem region that plays a central role in respiratory rhythm generation. While model neurons can be quiescent, bursting, or tonically spiking, simulations revealed that the parameter regime over which bursting occurs in a pair of model neurons coupled
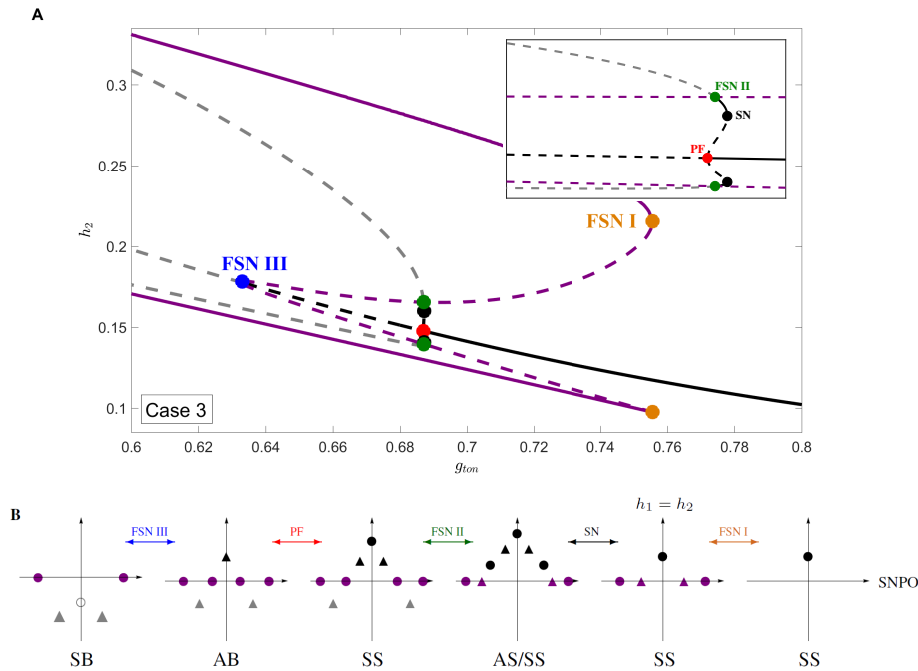
92

Figure 5.26: Bifurcations for $g_{syn} = 6.5$, Case 3. *A:* Continuation of averaged equilibria projected into the (g_{ton}, h_2) plane. Inset diagram shows a zoom near PF. *B:* Summary of all the averaged equilibria and folded singularities of Case 3.

by synaptic excitation is broader than that for a single, isolated neuron [20, 21]. Best et al. refined this investigation by uncovering different types of bursting and spiking regimes in a two-neuron network [11]. Their analysis used geometric singular perturbation theory and averaging techniques to illustrate the dynamic regimes in a reduced phase space that are responsible for these different activity patterns. They also used numerical simulations to establish the boundary curves separating these solution types in parameter space.

Our work builds on these earlier studies in several significant directions. We provided the first use of numerical continuation methods to follow bifurcation curves associated with the full two-neuron system. Our numerical analysis established that certain bifurcations correspond precisely to transitions between particular types of activity patterns, while others approximately indicate where such transitions occur (as long as we stay away from the weak coupling regime corresponding to small g_{syn}). The continuation results from the full system thus provided an improved view of where within parameter space the transitions between activity patterns occur, relative to earlier simulation results. Furthermore, our direct simulations, guided by results of the bifurcation analysis, also identified interesting variations on activity patterns, such as amplitude modulated spiking, which arise near these transitions and had not been observed previously.

While bifurcation analysis of the full system allowed us to estimate closely where activity transitions occur, it provided limited information about the properties of solutions involved and the dynamic mechanisms responsible for solution behaviours. We obtained a more precise representation of the structures that may be associated with the model's
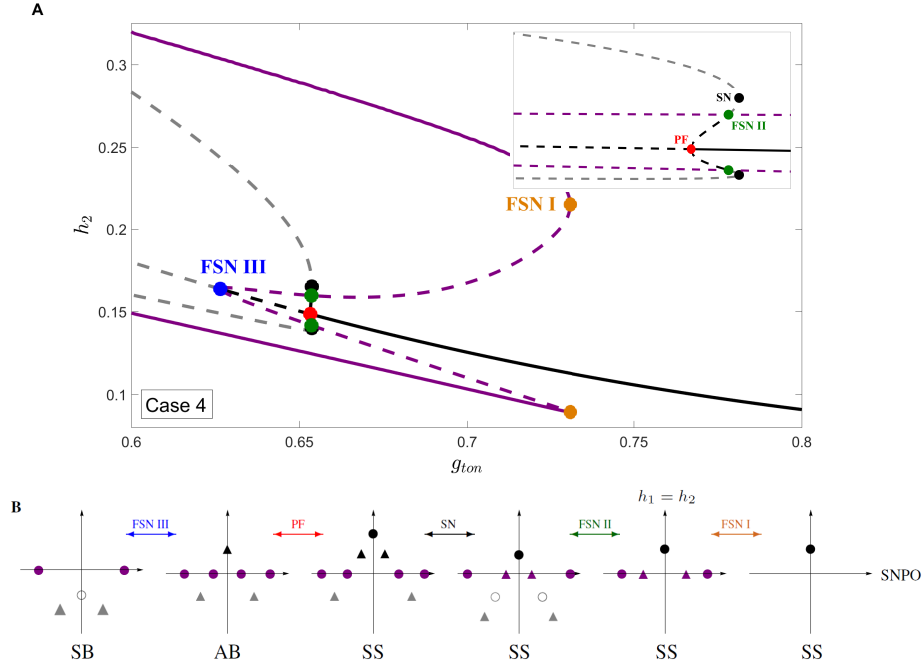
Figure 5.27: Bifurcations for $g_{syn} = 7$, Case 4. *A:* Continuation of averaged equilibria projected into the (g_{ton}, h_2) plane. Inset diagram shows a zoom near PF. *B:* Summary of all the averaged equilibria and folded singularities of Case 4.

activity patterns and the dynamic events associated with transitions between them by using a GSPT approach wherein numerical continuation is performed, using the continuation software AUTO [34], on the averaged reduced system that Best et al. simulated [11]. Continuation in this setting allowed us to track equilibrium states of the averaged reduced equations in parameter space and to unravel the underlying bifurcation structure that leads to activity pattern changes in that system. Our numerical continuation methods also enabled us to identify folded singularities of the averaged reduced system (i.e. toral folded singularities), and utilising interpolation, we constructed a continuation curve in parameter space of the toral folded singularities. This approach leads us to the new observation that equilibrium and folded singularity curves of the averaged reduced system interact in various FSN bifurcations. We identified three different types: the FSN I, FSN II and FSN III. The detection of folded singularities and corresponding bifurcations in such coupled neuron models is a novel step, presented here for the first time. Moreover, the FSN III is itself novel and is a consequence of $\mathbb{Z}_2$-symmetry arising from coupling two identical cells. A detailed analysis of the FSN III bifurcation will be tackled in Chapter 7 of this thesis.

Also open for subsequent studies is the rigorous establishment of the relation between the averaged reduced system and the full model. In the past, averaging theory was developed for singularly perturbed systems with hyperbolic periodic orbits of the layer problem (known as *Pontryagin-Rodygin Theory* [83]), and applied to bursting in models with one or two slow variables [55, 86, 44], excluding solutions which pass near an SNPO bifurcation curve. Our numerical simulations show the existence of torus canards, special solutions which
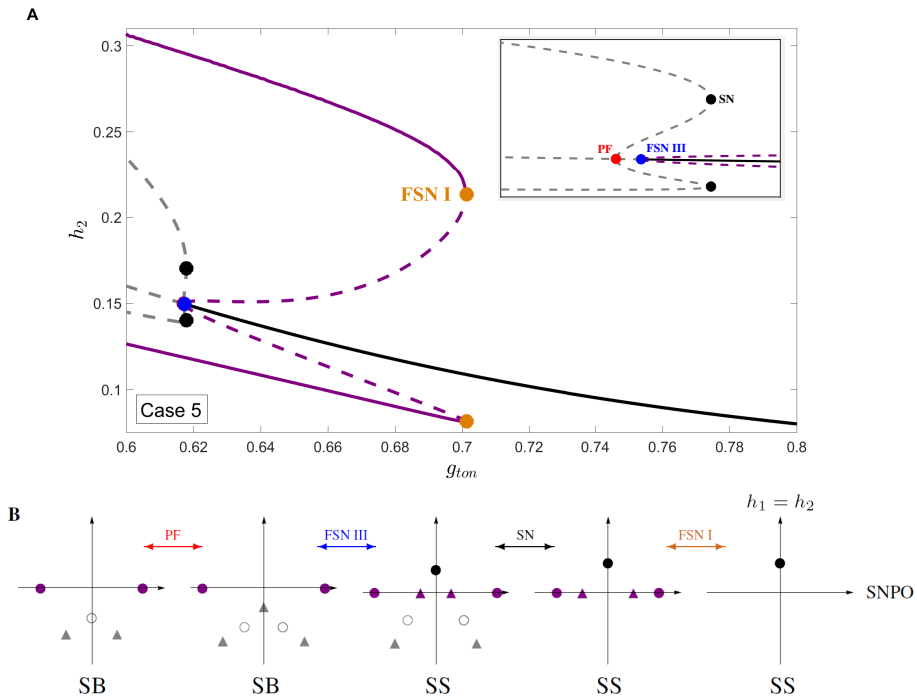
94

Figure 5.28: Bifurcations for $g_{syn} = 7.528$, Case 5. *A:* Continuation of averaged equilibria projected into the (g_{ton}, h_2) plane. Inset diagram shows a zoom near PF. *B:* Summary of all the averaged equilibria and folded singularities of Case 5.

drift across a SNPO curve and track a repelling family of periodic orbits, in the Butera model. Furthermore, our computational evidence suggests that torus canards, as well as an associated torus breakdown and torus canard explosion, mediate the transition between bursting and tonic spiking. Using a combination of GSPT and numerical averaging, we inferred the dynamics and behaviour of torus canards and toral folded singularities in the Butera model. The torus canard phenomenon has been observed in numerous neural models such as the WCI, Hindmarsh-Rose and Purkinje cell model. Only recently has averaging theory been extended to singularly perturbed systems where solutions pass near a SNPO bifurcation of the layer problem [104]. Vo [104] rigorously established for a general singularly perturbed model with any number of slow variables, up to two fast variables, and a layer problem family of periodic orbits with SNPO bifurcation, that the averaged reduced system is an $\mathcal{O}(\varepsilon)$ approximation of the full system; in other words, the average of a torus canard is indeed a folded singularity canard. Furthermore, Vo proved that many well know results of canard theory (such as the rotational properties of folded node canards and the existence of maximal canards) carry over to toral folded singularities. As the Butera model has six fast variables, our numerics suggests that the results of [104] should extend naturally to higher dimensions, but it remains to formally justify this.
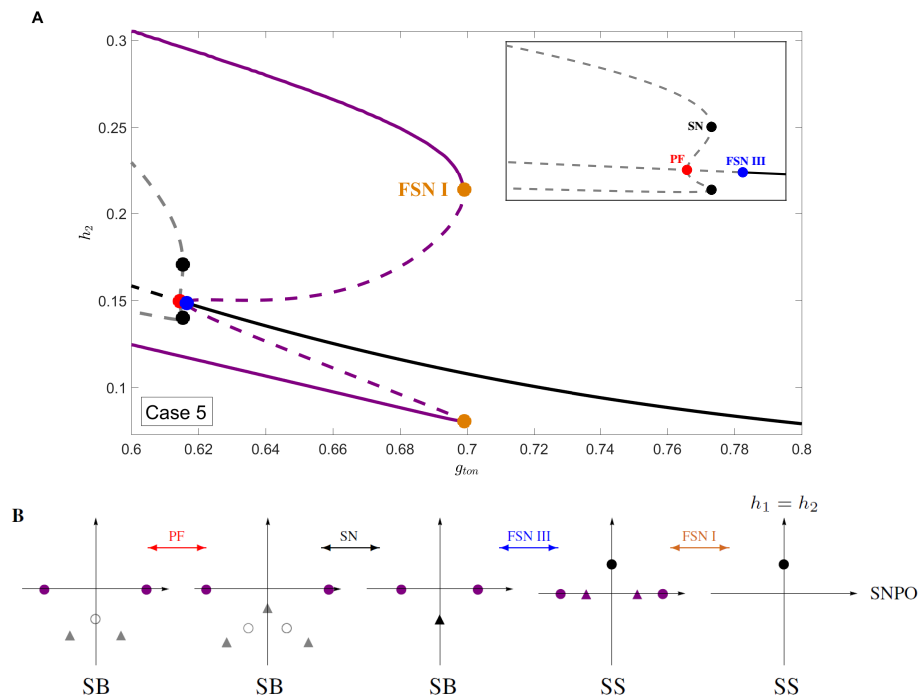
Figure 5.29: Bifurcations for $g_{syn} = 7.565$, Case 6. *A:* Continuation of averaged equilibria projected into the (g_{ton}, h_2) plane. Inset diagram shows a zoom near PF. *B:* Summary of all the averaged equilibria and folded singularities of Case 6.

Chapter 6

Canonical Model of the Organising Centre

Author's Contributions: This chapter is published as part of [87]. The canonical model was conceived by JR and MW, and analysed by all authors. The manuscript was written and edited by all authors.

In the previous chapter, we showed that the averaged reduced problem (5.5) holds the key to the understanding of the different activity patterns observed in the Butera model (5.1). We identified a variety of averaged equilibria and numerically identified various toral folded singularities, many of which interact in bifurcations as g_{ton} is varied, the order of which depends on g_{syn}. In particular, the analysis in Chapter 5 identified four important codim-1 bifurcation curves in (g_{ton}, g_{syn}) space – PF, FSN III, FSN II, and SN – as well as three related codim-2 bifurcations (see Figure 5.10B) that arise due to the interaction of these codim-1 bifurcation curves. Since these codim-2 points lie in close proximity of each other, these observations suggest that we are dealing with a particular unfolding of a codim-3 (or higher) organising centre in the underlying problem. The aim of this chapter is to support the numerical results of Chapter 5 by proposing and analysing a canonical model system that can be seen analytically to encompass the key structures and bifurcations identified in the averaged reduced problem.

We now formulate a local canonical system that describes the dynamics of (5.5) near the fold of the critical manifold for parameter values close to such an organising centre for all of the cases we have considered. For this canonical system, we can analytically establish that all of the putative singularities and bifurcations do indeed exist, along with pathways in parameter space that cover the six cases found for system (5.5). The local canonical system is given by

$$
\begin{aligned}
\dot{x} &= -z + \alpha - y^2, \\
\dot{y} &= -y\left(\beta - \gamma y^2 + y^4\right), \\
\varepsilon \dot{z} &= x - z^2,
\end{aligned}
\tag{6.1}
$$

where (x, y) are slow variables and z is a fast variable, $0 < \varepsilon \ll 1$ is the singular perturbation parameter, and $(\alpha, \beta, \gamma) \in \mathbb{R}^3$ are the bifurcation parameters. Note that system (6.1) has the $\mathbb{Z}_2$ symmetry $y \leftrightarrow -y$. Hence, y represents deviation from the symmetry axis, and $y = 0$

corresponds to $h_1 = h_2$ in the Butera model (5.1). The fast variable z should be seen as a representative of the original 6D fast system. While bursting and spiking activity patterns are not possible in system (6.1) and we do not provide a mapping between (α, β, γ) and (5.1), this local canonical system encodes all the mechanisms needed to explain the dynamics associated with observed transitions of activity patterns in system (5.5).

6.1 Bifurcation Structure in the Reduced Problem

Setting $\varepsilon = 0$ in system (6.1) gives the reduced problem

$$
\begin{aligned}
\dot{x} &= -z + \alpha - y^2, \\
\dot{y} &= -y\left(\beta - \gamma y^2 + y^4\right), \\
0 &= x - z^2,
\end{aligned}
$$

which is a differential-algebraic system that describes the evolution of the slow variables (x, y) restricted to the folded critical manifold $\{x = z^2\}$. Since the critical manifold is a graph over (y, z) coordinate space (although independent of y), we can study the reduced flow in a neighbourhood of the fold by first differentiating the algebraic constraint $x = z^2$ with respect to time to obtain

$$
\begin{aligned}
\dot{y} &= -y\left(\beta - \gamma y^2 + y^4\right), \\
2z\dot{z} &= -z + \alpha - y^2.
\end{aligned}
\tag{6.2}
$$

Desingularisation (i.e. rescaling time $dt = 2z\,ds$) of (6.2) removes the singular term at the fold $z = 0$, and yields the desingularised system

$$
\begin{aligned}
\dot{y} &= -2zy\left(\beta - \gamma y^2 + y^4\right), \\
\dot{z} &= -z + \alpha - y^2,
\end{aligned}
\tag{6.3}
$$

where the overdot denotes differentiation with respect to the rescaled time s. In both systems, (6.2) and (6.3), z represents deviation from the fold $z = 0$ on the critical manifold. Note that the direction of the flow in the desingularised system (6.3) must be reversed on the repelling sheet of the critical manifold ($z < 0$) to obtain a flow equivalent to (6.2). While system (6.2) describes the reduced flow on the critical manifold, it is straightforward to compute conditions for the existence of equilibria, folded singularities and their bifurcations from the desingularised system (6.3). Symmetric and asymmetric equilibria are given by

$$
\begin{aligned}
(y_s, z_s) &= (0, \alpha), \\
(y_a, z_a) &= (\pm\sqrt{\xi_\pm}, \alpha - \xi_\pm),
\end{aligned}
$$

where $\xi_\pm := (\gamma \pm \sqrt{\gamma^2 - 4\beta})/2$, assuming that the quantities under the radicals are non-negative Thus system (6.3) has four asymmetric equilibria when $\beta < 0$, two asymmetric equilibria when $\gamma > 0$ and $0 < \beta < \gamma^2/4$, and zero asymmetric equilibria when these conditions fail.

The Jacobian matrix for system (6.3) is given by

$$J = \begin{pmatrix} -2z(\beta - 3\gamma y^2 + 5y^4) & -2y(\beta - \gamma y^2 + y^4) \\ -2y & -1 \end{pmatrix}. \qquad (6.4)$$

Evaluating J for a symmetric equilibrium yields a diagonal matrix with eigenvalues $\lambda_1 = -2\alpha\beta$, $\lambda_2 = -1$. As we move through quadrants I, II, III and IV in the (α, β) plane, the symmetric equilibrium switches from a stable node to a saddle to stable node to saddle, independent of γ. For an asymmetric equilibrium, J becomes a lower triangular matrix, with eigenvalues $\lambda_1 = -1$ and $\lambda_2 = -2(\alpha - \xi_\pm)(\beta - 3\gamma\xi_\pm + 5\xi_\pm^2)$. Note that

$$\beta - 3\gamma\xi_\pm + 5\xi_\pm^2 = \sqrt{\gamma^2 - 4\beta}\left(\sqrt{\gamma^2 - 4\beta} \pm \gamma\right),$$

with $\gamma^2 > 4\beta$ for (γ, β) values where asymmetric equilibria exist. Away from the fold $z = 0$, we observe two different bifurcations of equilibria:

- a pitchfork (PF) bifurcation for $\beta = 0$ and
- a pair of saddle-node (SN) bifurcations for $\beta = \gamma^2/4$ where $\gamma > 0$.

Folded singularities are given by

$$(y_f, z_f) = \left(\pm\sqrt{\alpha}, 0\right).$$

Note that folded singularities are not equilibria of the reduced problem (6.2), but nonetheless can generate interesting dynamics; see Section 2.3. At these folded singularities, which only exist for $\alpha > 0$, trace$(J) = -1$ and det$(J) = -2\alpha(\beta - \gamma\alpha + \alpha^2)$. Thus the folded singularities can switch from node to saddle type. These changes are due to two types of bifurcations that involve both folded singularities and equilibria:

- a pair of folded saddle-node type II (FSN II) bifurcations away from the symmetry axis at $\alpha = \pm\xi_\pm > 0$ (or $\gamma = \beta/\alpha + \alpha$ for $\alpha > 0$, which always satisfies $\gamma^2 > 4\beta$), each of which corresponds to a transcritical bifurcation of an equilibrium and a folded singularity, and
- a folded saddle-node type III (FSN III) bifurcation at the origin $\alpha = 0$, which corresponds to a pitchfork bifurcation of an equilibrium and two folded singularities. The FSN III bifurcation is due to the underlying $\mathbb{Z}_2$-symmetry and has not been reported before in the literature.

We illustrate bifurcation curves for system (6.3) and their dependence on α, β, and γ pictorially, as shown in Figure 6.1. These diagrams come directly from the formulas above. We can pick out paths in these diagrams that correspond one-to-one to the cases derived from parameter continuation of g_{ton} in Section 5.3, as labelled in Figure 5.10B. Importantly, the sets of singularities present in the regions traversed by each path match those presented below the continuation diagrams in Figures 5.15B, 5.25B-5.29B. We leave it to the reader to check this equivalence.

Similar to the Butera model, we observe multiple different symmetric bursting regimes, i.e. there are several different singularity configurations in which there are no singularities
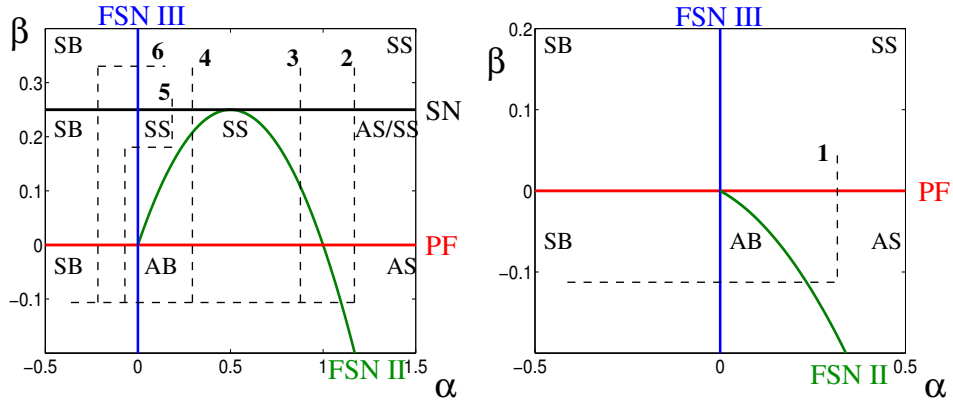
Figure 6.1: Bifurcation curves for system (6.3) in the (α, β) parameter plane for $\gamma > 0$ (top) and $\gamma < 0$ (bottom). The text within the figure indicates the bifurcation types separating regions (largest, colour-coded font) and the activity patterns within each region (intermediate-sized black font). Paths through (α, β) parameter space correspond to the numbered cases in Section 5.3 (see also Figure 5.10B). All paths start in quadrant III and progress initially in the direction of increasing α.
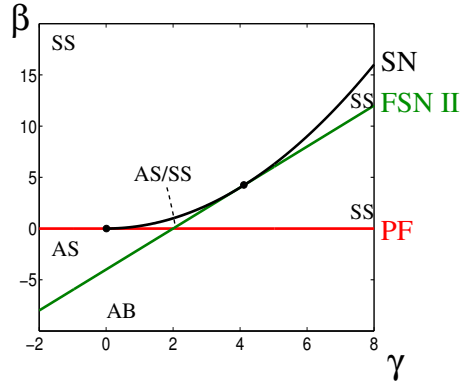

Figure 6.2: Bifurcation curves for system (6.3) in the (β, γ) parameter plane for $\alpha > 0$. The text within the figure indicates the bifurcation types separating regions (largest, colour-coded font) and the activity patterns within each region (intermediate-sized black font), as in Figure 6.1. Black dots denote codim-2 points. The case for $\alpha < 0$ features the same PF and SN curves as appear for $\alpha > 0$ but no FSN II curve (not shown).

on the attracting sheet of the critical manifold (e.g., with $\gamma > 0$ and $\alpha < 0$, compare $\beta < 0$ versus $0 < \beta < \gamma^2/4$ versus $\beta > \gamma^2/4$); cf. Figures 5.28 and 5.29. There are also multiple symmetric spiking regimes, all with a symmetric stable node on the attracting sheet of the critical manifold, as well a regime with bistability of asymmetric and symmetric spiking found for $\gamma, \alpha > 0$ and $\alpha\gamma - \alpha^2 < \beta < \gamma^2/4$ (cf. Figures 5.12, 5.25, 5.26). Moreover, the results in Figure 6.1 make very clear that for parameter regimes corresponding to $\gamma > 0$, which include g_{syn} values corresponding to Cases 2-6 in our earlier results, generic transitions between symmetric and asymmetric spiking involve regimes of bistability between the two solution types (see Cases 2-3).

We also identify the three codim-2 bifurcation curves in (α, β, γ) parameter space as

described for the averaged reduced flow of the Butera model at the end of Section 5.3:

- $\{(0,0,\gamma)\}$ where the FSN III and PF bifurcations collide and the FSN II bifurcation terminates (Figure 6.1),

- $\{(\alpha,0,0)\}$ where the SN bifurcation terminates at the PF bifurcation, and PF changes criticality (Figure 6.2), and

- $\{(\alpha,\alpha^2,2\alpha)\}$ within $\{\alpha > 0\}$, where the SN and FSN II bifurcations meet (Figures 6.1 and 6.2).

These three codim-2 curves are born out of the codim-3 point at the origin.

6.2   Bifurcation Structure in the Full System

To understand the relationship between the FSN III bifurcation in the reduced problem and the singular AH bifurcation in system (6.1), one has to consider the Jacobian of the full system (6.1) with $\epsilon > 0$, evaluated along the symmetric equilibrium $(x_s, y_s, z_s) = (\alpha^2, 0, \alpha)$. This Jacobian is given by

$$\begin{pmatrix} 0 & 0 & -1 \\ 0 & -\beta & 0 \\ 1/\epsilon & 0 & -2\alpha/\epsilon \end{pmatrix} \tag{6.5}$$

and the corresponding eigenvalues are

$$\lambda_1 = -\beta,$$
$$\lambda_{2/3} = \left(-\alpha \pm \sqrt{\alpha^2 - \epsilon}\right)/\epsilon.$$

Thus we have an AH bifurcation for $\alpha = 0$. Notice that the onset frequency of the bifurcating limit cycles is $O(1/\sqrt{\epsilon})$, which is an intermediate time scale of the slow-fast problem (6.1). Furthermore, $\lambda_{2/3}$ are only complex conjugate eigenvalues for $|\alpha| < \sqrt{\epsilon}$. Thus we conclude that the AH bifurcation is in fact singular. Clearly, the singular AH bifurcation at $(x_s^{ah}, y_s^{ah}, z_s^{ah}) = (0, 0, 0)$ corresponds to the FSN III point of the reduced flow for $(\beta \neq 0, \gamma \neq 0)$.

The Jacobian of the full system (6.1) with $\epsilon > 0$, evaluated along one of the possible asymmetric equilibria $(x_a, y_a, z_a) = ((\alpha - \xi_\pm)^2, \pm\sqrt{\xi_\pm}, \alpha - \xi_\pm)$, is given by

$$\begin{pmatrix} 0 & \mp 2\sqrt{\xi_\pm} & -1 \\ 0 & -2\xi_\pm(2\xi_\pm - \gamma) & 0 \\ 1/\epsilon & 0 & -2(\alpha - \xi_\pm)/\epsilon \end{pmatrix} \tag{6.6}$$

and the corresponding eigenvalues are

$$\lambda_1 = -2\xi_\pm(2\xi_\pm - \gamma),$$
$$\lambda_{2/3} = (\alpha - \xi_\pm) \pm \sqrt{(\alpha - \xi_\pm)^2 - 1/\varepsilon}.$$

Similarly, we identify two AH bifurcations for $\alpha = \xi_\pm$. Once again, the AH bifurcations are singular since the onset frequency of the bifurcating limit cycles is $O(1/\sqrt{\epsilon})$. The pair of

singular AH bifurcations at $(x_a^{ah}, y_a^{ah}, z_a^{ah}) = (0, \pm\sqrt{\alpha}, 0)$ for $\alpha > 0$ and $\beta = \alpha(\gamma - \alpha) \leq \gamma^2/4$ corresponds to the pair of FSN II bifurcations discussed previously. We also identify the two previously found codim-1 bifurcation of equilibria:

- a PF bifurcation at $(x^{pf}, y^{pf}, z^{pf}) = (\alpha^2, 0, \alpha)$, which occurs for $\beta = 0$ and $\alpha \neq 0$, and
- a SN bifurcation at $(x^{sn}, y^{sn}, z^{sn}) = ((\alpha - \gamma/2)^2, \pm\sqrt{\gamma/2}, \alpha - \gamma/2)$, which occurs for $\beta = \gamma^2/4$ and $\gamma > 0$.

Together, these codim-1 bifurcations are involved in three codim-2 bifurcations. Away from the symmetry axis, we have for $\gamma = 2\alpha$, $\beta = \alpha^2$ and $\gamma > 0$ a pair of SN/singular AH bifurcation points, i.e. we have a zero eigenvalue and a pair of purely imaginary eigenvalues (Figures 6.1, 6.2). At the symmetry axis, we have for $\beta = \gamma = 0$ and $\alpha \neq 0$ a degenerate PF bifurcation, i.e. we have a single zero eigenvalue and the coefficient of the nonlinear term that determines the criticality of the PF bifurcation vanishes. Thus the pitchfork bifurcation changes from super to subcritical and the corresponding branch of saddle-node points terminates (Figure 6.2). For $\alpha = \beta = 0$, a PF/singular AH bifurcation occurs due to $\mathbb{Z}_2$-symmetry (Figures 6.1, 6.2). Note that this $\mathbb{Z}_2$-symmetric codim-2 point involves both singular AH bifurcations (FSN II/III) and the PF bifurcation ($\beta = 0$), i.e. we have a zero eigenvalue and a pair of purely imaginary eigenvalues as well as $\mathbb{Z}_2$ symmetry.

Finally, in the case $\alpha = \beta = \gamma = 0$, we are dealing with a codim-3 degenerate PF/singular AH bifurcation, i.e. we have a zero eigenvalue and a pair of purely imaginary eigenvalues, and the coefficient of the nonlinear term that determines the criticality of the PF bifurcation also vanishes. This codim-3 point forms the organising centre of the various activity patterns, either symmetric or asymmetric in nature, that we have identified.

Remark 6.1. While such codim-3 bifurcations have been studied for regular perturbation problems (for example, see [3, 62]), these have not been analysed so far in the context of singularly perturbed systems. A detailed study of the canonical model (6.1) (including a blow-up analysis) goes well beyond the aim of this work and is left for the future.

6.3   Discussion

In this chapter we presented and analysed via direct calculation what we call a canonical system, which features three parameters and encompasses all of the equilibria, (toral) folded singularities, and bifurcations observed and in the averaged reduced problem (5.5) of the Butera model. We found that the canonical system dynamics agree with the activity patterns observed in the GSPT/averaging framework and in the full system (5.1), in all of the parameter regimes that were considered. Furthermore, we found paths in parameter space for the canonical system that correspond to all of the paths between activity patterns attained by parameter variation in the neuronal model. These results validate the suggestions from the GSPT/averaging analysis of Chapter 5 concerning the dynamical mechanisms underlying model activity patterns and transitions between them.

Chapter 7

The Folded Saddle-Node Type III

In Chapter 5, we studied the transition between various bursting and spiking states in the Butera model, a coupled two neuron model. Using a combination of GSPT and numerical averaging, we were able to analyse an averaged reduced system and identify various (toral) folded singularities and their associated FSN bifurcations. Near the asymmetric to symmetric bursting transition, we observed the novel FSN type III, a pitchfork bifurcation of two folded singularities and an ordinary singularity, arising as a consequence of the $\mathbb{Z}_2$-symmetry of the Butera model. This FSN III corresponded to a singular torus bifurcation of the full system.

The more well known FSN bifurcations, type I and II, are common in a variety of applications and can lead to complex dynamics. The FSN I occurs in various neural models [101, 106, 112], and generates mixed-mode oscillations (MMOs) in the forced van der Pol oscillator [12, 46, 49, 100]. The FSN II, which is the dynamic unfolding of the 2D singular Andronov-Hopf bifurcation, generates the canard explosion in planar singularly perturbed systems [37, 64], which mediates the transition from quiescence to relaxation oscillations. The FSN II also frequently occurs in cell models [88, 90, 91, 105, 50], and plays a role in the creation of MMOs [5, 13, 45]. We also see neural models were both the FSN I and II occur, and they demarcate the region in parameter space where MMOs are observed [39, 101].

The local dynamics near both the FSN I and II has been studied extensively in $\mathbb{R}^3$. In the case of the FSN II, the full system singular Andronov-Hopf bifurcation generates periodic orbits that can undergo secondary bifurcations. In [45], these periodic orbits and their associated bifurcations were studied in the $\mu = \mathcal{O}(\varepsilon)$ regime. Krupa *et al.* [66] added to this by studying the $\mu = \mathcal{O}(\sqrt{\varepsilon})$ regime, where the periodic orbits can be ignored. Finally the transition between the two regimes was dealt with in [25, 31]. Using similar techniques to [66], Vo *et al.* [108] analysed the dynamics near the FSN I in the $\mu = \mathcal{O}(\varepsilon^k)$, $k \geq 1/4$ regime. Note that although the FSN I does not posses a full system Andronov-Hopf bifurcation, oscillatory dynamics still arise. Of particular interest is that these various studies prove that both the FSN I and II generate canards for $0 < \varepsilon \ll 1$. The goal of this chapter is to combine techniques from GSPT (the blow-up) and dynamic bifurcation theory (analytic continuation into the complex plane) to extend the current FSN I and II canard theory to the FSN III case.

The remainder of this chapter is outlined as follows. In Section 7.1 we study a canonical model of the FSN III and briefly examine the local dynamics of the reduced and layer

problems. Taking inspiration from classic integrate-and-fire neural models, we modify the canonical model and create a return mechanism which generates interesting MMO behaviour. In Section 7.2 we perform a blow-up analysis of the canonical model and study the dynamics in the entry chart and the rescaling chart (which is an $\mathcal{O}(\sqrt{\varepsilon})$ zoom of the dynamics in a small neighbourhood of the FSN III singularity). In the rescaling chart, we identify two layer problem Andronov-Hopf (AH) bifurcations; the reduced flow moves trajectories slowly through these bifurcations, causing a delayed loss of stability. In Section 7.3, we sate our main results on the existence of canards and faux canards (for Case 1), and define the way-in/way-out function that quantifies the expected delay caused by slow passage through the AH bifurcations in the rescaling chart. Taking a similar approach to [64, 108], we study the dynamics of trajectories during the slow passage through the AH by analytically extending the rescaling chart into the complex plane. In Section 7.4, we analyse the properties of the linearised complex flow along special paths called elliptic contours, where solutions neither grow or decay. These results are extended to the non-linear case in Section 7.5. In Section 7.6, we utilise the elliptic paths to track invariant manifolds and formally prove the existence of canards. In Section 7.7, we expand the main theorems and proofs to include all four cases of the FSN III. We conclude with a discussion in Section 7.8.

7.1 Canonical Model

Drawing from the canonical model of the organising centre (6.1) in Section 6, we formulate a canonical form of the FSN III

$$
\begin{aligned}
\dot{x} &= -z + \delta_1(\alpha - y^2) + \mathcal{O}(\varepsilon, x, z^2, zy^2, y^4), \\
\dot{y} &= \delta_2 y(1 + \mathcal{O}(\varepsilon, x, z, y^2)), \\
\varepsilon\dot{z} &= x - z^2 + \mathcal{O}(xz^2, z^3, \varepsilon(x+z), \varepsilon^2, \varepsilon y^2),
\end{aligned}
\tag{7.1}
$$

where $\varepsilon \ll 1$, $\delta_1, \delta_2 = \pm 1$, and $(x, y) \in \mathbb{R}^2$ are slow, while $z \in \mathbb{R}$ is fast. Note that the only difference between (6.1) and (7.1) arises in the $\dot{y}$ equation: the FSN III does not explicitly require the $\mathcal{O}(y^2)$ and $\mathcal{O}(y^4)$ terms. To leading order the canonical model is $\mathbb{Z}_2$-equivariant, i.e. $y \leftrightarrow -y$. The higher order terms seen in (7.1) are also symmetric; this restriction ensures that the critical manifold is invariant up to $\mathcal{O}(\varepsilon)$ perturbations, which will become important in later proofs. Various combinations of the parameters δ_1 and δ_2 create four different *cases*, which will be referred to throughout the rest of this chapter. The cases are defined as follows:

- *Case 1*: $\delta_1 = \delta_2 = 1$,
- *Case 2*: $\delta_1 = 1$, $\delta_2 = -1$,
- *Case 3*: $\delta_1 = -1$, $\delta_2 = 1$,
- *Case 4*: $\delta_1 = \delta_2 = -1$.

Locally near the origin, the critical manifold of (7.1) is a 2D parabolic cylinder

$$
\mathcal{S} := \{(x, y, z) : x = z^2 + \mathcal{O}(z^3)\},
$$

	δ_1	δ_2	$\mathcal{E}$		$\mathcal{F}$
Case 1	1	1	$\alpha < 0$	UN ($\mathcal{S}_r$)	-
			$0 < \alpha < \frac{1}{16}$	S ($\mathcal{S}_a$)	FN
			$\alpha > \frac{1}{16}$	S ($\mathcal{S}_a$)	FF
Case 2	1	-1	$\alpha < 0$	S ($\mathcal{S}_r$)	-
			$\alpha > 0$	SN ($\mathcal{S}_a$)	FS
Case 3	-1	1	$\alpha < 0$	S ($\mathcal{S}_a$)	-
			$\alpha > 0$	UN ($\mathcal{S}_r$)	FS
Case 4	-1	-1	$\alpha < 0$	SN ($\mathcal{S}_a$)	-
			$0 < \alpha < \frac{1}{16}$	S ($\mathcal{S}_r$)	FN
			$\alpha > \frac{1}{16}$	S ($\mathcal{S}_r$)	FF

Table 7.1: A summary of the type/stability of the ordinary singularities $\mathcal{E}$ and folded singularities $\mathcal{F}$ of (7.2) for various values of δ_1, δ_2 and α. FN and FS denote folded node and folded saddle, while SN, UN and S denote stable node, unstable node and saddle, respectively. The dashes indicates parameter regions where the folded singularities do not exist.

which has an attracting sheet $\mathcal{S}_a$ ($z > 0$) and a repelling sheet $\mathcal{S}_r$ ($z < 0$), separated by the fold curve

$$\mathcal{L} := \{(x, y, z) : x = z = 0\},$$

which is simply the y-axis. The desingularised reduced system of (7.1) is given by

$$\dot{y} = \delta_2 y(2z + \mathcal{O}(z^2, y^2 z, z^3)), \tag{7.2}$$
$$\dot{z} = -z + \delta_1(\alpha - y^2) + \mathcal{O}(z^2, z^3, yz^2, y^4).$$

System (7.2) has an ordinary singularity (or equilibria) $\mathcal{E} := (\alpha^2, 0, \delta_1\alpha)$, and two folded singularities $\mathcal{F}^\pm := (0, \pm\sqrt{\alpha}, 0)$. Clearly the folded singularities only exist for $\alpha > 0$, and when $\alpha = 0$, two folded singularities collide with the ordinary singularity at a FSN III bifurcation. The Jacobian of (7.2) is given by

$$A(y, z) = \begin{pmatrix} 2\delta_2 z + \mathcal{O}(z^2, y^2 z) & 2\delta_2 y + \mathcal{O}(yz, y^3) \\ -2\delta_1 y + \mathcal{O}(z^2, y^3) & -1 + \mathcal{O}(z, yz) \end{pmatrix}, \tag{7.3}$$

and linearising about $\mathcal{E}$, we find that the eigenvalues are

$$\lambda_1 = 2\delta_1\delta_2\alpha + \mathcal{O}(\alpha^2),$$
$$\lambda_2 = -1 + \mathcal{O}(\alpha).$$

At the folded singularities $\mathcal{F}^\pm$, we find that

$$\text{Tr}(A) = -1,$$
$$\text{Det}(A) = 4\delta_1\delta_2\alpha + \mathcal{O}(\alpha^2),$$
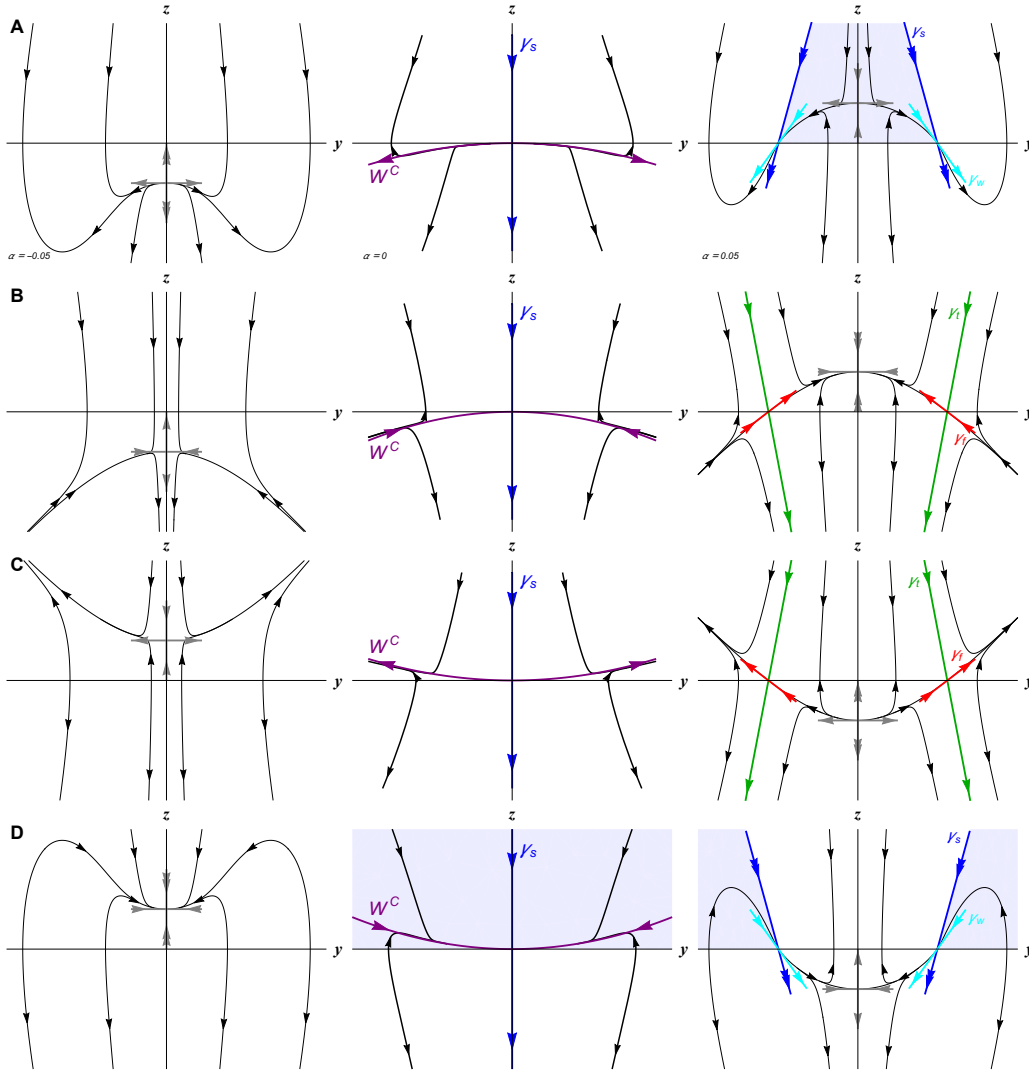$$\Delta = 1 - 16\delta_1\delta_2\alpha + \mathcal{O}(\alpha^2).$$

Figure 7.1: Flow of the desingularised reduced system (7.2) for Cases 1 through 4 (corresponding to rows A through D). The parameter α varies between the three columns: $\alpha = -0.05$ for figures in the left column, $\alpha = 0$ for figures in the middle column, and $\alpha = 0.05$ for figures in the right column. In all figures, the fold is the y-axis, S_a is the region $z > 0$, and S_r is the region $z < 0$. For folded node singularities, the strong canard (shown in blue) is labelled γ_s, and the weak canard (cyan) is γ_w. The funnel region is shaded blue. Note that for Case 4, the funnel region persists in the $\alpha = 0$ limit, while in Case 1 it vanishes. For folded saddle singularities, the true canard (green) is labelled γ_t, while the faux canard (red) is γ_f. The eigendirections (grey) of ordinary singularities are indicated in the figure. See also Table 1.

The type and/or stability of the singularities depends on the parameters δ_1, δ_2 and α. Table 7.1 shows a summary of the regular and folded singularities, as well as their type/stability, for each case. A complete picture of the reduced flow for each case can be seen in Figure 7.1. The left column shows the flow for $\alpha < 0$, the middle column $\alpha = 0$, and the right column $\alpha > 0$.
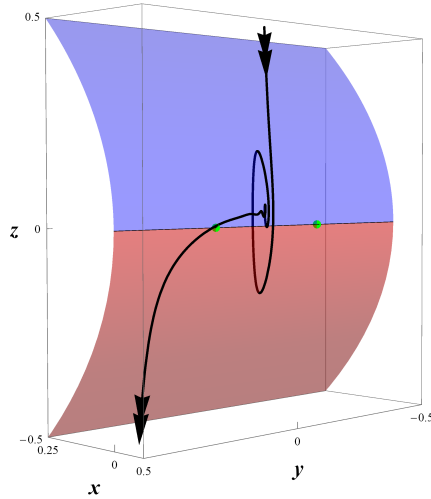
Figure 7.2: A canard solution of (7.1) for $\alpha = 1/30$ and $\varepsilon = 0.025$, Case 1 (cf. Figure 7.11). The attracting and repelling sheets of the critical manifold are shown in blue and red, respectively. The fold $\mathcal{L}$ is simply the y-axis. The green dots mark the folded node singularities of the reduced system (7.2).

Figure 7.2 shows a canard solution of system (7.1), for Case 1, oscillating near one of folded nodes. After oscillating near the origin and passing through the canard point, the solution eventually falls off the critical manifold near the origin, and follows the fast fibres of the layer problem away from $\mathcal{S}$. Similar to classic integrate-and-fire neural models [72, 58, 14, 17], we set up a 'global return mechanism'. After a solution spikes, i.e. crosses a threshold, all variables are reset to allow the solution to return to the funnel on $\mathcal{S}_a$. We define the spiking threshold $z_{th} = -1$, and reset values $x_{re} = x(0)$, $y_{re} = y(0)$, $z_{re} = z(0)$. The local canonical model (7.1), combined with the global return mechanism described above, allows for complex oscillatory patterns; see Figures 7.3 and 7.12 for examples of MMOs [16, 15, 91, 28, 105].

When $\alpha = 0$, the centre manifold W^c at the origin is given by $z = -\delta_1 y^2 + \mathcal{O}(y^4)$ and the flow on W^C is $\dot{y} = -2\delta_1\delta_2 y^3 + \mathcal{O}(y^5)$. Thus δ_1 controls the position of W^C; when $\delta = 1$, W^C lies on $\mathcal{S}_r$, and when $\delta_1 = -1$, W^C lies on $\mathcal{S}_a$. The product $\delta_1\delta_2$ dictates the direction of the flow along W^C locally near the origin. If $\delta_1\delta_2 > 0$, then the flow is towards the origin; if $\delta_1\delta_2 < 0$, the flow is away from the origin (however, the flow must be reversed in Cases 1 and 2 when W^C lies on on S_r). See Figure 7.1, middle column, which shows the positioning and flow on W^C for each case. The FSN III identified in the study of the Butera model [87] corresponds to Case 1.

7.2 Folded Saddle-Node Type III Blow-Up

We now shift our attention to formally proving the existence of canards in (7.1), near the FSN III limit ($\alpha = 0$). We will focus on Case 1, and address Cases 2–4 later in Section 7.7. Note that due to the structure of the FSN III, there are only faux canards in Cases 2 and
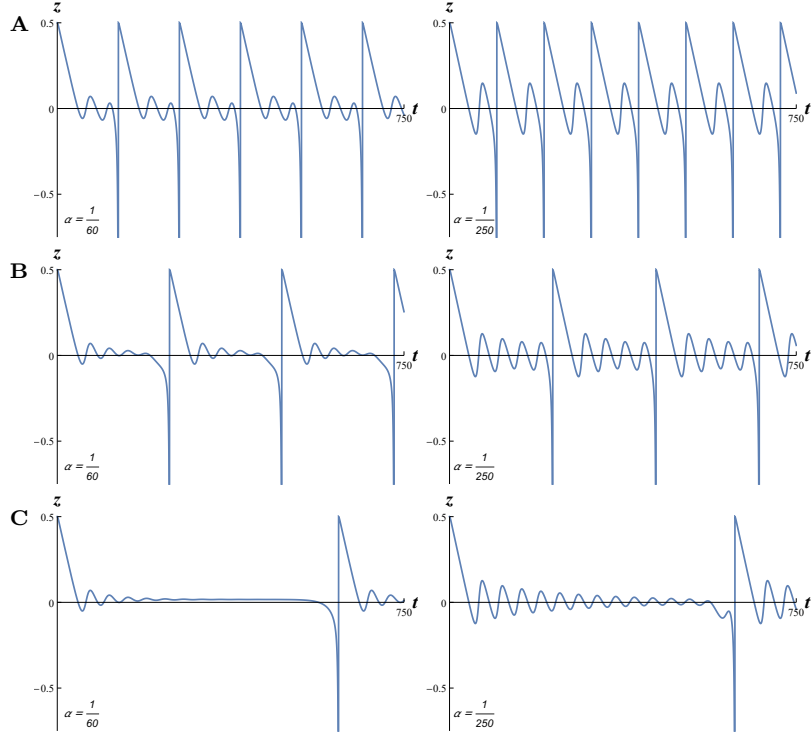
Figure 7.3: MMO solutions of (7.1), for Case 1 ($\delta_1 = \delta_2 = 1$), $\varepsilon = 0.025$ and various values of α, which are indicated on the respective plot. For all these plots $z_{th} = -0.5$, $x_{re} = 0.25$, $z_{re} = 0.5$, while the value of y_{re} varies. *Row A: $y_{re} = 0.015$, Row B: $y_{re} = 0.001$, Row C: $y_{re} = 10^{-7}$.* Compare with Figure 7.12 which shows similar patterns for Case 4.

3; theorems on their existence will be dealt with in Section 7.7. In this section we define the map induced by the flow of (7.1) and perform a (partial) blow-up analysis.

7.2.1 Transition map and cross-sections

Naturally, we are interested in analysing the flow of (7.1) in a neighbourhood of the fold $\mathcal{L}$, near the FSN III singularity. To this end, we introduce the transition map $\Pi : \Sigma_1 \to \Sigma_2$, induced by the flow of (7.1), with cross-sections

$$\begin{aligned}
\Sigma_1 &:= \{(x, y, z) : x = \sigma_1, \, \sigma_1 > 0\}, \\
\Sigma_4 &:= \{(x, y, z) : z = -\sigma_4, \, \sigma_4 > 0\}.
\end{aligned} \tag{7.4}$$

To analyse Π in the vicinity of the FSN III singularity, we define two intermediate ε-dependent (i.e. singular) cross-sections

$$\begin{aligned}
\Sigma_2 &:= \{(x, y, z) : x = \varepsilon\sigma_2, \sigma_2 > 0\}, \\
\Sigma_3 &:= \left\{(x, y, z) : z = -\sqrt{\varepsilon}\sigma_3, \sigma_3 > 0\right\},
\end{aligned} \tag{7.5}$$

which are used in the blow-up analysis of folded singularities (see [15, 99, 110]). Figure 7.4 shows all four cross-sections in the (x, z)-plane. At $\mathcal{O}(1)$ distances away from $\mathcal{L}$, the flow of
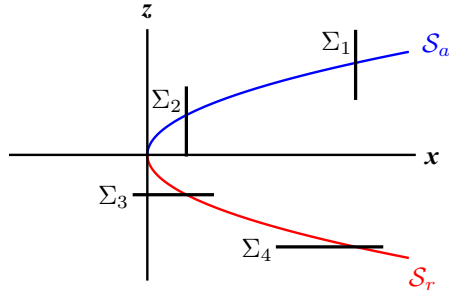
108

Figure 7.4: Cross-sections Σ_1–Σ_4, projected onto the (x, z)-plane. The manifolds $\mathcal{S}_a$ and $\mathcal{S}_r$ are plotted in blue and red, respectively.

(7.1) for $0 < \varepsilon \ll 1$ is completely described by Fenichel theory. In other words, there exist invariant slow manifolds $\mathcal{S}_a^\varepsilon$ and $\mathcal{S}_r^\varepsilon$, which are $\mathcal{O}(\varepsilon)$ close to their singular counterparts $\mathcal{S}_a$ and $\mathcal{S}_r$ (see Chapter 2). Blow-up analysis enables the extension of Fenichel theory $\mathcal{O}(\varepsilon)$ close to the fold $\mathcal{L}$. Thus the slow manifolds $\mathcal{S}_a^\varepsilon$ and $\mathcal{S}_r^\varepsilon$ can be extended up to sections Σ_2 and Σ_3, respectively. We have the following result:

Proposition 7.1 (see [109, 66])**.** For system (7.1), the sets $\mathcal{S}_a^{\sqrt{\varepsilon}}$ and $\mathcal{S}_r^{\sqrt{\varepsilon}}$ are smooth locally invariant normally hyperbolic manifolds, and $\mathcal{O}(\sqrt{\varepsilon})$ smooth perturbations of $\mathcal{S}$. The flow on $\mathcal{S}_a^{\sqrt{\varepsilon}}$ and $\mathcal{S}_r^{\sqrt{\varepsilon}}$ is an $\mathcal{O}(\sqrt{\varepsilon})$ perturbation of the reduced flow. Furthermore, $\mathcal{S}_a^{\sqrt{\varepsilon}}$ and $\mathcal{S}_r^{\sqrt{\varepsilon}}$ consist of solutions which grow algebraically in backward and forward time, respectively.

7.2.2 Blow-up transformation

The first step in our analysis of the map Π involves the blow-up technique. Recall from Section 2.5 that the blow-up [36, 37, 99, 111] is a co-ordinate transformation which inflates the degenerate singularities of (7.2) to a k-sphere (for this problem $k = 3$). As a result of the transformation, sufficient normal hyperbolicity is gained to allow analysis using standard techniques. Note that ε must be included in the blow-up analysis, and so we extend system (7.1) and switch to the fast timescale

$$
\begin{aligned}
x' &= \varepsilon(-z + \delta_1(\alpha - y^2) + \mathcal{O}(\varepsilon, x, z^2, zy^2, y^4)), \\
y' &= \varepsilon\delta_2 y(1 + \mathcal{O}(\varepsilon, x, z, y^2)), \\
z' &= x - z^2 + \mathcal{O}(xz^2, z^3, \varepsilon(x + z), \varepsilon^2, \varepsilon y^2), \\
\varepsilon' &= 0.
\end{aligned}
\tag{7.6}
$$

For the FSN III, the blow-up is a mapping $\Phi : B = \mathbb{S}^3 \times \mathbb{R}^1 \to \mathbb{R}^4$ given by

$$
(x, y, z, \varepsilon) = (\bar{r}^4 \bar{x}, \bar{r}\bar{y}, \bar{r}^2 \bar{z}, \bar{r}^4 \bar{\varepsilon}),
\tag{7.7}
$$

with $(\bar{x}, \bar{y}, \bar{z}, \bar{\varepsilon}) \in \mathbb{S}^3 \times \mathbb{R}^1$. The parameter α is also rescaled as $\alpha = \sqrt{\varepsilon}\alpha_2$ so that $\lim_{\varepsilon \to 0} \alpha = 0$, and thus we have a FSN III singularity for all $\alpha = \mathcal{O}(\sqrt{\varepsilon})$.

To avoid using spherical co-ordinates, we instead study the dynamics in co-ordinate charts $\bar{u} = \pm 1$, $\bar{u} \in \{x, y, z, \varepsilon\}$. For this particular problem it is sufficient to consider two charts, the entry chart $\kappa_1 : \bar{x} = 1$, and the rescaling chart $\kappa_2 : \bar{\varepsilon} = 1$. Let κ_{pk} denote the

change of coordinates that takes solutions in chart κ_k and maps them to chart κ_p. Thus κ_{12} and κ_{21} are given by

$$
\begin{aligned}
\kappa_{12}: \quad (r_1, y_1, z_1, \varepsilon_1) &= \left(r_2(x_2)^{1/4}, y_2(x_2)^{-1/4}, z_2(x_2)^{-1/2}, (x_2)^{-1} \right), \\
\kappa_{21}: \quad (r_2, z_2, y_2, x_2) &= \left(r_1(\varepsilon_1)^{1/4}, z_1(\varepsilon_1)^{-1/4}, y_1(\varepsilon_1)^{-1/2}, (\varepsilon_1)^{-1} \right).
\end{aligned}
\tag{7.8}
$$

7.2.3 Entry chart

In chart κ_1 the coordinate transformation is given by

$$
(x, y, z, \varepsilon) = \left(r_1^4, r_1 y_1, r_1^2 z_1, r_1^4 \varepsilon_1 \right),
\tag{7.9}
$$

and, after substituting this into (7.6) and rescaling time by a factor of $4r_1^2$, we obtain

$$
\begin{aligned}
r_1' &= \varepsilon_1 r_1 \mathcal{R}, \\
y_1' &= \varepsilon_1 y_1 (4\delta_2 r_1^2 + \mathcal{O}(r_1^2(z_1 + y_1^2 + r_1^2 + r_1^2 \varepsilon_1)) - \mathcal{R}), \\
z_1' &= 4(1 - z_1^2) + \mathcal{O}(r_1^4(\varepsilon_1 z_1 + z_1^3 + \varepsilon_1 y_1^2)) - 2\varepsilon_1 z_1 \mathcal{R}, \\
\varepsilon_1' &= -4\varepsilon_1^2 \mathcal{R},
\end{aligned}
\tag{7.10}
$$

where

$$
\mathcal{R} := -z_1 + \delta_1(\alpha_2 \sqrt{\varepsilon_1} - y_1^2) + \mathcal{O}(r_1^2(1 + \varepsilon_1 + z_1^2 + y_1^2 z_1)).
$$

System (7.10) has two invariant subspaces, $\varepsilon_1 = 0$ and $r_1 = 0$, which intersect along lines of equilibria given by $L_{a,1} = (0, y_1, 1, 0)$ and $L_{r,1} = (0, y_1, -1, 0)$ that have non-zero eigenvalue ∓ 8, respectively. Contained in the $\varepsilon_1 = 0$ invariant subspace are normally hyperbolic surfaces of equilibria $\mathcal{S}_{a,1}$ and $\mathcal{S}_{r,1}$, defined by $(r_1, y_1, z_1, \varepsilon_1) = (r_1, y_1, \pm 1, 0)$. These surfaces correspond to the attracting and repelling sheets of the critical manifold $\mathcal{S}$.

If we restrict ourselves to the invariant subspace $r_1 = 0$ and examine the resulting 3D system, there exist 2D centre manifolds $C_{a,1}$ and $C_{r,1}$ of the lines of equilibria $L_{a,1}$ and $L_{r,1}$, respectively. The $\varepsilon_1 \geq 0$ branch of $C_{a,1}$ is unique for $-1 + \delta_1(\alpha\sqrt{\varepsilon_1} - y_1^2) < 0$, while the $\varepsilon_1 \geq 0$ branch $C_{r,1}$ is unique for $1 + \delta_1(\alpha\sqrt{\varepsilon_1} - y_1^2) > 0$.

Proposition 7.2. For system (7.10), we have the following results:

1. There exists a 3D attracting centre manifold $M_{a,1}$ of the line of equilibria $L_{a,1}$. The manifold $M_{a,1}$ contains the surface of equilibria $\mathcal{S}_{a,1}$ and the centre manifold $C_{a,1}$, and is given by $z_1^a(r_1, y_1, \varepsilon_1) = 1 + \mathcal{O}(\varepsilon_1, (r_1 + y_1 + \varepsilon_1)^2)$.

2. There exists a 3D repelling centre manifold $M_{r,1}$ of the line of equilibria $L_{r,1}$. The manifold $M_{r,1}$ contains the surface of equilibria $\mathcal{S}_{r,1}$ and the centre manifold $C_{r,1}$, and is given by $z_1^r(r_1, y_1, \varepsilon_1) = -1 + \mathcal{O}(\varepsilon_1, (r_1 + y_1 + \varepsilon_1)^2)$.

Substituting $z_1^a = 1 + \mathcal{O}(\varepsilon_1, (r_1 + y_1 + \varepsilon_1)^2)$ into (7.10) and desingularising, we obtain the flow on the attracting centre manifold $M_{a,1}$

$$
\begin{aligned}
r_1' &= r_1 \tilde{\mathcal{R}}, \\
y_1' &= y_1 \left(4\delta_2 r_1^2 - \tilde{\mathcal{R}} \right), \\
\varepsilon_1' &= -4\varepsilon_1 \tilde{\mathcal{R}},
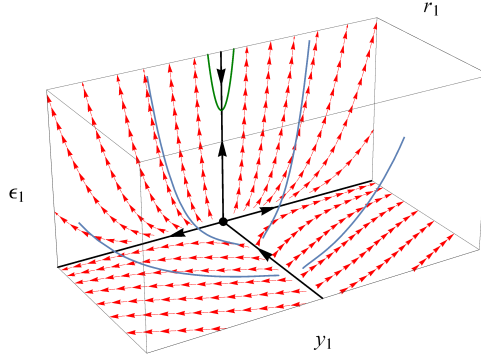\end{aligned}
\tag{7.11}
$$

Figure 7.5: Dynamics of system (7.11), i.e. the flow on the attracting centre manifold $M_{a,1}$, for Case 1, $\alpha_2 = 0.5$. The stream plots in the $r_1 = 0$ and $\varepsilon_1 = 0$ invariant planes are shown in red, and their equilibria are indicated by black dots, while the solid black lines correspond to the eigendirections of the respective equilibria. Branches of equilibria are shown in solid dark green, and trajectories of (7.11), with non-zero $\varepsilon = r_1^4 \varepsilon_1$, are shown in blue.

where $\tilde{\mathcal{R}} := -1 + \delta_1(\alpha_2\sqrt{\varepsilon_1} - y_1^2) + \mathcal{O}(r_1^2(1 + \varepsilon_1 + y_1^2))$. System (7.11) has three invariant subspaces, $r_1 = 0$, $\varepsilon_1 = 0$, and $y_1 = 0$ (which corresponds to the pole). In the $r_1 = 0$ plane, the flow on $M_{a,1}$ is given by

$$
\begin{aligned}
y_1' &= y_1\left(1 - \delta_1\left(\alpha\sqrt{\varepsilon_1} - y_1^2\right)\right), \\
\varepsilon_1' &= 4\varepsilon_1\left(1 - \delta_1\left(\alpha\sqrt{\varepsilon_1} - y_1^2\right)\right).
\end{aligned}
\tag{7.12}
$$

On the other hand, the flow on $M_{a,1}$ in $\varepsilon_1 = 0$ plane is given by

$$
\begin{aligned}
r_1' &= -r_1(1 + \delta_1 y_1^2), \\
y_1' &= y_1(1 + \delta_1 y_1^2 + 4\delta_2 r_1^2).
\end{aligned}
\tag{7.13}
$$

It is important to realise that the above flow, i.e. flow on $M_{a,1}$ in the $\varepsilon_1 = 0$ invariant plane, corresponds to the desingularised flow (7.2) on $\mathcal{S}_a$ for $\alpha = 0$. As such, the strong eigendirection of the origin in (7.13) corresponds to the singular strong canard γ_s of the FSN III bifurcation (see Figure 7.1, middle column). Note that for Case 1, the centre direction W^C lies on $\mathcal{S}_r$, and hence there is no corresponding structure on $M_{a,1}$. Linear stability analysis of systems (7.12) and (7.13) gives the following results:

- In the $r_1 = 0$ plane, there is an unstable node at the origin and branches of equilibria $(\bar{y}_1, \bar{\varepsilon}_1) = (\pm\sqrt{\alpha\sqrt{\varepsilon_1} - 1}, \varepsilon_1)$, originating at $(0, 1/\alpha^2)$.

- In the $\varepsilon_1 = 0$ plane, there is a saddle equilibrium at the origin, and the strong eigendirection of the saddle corresponds to γ_s of the FSN III singularity.

The dynamics on $M_{a,1}$ for Case 1 is shown in Figure 7.5. See Appendix A for a description of the dynamics on $M_{a,1}$ for Cases 2–4.

7.2.4 Transition from chart κ_1 to κ_2

Before we study the dynamics in chart κ_2, we discuss how trajectories transition from chart κ_1 to κ_2, and estimate transition times from Σ_1 to Σ_2. Define the transition map

$\Pi_1 : \Sigma_1 \to \Sigma_2$. In terms of chart κ_1 coordinates, the cross-sections are given by

$$\Sigma_1 := \left\{ (r_1, y_1, z_1, \varepsilon_1) : r_1 = \sigma_1^{1/4} \right\},$$
$$\Sigma_2 := \left\{ (x_1, y_1, z_1, \varepsilon_1) : r_1 = (\varepsilon\sigma_2)^{1/4} \right\}.$$

Linearising (7.11) about the origin yields a decoupled system (independent of $\delta_{1,2}$, and thus valid for all cases) with solutions

$$\begin{aligned} r_1(t) &= \tilde{r}_1 \exp(-t), \\ y_1(t) &= \tilde{y}_1 \exp(t), \\ \varepsilon_1(t) &= \tilde{\varepsilon}_1 \exp(4t), \end{aligned} \tag{7.14}$$

with initial condition $\tilde{q}_1 = q_1(0)$, for $q_1 = \{r_1, y_1, \varepsilon_1\}$. Thus the transition time from $\tilde{r}_1 = \sigma_1^{1/4}$ to $r_1 = (\varepsilon\sigma_2)^{1/4}$, i.e. $\Sigma_1 \cap M_{a,1} \to \Sigma_2$, for Case 1 is

$$T_s = \ln(\mathcal{O}(\varepsilon^{-1/4})).$$

Consider an initial condition in Σ_1, an $\mathcal{O}(\varepsilon^{1/4})$ distance away from γ_s, the strong eigendirection of the saddle in (7.13). Then $\Pi_1 : \Sigma_1 \to \Sigma_2$ maps the initial point to an $\mathcal{O}(1)$ neighbourhood of γ_s in Σ_2. We define the auxiliary exit cross section

$$\Sigma_2^{out} := \left\{ (r_1, y_1, z_1, \varepsilon_1) : \varepsilon_1 = \sigma_2^{-1} \right\},$$

where trajectories leave κ_1 and enter κ_2. If $\varepsilon_1(T_s) = \sigma_2^{-1}$, then it follows from system (7.14) that $\tilde{\varepsilon}_1 = \mathcal{O}(\varepsilon)$. The additional constraint $\tilde{\varepsilon}_1 = \mathcal{O}(\varepsilon)$ gives the restricted map

$$\Pi_1^{out} : \Sigma_1 \cap M_{a,1} \to \Sigma_2 \cap \Sigma_2^{out}.$$

The transition times for Cases 2–4 are calculated in Appendix C.

Remark 7.1. The above analysis implies that only trajectories an $\mathcal{O}(\varepsilon^{1/4})$ distance away from γ_s in Σ_1 enter the attracting region of CM in chart κ_2. For Case 1, the domain of attraction of CM in κ_2 is the interval $y_2 \in (-\sqrt{\alpha}, \sqrt{\alpha}) := d$, where $d = \mathcal{O}(1)$ since $\alpha_2 = \mathcal{O}(1)$ by assumption (see Section 7.2.5 and Figure 7.6A). Let $\mathcal{D}$ be the domain in Σ_2 defined by $(x_2, y_2, z_2) = (\sigma_2, d, \sqrt{\sigma_2})$. Applying the change of coordinates κ_{12} gives

$$\begin{aligned} \kappa_{12}(\mathcal{D}) : \quad (r_1, y_1, \varepsilon_1) &= (\varepsilon\sigma_2)^{1/4}, d\sigma_2^{-1/4}, \sigma_2^{-1}), \\ &= \mathcal{O}(\varepsilon^{1/4}) \times \mathcal{O}(1) \times \mathcal{O}(1). \end{aligned}$$

Hence, only trajectories in an $\mathcal{O}(\varepsilon^{1/4})$ neighbourhood of γ_s in Σ_1 transition to $\kappa_{12}(\mathcal{D})$ in Σ_2.

7.2.5 Rescaling chart

The next chart we will examine is the classical or rescaling chart, $\bar{\varepsilon} = 1$. The coordinate transformation is given by

$$(x, y, z, \varepsilon) = \left(r_2^4 x_2, r_2 y_2, r_2^2 z_2, r_2^4 \right). \tag{7.15}$$

Notice that $r_2^2 = \sqrt{\varepsilon}$ and thus the classical chart is simply an ε-dependent rescaling (or zoom) of the full system (7.6). Substituting (7.15) into (7.6) and desingularising by a factor of $\sqrt{\varepsilon}$, we obtain

$$\begin{aligned}
x_2' &= -z_2 + \delta_1(\alpha_2 - y_2^2) + \mathcal{O}(\sqrt{\varepsilon}(1+x_2+z_2^2+y_2^2 z_2)), \\
y_2' &= \sqrt{\varepsilon}\delta_2 y_2(1 + \mathcal{O}(\sqrt{\varepsilon}(z_2+y_2^2), \varepsilon(1+x_2))), \\
z_2' &= x_2 - z_2 + \mathcal{O}(\sqrt{\varepsilon}(z_2 + y_2^2 + z_2^3), \varepsilon(1 + x_2 + x_2 z_2^2)).
\end{aligned} \tag{7.16}$$

We have converted the 1-fast/2-slow system (7.6) into a 2-fast/1-slow system (7.16), which describes the dynamics in an $\mathcal{O}(\sqrt{\varepsilon})$ neighbourhood of the FSN III singularity. The layer problem of (7.16) is given by

$$\begin{aligned}
\dot{x}_2 &= -z_2 + \delta_1(\alpha_2 - y_2^2), \\
\dot{z}_2 &= x_2 - z_2^2,
\end{aligned} \tag{7.17}$$

where $y_2 \in \mathbb{R}$ is a parameter. The critical manifold CM is defined as

$$CM := \{(x_2, y_2, z_2) : ((\alpha_2 - y_2^2)^2, y_2, \delta_1(\alpha_2 - y_2^2)) : y_2 \in \mathbb{R}\}, \tag{7.18}$$

which is the set of equilibria of the layer problem. By linear stability analysis, the eigenvalues along CM are

$$\lambda = -\delta_1(\alpha_2 - y^2) \pm \sqrt{(\alpha_2 - y^2)^2 - 1}, \tag{7.19}$$

which is independent of δ_2. The stability properties of CM for Case 1 is summarised in Figure 7.6. It is clear from Figure 7.6 that for $\alpha_2 < 0$, the stability of CM is the same for all values of y_2; we ignore this case and instead focus on $\alpha_2 > 0$. For a fixed value of $\alpha_2 > 1$, the eigenvalues along the y_2-axis alternate between between a real and complex structure; see Figure (7.6), bottom panel. Note that when $0 < \alpha < 1$, the region around the origin where λ is real disappears. The stability of CM changes at $y_2 = \pm\sqrt{\alpha_2}$ via a Hopf bifurcation (except when $\alpha_2 = 0$). The structure of CM for Cases 2–4 is discussed in Appendix D.

The critical manifold CM is an important geometric object because it connects the attracting and repelling slow manifolds, $S_{a,2}$ and $S_{r,2}$, of (7.16) for $\varepsilon = 0$. Note that CM returns to the manifold on which it started. As discussed in [66, 108], CM is the orbital limit of the folded node primary weak canard (Cases 1 and 4), or the folded saddle faux canard (Cases 2 and 3). Away from CM, there exist two explicit solutions of (7.17) given by

$$\gamma_\pm(t_2) : \quad (x_2, y_2, z_2) = \left(\frac{1}{4}t_2^2 - \frac{1}{2}, \pm\sqrt{\alpha_2}, -\frac{1}{2}t_2\right). \tag{7.20}$$

The solutions $\gamma_\pm$ represent a connection from S_a to S_r, which are defined as the $\varepsilon \to 0$ limit of $S_{a,\sqrt{\varepsilon}}$ and $S_{a,\sqrt{\varepsilon}}$ in (7.16). Thus $\gamma_\pm$ can be considered an extension of the folded node singular strong canard (Cases 1 and 4), or the folded saddle singular true canard (Cases 2 and 3), of the reduced flow (7.2).

Proposition 7.3 (See [66, 99]). The singular strong canards $\gamma_\pm$ of the FSN III singularity always perturb to maximal strong canards (of folded node/saddle type) for $0 < \varepsilon \ll 1$ sufficiently small.
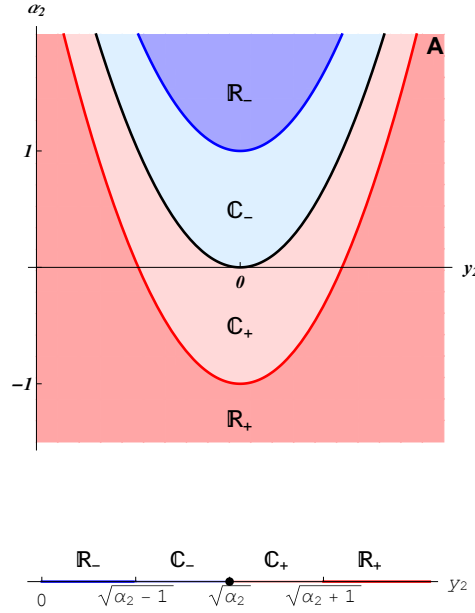
Figure 7.6: Structure of the eigenvalues λ of (7.17) along CM, for Case 1. The top panel shows the stability in the (y_2, α_2)-plane. The type and sign of the real part of the eigenvalues in various regions are indicated on the figure. Blue (red) regions are (un)stable, while the light (dark) shading indicates a real (complex) eigenvalue structure. The solid black line is the curve $y_2^2 = \alpha_2$. The bottom panel shows the stability along the positive y_2-axis, for a fixed value of $\alpha_2 > 1$. Compare with Figure 7.14, which shows all four cases.

Solutions exponentially close to the maximal strong canards cross to the repelling sheet of the critical manifold $\mathcal{S}_r$, and follow it for $\mathcal{O}(1)$ time. All other trajectories in Σ_2 within the funnel of the folded nodes are quickly attracted to CM. Transforming $\gamma_\pm$ back to chart κ_1 gives

$$\kappa_{12}(\gamma_\pm(t_2)): \quad (r_1, y_1, z_1, \varepsilon_1) = \left(0, \pm\sqrt{\alpha_2}\tilde{t}_2^{-1/4}, -\frac{1}{2}t_2\tilde{t}_2^{-1/2}, \tilde{t}_2^{-1}\right),$$

where $\tilde{t}_2 = \frac{1}{4}t_2^2 - \frac{1}{2}$. Consider the limit $t_2 \to \pm\infty$, and define the points

$$p_a: \quad \lim_{t_2 \to -\infty} \kappa_{12}(\gamma_\pm(t_2)) = (0, 0, 1, 0),$$
$$p_r: \quad \lim_{t_2 \to \infty} \kappa_{12}(\gamma_\pm(t_2)) = (0, 0, -1, 0).$$

Notice that $p_{a/r} \in L_{a/r} = (0, y_1, \pm 1, 0)$. In particular, $\gamma_\pm$ emanate from the origin in (7.11); see Figure 7.5. Thus the strong canards $\gamma_\pm$ connect the point $p_a \in L_{a,1}$ to $p_r \in L_{r,1}$ (for all Cases). Recall that in chart κ_1 we defined centre manifolds $C_{a/r,1}$ of $L_{a/r}$ which were unique under certain conditions. We have the following result:

Proposition 7.4. Let β be sufficiently large. Then $\gamma_\pm(t_2)$, for $t_2 \in (-\infty, \beta)$, forms part of the unique centre manifold $C_{a,1}$ in the $r_1 = 0$ invariant plane, with $\varepsilon_1 > 0$. Similarly, $\gamma_\pm(t_2)$, for $t_2 \in (\beta, \infty)$ forms part of the unique centre manifold $C_{r,1}$ in the $r_1 = 0$ invariant plane, with $\varepsilon_1 > 0$.

Proof. Recall that the $\varepsilon_1 \geq 0$ branch of $C_{a,1}$ is unique for $-1 + \delta_1(\alpha\sqrt{\varepsilon_1} - y_1^2) < 0$, while the $\varepsilon_1 \geq 0$ branch $C_{r,1}$ is unique for $1 + \delta_1(\alpha\sqrt{\varepsilon_1} - y_1^2) > 0$. Thus $C_{a,1}$ is unique at the point p_a, while $C_{r,1}$ is unique at p_r. In chart κ_1, the tangent vectors at the points are given by

$$
\begin{aligned}
p_a : &\quad \lim_{t_2 \to -\infty} \frac{\frac{d}{dy_2}\kappa_{12}(\gamma_\pm(t_2))}{||\kappa_{12}(\gamma_\pm(t_2))||} = (0, \pm 1, 0, 0)\,, \\
p_r : &\quad \lim_{t_2 \to \infty} \frac{\frac{d}{dy_2}\kappa_{12}(\gamma_\pm(t_2))}{||\kappa_{12}(\gamma_\pm(t_2))||} = (0, \mp 1, 0, 0)\,.
\end{aligned}
$$

Linearising (7.10) about $L_{a/r}$ in the $r_1 = 0$ invariant plane yields two zero eigenvalues (as well as a non-zero eigenvalue) with one of the corresponding zero eigenvectors being $(y_1, z_1, \varepsilon_1) = (1, 0, 0)$. Thus the trajectories $\gamma_\pm$ are tangent to the centre manifolds $C_{a/r,1}$ at the points $p_{a/r}$. $\qquad \square$

Returning to the analysis of (7.16), the associated reduced problem is

$$
\begin{aligned}
0 &= -z_2 + \delta_1(\alpha_2 - y_2^2), \\
\dot{y}_2 &= \delta_2 y_2, \\
0 &= x_2 - z_2^2,
\end{aligned}
\tag{7.21}
$$

which describes the slow evolution of y_2 restricted to CM. Since the equation for y_2 is decoupled, the equilibrium is simply $y_2 = 0$. The reduced (slow) flow near this equilibrium is determined by the sign of δ_2, with $\delta_2 = -1$ resulting in attraction, and $\delta_2 = 1$ repulsion.

7.3 Statement of Main Results

Through the blow-up transformation in chart κ_2, we converted the original 1-fast/2-slow system (7.1) to the 2-fast/1-slow system (7.23), where y_2 is a slow variable. The direction of the slow flow along CM, on either side of the equilibrium $y_2 = 0$, is determined by the sign of δ_2. Recall that in the layer problem (7.17) we identified two Hopf bifurcations at $y_2 = \pm\sqrt{\alpha_2}$. For $\varepsilon \neq 0$, y_2 slowly tracks through the Hopf bifurcations and a bifurcation delay is observed; trajectories pass over the Hopf bifurcation point, but do not immediately leave the repelling section of CM. In this section we present the main results on this delayed loss of stability and canards, using the *way-in/way-out function*.

7.3.1 Preliminary setup

We can straighten CM by making a co-ordinate transformation

$$
(\tilde{x}_2, \tilde{z}_2) = \left(x_2 - (\alpha_2 - y_2^2)^2, z_2 - \delta_1(\alpha_2 - y_2^2)\right).
\tag{7.22}
$$

Differentiating (7.22), we find that

$$
\begin{aligned}
\dot{\tilde{x}}_2 &= \dot{x}_2 + 4y_2\dot{y}_2(\alpha_2 - y_2^2), \\
\dot{\tilde{z}}_2 &= \dot{z}_2 + 2\delta_1 y_2\dot{y}_2,
\end{aligned}
$$

and thus (7.16) becomes, after dropping the tilde notation,

$$\dot{x}_2 = -z_2 + \mathcal{O}(\sqrt{\varepsilon}(1+x_2+z_2+y_2^2+z_2^2)),$$
$$\dot{y}_2 = \sqrt{\varepsilon}\delta_2 y_2(1 + \mathcal{O}(\sqrt{\varepsilon}(1+z_2+y_2^2), \varepsilon(1+x_2+y_2^2))),$$
$$\dot{z}_2 = x_2 - 2\delta_1 z_2\gamma - z_2^2 + \mathcal{O}(\sqrt{\varepsilon}(1+z_2+y_2^2), \varepsilon(1+x_2+z_2+y_2^2)),$$

(7.23)

where CM is now simply the y_2-axis.

Proposition 7.5. There is a smooth change of coordinates that transforms system (7.23) to

$$\dot{x}_2 = -z_2 + \mathcal{O}(\sqrt{\varepsilon}(x_2 + z_2), \varepsilon),$$
$$\dot{y}_2 = \sqrt{\varepsilon}\delta_2 y_2,$$
$$\dot{z}_2 = x_2 - 2\delta_1 z_2\gamma - z_2^2 + \mathcal{O}(\sqrt{\varepsilon}(x_2 + z_2), \varepsilon).$$

(7.24)

Proof. See Appendix E. $\qquad\square$

In equation (7.24), the y_2-axis (i.e. CM) is invariant up to $\mathcal{O}(\varepsilon)$, while in (7.23) it is only invariant up to $\mathcal{O}(\sqrt{\varepsilon})$. This will become important in our subsequent analysis. We define

$$\lambda_1(y_2, \alpha_2, \delta_1, \sqrt{\varepsilon}) = -\delta_1\gamma - i\sqrt{1-\gamma^2} + \sqrt{\varepsilon}h_1(y_2)$$
$$\lambda_2(y_2, \alpha_2, \delta_1, \sqrt{\varepsilon}) = -\delta_1\gamma + i\sqrt{1-\gamma^2} + \sqrt{\varepsilon}h_2(y_2)$$

(7.25)

where $\lambda_{1,2}(y_2, \alpha_2, \delta_1, 0)$ corresponds to the eigenvalues of the layer problem of system (7.24). Note that straightening the critical manifold (or any other smooth change of coordinates) does not alter the structure of the eigenvalues along CM. Next, we rescale time via the transformation $t = \sqrt{\varepsilon}\delta_2 y_2\tau$, and rewrite (7.24) as a two-dimensional system with y_2 as 'slow time':

$$\delta_2\sqrt{\varepsilon}y_2\frac{dx_2}{dy_2} = -z_2 + \mathcal{O}(\sqrt{\varepsilon}(x_2 + z_2), \varepsilon),$$
$$\delta_2\sqrt{\varepsilon}y_2\frac{dz_2}{dy_2} = x_2 - z_2^2 - 2\delta_1 z_2\gamma + \mathcal{O}(\sqrt{\varepsilon}(x_2 + z_2), \varepsilon).$$

(7.26)

The eigenvalues of (7.26) are simply

$$\Lambda_{1,2}(y_2, \alpha_2, \delta_{1,2}, \sqrt{\varepsilon}) := \delta_2\lambda_{1,2}(y_2, \alpha_2, \delta_1, \sqrt{\varepsilon})/y_2.$$

It is important to note that when $\delta_2 y_2 < 0$, the transformation $t = \sqrt{\varepsilon}\delta_2 y_2\tau$ is orientation reversing, and we will need to reverse time in system (7.26) to obtain trajectories equivalent to (7.24). Figure 7.7 shows the structure of the eigenvalues $\Lambda_{1,2}$ for Case 1, where $\Lambda_{1,2}$ has been reflected across the y_2-axis for $\delta_2 y_2 < 0$. We refer the reader to Figures 7.15 and 7.16 for similar diagrams of $\Lambda_{1,2}$ for Cases 2–4. Due to the division by y_2, or y_2 appearing on the left-hand side of equation (7.26), $y_2 = 0$ is a pole of the system.

The integrals

$$I_{\Lambda_1}(y_{in}, y_{out}, \alpha_2, \delta_{1,2}) = \frac{1}{\sqrt{\varepsilon}}\int_{y_{in}}^{y_{out}} \operatorname{Re}\Lambda_1(y_2, \alpha_2, \delta_{1,2})\, dy_2,$$
$$I_{\Lambda_2}(y_{in}, y_{out}, \alpha_2, \delta_{1,2}) = \frac{1}{\sqrt{\varepsilon}}\int_{y_{in}}^{y_{out}} \operatorname{Re}\Lambda_2(y_2, \alpha_2, \delta_{1,2})\, dy_2,$$
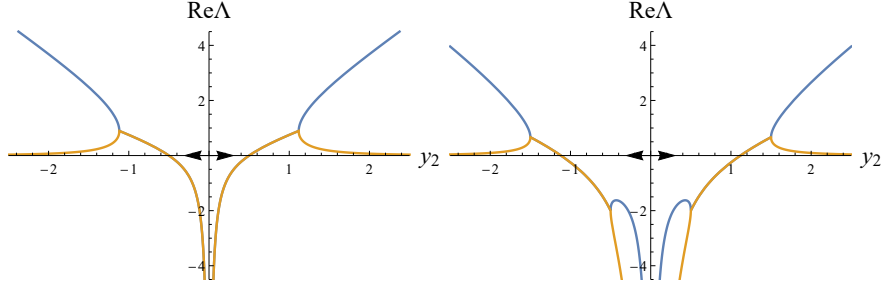
(7.27)

116

Figure 7.7: Real part of the eigenvalues $\Lambda_{1,2}$ of (7.26), for Case 1, $\alpha_2 = 0.25$ (left) and $\alpha_2 = 1.25$ (right). The eigenvalues Λ_1 and Λ_2 are shown in blue and orange, respectively. The arrows on the y_2-axis indicate the direction of the reduced flow along CM. Note that for $y_2 < 0$, the eigenvalues have been reflected in the y_2-axis to preserve the orientation of trajectories in (7.24).

measure leading order expansion and contraction along CM. When the eigenvalues are elliptic (complex), $I_{\Lambda_1} = I_{\Lambda_2}$, but this does not hold when the eigenvalues are hyperbolic (real). The way-in/way-out function $y_{out}(y_{in}, \alpha_2, \delta_{1,2})$ is defined implicitly by

$$I_{\Lambda_i}(y_{in}, y_{out}, \alpha_2, \delta_{1,2}) = 0, \qquad i = 1, 2, \tag{7.28}$$

and measures the point where the accumulative contraction on CM_a counter-balances the accumulative repulsion on CM_r, i.e. when trajectories leave a small neighbourhood of CM (via a fast fibre in the hyperbolic regions). For ease of notation, we suppress the α_2 and $\delta_{1,2}$ dependence. For generic solutions starting near CM that experience a delayed loss of stability, (7.28) measures the balance of weak contraction and strong repulsion. Thus we set $i = 1$, and the way-in/way-out function $y_{out}(y_{in})$ is defined implicitly by

$$I_{\Lambda_1}(y_{in}, y_{out}) = 0, \quad \alpha_2 > 0, \tag{7.29}$$

for all Cases. For canard solutions (which also experience a form of delay), equation (7.28) measures the balance of weak contraction and weak repulsion. Thus for $\alpha_2 < 1$, we set $i = 1$ for Cases 1 and 2, and $i = 2$ for Cases 3 and 4; refer to Figures 7.15 and 7.16 for the eigenvalue structure of Cases 2–4. When $\alpha_2 > 1$, we must branch switch at $\alpha_2 = \sqrt{\alpha_2 + 1}$. In summary, $y_{out}(y_{in})$ is defined implicitly by

$$\begin{aligned}
I_{\Lambda_2}(y_{in}, y_{out}) &= 0, \quad 0 < \alpha_2 < 1, \text{ Cases 1 \& 2,} \\
I_{\Lambda_1}(y_{in}, y_{out}) &= 0, \quad 0 < \alpha_2 < 1, \text{ Cases 3 \& 4,} \\
I_{\Lambda_1}(y_{in}, \sqrt{\alpha_2+1}) + I_{\Lambda_2}(\sqrt{\alpha_2+1}, y_{out}) &= 0, \quad \alpha_2 > 1.
\end{aligned} \tag{7.30}$$

7.3.2 Canards

In the blow-up analysis, we identified the singular strong canards and showed that they persist under small perturbations. Furthermore, we established that solutions within the funnel that are not exponentially close to the strong canard become exponentially close to CM in Σ_2. Thus we now turn our attention to solutions near CM, i.e. we want to understand the behaviour of the weak and secondary canards. For Case 1 and $\alpha_2 < 1$, consider a trajectory starting at some point $y_2 = y_{in} \in CM_a$. As we move forward in

time, how long does the trajectory remain close to CM, before separating and following the fast directions? In this section and the following, we present theorems on the existence of canards and the delay phenomenon to address this question.

In hyperbolic regions of CM, there exists a weak stable foliation W^s along CM_a and a weak unstable foliation W^u along CM_r. These foliations are equivalent to the invariant manifolds $S_{a,2}$ and $S_{r,2}$, locally near CM in system (7.24). By Fenichel theory, these invariant manifolds will persist as $S_{a,\sqrt{\varepsilon}}$ and $S_{r,\sqrt{\varepsilon}}$. We can use the linear subspaces to track the trajectory along the hyperbolic segment of CM_r. However, CM_a is elliptic and we can not track the manifold using conventional methods. In such cases we must use special properties of the layer flow to understand the dynamics near CM_a.

Remark 7.2 (Remark on notation). In the following section, y_{in} denotes the 'entry point', or the initial y_2 point of a trajectory on CM, while y_{out} denotes the 'exit point' where the trajectory leaves a small neighbourhood of CM. For canards, $y_{in} \in CM_a$ and $y_{out} \in CM_r$. For faux canards the opposite is true, $y_{in} \in CM_r$ and $y_{out} \in CM_a$. In the theorems and proofs that will follow, it is critical to distinguish between entry and exit points that lie on hyperbolic and elliptic segments of CM. Let $y_{2,0}$ be the entry/exit point in the region where CM is hyperbolic. Similarly, let $y_{2,*}$ be the entry/exit point in the elliptic region of CM. When both the entry and exit point lie in hyperbolic regions of CM, let $y_{in} = y_{2,0}$ and $y_{out} = y_{2,*}$.

In addition to Σ_1–Σ_4, we define the auxiliary cross sections

$$\Sigma_2^\pm := \left\{ (x_2, y_2, z_2) : y_2 = y_{2,0}, y_{2,0} \approx \pm\sqrt{\alpha_2 + \sqrt{\sigma_2}} \right\},$$

$$\tilde{\Sigma}_* := \left\{ (z_2, y_2, z_2) : y_2 = \tilde{y}_{2,*} \right\},$$

such that $\Sigma_2^\pm \approx \Sigma_2 \cap CM$. We are now in a position to state the Theorems on the existence of canards and faux canards.

Theorem 7.1. *(Existence of Canards) Let $0 < \alpha_2 < 1$ and $\tilde{\Sigma}_* : y_2 = \tilde{y}_{2,*}$, for some $\tilde{y}_{2,*} \approx y_{2,*}$. For Case 1 and $|y_{2,0}| > \sqrt{\alpha_2 + 1}$ chosen to define $\Sigma_2^\pm$ such that*

$$I_{\Lambda_1}(y_{2,*}, y_{2,0}) = 0,$$

with $|y_{2,*}| \in (\delta, \sqrt{\alpha_2})$, there exists a canard solution $\mathcal{O}(\sqrt{\varepsilon})$ away from CM, connecting $S_a^{\sqrt{\varepsilon}} \cap \tilde{\Sigma}_*$ to $S_r^{\sqrt{\varepsilon}} \cap \Sigma_2^\pm$, and continuing to a point in $S_r^\varepsilon \cap \Sigma_1$.

Idea of Proof. The proof is similar to the FSN I [108] and II [66]. Here we provide only an outline of the proof; see Section 7.6.1 for a details. Define an invariant subset of the repelling manifold $\mathcal{S}_r^\varepsilon \cap \Sigma_1$ and show that $\Pi_1(\mathcal{S}_r^\varepsilon \cap \Sigma_1)$ is a ray in $\mathcal{S}_r^{\sqrt{\varepsilon}} \cap \Sigma_2$. The ray can be extended into the complex plane and transported, via a suitable elliptic path in backward time, to a line segment $\mathcal{O}(\sqrt{\varepsilon})$ close to CM in Σ_2. Using the linearisation of the layer flow near a stable focus, it can be shown that the line segment winds out in backward time and intersects $\mathcal{S}_a^{\sqrt{\varepsilon}}$ transversally. □

We now consider the case $\alpha_2 > 1$. Trajectories which have an entry point y_{in} in a hyperbolic region of CM, and exit point y_{out} in an elliptic region of CM (or vice versa) – we refer to this as the elliptic case. In the elliptic case, the results for existence of canards is similar to that of Theorem 7.1, and the proof is the same.

Theorem 7.2. *(Existence of canards: Elliptic case) Consider Case 1 with $\alpha_2 > 1$.*

i) For $|y_{2,0}| > \sqrt{\alpha_2 + 1}$ chosen to define $\Sigma_2^{\pm}$ such that

$$I_{\Lambda_2}(y_{2,*}, y_{2,0}) = 0,$$

with $|y_{2,*}| \in (\sqrt{\alpha_2 - 1}, \sqrt{\alpha_2})$, there exists a canard solution $\mathcal{O}(\sqrt{\varepsilon})$ away from CM, connecting $S_a^{\sqrt{\varepsilon}} \cap \tilde{\Sigma}_*$ to $S_r^{\sqrt{\varepsilon}} \cap \Sigma_2^{\pm}$, and continuing to a point in $S_r^{\varepsilon} \cap \Sigma_1$.

ii) For $|y_{2,0}| \in (\delta, \sqrt{\alpha_2 - 1})$ chosen to define $\Sigma_2^{\pm}$ such that

$$I_{\Lambda_1}(y_{2,0}, y_{2,*}) = 0,$$

with $|y_{2,*}| \in (\sqrt{\alpha_2}, \sqrt{\alpha_2 + 1})$, there exists a canard solution originating in $S_a^{\varepsilon} \cap \Sigma_1$, passing through $S_a^{\sqrt{\varepsilon}} \cap \Sigma_2^{\pm}$ an $\mathcal{O}(\sqrt{\varepsilon})$ distance away from CM, and connecting to $S_r^{\sqrt{\varepsilon}} \cap \tilde{\Sigma}_*$.

Proof. The proof is the same as in Theorem 7.1; see Section 7.6.2. $\square$

When both y_{in} and y_{out} are in hyperbolic regions of CM (we refer to this as the hyperbolic case), we can prove the existence of canards for most values of α_2.

Theorem 7.3. *(Existence of canards: Hyperbolic case) Consider Case 1 with $\alpha_2 > 1$, and $\Sigma_* : y_2 = y_{2,*}$. Let $|y_{2,0}| \in (\delta, \sqrt{\alpha_2 - 1})$ define $\Sigma_2^{\pm}$ such that*

$$I_{\Lambda_1}(y_{2,0}, \sqrt{\alpha_2 + 1}) + I_{\Lambda_2}(\sqrt{\alpha_2 + 1}, y_{2,*}) = 0,$$

where $|y_{2,*}| > \sqrt{\alpha_2 + 1}$. Then for most $\alpha_2 \in A$ (an open set of almost full measure), there exists a canard solution, uniformly $\mathcal{O}(\sqrt{\varepsilon})$ close to CM, that connects $S_a^{\sqrt{\varepsilon}} \cap \Sigma_2^+$ to $S_r^{\sqrt{\varepsilon}} \cap \Sigma_*$.

Idea of Proof. Define an elliptic path that connects $y_{2,0}$ to $y_{2,*}$, and two invariant bundles, $S_a^{\sqrt{\varepsilon}} \cap \Sigma_2$ and $S_r^{\sqrt{\varepsilon}} \cap \Sigma_*$. We transport $S_a^{\sqrt{\varepsilon}} \cap \Sigma_2$ forward along the elliptic path, while $S_r^{\sqrt{\varepsilon}} \cap \Sigma_*$ is transported backwards along the same path. It can be shown that the bundles rotate in opposite directions, and therefore they will intersect transversally for almost all values of $\alpha_2 \in A$. See Section 7.6.2 for further details. $\square$

7.3.3 Bifurcation delay and buffer points

Recall that the way-in/way-out function, defined in (7.29) and (7.30), balances the accumulative contraction and repulsion along CM. Thus the delay or distanced travelled by a trajectory along CM_r depends on the prior accumulative contraction. Using the way-in/way-out function, we can quantify both the minimal and maximal delay.

Theorem 7.4. *(Minimal delay estimates) Consider Case 1 with $\alpha_2 > 0$. Let (x_2, y_2, z_2) denote a trajectory of (7.24) with initial condition $(x_2, y_2, z_2)(0)$ that is $\mathcal{O}(\sqrt{\varepsilon})$ close to CM, and let $y_2(0) = y_{in}$. Let $y_{out}(y_{in})$ be defined by $I_{\Lambda_1}(y_{in}, y_{out}) = 0$, and let $y_{2,0} = y_{out}$ define $\Sigma_2^{\pm}$. Then the trajectory (x_2, y_2, z_2) stays $\mathcal{O}(\sqrt{\varepsilon})$ close to CM for all $y_{in} \leq y_2 \leq y_{out} + o(1)$.*

Idea of Proof. Use the way-in/way-out function to balance weak contraction and strong repulsion. Using an elliptic path and properties of the complexified system, it can be shown that the trajectory stays $\mathcal{O}(\sqrt{\varepsilon})$ close to CM. See Section 7.6.3 for more details. $\qquad\square$

The maximal distance trajectories can travel on CM_r before leaving a small neighbourhood, is known as the *buffer point*.

Definition 7.1. (Buffer Points) Consider Case 1 with $\alpha_2 > 0$. For $\alpha_2 < 1$, the buffer point $y_{2,B}$ is

$$|y_{2,B}| := \lim_{|y_{in}| \to b} y_{out}(y_{in}),$$

for some $b > 0$, where $y_{out}(y_{in})$ is defined in (7.29). The canard buffer point $y_{2,C}$ is

$$|y_{2,C}| := \lim_{|y_{in}| \to c} y_{out}(y_{in}),$$

where $0 < b < c$, and $y_{out}(y_{in})$ is defined in (7.30). For $\alpha_2 > 1$, the definition of the buffer points is the same, except b and c are replaced with $\tilde{b}$ and $\tilde{c}$.

Lemma 7.1. *For Case 1, $|y_{2,B}| = |y_{2,C}| = \infty$.*

Proof. Consider Case 1 with $\alpha_2 < 1$. Given a general trajectory with entry point $0 < y_{in} < \sqrt{\alpha_2}$, the way-in/way-out function y_{out}, or exit point, is defined implicitly by $I_{\Lambda_1}(y_{in}, \phi) = 0$. In the case of a canard trajectory, with entry point $0 < y_{in}^c < \sqrt{\alpha_2}$, the exit point y_{out}^c is defined implicitly by $I_{\Lambda_2}(y_{in}^c, y_{out}^c) = 0$. When $y_{in} = y_{in}^c$, due the form of the eigenvalues, $y_{out} < y_{out}^c$, i.e. the canard trajectory travels further along CM_r. Taking limit $y_{out}, y_{out}^c \to \infty$, we observe that $y_{in} \to b$, and $y_{in} \to c$, where $0 < b < c$. Thus the maximal delay for a general trajectory (or canard) is infinity. Similar arguments can be made when $\alpha_2 > 1$, with different constants $\tilde{b}$ and $\tilde{c}$.

Remark 7.3. We know that $b, \tilde{b} > 0$ since there is no elliptic contour that connects to the pole $y_{2,P} = 0$. See Lemma 7.3.

$\qquad\square$

Note that Lemma 7.1 implies that trajectories that start sufficiently close the pole on CM_a experience an 'infinite delay'. They track the entire length of CM_a, which stretches to $|y_2| = \infty$, on either side of the pole. This kind of infinite delay is not possible in the FSN I or II.

For Case 1 and 2, define an open subset $J_+ \subset \mathcal{S}_a^\varepsilon \cap \Sigma_1$. Note that J_+ is a curve parametrised by $y \subset I_+$, for some interval I_+. Let the closure of J_+ be contained in the open interval defined by $-K\sqrt{\varepsilon} < y < K\sqrt{\varepsilon}$, for some positive constant K, i.e. $\mathcal{O}(\sqrt{\varepsilon})$ close to the strong canard γ_s. Similarly for Case 3 and 4, define an open subset $J_- \subset \mathcal{S}_a^\varepsilon \cap \Sigma_1$, that is parametrised by $y \subset I_-$. Let the closure of J_- be contained in the open interval $0 < |y| < \sigma_1^{1/4}$, i.e. between the centre manifold and the strong canard. The following theorem gives an estimate of the maximal delay trajectories in J_+ and J_- experience, before leaving CM and entering Σ_3.

Theorem 7.5. *(Maximal delay estimates) Let $\alpha_2 > 0$. Given any solution starting in $J_\pm$, there exists a function $d(\varepsilon)$ satisfying $\lim_{\varepsilon \to 0} d(\varepsilon) = 0$, such that the endpoint of the solution in Σ_3 satisfies $y_2 < y_{2,B} + d(\varepsilon)$.*

Proof. See Section 7.6.3. $\qquad\qquad\square$

7.4 Linearised Complex Flow and Elliptic Paths

We are interested in proving the existence of canards in system (7.26), which are defined as the intersection of the attracting and repelling slow manifolds $\mathcal{S}_a^{\sqrt{\varepsilon}}$ and $\mathcal{S}_r^{\sqrt{\varepsilon}}$. Naturally, it becomes important to track the slow manifolds. Due to the complex eigenvalue structure, this is not possible with standard techniques like Melnikov theory. To solve this problem, in this section we analytically extend the vector field (7.26) into the complex plane (as in FSN I and II analysis). We then identify special elliptic contours of the linearised complex flow that connect two points on the real y_2-axis. Finally, we study the rotational properties as well as the rates of expansion/contraction along the elliptic contours.

7.4.1 Complexification

In order to track the invariant attracting and repelling manifolds across complex regions of CM, we extend the vector field into the complex domain by letting $(x_2, y_2, z_2) \in \mathbb{C}^3$. For ease of notation, let $\gamma := \alpha_2 - y_2^2$. We linearise about CM using the complex co-ordinate transformation

$$
\begin{aligned}
u_2 &= z_2 + i\frac{x_2 - \delta_1\gamma z_2}{\sqrt{1 - \gamma^2}} + \mathcal{O}(\sqrt{\varepsilon}), \\
v_2 &= z_2 - i\frac{x_2 - \delta_1\gamma z_2}{\sqrt{1 - \gamma^2}} + \mathcal{O}(\sqrt{\varepsilon}),
\end{aligned}
\tag{7.31}
$$

which brings the linear part of (7.26) into Jordan normal form. Note that this transformation is singular (to leading order) at the branch points of the square root, i.e. when
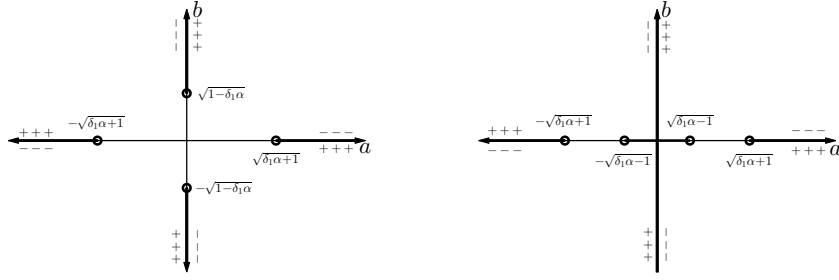
Figure 7.8: Branch cuts for *left:* $0 < \alpha_2 < 1$ and *right:* $\alpha_2 > 1$. The positive and negative signs indicate the sign of the square root $\sqrt{\gamma^2 - 1} = i\sqrt{1 - \gamma^2}$.

$|\alpha_2 - y_2^2| = 1$. The domain of analyticity must exclude these points. Applying transformation (7.31) to (7.26) gives

$$\delta_2 \sqrt{\varepsilon} y_2 u_2' = \lambda_1 u_2 - \frac{1}{4}(u_2 + v_2)^2 \left(1 - i\frac{\delta_1 \gamma}{\sqrt{1 - \gamma^2}}\right) + \mathcal{O}(\varepsilon, \sqrt{\varepsilon}(|u_2 + v_2|^2)),$$

$$\delta_2 \sqrt{\varepsilon} y_2 v_2' = \lambda_2 v_2 - \frac{1}{4}(u_2 + v_2)^2 \left(1 + i\frac{\delta_1 \gamma}{\sqrt{1 - \gamma^2}}\right) + \mathcal{O}(\varepsilon, \sqrt{\varepsilon}(|u_2 + v_2|^2)).$$

(7.32)

Note that not all solutions of (7.32) correspond to real solutions of (7.23).

Now let $y_2 = a + ib$, and define the complex function $y_2 \to \sqrt{1 - \gamma^2}$ using the standard definition of $\sqrt{z}$. Let $\theta = Arg(z)$ where $\theta \in [-\pi, \pi)$, and take the branch cut along the negative real axis, i.e. $\theta = \pi$. Thus $z = |z| \exp(i\theta)$ and

$$\sqrt{z} = \sqrt{|z|} \exp\left(i\frac{\theta}{2}\right),$$

where $\frac{\theta}{2} \in \left[-\frac{\pi}{2}, \frac{\pi}{2}\right)$. Applying this to $y_2 \to \sqrt{1 - \gamma^2}$, the modulus and argument of the square root are given by

$$\left|\sqrt{1 - \gamma^2}\right| = \{\left(1 - [\alpha_2 - a^2 + b^2]\right)^2 + 4a^2 b^2) \times$$

$$\left(1 + [\alpha_2 - a^2 + b^2]\right)^2 + 4a^2 b^2)\}^{1/4}$$

$$Arg\left(\sqrt{1 - \gamma^2}\right) = \begin{cases} \frac{\pi}{4} - \frac{1}{2}\arctan\left(\frac{\mathrm{Re}(1-\gamma^2)}{\mathrm{Im}(1-\gamma^2)}\right) \in \left(0, \frac{\pi}{2}\right), & \text{if } \mathrm{Im}(1 - \gamma^2) > 0, \\ -\frac{\pi}{4} - \frac{1}{2}\arctan\left(\frac{\mathrm{Re}(1-\gamma^2)}{\mathrm{Im}(1-\gamma^2)}\right) \in \left[-\frac{\pi}{2}, 0\right], & \text{if } \mathrm{Im}(1 - \gamma^2) \leq 0, \end{cases}$$

(7.33)

where $\mathrm{Re}(1 - \gamma^2) := 1 + 4a^2 b^2 - (\alpha_2 - (a^2 - b^2))^2$ and $\mathrm{Im}(1 - \gamma^2) := -4ab(\alpha_2 - (a^2 - b^2))$ are the real and imaginary parts of $1 - \gamma^2$, respectively. The branch cut of $y_2 \to \sqrt{1 - \gamma^2}$ is defined by $\mathrm{Arg}(1 - \gamma^2) = \pi$ and $\mathrm{Re}(1 - \gamma^2) \leq 0$, which gives the α_2-dependent system

$$\mathrm{Im}(1 - \gamma^2) = -4ab(\alpha_2 - (a^2 - b^2)) = 0,$$

$$\mathrm{Re}(1 - \gamma^2) = 1 + 4a^2 b^2 - (\alpha_2 - (a^2 - b^2))^2 < 0.$$

The branch cuts along the a and b-axis can be summarised as follows (see Figure 7.8):

$$a = 0: \implies \begin{cases} |b| > \sqrt{1 - \alpha_2}, & \text{if } 0 < \alpha_2 < 1, \\ b \in \mathbb{R}, & \text{if } \alpha_2 > 1, \end{cases}$$

$$b = 0: \implies \begin{cases} |a| > \sqrt{\alpha_2 + 1}, & \text{if } 0 < \alpha_2 < 1, \\ |a| < \sqrt{\alpha_2 - 1}, |a| > \sqrt{\alpha_2 + 1}, & \text{if } \alpha_2 > 1. \end{cases}$$

7.4.2 Linearisation

The linear, homogeneous flow of (7.32) is given by

$$\sqrt{\varepsilon}\delta_2 y_2 \frac{du_2}{dy_2} = \lambda_1(y_2, \delta_1, \alpha_2, \sqrt{\varepsilon})u_2,$$
$$\sqrt{\varepsilon}\delta_2 y_2 \frac{dv_2}{dy_2} = \lambda_2(y_2, \delta_1, \alpha_2, \sqrt{\varepsilon})v_2, \tag{7.34}$$

where y_2 is treated as complex slow time. Alternatively, we study (7.34) with the leading order eigenvalues $\lambda_{1,2}(y_2, \delta_1, \alpha_2, 0)$

$$\sqrt{\varepsilon}\delta_2 y_2 \frac{du_2}{dy_2} = \lambda_1(y_2, \delta_1, \alpha_2, 0)u_2,$$
$$\sqrt{\varepsilon}\delta_2 y_2 \frac{dv_2}{dy_2} = \lambda_2(y_2, \delta_1, \alpha_2, 0)v_2. \tag{7.35}$$

We will establish later in this section that solutions of (7.35) and their behaviour persist under small $\mathcal{O}(\sqrt{\varepsilon})$ perturbations, justifying our use of the leading order eigenvalues. Furthermore, we will prove that the inclusion of non-linear terms in (7.34) does not significantly alter the dynamics. Notice that system (7.35) is decoupled, and so we only study the first complex ODE given by

$$\sqrt{\varepsilon}\delta_2 y_2 \frac{du}{dy_2} = \lambda_1(y_2, \delta_1, \alpha_2, 0)u. \tag{7.36}$$

Solutions $u_2(y_2)$ can be easily obtained by elementary methods,

$$\sqrt{\varepsilon}\delta_2 y_2 \frac{du_2}{dy_2} = \lambda_1(y_2, \delta_1, \alpha, 0)u_2,$$
$$\implies \int_{\tilde{u}_2}^{u_2} \frac{1}{u_2} du_2 = \frac{\delta_2}{\sqrt{\varepsilon}} \int_{\Gamma} \frac{\lambda_1(w, \delta_1, \alpha_2, 0)}{w} dw,$$
$$\implies u_2(y) = \tilde{u}_2 \exp\left[\frac{\delta_2}{\sqrt{\varepsilon}} \int_{\Gamma} \frac{\lambda_1(w, \delta_1, \alpha_2, 0)}{w} dw\right], \tag{7.37}$$

where $u_2(\tilde{y}_2) = \tilde{u}_2$ is the initial condition, and Γ is a contour connecting $\tilde{y}_2$ to y_2. The behaviour of the solution $u_2(y_2)$ depends on the properties of the exponent

$$\psi(y_2) := \delta_2 \int_{\Gamma} \frac{\lambda_1(w, \delta_1, \alpha_2, 0)}{w} dw, \tag{7.38}$$

123

along contours of integration Γ. Define a contour parametrization

$$y_2(\tau) = a(\tau) + ib(\tau), \quad \tau \in \mathbb{R}, \tag{7.39}$$

such that $y_2(0) = a(0) + ib(0) = \tilde{y}_2$. We identify two special contours, *elliptic* and *hyperbolic contours*.

Definition 7.2. *Elliptic contours* of (7.37) are level curves of ψ with constant growth, i.e. $\mathrm{Re}(\psi) = const$.

Definition 7.3. *Hyperbolic contours* of (7.37) are level curves of ψ with constant oscillatory growth, i.e. $\mathrm{Im}(\psi) = const$.

Define Λ_1 and φ

$$\Lambda_1(a + ib, \delta_{1,2}, \alpha_2, 0) := \varphi(\delta_2, a + ib)\lambda_1(a + ib, \delta_1, \alpha_2, 0),$$
$$\varphi(\delta_2, a + ib) := \frac{\delta_2}{a + ib}.$$

Taking the derivative of $\mathrm{Re}(\psi) = const$, with respect to τ, yields

$$\mathrm{Re}\left(\Lambda_1(a + ib, \delta_{1,2}, \alpha_2, 0)\right) \frac{da}{d\tau} - \mathrm{Im}\left(\Lambda_1(a + ib, \delta_{1,2}, \alpha_2, 0)\right) \frac{db}{d\tau} = 0, \tag{7.40}$$

which can be rewritten as a system of equations

$$\begin{aligned} a' &= -\mathrm{Im}\left(\Lambda_1(a(\tau) + ib(\tau), \delta_{1,2}, \alpha_2, 0)\right), \\ b' &= -\mathrm{Re}\left(\Lambda_1(a(\tau) + ib(\tau), \delta_{1,2}, \alpha_2, 0)\right), \end{aligned} \tag{7.41}$$

where $' = d/d\tau$. Taking the derivative of $\mathrm{Im}(\psi) = $ constant gives

$$\mathrm{Im}\left(\Lambda_1(a + ib, \delta_{1,2}, \alpha_2, 0)\right) \frac{da}{d\tau} + \mathrm{Re}\left(\Lambda_1(a + ib, \delta_{1,2}, \alpha_2, 0)\right) \frac{db}{d\tau} = 0,$$

which can be rewritten as

$$\begin{aligned} a' &= \mathrm{Re}\left(\Lambda_1(a(\tau) + ib(\tau), \delta_{1,2}, \alpha_2, 0)\right), \\ b' &= -\mathrm{Im}\left(\Lambda_1(a(\tau) + ib(\tau), \delta_{1,2}, \alpha_2, 0)\right). \end{aligned}$$

7.4.3 Elliptic contours

In studying elliptic or hyperbolic contours, our objective is to identify contours that connect different points on the y_2-axis, which enables us to 'circumvent' the elliptic regions of CM where we cannot track invariant manifolds. It turns out that there are no hyperbolic contours that connect two points on the y_2-axis. Thus we only study the elliptic contours, which are solutions of the differential equation (7.41).

Proposition 7.6. For $0 < \alpha_2 < 1$, (7.41) has the following properties along the real y_2-axis $(b = 0)$:

$$\text{sgn } a' = \begin{cases} 0, & \text{for } |a| \geq \sqrt{\alpha_2 + 1}, \\ \text{sgn}(\delta_2 a), & \text{for } |a| < \sqrt{\alpha_2 + 1}, \end{cases}$$

$$\text{sgn } b' = \begin{cases} -\text{sgn}(\delta_1 \delta_2 a), & \text{for } |a| > \sqrt{\alpha_2}, \\ 0, & \text{for } |a| = \sqrt{\alpha_2}, \\ \text{sgn}(\delta_1 \delta_2 a), & \text{for } |a| < \sqrt{\alpha_2}. \end{cases}$$

For $\alpha_2 > 1$, (7.41) has the following properties along the real y_2-axis $(b = 0)$:

$$\text{sgn } a' = \begin{cases} 0, & \text{for } |a| \geq \sqrt{\alpha_2 + 1}, |a| \leq \sqrt{\alpha_2 - 1}, \\ \text{sgn}(\delta_2 a), & \text{for } \sqrt{\alpha_2 - 1} < |a| < \sqrt{\alpha_2 + 1}, \end{cases}$$

$$\text{sgn } b' = \begin{cases} -\text{sgn}(\delta_1 \delta_2 a), & \text{for } |a| > \sqrt{\alpha_2}, \\ 0, & \text{for } |a| = \sqrt{\alpha_2}, \\ \text{sgn}(\delta_1 \delta_2 a), & \text{for } |a| < \sqrt{\alpha_2}. \end{cases}$$

Proof. See Appendix F. $\qquad\square$

Proposition 7.7. For $0 < \alpha_2 < 1$, system (7.41) has the following properties along the imaginary y_2-axis $(a = 0)$:

$$\text{sgn } a' = \left\{ -\text{sgn}(\delta_1 \delta_2 b), \quad \text{for } b \in \mathbb{R}, \right.$$

$$\text{sgn } b' = \begin{cases} 0, & \text{for } |b| \geq \sqrt{1 - \alpha_2}, \\ \text{sgn}(\delta_2 b), & \text{for } |b| < \sqrt{1 - \alpha_2}. \end{cases}$$

For $\alpha_2 > 1$, system (7.41) has the following properties along the imaginary y_2-axis $(a = 0)$:

$$\text{sgn } a' = \left\{ -\text{sgn}(\delta_1 \delta_2 b), \quad \text{for } b \in \mathbb{R}, \right.$$

$$\text{sgn } b' = \left\{ 0, \quad \text{for } b \in \mathbb{R}. \right.$$

Proof. See Appendix F. $\qquad\square$

Proposition 7.8. Let $\alpha_2 > 0$ and $y_2 = a + ib$, with $|y_2| \gg 1$. Consider first Case 1 and 2. In the first and third quadrants, the elliptic contours are asymptotic to the family of Lemniscate curves [9, 4]

$$(b^2 + a^2)^2 = \frac{1}{C_1}(a^2 - b^2), \tag{7.42}$$

where $0 < C_1 \ll 1$. In the second and fourth quadrants, the elliptic contours are asymptotic to the family of hyperbolic curves

$$a^2 - b^2 = C_2, \tag{7.43}$$

where $C_2 \gg 1$. Now consider Cases 3 and 4. In the first and third quadrants, the elliptic contours are asymptotic to the hyperbolic curves (7.43), and in the second and third quadrants, the elliptic contours are asymptotic to the Lemniscate curves (7.42).
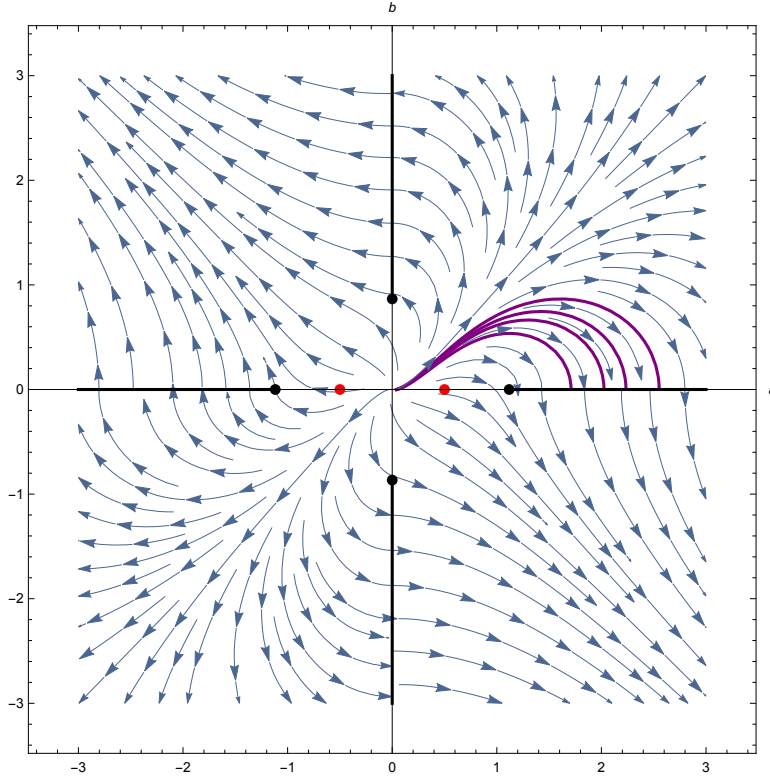
Figure 7.9: Stream plot (blue) of (7.41) for Case 1 and $\alpha_2 = 0.5$. Trajectories, i.e. elliptic contours, are shown in purple. Initial conditions for trajectories are taken along the real y_2−axis ($b = 0$), with $a > 0$. Branch cuts and branch points are indicated by solid black lines and circles, respectively. The two Hopf bifurcation of the layer problem $y_2 = \pm\sqrt{\alpha_2}$ are indicated by the red circles.

Proof. See Appendix G. □

Figure 7.9 shows a stream plot of (7.41), including various elliptic contours that connect points on the positive y_2-axis.

7.4.4 Hamiltonian properties

In this section, we present some of the basic properties of the elliptic contours. In particular, we show that the elliptic contours are level curves of a Hamiltonian system, and as a result they cannot connect to the pole $y_{2,p} = 0$.

Proposition 7.9. The elliptic contours are the level curves of the Hamiltonian

$$\mathcal{H}(y_2, \delta_{1,2}, \alpha_2) = Re\left(\int_\Gamma \Lambda_1(z, \delta_{1,2}, \alpha_2, 0)\right) dz. \tag{7.44}$$

Proof. See Appendix H. □

Lemma 7.2. *Let Γ_e be and elliptic path connecting two points $y_{2,0} < y_{2,*}$ on the real y_2-axis. Then we have*

$$\int_{\Gamma_e} Re\Lambda_1(z)dz = 0.$$

Proof. Along any elliptic path, the Hamiltonian $\mathcal{H}$ must be constant and hence $\mathcal{H}(y_{2,0}) = \mathcal{H}(y_{2,*})$. Since integration is a linear operation, we can swap the integral and taking the real part:

$$\int_{\Gamma_e^0} Re\Lambda_1(z)dz - \int_{\Gamma_e^*} Re\Lambda_1(z)dz = 0,$$
$$\Rightarrow \int_{\Gamma_e} Re\Lambda_1(z)dz = 0.$$

$\square$

Lemma 7.3. *Let Γ_e be and elliptic path connecting two points $y_{2,0} < y_{2,*}$ on the real y_2-axis. Then $y_{2,0}$ stays out of a small neighbourhood of the pole, $y_{2,p} = 0$. In other words, there is no elliptic path connecting to the pole.*

Proof. Suppose there is an elliptic path Γ_e^p connecting to $y_{2,p} = 0$. Then,

$$\int_{\Gamma_e^p} Re\Lambda_1(z)dz = \infty,$$

since the eigenvalue Λ_1 blows up at the pole. For an elliptic path Γ_e connecting to any other point $y_{2,0}$ on the real y_2-axis we know that

$$\int_{\Gamma_e} Re\Lambda_1(z)dz < \infty.$$

Thus $\mathcal{H}(y_{2,p}) \neq \mathcal{H}(y_{2,0})$, which contradicts Proposition 7.9. $\square$

7.4.5 Rotation and expansion/contraction along elliptic contours

We wish to study the flow of (7.35) along the elliptic paths defined by (7.41). Note that we can rewrite (7.34) as

$$\sqrt{\varepsilon}\frac{du_2}{dy} = \Lambda_1(y(\tau), \delta_{1,2}, \alpha_2, 0)u_2,$$
$$\sqrt{\varepsilon}\frac{dv_2}{dy} = \Lambda_2(y(\tau), \delta_{1,2}, \alpha_2, 0)v_2,$$

$$(7.45)$$

where $\Lambda_{1,2} = \varphi\lambda_{1,2}$. Using the chain rule and (7.41),

$$\frac{dy}{d\tau} = \frac{da}{d\tau} + i\frac{db}{d\tau},$$
$$= -Im\Lambda_1 - iRe\Lambda_1,$$
$$\Rightarrow dy = -i\left(Re\Lambda_1 - iIm\Lambda_1\right),$$
$$= -i\overline{\Lambda}_1.$$

127

Hence we can transform (7.45) along the elliptic paths:

$$\sqrt{\varepsilon}\frac{du_2}{d\tau} = -i\Lambda_1(y(\tau),\delta_{1,2},\alpha_2,0)\overline{\Lambda}_1(y(\tau),\delta_{1,2},\alpha_2,0)u_2,$$
$$\sqrt{\varepsilon}\frac{dv_2}{d\tau} = -i\Lambda_2(y(\tau),\delta_{1,2},\alpha_2,0)\overline{\Lambda}_1(y(\tau),\delta_{1,2},\alpha_2,0)v_2. \tag{7.46}$$

The real and imaginary parts of the eigenvalues of (7.46) determine the rate of growth (or decay) and the amount rotation along an elliptic path. By construction, the eigenvalue of the u_2 equation is purely imaginary and the growth rate is zero. However, the growth rate is not zero for v_2.

Proposition 7.10. The real and imaginary parts of the v_2 equation in system (7.46) are given by

$$\mathrm{Re}(-i\Lambda_2\overline{\Lambda}_1) = -\frac{2\delta_1}{a^2+b^2}\left(Re(\gamma)Re(\sqrt{1-\gamma^2})+Im(\gamma)Im(\sqrt{1-\gamma^2})\right),$$
$$\mathrm{Im}(-i\Lambda_2\overline{\Lambda}_1) = \frac{1}{a^2+b^2}\left(\sqrt{1-\gamma^2}\overline{\sqrt{1-\gamma^2}}-\gamma\overline{\gamma}\right).$$

Proof. See Appendix I. $\square$

Let $\Omega := \mathrm{Re}(-i\Lambda_2\overline{\Lambda}_1)$. The sign of Ω determines whether v_2 grows or decays along the elliptic paths. Let H be the hyperbola defined by

$$H := \{y_2 = a + ib : a^2 - b^2 = \alpha_2\}. \tag{7.47}$$

Proposition 7.11. The sign of Ω depends on δ_1 and is given by

$$\mathrm{sgn}(\Omega) = \begin{cases} -\mathrm{sgn}(\delta_1), & a^2 - b^2 < \alpha_2, \\ \mathrm{sgn}(\delta_1), & a^2 - b^2 > \alpha_2. \end{cases}$$

Furthermore, $\Omega = 0$ along the Hyperbola H, as well as the branch cuts (see Figure 7.8).

Proof. See Appendix J. $\square$

The sign of Ω in different regions of the complex plane is shown in Figure 7.10. In general, we can define a path $y_2 = y_2(\tau)$ in the complex plane, parametrised by $\tau \in [0, T]$. The amount of rotation (in u_2) along such a path is

$$R := \frac{1}{\sqrt{\varepsilon}}\int_0^T \mathrm{Im}\left(\Lambda_1(y_2(\tau),\delta_{1,2},\alpha_2,0)\frac{dy_2}{d\tau}\right)d\tau. \tag{7.48}$$

It is important to note that R is path independent, and we can evaluate the integral along the real y_2-axis, or any convenient path. We compute the amount of rotation along an elliptic path Γ_e by evaluating (7.48) along the real axis and H, thus proving that R is bounded and that there are $\mathcal{O}(\varepsilon^{-1/2})$ rotations.
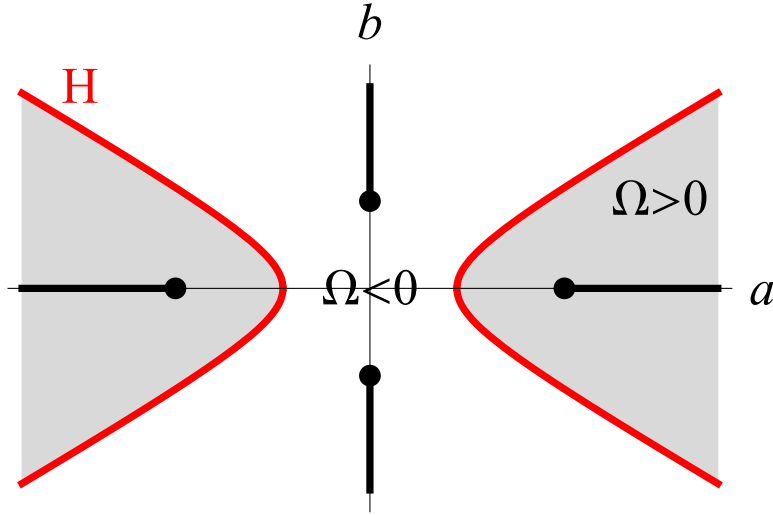
Figure 7.10: Regions of growth/decay of v_2 in (7.46) for Case 1. The Hyperbola H is shown in red, while the branch cuts are thick black lines. Along both of these $\Omega = 0$. The shading of the plot indicates the sign of Ω. In the grey region $\Omega > 0$ (growth), while $\Omega < 0$ (decay) in the white region.

Proposition 7.12. Assume that $\alpha_2 > 0$. Let $y_{2,0} < \sqrt{\alpha_2}$ and $y_{2,*} > \sqrt{\alpha_2}$ be two points on the real y_2-axis joined by an elliptic path Γ_e. Then there exist constants m, $M \in \mathbb{R}$, with $0 < m < M < \infty$, such that

$$m\varepsilon^{-1/2} \leq R \leq M\varepsilon^{-1/2}.$$

Proof. Consider the Case 1 with $0 < \alpha_2 < 1$, where $y_{2,*} \in \left(\bar{\delta}, \sqrt{\alpha_2}\right)$ and $y_{2,0} > \sqrt{1+\alpha_2}$. Let $(a,b) = (a_H, b_H)$ be the point in the complex plane where the elliptic contour Γ_e intersects the hyperbola H.

First, we calculate the amount of rotation R_+ from $(y_{2,0}, 0)$ to (a_H, b_H) by integrating backwards along the real y_2-axis from $(y_{2,0}, 0)$ to $(\sqrt{\alpha_2}, 0)$, and then integrating along H from $(\sqrt{\alpha_2}, 0)$ to (a_H, b_H). Thus R_+ is given by

$$R_+ := \frac{1}{\sqrt{\varepsilon}} \int_{y_{2,0}}^{\sqrt{\alpha_2}} \mathrm{Im}\Lambda_1(s)ds + \frac{1}{\sqrt{\varepsilon}} \int_{\sqrt{\alpha_2}}^{a_H} \mathrm{Im}\Lambda_1(a+ib_H(a))\frac{db_H}{da}ds.$$

Next, we calculate the amount of rotation R_- from $(a,b) = (y_{2,*}, 0)$ to (a_H, b_H) by integrating forwards along the real y_2-axis from $(y_{2,*}, 0)$ to $(\sqrt{\alpha_2}, 0)$ and then integrating along H from $(\sqrt{\alpha_2}, 0)$ to (a_H, b_H). Thus R_- is given by

$$R_- := \frac{1}{\sqrt{\varepsilon}} \int_{y_{2,*}}^{\sqrt{\alpha_2}} \mathrm{Im}\Lambda_1(s)ds + \frac{1}{\sqrt{\varepsilon}} \int_{\sqrt{\alpha_2}}^{a_H} \mathrm{Im}\Lambda_1(a+ib_H(a))\frac{db_H}{da}ds.$$

Hence the total amount of rotation R_T is given by

$$R_T := R_+ - R_-,$$
$$= -\int_{y_{2,*}}^{y_{2,0}} \text{Im}\Lambda_1(s)ds,$$
$$= -\int_{y_{2,*}}^{\sqrt{\alpha_2+1}} \text{Im}\Lambda_1(s)ds,$$
$$= -\delta_2 \int_{y_{2,*}}^{\sqrt{\alpha_2+1}} \frac{\sqrt{1-\gamma(s)^2}}{s}ds,$$

where the third line is obtained by noting that there is no rotation outside the elliptic regions of Λ_1, i.e. $1 - \gamma^2 > 0$. Since we stay out of a small neighbourhood of the pole, and the domain on which we evaluate the integral is compact, we can prove that the integral is bounded above (below) by the maximum (minimum) multiplied by the length of the domain. The result then follows. □

7.5   Non-Linear Flow

From Proposition 7.6, there always exist elliptic contours Γ_e which cross the real y_2-axis transversally. Note that at $y_2 = \pm\sqrt{\alpha_2}$, the contour Γ_e is tangential to the real y_2-axis. It follows that under small $\mathcal{O}(\sqrt{\varepsilon})$ perturbations of the vector field, the elliptic contours will persist. Thus for the perturbed linear system

$$\sqrt{\varepsilon}\frac{du_2}{dy} = \Lambda_1(y(\tau), \delta_{1,2}, \alpha_2, \sqrt{\varepsilon})u_2,$$
$$\sqrt{\varepsilon}\frac{dv_2}{dy} = \Lambda_2(y(\tau), \delta_{1,2}, \alpha_2, \sqrt{\varepsilon})v_2,$$

(7.49)

we can find elliptic contours Γ_e^ε which are solutions of

$$a' = -\text{Im}\Lambda_1(a(\tau)+ib(\tau), \delta_{1,2}, \alpha_2, \sqrt{\varepsilon}),$$
$$b' = -\text{Re}\Lambda_1(a(\tau)+ib(\tau), \delta_{1,2}, \alpha_2, \sqrt{\varepsilon}).$$

(7.50)

Hence the perturbed elliptic contours Γ_e^ε are $\mathcal{O}(\sqrt{\varepsilon})$ close to the unperturbed contours Γ_e. Transforming system (7.32) along an elliptic contour Γ_e^ε, with $\varepsilon \neq 0$, gives

$$\sqrt{\varepsilon}\frac{du_2}{d\tau} = -i\Lambda_1(\tau, \sqrt{\varepsilon})\overline{\Lambda}_1(\tau, \sqrt{\varepsilon})u + G_1(\tau, \delta_{1,2}, u_2, v_2),$$
$$\sqrt{\varepsilon}\frac{dv_2}{d\tau} = -i\Lambda_2(\tau, \sqrt{\varepsilon})\overline{\Lambda}_1(\tau, \sqrt{\varepsilon})v + G_2(\tau, \delta_{1,2}, u_2, v_2),$$

(7.51)

where $G_{1,2}(u_2, v_1, \varepsilon) = \mathcal{O}(\varepsilon, \sqrt{\varepsilon}(|u_2|^2 + |v_2|^2))$, and we have suppressed the $\delta_{1,2}$ and α_2 dependence in $\Lambda_{1,2}$ for ease of notation. Note that the growth and decay properties of the linear part are the same as in the unperturbed case (see Propositions 7.10 and 7.11 and Figure 7.10).

For solutions of (7.51) to exist and be unique, we require that the vector field be analytic, bounded and Lipschitz in a closed disc around the initial condition. Solutions can be

analytically continued along a path, as long as the vector field can also be extended along the path. We have existence and uniqueness for paths everywhere inside the domain of analyticity; this excludes a small neighbourhood of the pole and the branch points.

Proposition 7.13. The linear flow of (7.51) is given by the transition matrix

$$\Phi(\tau,\tau_0) := \begin{pmatrix} \exp\left(\frac{-i}{\sqrt{\varepsilon}} \int_{\tau_0}^{\tau} \Lambda_1(\sigma)\overline{\Lambda}_1(\sigma)\right) & 0 \\ 0 & \exp\left(\frac{-i}{\sqrt{\varepsilon}} \int_{\tau_0}^{\tau} \Lambda_2(\sigma)\overline{\Lambda}_1(\sigma)\right) \end{pmatrix},$$

and (7.51) can be rewritten in integral form as

$$U(\tau) = U_0\Phi(\tau,0) + \frac{1}{\sqrt{\varepsilon}} \int_0^{\tau} G(U,\sigma)\Phi(\tau,\sigma)d\sigma,$$

where $U = (u_2, v_2)$, $U_0 = U(0) = (u_2(0), v_2(0))$ and $G = (G_1, G_2)$.

Proof. See Appendix K. □

Proposition 7.14. Let $0 < c < \frac{1}{2}$ be a constant, and assume that $|U_0| = \mathcal{O}(\varepsilon^{1/2+c})$. Let $y_2(\tau)$ parametrise an elliptic path Γ_e^{ε} where $\mathrm{Re}(-i\Lambda_2\overline{\Lambda}_1) < 0$ (i.e. where v_2 decays). Then

$$U(\tau, U_0) = \mathcal{O}(\sqrt{\varepsilon}).$$

Proof. First, we rewrite the nonlinearities $G(U,\tau) = g_1(\varepsilon) + g_2(U, \sqrt{\varepsilon})$, where $g_1 = \mathcal{O}(\varepsilon)$ and $g_2 = \mathcal{O}(U^2, \sqrt{\varepsilon}U^2)$. Hence,

$$|U(\tau, U_0)| \le |U_0\Phi(\tau,0)| + \frac{|g_1(\varepsilon)|}{\sqrt{\varepsilon}} \int_0^{\tau} |\Phi(\tau,\sigma)|d\sigma + \frac{1}{\sqrt{\varepsilon}} \int_0^{\tau} |g_2(U_2,\varepsilon)\Phi(\tau,\sigma)|d\sigma. \quad (7.52)$$

Assuming that $|U_0| = \mathcal{O}(\varepsilon^{1/2+c})$ and $\mathrm{Re}(-i\Lambda_2\overline{\Lambda}_1) < 0$ (u_2 has no growth or decay, and we restrict ourselves to regions where v_2 decays), we conclude that $|U_0\Phi(\tau,0)| = \mathcal{O}(\varepsilon^{1/2+c})$. The condition $\mathrm{Re}(-i\Lambda_2\overline{\Lambda}_1) < 0$ depends on the position in the complex $y_2(\tau)$-plane relative to H, as well as δ_1; see Proposition 7.11 and Figure 7.10. From the form of Φ, we deduce that $\int_0^{\tau} \Phi(\tau,\sigma)d\sigma = \mathcal{O}(\sqrt{\varepsilon})$, for $\mathcal{O}(1)$ times τ. Applying this to equation (7.52), we find that

$$|U(\tau, U_0)| \le C_1\varepsilon^{1/2+c} + C_2\varepsilon + \frac{1}{\sqrt{\varepsilon}} \int_0^{\tau} |g_2(U_2,\varepsilon)\Phi(\tau,\sigma)|d\sigma. \quad (7.53)$$

Let $U = \varepsilon^{1/2+c}\overline{U}$, where $\overline{U} = \mathcal{O}(1)$. Hence, $g_2(U, \sqrt{\varepsilon}) = \varepsilon^{1+2c}\overline{g}_2(\overline{U}, \sqrt{\varepsilon})$, where $\overline{g}_2 = \mathcal{O}(1)$. Equation (7.53) becomes

$$|\overline{U}| \le C_1 + C_2\varepsilon^{1/2-c} + \frac{C_3\varepsilon^{1/2+c}}{\sqrt{\varepsilon}} \int_0^{\tau} |\Phi(\tau,\sigma)|d\sigma,$$

$$\le C_1 + C_2\varepsilon^{1/2-c} + C_3\varepsilon^{1/2+c}, \quad (7.54)$$

which implies that $\overline{U}$ is indeed $\mathcal{O}(1)$, for $0 < c < \frac{1}{2}$. Hence $U(\tau, U_0) = \mathcal{O}(\sqrt{\varepsilon})$.

Remark 7.4. The same result is obtained for $\mathrm{Re}(-i\Lambda_2\overline{\Lambda}_1) > 0$ by reversing time.

□

7.6 Proof of Main Results

In this section we will formally prove the existence of canards and faux canards for the two sub-cases of Case 1: $0 < \alpha_2 < 1$ and $\alpha_2 > 1$. However, we first summarise some important properties of the layer problem of (7.16) that will be needed in the proofs. The results stated here have been adapted from [66].

The layer problem of (7.16) is

$$\begin{aligned}\dot{x}_2 &= \delta_1\gamma - z_2,\\ \dot{z}_2 &= x_2 - z_2^2,\end{aligned} \tag{7.55}$$

where $\gamma := \alpha_2 - y_2^2$. The equilibria $(\bar{x}_2, \bar{z}_2) = (\gamma^2, \delta_1\gamma)$ have complex conjugate eigenvalues when $0 < \gamma^2 < 1$, which have negative real part when $\delta_1\gamma > 0$. Thus for Case 1 (and 2), the equilibria of the layer problem are stable foci when $y_2 < \alpha_2$. Furthermore, for every fixed γ, (7.55) has a unique trajectory $S_{a,\gamma}$ that is algebraic in *backward* time. The union of $S_{a,\gamma}$ over γ provides a close approximation of $S_a^{\sqrt{\varepsilon}}$. Define the return map Π_γ, and the cross-section Σ_γ

$$\Pi_\gamma : \Sigma_\gamma := \left\{(x_2, z_2) : z_2 = \delta_1\gamma, x_2 > \gamma^2\right\} \to \Sigma_\gamma. \tag{7.56}$$

In backward time, the stable foci exponentially expand the distance between points in a neighbourhood of CM. Given any point $(x_2, \delta_1\gamma) \in \Sigma_\gamma$, it takes $m = \left\lfloor -\ln|x_2 - \gamma^2| \right\rfloor$ iterations of the map Π_γ to be a distance $d > 0$ away from the equilibrium $(\gamma^2, \delta_1\gamma)$. In other words, there exists a constant $d > 0$ such that for any $(x_2, \delta_1\gamma) \in \Sigma_\gamma$ and $m = \left\lfloor -\ln|x_2 - \gamma^2| \right\rfloor$, we have

$$\text{dist}\left(\Pi_\gamma^m(x_2, \delta_1\gamma), (\gamma^2, \delta_1\gamma)\right) \geq d.$$

Furthermore, if $(x_{2,0}, \delta_1\gamma)$, $(x_{2,1}, \delta_1\gamma) \in \Sigma_\gamma$ and $(x_{2,1}, \delta_1\gamma)$ is on the forward orbit of $(x_{2,0}, \delta_1\gamma)$ and does not return to Σ_γ, then there exists a point $(x_{2,*}, \delta_1\gamma) \in S_a^{\sqrt{\varepsilon}}$ with $x_{2,0} < x_{2,*} < x_{2,1}$.

Remark 7.5. Note that similar properties hold for Cases 3 and 4 ($\delta_1 = -1$). The equilibria of the layer problem are unstable foci for $y_2 < \alpha_2$, and for every fixed γ, (7.55) has a unique trajectory $S_{r,\gamma}$, which is algebraic in *forward* time. The union of $S_{r,\gamma}$ over γ provides a close approximation of $S_r^{\sqrt{\varepsilon}}$. Thus in forward time, the unstable foci exponentially expand the distance between points near CM, and all the results discussed above hold.

7.6.1 Canards for $0 < \alpha < 1$

We are now in a position to formally prove Theorem 7.1.

Proof. (Theorem 7.1) Consider Case 1 with a set of initial conditions $J_1 \in \Sigma_1 \cap S_r^\varepsilon$, with end points p and q. The repelling critical manifold CM_r perturbs to CM_r^ε. Due to the exponential contraction (in backward time) of $\Pi_1 : \Sigma_1 \to \Sigma_2$, $\Pi_1(p)$ must be $\mathcal{O}(\varepsilon)$ close to CM. Choose the other end point q such that $\Pi_1(q)$ is $\mathcal{O}(\varepsilon^{1/2+c})$ close to CM in Σ_2^+. Thus $J_2 = \Pi_1(J_1)$ is $\mathcal{O}(\sqrt{\varepsilon})$ close to CM. Next, we transport J_2 to Σ_* (backwards in time) via an elliptic path. By Proposition 7.2, $J_* = \Sigma_*(J_2)$ is a curve of length $\mathcal{O}(\sqrt{\varepsilon})$ in Σ_*

(i.e. J_* is $\mathcal{O}(\sqrt{\varepsilon})$ close to CM). Transforming back to (x_2, y_2, z_2)-coordinates, we now use properties of the layer problem (7.55), in backward time, to show that J_* will intersect $S_a^{\sqrt{\varepsilon}}$ transversally. Without loss of generality, we may assume that J_* is a line segment contained in Σ_*. We know that one end point of J_* is $\mathcal{O}(\varepsilon)$ close to CM, while the other end point satisfies $x_2 - \gamma_*^2 < k\sqrt{\varepsilon}$, where k is a positive constant. By properties of the layer problem (7.55) near CM, there exist points $\tilde{x}_{2,0}$ and $\tilde{x}_{2,1} \in J_*$ and a constants $d_{1,2} > 0$ such that

$$\text{dist}\left(\Pi_{\gamma_*}^m(\tilde{x}_{2,0}, \gamma_*), (\gamma_*^2, \gamma_*)\right) \geq d_1, \quad \text{dist}\left(\Pi_{\gamma_*}^m(\tilde{x}_{2,1}, \gamma_*), (\gamma_*^2, \gamma_*)\right) \geq d_2,$$

where

$$\begin{aligned} m &= \left\lfloor -\ln|x_2 - \gamma_*^2| \right\rfloor, \\ &= \mathcal{O}(-\ln(\varepsilon^{1/2})), \\ &= \mathcal{O}(-\ln\varepsilon). \end{aligned}$$

Then the points $x_{2,0}$ and $x_{2,1}$ defined by

$$x_{2,0} = \Pi_{\gamma_*}(\tilde{x}_{2,0}, \gamma_*), \quad x_{2,1} = \Pi_{\gamma_*}(\tilde{x}_{2,1}, \gamma_*).$$

are such that $x_{2,1}$ is on the forward orbit of $x_{2,0}$, and does not return to Σ_{γ_*}. Thus there exists a point $x_{2,*} \in S_{a,\gamma_*}$, with $x_{2,0} < x_{2,*} < x_{2,1}$. For γ close to γ_*, let $x_{2,*}(\gamma) = (x_{2,*}(\gamma), \delta_1\gamma)$ denote the unique point in $\Sigma_\gamma \cap S_{a,\gamma}$. Varying $\gamma(y_2)$, we can construct a curve $(x_{2,*}(\gamma), \delta_1\gamma)$ which will intersect the interval $\Pi_{\gamma_*}^m(J_*)$ transversally. In other words, it takes m iterations for the interval J_* to wind out (or expand sufficiently) to an $\mathcal{O}(1)$ distance d away from the equilibrium and intersect the attracting critical manifold.

It can be easily shown that the transverse intersection will persist under small perturbations. Let $\tilde{\Pi}$ be the return map

$$\tilde{\Pi} : \tilde{\Sigma} \to \tilde{\Sigma},$$

under the flow of (7.16) (for $\varepsilon \neq 0$), defined on the cross-section

$$\tilde{\Sigma} = \{(x_2, y_2, z_2) : z_2 = \delta_1\gamma(y_2), x_2 > \gamma^2(y_2)\}.$$

Note that the map $\tilde{\Pi}$ is a small perturbation of Π_{γ_*}. From equation (7.16), $\dot{y}_2 = \delta_2\sqrt{\varepsilon}y_2(1 + \mathcal{O}(\sqrt{\varepsilon}))$, and thus y_2 will vary by $\mathcal{O}(\sqrt{\varepsilon}\ln\varepsilon)$ over $m = \mathcal{O}(-\ln\varepsilon)$ iterations of $\tilde{\Pi}$. It follows that $\tilde{\Pi}^m$ is $\mathcal{O}(\sqrt{\varepsilon}\ln\varepsilon)$ close to Π^m, and the curve $(x_{2,*}(\gamma(y_2)), y_2, \gamma(y_2))$ intersects $\tilde{\Pi}^m(J_*)$ transversally.

Remark 7.6. The proof for Case 1 is constructed in backward time, starting from the point $y_{2,0} = y_{out}$. A similar proof for Case 4 can be constructed by integrating forward in time from $y_{2,0} = y_{in}$.

$\square$

7.6.2   Canards for $\alpha_2 > 1$

For $\alpha_2 > 1$, we identified two further sub-cases: the elliptic and hyperbolic cases. In the elliptic regime, the real segments of $CM_{a/r}$ have no impact on the canard dynamics

(Theorems 7.2 and 7.9), and we can construct similar proofs as in the $0 < \alpha_2 < 1$ case. In the hyperbolic regime, the real segments of $CM_{a/r}$ do impact the dynamics of canards, and proofs of their existence in Theorem 7.3 must be altered – the invariant manifolds are tracked using their linear subspaces.

Proposition 7.15. Consider Case 1 with $\alpha_2 > 1$. Let R_+ be the amount of rotation from $y_{2,0} > \sqrt{\alpha_2 + 1}$ backwards along an elliptic path Γ_e to the hyperbola H. Let R_- be the amount of rotation from $y_{2,*} \in (\delta, \sqrt{\alpha_2 - 1})$ along Γ_e to H. Thus the amount of rotation backward along Γ_e from $y_{2,0}$ to $y_{2,*}$ would be $R_+ - R_-$. Then

$$\frac{d}{d\alpha_2}(R_+ - R_-) \neq 0.$$

Proof. Similar to previous calculations,

$$R_+ - R_- = -\delta_2 \int_{\sqrt{\alpha_2 - 1}}^{\sqrt{\alpha_2 + 1}} \frac{\sqrt{1 - \gamma(s)^2}}{s} ds, \tag{7.57}$$

where $\gamma(s) = \alpha_2 - s^2$. Calculating the derivative, we find that

$$\frac{d}{d\alpha_2}(R_+ - R_-) = \int_{\sqrt{\alpha_2 - 1}}^{\sqrt{\alpha_2 + 1}} \frac{\gamma(s)}{s\sqrt{1 - \gamma(s)^2}} ds,$$
$$= \frac{\pi}{2}\left(\frac{\alpha_2}{\sqrt{\alpha_2^2 - 1}} - 1\right),$$
$$> 0.$$

Remark 7.7. For Case 4, $\delta_1 = \delta_2 = -1$, the amount of rotation forward along Γ_e from $y_{2,0}$ to $y_{2,*}$ is given by (7.57), i.e. it is the same as in Case 1 and the result still holds.

$\square$

Let $u_{2,0}(\tau, \alpha_2)$ be a solution of (7.36) along an elliptic path Γ_e parametrised by $y(\tau)$, with $y_2(0) > \sqrt{\alpha_2 + 1}$. Let $u_{2,0}^H(\alpha_2) = u_{2,0}(\tau_H, \alpha_2)$, where τ_H is chosen such that $y_2(\tau_H) \in H$. Similarly, let $u_{2,*}(\tau, \alpha_2)$ be a solution of (7.36) with $u_{2,*}(T) \in (\delta, \sqrt{\alpha_2 - 1})$, and let $u_{2,*}^H(\alpha_2) = u_{2,*}(\tau_H, \alpha_2)$. The solutions $u_{2,0}^H(\alpha_2)$ and $u_{2,*}^H(\alpha_2)$ are interpreted as vectors in $\mathbb{R}^2$, with $\theta(\alpha_2)$ defined as the angle between the two vectors, and $\theta(\alpha_2) \in [0, 2\pi]$. Define the interval $A = [\alpha_{2,0}, \alpha_{2,1}]$ with $1 < \alpha_{2,0} < \alpha_{2,1}$ and

$$A_d := \{\alpha_2 : \theta(\alpha_2) \geq d, \text{ for all } \alpha_2 \in A \text{ and } d > 0\}.$$

Proposition 7.16. Let A_d^c be the compliment of A_d in A. There exists a constant $K > 0$ such that for each $d > 0$ and $0 < \varepsilon \ll 1$ sufficiently small, the total length of A_d^c is bounded by Kd.

Proof. Consider Case 1, $\delta_1 = \delta_2 = 1$. Integrating backwards in time, the amount of rotation along Γ_e from $y_{2,0}$ to H is

$$\frac{1}{\sqrt{\varepsilon}}R_+ \mod 2\pi, \tag{7.58}$$

134

while the amount of rotation along Γ_e from H to $y_{2,*}$ is

$$-\frac{1}{\sqrt{\varepsilon}}R_- \mod 2\pi. \tag{7.59}$$

From Proposition 7.15, $\theta(\alpha_2)$ increases monotonically in α_2 with non-zero derivative until it reaches 2π, and then is reset to zero. It follows from (7.58) and (7.59) that there are $\mathcal{O}(1/\sqrt{\varepsilon})$ intervals in A_d^c, each of length $d\mathcal{O}(\sqrt{\varepsilon})$.

Remark 7.8. A similar proof can be constructed for Case 4 in forward time.

$\square$

For ε-dependent elliptic paths Γ_e^ε, let A_d^ε and $A_d^{\varepsilon,c}$ denote the analogues of A_d and A_d^c, respectively.

Proposition 7.17. There exists a constant $K > 0$ such that for each $d > 0$ and $0 < \varepsilon \ll 1$ sufficiently small, the total length of $A_d^{c,\varepsilon}$ is bounded by Kd.

Proof. Γ_e^ε is uniformly $\mathcal{O}(\sqrt{\varepsilon})$ close to Γ_e. At lowest order, $\Gamma_e^\varepsilon = \Gamma_e$, and hence each of the intervals which make up $A_d^{c,\varepsilon}$ change in length by at most $\mathcal{O}(\varepsilon)$. $\square$

As a result of Propositions 7.15 and 7.17, for most values of α_2, the solution vectors $u_{2,0}^H(\alpha_2)$ and $u_{2,*}^H(\alpha_2)$ will intersect transversally (the vectors rotate in opposite directions). We are now in position to prove the existence of canards for $\alpha_2 > 1$, in the hyperbolic case (Theorem 7.3).

Outline of Proof. (Theorem 7.3) Take a set of initial conditions in $S_a^{\sqrt{\varepsilon}} \cap \Sigma_2^\pm$ that is $\mathcal{O}(\sqrt{\varepsilon})$ close to CM and evolve it forward in time along the elliptic path Γ_e^ε up to the hyperbola H. Similarly, take a set of initial conditions in $S_r^{\sqrt{\varepsilon}} \cap \Sigma_*$ that is $\mathcal{O}(\sqrt{\varepsilon})$ close to CM and evolve it backward in time along the elliptic path Γ_e^ε up to H. By Propositions 7.15 and 7.17, these invariant bundles rotate in opposite directions and will intersect transversally for most α_2. $\square$

7.6.3 Delay estimates

Having proved the existence of canards, we now turn our attention to general solutions which experience a delayed loss of stability. In this section we provide more detailed proofs of the delay estimates (Theorems 7.4 and 7.5), i.e. how long trajectories remain close to CM before escaping. First, we consider trajectories which start close to CM.

Outline of Proof. (Theorem 7.4; see Theorem 3.4 of [66] and 4.10 of [108]) We present the proof for Case 1, $\alpha_2 < 1$. Consider solutions (u_2, v_2, y_2) of (7.32) which correspond to real solutions of (7.26). In particular, let $U_2 = (u_2(\tau), v_2(\tau), y_2(\tau))$ and $U_2^* = (u_2^*(\tau), v_2^*(\tau), y_2^*(\tau))$ denote two solutions of (7.32), with initial conditions $(u_{2,0}, v_{2,0}, y_{2,0})$ and $(u_{2,*}, v_{2,*}, y_{2,*})$ chosen such that $(u_{2,*}, v_{2,*}) = \mathcal{O}(\sqrt{\varepsilon})$. Assume that $y_{2,0} > \sqrt{\alpha_2 + 1}$ and $\delta < y_{2,*}(T) < \sqrt{\alpha_2}$, where $(-\delta, \delta)$ defines a small neighbourhood of the pole $y_2 = 0$.

Now consider an elliptic path which connects U_2 and U_2^*. We follow U_2 backward and U_2^* forward in τ along the elliptic path, up to the Hyperbola H. It follows from Proposition

7.14 that the two solutions are $\mathcal{O}(\sqrt{\varepsilon})$ close. Next we follow the solutions (backward in τ) down H to the point $y_2 = \sqrt{\alpha_2}$. Solutions of (7.32) experience exponential contraction (in backward time) in the u_2 coordinate such that the distance between U_2 and U_2^* is given by

$$|u_2 - u_{2,*}|_{y_2 = \sqrt{\alpha_2}} = \mathcal{O}\left(\exp\left(\varepsilon^{-1/2}I_{\Lambda_1}(y_2, \sqrt{\alpha_2})\right)\right).$$

Since U_2 and U_2^* correspond to real solutions of (7.26), $v_2 = \bar{u}_2$ and $v_{2,*} = \bar{v}_{2,*}$. Thus the above estimate also holds for v_2 and $v_{2,*}$ at $y_2 = \sqrt{\alpha_2}$. The maximal expansion (in backward time) along a solution from $y_2 = \sqrt{\alpha_2}$ to any $\delta < y_2 < \sqrt{\alpha_2}$ is

$$\exp\left(\varepsilon^{-1/2}I_{\Lambda_1}(\sqrt{\alpha_2}, y_2)\right).$$

Thus for $\delta < y_2 < \sqrt{\alpha_2}$ such that $I_{\Lambda_2}(y_{2,0}, y_2) < 0$, the corresponding solution of (7.32) on the interval $(y_2, y_{2,0})$ must be $\mathcal{O}(\sqrt{\varepsilon})$. Similar proofs can be constructed for $\alpha_2 > 1$ and Case 4. $\qquad\square$

Now we estimate the maximal delay experienced by trajectories, before leaving CM and transitioning to Σ_3.

Outline of Proof. (Theorem 7.5; see Theorem 3.5 of [66] and 4.12 of [108]) Consider Case 1 with $\alpha_2 > 1$. Suppose that $y_{2,B} \in (\sqrt{\alpha_2}, \sqrt{\alpha_2 + 1})$ where CM_r is complex (elliptic). Fix a constant $K > 0$. Suppose we have a trajectory of (7.51) with

$$|(u_2, v_2)| \geq K\sqrt{\varepsilon}, \qquad \text{for all } y_{2,B} + d(\varepsilon), \tag{7.60}$$

and (u_2, v_2) is not exponentially close to $S_r^{\sqrt{\varepsilon}}$. Returning to the coordinates of (7.16), the above implies that (x_2, y_2, z_2) is $\mathcal{O}(\sqrt{\varepsilon})$ close to CM. Thus the trajectory follows the layer dynamics and reaches Σ_3 in $\mathcal{O}(-\ln\varepsilon)$ time (see Theorem 3.1 of [66]). It remains to prove that (7.60) holds for most trajectories.

Suppose that $p \in J_+$ such that

$$|(u_2, v_2)| < K\sqrt{\varepsilon}, \qquad \text{for all } y_{2,B} + d(\varepsilon). \tag{7.61}$$

Then to leading order, the flow about $\Pi_1(p)$ from Σ_2 to the section defined by $y_2 = y_{2,B} + d(\varepsilon)$ is an expansion with an expansion rate given by

$$\exp\left(\sqrt{\varepsilon}I_{\Lambda_1}(y_{2,0}, y_{2,*} + d(\varepsilon))\right). \tag{7.62}$$

We can show that the maximal contraction rate of Π_1 is smaller that the contraction rate (7.62); see Lemma 5.4 of [66]. Thus the transition from J_+ to the section defined by $y_2 = y_{2,*} + d(\varepsilon)$ exponentially expands the distance between p and any other point $q \in J_+$. It follows that q can only satisfy (7.61) if it is exponentially close to p, i.e. (7.60) must be satisfied for all points which are not exponentially close to p. Thus the result holds for all points in J_+, possibly with the exception of an exponentially small interval.

Now suppose that $y_{2,B} > \sqrt{\alpha_2 + 1}$ where CM_r is real (hyperbolic). Consider a solution (u_2, v_2) of (7.32), with an initial condition that is not exponentially close to the weak canard. By Theorem 7.3 (see also Propositions 7.15 and 7.17), the invariant manifolds $\mathcal{S}_a^{\sqrt{\varepsilon}}$ and $\mathcal{S}_r^{\sqrt{\varepsilon}}$

136

intersect transversally for most $\alpha_2 \in A$, and hence the angle between them is bounded below by some positive constant. It follows that $(u_2(\tau_H), v_2(\tau_H))$ has a large component in the strongly expanding direction, where $y_2(\tau_H) \in H$. By linearising (7.32) along CM, we can measure the evolution of the strongly expanding component. Continuing the solution down the hyperbola H to $y_2 = \sqrt{\alpha_2}$ on the real y_2-axis, the strongly expanding component shrinks by the factor

$$\exp\left(\sqrt{\varepsilon} I_{\Lambda_1}(y_{2,0}, \sqrt{\alpha_2})\right).$$

Continuing the solution along the real y_2-axis results in the expansion of the strong unstable direction up to $\mathcal{O}(1)$ when y_2 reaches a neighbourhood of the point $y_{2,*}$. □

7.7 Cases 2 to 4

In this section we restate the theorems on the existence of canards (Theorems 7.1–7.3) in full to cover all cases, and add new theorems to address the existence of faux canards for Cases 2 and 3. We also expand the minimal delay (Theorem 7.4) and buffer point results (Definition 7.1 and Lemma 7.1) to include all cases.

Theorem 7.6. *(Existence of canards) Let* $0 < \alpha_2 < 1$ *and* $\tilde{\Sigma}_* : y_2 = \tilde{y}_{2,*}$*, for some* $\tilde{y}_{2,*} \approx y_{2,*}$*. Then,*

i) *For Case 1, and* $|y_{2,0}| > \sqrt{\alpha_2 + 1}$ *chosen to define* $\Sigma_2^{\pm}$ *such that*

$$I_{\Lambda_1}(y_{2,*}, y_{2,0}) = 0,$$

with $|y_{2,*}| \in (\delta, \sqrt{\alpha_2})$*, there exists a canard solution* $\mathcal{O}(\sqrt{\varepsilon})$ *away from* CM*, connecting* $S_a^{\sqrt{\varepsilon}} \cap \tilde{\Sigma}_*$ *to* $S_r^{\sqrt{\varepsilon}} \cap \Sigma_2^{\pm}$*, and continuing to a point in* $S_r^{\varepsilon} \cap \Sigma_1$*.*

ii) *For Case 4, and* $|y_{2,0}| > \sqrt{\alpha_2 + 1}$ *chosen to define* $\Sigma_2^{\pm}$ *such that*

$$I_{\Lambda_2}(y_{2,0}, y_{2,*}) = 0,$$

with $|y_{2,*}| \in (\delta, \sqrt{\alpha_2})$*, there exists a canard solution originating in* $S_a^{\varepsilon} \cap \Sigma_1$*, passing through* $S_a^{\sqrt{\varepsilon}} \cap \Sigma_2^{\pm}$ *an* $\mathcal{O}(\sqrt{\varepsilon})$ *distance away from* CM*, and connecting to* $S_r^{\sqrt{\varepsilon}} \cap \tilde{\Sigma}_*$*.*

Proof. The proof for Case 4 is the same as Case 1, only constructed in forward time; see Section 7.6.1 for details. □

Theorem 7.7. *(Existence of faux canards) Let* $0 < \alpha_2 < 1$ *and* $\tilde{\Sigma}_* : y_2 = \tilde{y}_{2,*}$*, for some* $\tilde{y}_{2,*} \approx y_{2,*}$*. Then,*

i) *For Case 2, and* $|y_{2,0}| > \sqrt{\alpha_2 + 1}$ *chosen to define* $\Sigma_2^{\pm}$ *such that*

$$I_{\Lambda_2}(y_{2,0}, y_{2,*}) = 0,$$

with $|y_{2,*}| \in (\delta, \sqrt{\alpha_2})$*, there exists a faux canard solution originating in* $S_r^{\varepsilon} \cap \Sigma_1$*, passing through* $S_r^{\sqrt{\varepsilon}} \cap \Sigma_2^{\pm}$ *an* $\mathcal{O}(\sqrt{\varepsilon})$ *distance away from* CM*, and connecting to* $S_a^{\sqrt{\varepsilon}} \cap \tilde{\Sigma}_*$*.*

137

ii) For Case 3, and $|y_{2,0}| > \sqrt{\alpha_2 + 1}$ chosen to define $\Sigma_2^{\pm}$ such that

$$I_{\Lambda_1}(y_{2,*}, y_{2,0}) = 0,$$

with $|y_{2,*}| \in (\delta, \sqrt{\alpha_2})$, there exists a faux canard solution $\mathcal{O}(\sqrt{\varepsilon})$ away from CM, connecting $S_r^{\sqrt{\varepsilon}} \cap \tilde{\Sigma}_*$ to $S_a^{\sqrt{\varepsilon}} \cap \Sigma_2^{\pm}$, and continuing to a point in $S_a^{\varepsilon} \cap \Sigma_1$.

Proof. For Case 2, the proof is the same as Theorem 7.6(ii). On the other hand, the proof of Case 3 is the same as Theorem 7.6(i). See Section 7.6.1 for more details □

Theorem 7.8. *(Existence of canards: Elliptic case) Let $\alpha_2 > 1$.*

i) For Case 1, and $|y_{2,0}| > \sqrt{\alpha_2 + 1}$ chosen to define $\Sigma_2^{\pm}$ such that

$$I_{\Lambda_2}(y_{2,*}, y_{2,0}) = 0,$$

with $|y_{2,*}| \in (\sqrt{\alpha_2 - 1}, \sqrt{\alpha_2})$, the results of Theorem 7.6(i) hold.

ii) For Case 1, and $|y_{2,0}| \in (\delta, \sqrt{\alpha_2 - 1})$ chosen to define $\Sigma_2^{\pm}$ such that

$$I_{\Lambda_1}(y_{2,0}, y_{2,*}) = 0,$$

with $|y_{2,*}| \in (\sqrt{\alpha_2}, \sqrt{\alpha_2 + 1})$, the results of Theorem 7.6(ii) hold.

iii) For Case 4, and $|y_{2,0}| > \sqrt{\alpha_2 + 1}$ chosen to define $\Sigma_2^{\pm}$ such that

$$I_{\Lambda_1}(y_{2,0}, y_{2,*}) = 0,$$

with $|y_{2,*}| \in (\sqrt{\alpha_2 - 1}, \sqrt{\alpha_2})$, the results of Theorem 7.6(ii) hold.

iv) For Case 4, and $|y_{2,0}| \in (\delta, \sqrt{\alpha_2 - 1})$ chosen to define $\Sigma_2^{\pm}$ such that

$$I_{\Lambda_2}(y_{2,*}, y_{2,0}) = 0,$$

with $|y_{2,*}| \in (\sqrt{\alpha_2}, \sqrt{\alpha_2 + 1})$, the results of Theorem 7.6(i) hold.

Proof. The proof is the same as in Theorem 7.6; see Section 7.6.2. □

Theorem 7.9. *(Existence of faux canards: Elliptic case) Let $\alpha_2 > 1$.*

i) For Case 2, and $|y_{2,0}| > \sqrt{\alpha_2 + 1}$ chosen to define $\Sigma_2^{\pm}$ such that

$$I_{\Lambda_2}(y_{2,0}, y_{2,*}) = 0,$$

with $|y_{2,*}| \in (\sqrt{\alpha_2 - 1}, \sqrt{\alpha_2})$, the results of Theorem 7.7(i) hold.

ii) For Case 2, and $|y_{2,0}| \in (\delta, \sqrt{\alpha_2 - 1})$ chosen to define $\Sigma_2^{\pm}$ such that

$$I_{\Lambda_1}(y_{2,*}, y_{2,0}) = 0,$$

with $|y_{2,*}| \in (\sqrt{\alpha_2}, \sqrt{\alpha_2 + 1})$, the results of Theorem 7.7(ii) hold.

iii) For Case 3, and $|y_{2,0}| > \sqrt{\alpha_2 + 1}$ chosen to define $\Sigma_2^{\pm}$ such that

$$I_{\Lambda_1}(y_{2,*}, y_{2,0}) = 0,$$

with $|y_{2,*}| \in (\sqrt{\alpha_2 - 1}, \sqrt{\alpha_2})$, the results of Theorem 7.7(ii) hold.

iv) For Case 3, and $|y_{2,0}| \in (\delta, \sqrt{\alpha_2 - 1})$ chosen to define $\Sigma_2^{\pm}$ such that

$$I_{\Lambda_2}(y_{2,0}, y_{2,*}) = 0,$$

with $|y_{2,*}| \in (\sqrt{\alpha_2}, \sqrt{\alpha_2 + 1})$, the results of Theorem 7.7(i) hold.

Proof. The proof is the same as in Theorem 7.6; see Section 7.6.2. $\qquad\square$

Theorem 7.10. *(Existence of canards: Hyperbolic case) Let $\alpha_2 > 1$ and $\Sigma_* : y_2 = y_{2,*}$. For most $\alpha_2 \in A$ (an open set of almost full measure), there exists a canard solution, uniformly $\mathcal{O}(\sqrt{\varepsilon})$ close to CM, that*

i) for Case 1, and $|y_{2,0}| \in (\delta, \sqrt{\alpha_2 - 1})$ chosen to define $\Sigma_2^{\pm}$ such that

$$I_{\Lambda_1}(|y_{2,0}|, \sqrt{\alpha_2 + 1}) + I_{\Lambda_2}(\sqrt{\alpha_2 + 1}, |y_{2,*}|) = 0,$$

where $y_{2,*} > \sqrt{\alpha_2 + 1}$, connects $S_a^{\sqrt{\varepsilon}} \cap \Sigma_2^{+}$ to $S_r^{\sqrt{\varepsilon}} \cap \Sigma_*$.

ii) for Case 4, and $|y_{2,0}| > \sqrt{\alpha_2 + 1}$ chosen to define $\Sigma_2^{\pm}$ such that

$$I_{\Lambda_1}(|y_{2,0}|, \sqrt{\alpha_2 + 1}) + I_{\Lambda_2}(\sqrt{\alpha_2 + 1}, |y_{2,*}|) = 0,$$

where $|y_{2,*}| \in (\delta, \sqrt{\alpha_2 - 1})$, connects $S_a^{\sqrt{\varepsilon}} \cap \Sigma_2^{\pm}$ to $S_r^{\sqrt{\varepsilon}} \cap \Sigma_*$.

Proof. The proof for Case 4 is the same as Case 1. See Section 7.6.2 for further details. $\quad\square$

Theorem 7.11. *(Existence of faux canards: Hyperbolic case) Let $\alpha_2 > 1$ and $\Sigma_* : y_2 = y_{2,*}$. For most $\alpha_2 \in A$ (an open set of almost full measure), there exists a faux canard solution, uniformly $\mathcal{O}(\sqrt{\varepsilon})$ close to CM, that*

i) for Case 2, and $|y_{2,0}| > \sqrt{\alpha_2 + 1}$ chosen to define $\Sigma_2^{\pm}$ such that

$$I_{\Lambda_2}(|y_{2,0}|, \sqrt{\alpha_2 + 1}) + I_{\Lambda_1}(\sqrt{\alpha_2 + 1}, |y_{2,*}|) = 0,$$

where $|y_{2,*}| \in (\delta, \sqrt{\alpha_2 - 1})$, connects $S_r^{\sqrt{\varepsilon}} \cap \Sigma_2^{\pm}$ to $S_a^{\sqrt{\varepsilon}} \cap \Sigma_*$.

ii) for Case 3, and $|y_{2,0}| \in (\delta, \sqrt{\alpha_2 - 1})$ chosen to define $\Sigma_2^{\pm}$ such that

$$I_{\Lambda_2}(|y_{2,0}|, \sqrt{\alpha_2 + 1}) + I_{\Lambda_1}(\sqrt{\alpha_2 + 1}, |y_{2,*}|) = 0,$$

where $y_{2,*} > \sqrt{\alpha_2 + 1}$, connects $S_r^{\sqrt{\varepsilon}} \cap \Sigma_2^{\pm}$ to $S_a^{\sqrt{\varepsilon}} \cap \Sigma_*$.

Proof. The proof is the same as in Theorem 7.10; see Section 7.6.2. $\qquad\square$

Theorem 7.12. *(Minimal delay estimates) Let $\alpha_2 > 0$ and consider a trajectory of (7.24) with initial condition $(x_2, y_2, z_2)(0)$ that is $\mathcal{O}(\sqrt{\varepsilon})$ close to CM. We have the following results:*

i) *For Case 1, let $y_2(0) = y_{in}$. Let $y_{out}(y_{in})$ be defined by $I_{\Lambda_1}(y_{in}, y_{out}) = 0$, and let $y_{2,0} = y_{out}$ define $\Sigma_2^{\pm}$. Then the trajectory (x_2, y_2, z_2) stays $\mathcal{O}(\sqrt{\varepsilon})$ close to CM for all $y_{in} \leq y_2 \leq y_{out} + o(1)$.*

ii) *For Case 4, let $y_2(0) = y_{in}$, and let $y_{2,0} = y_{in}$ define $\Sigma_2^{\pm}$. Let $y_{out}(y_{in})$ be defined by $I_{\Lambda_1}(y_{in}, y_{out}) = 0$. Then the trajectory (x_2, y_2, z_2) stays $\mathcal{O}(\sqrt{\varepsilon})$ close to CM for all $y_{in} \leq y_2 \leq y_{out} + o(1)$.*

Proof. The proof for Case 4 is the same as Case 1, only it is constructed in forward time. See Section 7.6.3 for more details. $\qquad\square$

Definition 7.4. (Buffer points) Let $\alpha_2 > 0$.

i) For Case 1 and $\alpha_2 < 1$, the buffer point $y_{2,B}$ is

$$|y_{2,B}| := \lim_{|y_{in}| \to b} y_{out}(y_{in}),$$

for some $b > 0$, where $y_{out}(y_{in})$ is defined in (7.29). The canard buffer point $y_{2,C}$ is

$$|y_{2,C}| := \lim_{|y_{in}| \to c} y_{out}(y_{in}),$$

where $0 < b < c$, and $y_{out}(y_{in})$ is defined in (7.30). For $\alpha_2 > 1$, the definition of the buffer points is the same, except b and c are replaced with $\tilde{b}$ and $\tilde{c}$.

ii) For Case 4, the buffer point $y_{2,B}$ is

$$|y_{2,B}| := \lim_{|y_{in}| \to \infty} y_{out}(y_{in}),$$

where $y_{out}(y_{in})$ is defined in (7.29). The canard buffer point $y_{2,B}$ is

$$|y_{2,B}| := \lim_{|y_{in}| \to \infty} y_{out}(y_{in}),$$

where $y_{out}(y_{in})$ is defined in (7.30).

Lemma 7.4. *For Case 1, $|y_{2,B}| = |y_{2,C}| = \infty$. For Case 4 and $\alpha_2 < 1$, $|y_{2,B}| = |y_{2,C}| = c > 0$. For Case 4 and $\alpha > 1$, we have the result $|y_{2,B}| = \bar{b}$, $|y_{2,C}| = \tilde{c}$, where $0 < \tilde{c} < \bar{b}$.*

Proof. The results for Case 1 have already been proven; see Lemma 7.1. For Case 4, notice that the eigenvalues are the same as in Case 1, only they have been reflected across the y_2-axis (and Λ_1 and Λ_2 are interchanged); compare Figures 7.15 and 7.16. This structure gives the result $|y_{2,B}| = |y_{2,C}| = c$ for $\alpha_2 < 1$, and $|y_{2,C}| = \tilde{c}$ for $\alpha_2 > 1$. $\qquad\square$

Remark 7.9. The difference in buffer points across the different cases arises because of the positioning of CM_a relative to the pole. For Case 1, CM_a lies in the interval $|y_2| < \sqrt{\alpha_2}$. Note that trajectories with $y_{in} \in (0, b)$, or $y_{in} \in (0, \tilde{b})$ for $\alpha_2 > 1$, will still reach infinity. For Case 4, CM_a stretches to infinity on either side of the pole. Case 4 is similar to the FSN II in that the pole lies in the repelling region of CM, and it acts as a strict upper bound on the maximal delay.

7.8 Discussion

Generic folded singularities occur in singularly perturbed systems with at least two slow variables. When viewed as equilibria of the reduced flow, they are naturally classified as saddles, nodes or foci. Folded nodes and saddles are special structures that generate canards, trajectories that follow a repelling invariant manifold for $\mathcal{O}(1)$ times, which leads to complex behaviour. The dynamics near a folded node and saddle has been studied in depth for eigenvalue ratios μ bounded away from zero. Two types of co-dimension one bifurcations involving folded singularities, folded-saddle node (FSN) type I and II, have already been analysed in detail. Canard theory has been extended to the FSN II case for various regimes: $\mu = \mathcal{O}(\varepsilon)$ [45], $\mu = \mathcal{O}(\sqrt{\varepsilon})$ [66], as well as the transition between the two regimes [25, 31]. Similar theory has been established for the FSN I in the $\mu = \mathcal{O}(\varepsilon^k)$, $k \geq 1/4$ regime [108].

The final type of folded saddle-node bifurcation, the FSN III, was first discovered in a study [87] of the Butera model, a coupled two-neuron model. While the bifurcation was originally identified in a system where averaging was applied near family of periodic orbits of the layer problem, we proposed a canonical model of the bifurcation in an equilibrium manifold setting. In a similar manner to past work [66, 108], we utilised techniques from GSPT (the blow-up) and dynamic bifurcation theory (complex time path analysis) to analyse the dynamics in an $\alpha = \mathcal{O}(\sqrt{\varepsilon})$ neighbourhood of the FSN III singularity. We proved the existence of $\mathcal{O}(\sqrt{\varepsilon})$ canards and faux canards as intersections of stable and unstable invariant manifolds. These canards solutions rotate about the primary weak canard in the folded node case, or the primary faux canard in the folded saddle case.

In addition to the proving the existence of canards, we also analysed the growth and decay properties of both generic solutions and canards. We defined a way-in/way-out function to measure the delayed loss of stability, a phenomenon characteristic of dynamic Hopf bifurcations, experienced by trajectories passing through the FSN III singularity. We found that differences in the structure of the rescaling charts of the various FSN bifurcations impacted the maximal delay estimates. In the FSN II case, there is an ordinary singularity which creates a pole along the repelling manifold CM_r in the complexified system. Trajectories cannot pass the pole, and hence there is a strict upper bound on the delay. On the other hand, there is no pole in the FSN I case, and trajectories may traverse the entire length of CM_r. Like the FSN II, the FSN III has a pole which trajectories cannot cross, but it lies along the symmetry axis. Depending on parameter values, the pole may be situated in the middle of the attracting manifold CM_a with disjoint segments of CM_r on either side (Cases 1), or vice versa (Cases 4). For Case 1, both generic trajectories and canards can trace the entire length of (a disjoint segment of) CM_r, which stretches off to infinity. This infinite delay seems counter-intuitive since trajectories only trace a finite distance along CM_a, but this arises naturally from the pole's effect on the way-in/way-out function. For Case 4, trajectories can only trace CM_r a finite distance before they are repelled. Using Hamiltonian properties of the complexified system, we proved that in both cases, trajectories must stay out of a small neighbourhood of the pole.

Our analysis of the FSN III has left some open questions. With the exception of the Butera model, we are not aware of any other model which possess a FSN III bifurcation. Such a model would need to satisfy symmetry conditions (at least locally), like the Butera

141

model. We presented a brief numerical study of the canonical model coupled with a reset mechanism (inspired by classic integrate-and-fire neural models), and illustrated the existence of MMOs for the folded node case. However, it remains to find more 'applicable' examples of the FSN III. A recent study of the folded saddle singularity by Mitry *et al.* [76, 78] uncovered a myriad of different faux canard solutions, with distinct behaviour and rotational properties. In particular, the folded saddle has secondary faux canards of type α and β, as well as switching solutions where trajectories switch between the faux and true canard. While we proved the existence of the primary faux canard (and hence a family of secondary faux canards) for the FSN III, it remains to formally establish the existence of the various types of secondary faux canards. Such faux canards could yield interesting behaviour for Cases 2 and 3 of the FSN III.

7.9 Appendix

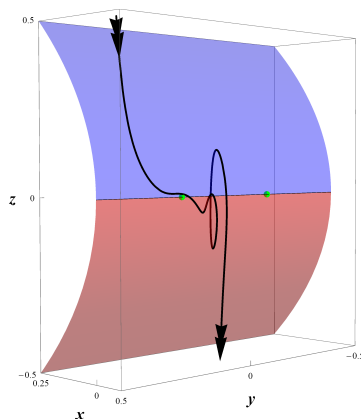## A Additional plots of the integrate-and-fire model

Figure 7.11: A canard solution of (7.1) for $\alpha = 1/30$ and $\varepsilon = 0.025$, Case 4 (cf. Figure 7.2). The attracting and repelling sheets of the critical manifold are shown in blue and red. The fold $\mathcal{L}$ is simply the y-axis. The green dots mark the folded node singularities of the reduced system (7.2).
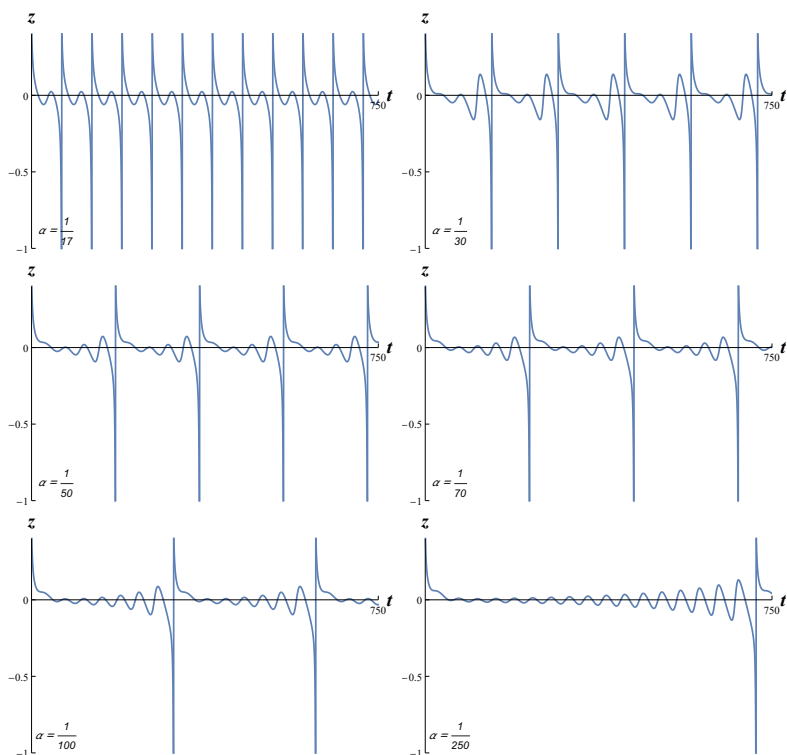

Figure 7.12: MMO solutions of (7.1), for Case 4 ($\delta_1 = \delta_2 = -1$), $\varepsilon = 0.025$ and various values of α, which are indicated on the respective plot. For all these plots $z_{th} = -1$, $x_{re} = 0.0125$, $y_{re} = 0.416$ and $z_{re} = 0.5$. Compare with Figure 7.3 which shows similar patterns for Case 1.
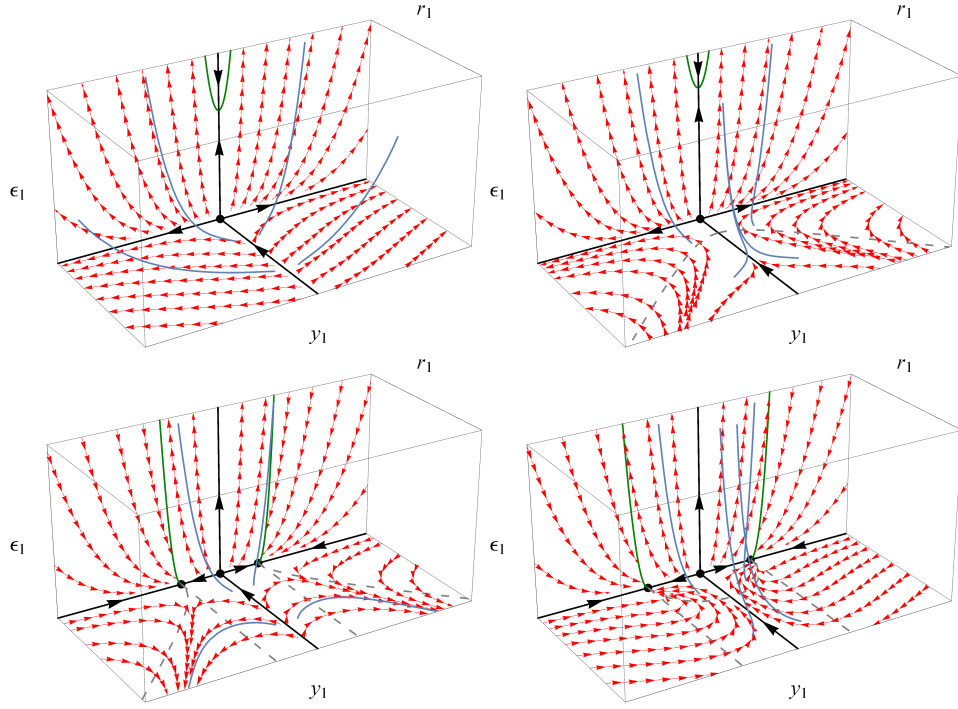
Figure 7.13: Dynamics of system (7.11), i.e. the flow on the attracting centre manifold $M_{a,1}$, for *A:* Case 1, *B:* Case 2, *C:* Case 3, *D:* Case 4. In all Cases, $\alpha_2 = 0.5$. The stream plots in the $r_1 = 0$ and $\varepsilon_1 = 0$ invariant planes are shown in red, and their equilibria are indicated by black dots, with the solid black lines being the eigendirections of the respective equilibria. Nullclines are shown in dashed grey and branches of equilibria in solid dark green. Finally, trajectories of (7.11) with non-zero $\varepsilon = r^4 \varepsilon_1$ are shown in blue.

B Flow on the attracting manifold $M_{a,1}$ in chart κ_1

We summarise the dynamics of systems (7.12) and (7.13) for the various cases. For Case 2, we have the following results:

- In the $r_1 = 0$ plane, there is an unstable node at the origin and branches of equilibria $(\bar{y}_1, \bar{\varepsilon}_1) = (\pm\sqrt{\alpha\sqrt{\varepsilon_1} - 1}, \varepsilon_1)$, originating at $(0, 1/\alpha^2)$.

- In the $\varepsilon_1 = 0$ plane, there is a saddle equilibrium at the origin, and the strong eigendirection of the saddle corresponds to γ_s of the FSN III singularity.

- In the $\varepsilon_1 = 0$ plane, there is a parabolic nullcline $r_1^2 = y_1^2/4 + 1/4$, originating at $(r_1, y_1) = (1/2, 0)$.

Note that the only difference between Case 1 and 2 is that the later, in the $\varepsilon_1 = 0$ plane, has the additional parabolic nullcline. However, the local dynamics near the origin ($r_1 < 1/2$) are the same. For Cases 3 and 4 we have the following results:

- In the $r_1 = 0$ plane, there is an unstable node at the origin and two disjoint parabolic branches of equilibria $(\bar{y}_1, \bar{\varepsilon}_1) = (\pm\sqrt{\alpha\sqrt{\varepsilon_1} + 1}, \varepsilon_1)$, originating at $(\pm 1, 0)$.

- In the $\varepsilon_1 = 0$ plane, there is a saddle equilibrium at the origin, and the strong eigendirection corresponds to γ_s of the FSN III singularity.

- In the $\varepsilon_1 = 0$ plane, there are two saddle-nodes $(\bar{r}_1, \bar{y}_1) = (0, \pm 1)$, with attracting centre manifolds $W_\pm^C$ given by

$$y_1 = \pm 1 \pm 2\delta_2 r_1^2 + \mathcal{O}(r_1^4). \tag{7.63}$$

The centre manifolds $W_\pm^C$ correspond to the centre eigendirections W^C of the FSN III singularity. The blow-up has effectively split the strong and centre eigendirections.

For both Cases 3 and 4, in the $\varepsilon_1 = 0$ plane, we also find the nullcline

$$y_1^2 - 4\delta_2 r_1^2 = 1.$$

For Case 3, the nullcline comprises of two disjoint, parabolic branches originating at $(r_1, y_1) = (0, \pm 1)$. In Case 4 the nullcline is a half-ellipse, centred at the origin, with semi-major axis $y_1 = 1$, and semi-minor axis $r_1 = 1/2$. Thus the local dynamics near the origin is consistent across all four cases for $4r_1^2 + y_1^2 \leq 1$.

The dynamics on $M_{a,1}$ for Cases 2–4 (and Case 1 for comparison) is shown in Figure 7.13.

C Transition times from chart κ_1 to κ_2

Recall that linearisation of (7.11) about the origin yielded system (7.14), which was independent of $\delta_{1,2}$. Thus the transition time $T_s = \ln(\mathcal{O}(\varepsilon^{-1/4}))$ for $\Sigma_1 \cap M_{a,1} \to \Sigma_2$ is valid for all cases.

For Case 4, we can estimate the transition time $\Sigma_1 \to \Sigma_2$ by linearising (7.13) about the saddle-nodes at $y_1 = \pm 1$. The leading order flow on the centre manifold (7.63) is given by

$$r_1' = 4\delta_2 r_1^3 + \mathcal{O}(r_1^5),$$
$$\Rightarrow r_1^2(t) = -\frac{1}{2(4\delta_2 t + \beta)},$$

where $\delta_2 = -1$ and $\beta = -1/(2\tilde{r}_1^2)$. Hence the transition time T_c, for $\Sigma_1 \to \Sigma_2$, is given by

$$T_c = \mathcal{O}(\varepsilon^{-1/2}).$$

Given an initial condition $\mathcal{O}(1)$ away from the centre eigendirection in Σ_1 (but not $\mathcal{O}(\varepsilon^{1/4})$ close to γ_s), then Π_1 maps the initial point to an $\mathcal{O}(\sqrt{\varepsilon})$ neighbourhood of the centre eigendirection in Σ_2.

Note that we only calculate the transition time T_c for Case 4. In Case 3, the centre manifold obtained by linearising about the saddle-nodes exists for $|y_1| > 1$. Any trajectory starting outside of a $\mathcal{O}(\varepsilon^{1/4})$ neighbourhood of γ_s will eventually reach $W_\pm^C$ and flow away from the origin, with r_1 increasing. In general, the trajectory will never reach Σ_2.
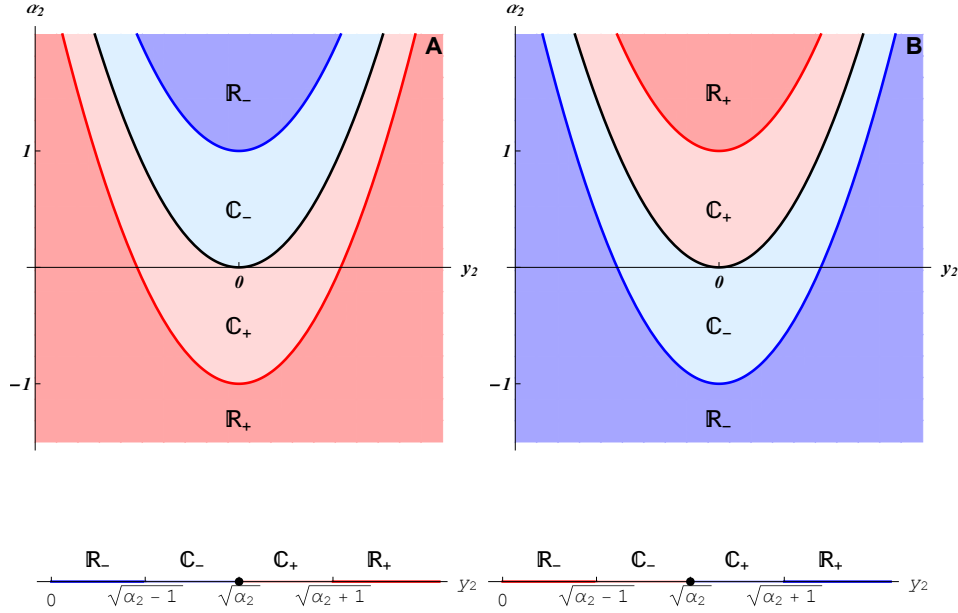
Figure 7.14: Eigenvalue structure of (7.17) along CM for A: $\delta_1 = 1$ (Cases 1 and 2), and B: $\delta_1 = -1$ (Cases 3 and 4). The top row shows the stability in the (y_2, α_2)-plane. The type and sign of the real part of the eigenvalues in various regions are indicated on the figure. Blue (red) regions are (un)stable, while the light (dark) shading indicates a real (complex) eigenvalue structure. The solid black line is the curve $y_2^2 = \alpha_2$. The bottom row shows the stability along the positive y_2-axis, for a fixed value of $\alpha_2 > 1$.

D   Structure of CM for Cases 2–4

The structure and stability properties of CM for Cases 1 and 2 are the same. However, for Cases 3 and 4 we see a switch in stability. Figure 7.14 shows a comparison of the stability properties of CM for all cases. Furthermore, CM connects to the pair of saddle-nodes identified in chart κ_1, for Cases 3 and 4.

Lemma 7.5. *For Cases 3 and 4, CM emanates from the pair of saddle-nodes $y_1 = \pm 1$ on $M_{a,1}$ (in the $\varepsilon_1 = 0$ invariant plane) in chart κ_1 and approaches them tangent to the y_1-axis.*

Proof. Recalling that $r_2 = \varepsilon^{1/4} = 0$ in κ_2, we apply the change of coordinates κ_{12}, which gives

$$\kappa_{12}(CM): \quad (r_1, y_1, z_1, \varepsilon_1) = \left(0, \frac{y_2}{(\tilde{\gamma}^2)^{1/4}}, \frac{\delta_1 \tilde{\gamma}}{(\tilde{\gamma}^2)^{1/2}}, \frac{1}{\tilde{\gamma}^2}\right), \tag{7.64}$$

where $\tilde{\gamma} = \alpha_2 - y_2^2$. If we restrict $\kappa_{12}(CM)$ to $M_{a,1}$, then $z_1 = -1$ and thus for $\delta_1 = -1$, we have $\tilde{\gamma} < 0$. Recall that the branch of equilibria in κ_1 is defined by $(\bar{y}_1, \bar{\varepsilon}_1) = \left(\pm\sqrt{\alpha_2\sqrt{\varepsilon_1} - 1}, \varepsilon_1\right)$. A simple calculation involving the y_1 and ε_1 components of (7.64)

146

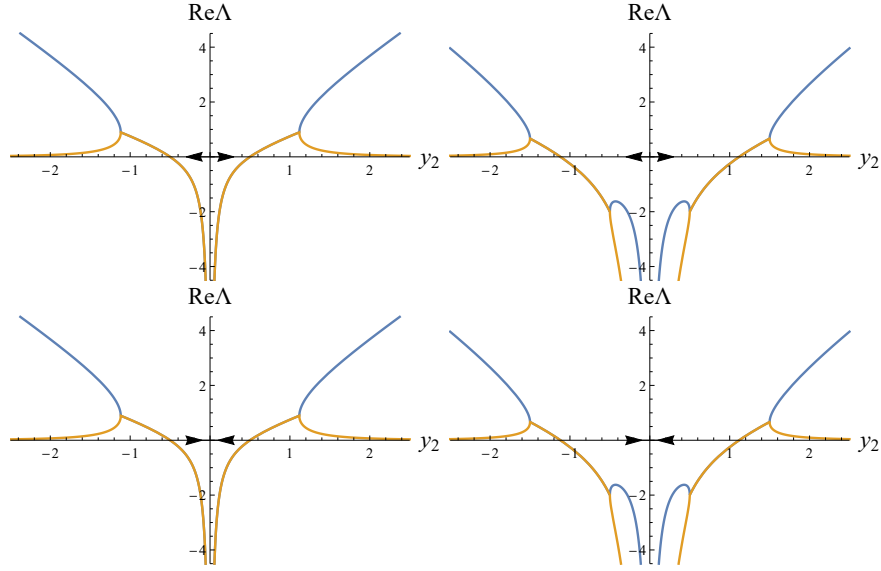**Figure 7.15:** Real part of the eigenvalues $\Lambda_{1,2}$ of (7.26), for Cases 1 and 2, where the blue and orange curves indicate Λ_1 and Λ_2, respectively. The arrows on the y_2-axis indicate the direction of the reduced flow along CM. *Top row:* Case 1, $\alpha_2 = 0.25$ (left) and $\alpha_2 = 1.25$ (right). Note that for $y_2 < 0$, the eigenvalues have been reflected in the y_2-axis to preserve the orientation of trajectories in (7.24). *Bottom row:* Case 2, $\alpha_2 = 0.25$ (left) and $\alpha_2 = 1.25$ (right). For $y_2 > 0$, the eigenvalues have been reflected in the y_2-axis.

gives

$$
\begin{aligned}
\alpha_2\sqrt{\varepsilon_1} - \delta_1 &= \frac{\alpha_2 + sgn(\tilde{\gamma})\tilde{\gamma}}{(\tilde{\gamma}^2)^{1/2}}, \\
&= \frac{y_2^2}{(\tilde{\gamma}^2)^{1/2}}, \\
&= y_1^2,
\end{aligned}
$$

which shows that CM lies on the branch of equilibria. Furthermore,

$$
\lim_{y_2 \to \pm\infty} \kappa_{12}(CM): \quad (r_1, y_1, z_1, \varepsilon_1) = (0, \pm 1, 0, 0),
$$

i.e. CM originates from the pair of saddle-nodes in κ_1. The tangent vectors at the saddles-nodes are

$$
\lim_{y_2 \to \pm\infty} \frac{\frac{d}{dy_2}\kappa_{12}(CM)}{||\kappa_{12}(CM)||} = (0, -1, 0, 0),
$$

and hence CM approaches tangent to the y_1-axis. $\qquad\square$

Closely related to CM are the eigenvalues $\Lambda_{1,2}$ of system (7.26), where y_2 is treated as 'slow time'. The structure of $\Lambda_{1,2}$ is very important as its integral (7.27) forms the way-in/way-out function. Figures 7.15 and 7.16 shows a comparison of the real part of Λ_1 and Λ_2 for all four cases.
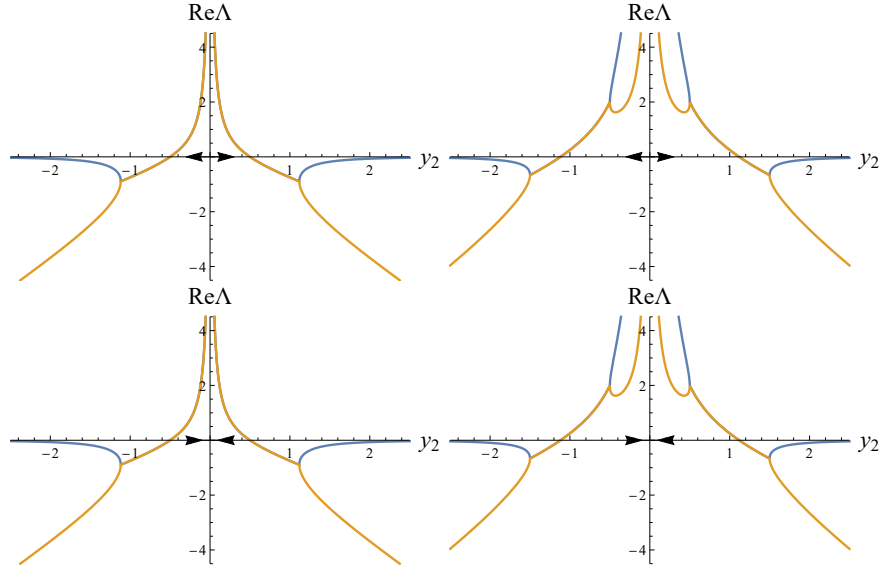
147

Figure 7.16: Real part of the eigenvalues $\Lambda_{1,2}$ of (7.26), for Cases 3 and 4, where the blue and orange curves indicate Λ_1 and Λ_2, respectively. The arrows on the y_2-axis indicate the direction of the reduced flow along CM. *Top row:* Case 3, $\alpha_2 = 0.25$ (left) and $\alpha_2 = 1.25$ (right). Note that for $y_2 < 0$, the eigenvalues have been reflected in the y_2-axis to preserve the orientation of trajectories in (7.24). *Bottom row:* Case 4, $\alpha_2 = 0.25$ (left) and $\alpha_2 = 1.25$ (right). For $y_2 > 0$, the eigenvalues have been reflected in the y_2-axis.

E   Proof of Proposition 7.5

Proof. We can rewrite (7.23), grouping together all the $\mathcal{O}(\sqrt{\varepsilon}(1+y_2^2+\ldots))$ terms in $\dot{x}_2$ and $\dot{z}_2$:

$$
\begin{aligned}
\dot{x}_2 &= -z_2 + \sqrt{\varepsilon}N_1(y_2) + \mathcal{O}(\sqrt{\varepsilon}(x_2 + z_2)), \\
\dot{y}_2 &= \sqrt{\varepsilon}\delta_2 y_2(1 + \mathcal{O}(\sqrt{\varepsilon})), \\
\dot{z}_2 &= x_2 - 2\delta_1 z_2 \gamma - z_2^2 + \sqrt{\varepsilon}N_2(y_2) + \mathcal{O}(\sqrt{\varepsilon}(z_2), \varepsilon(1+x_2+z_2+y_2^2)),
\end{aligned}
\tag{7.65}
$$

where $N_{1,2}(y_2) = \mathcal{O}(1 + y_2^2 + \ldots)$. We transform the system in three steps. First, let $\tilde{z}_2 = z_2 - \sqrt{\varepsilon}N_1(y_2)$. Applying this transformation yields the system

$$
\begin{aligned}
\dot{x}_2 &= -\tilde{z}_2 + \mathcal{O}(\sqrt{\varepsilon}(x_2 + \tilde{z}_2), \varepsilon(1 + y_2^2)), \\
\dot{y}_2 &= \sqrt{\varepsilon}\delta_2 y_2(1 + \mathcal{O}(\sqrt{\varepsilon})), \\
\dot{\tilde{z}}_2 &= x_2 - 2\delta_1 \tilde{z}_2 \gamma - \tilde{z}_2^2 + \sqrt{\varepsilon}\tilde{N}_2(y_2) + \mathcal{O}(\sqrt{\varepsilon}(\tilde{z}_2), \varepsilon(1 + x_2 + \tilde{z}_2 + y_2^2)),
\end{aligned}
$$

where $\tilde{N}_2(y_2) = \mathcal{O}(1+y_2^2+\ldots)$. Next, applying the transformation $\tilde{x}_2 = x_2 + \sqrt{\varepsilon}\tilde{N}_2(y_2)$, and dropping the tildes, gives

$$
\begin{aligned}
\dot{x}_2 &= -z_2 + \mathcal{O}(\sqrt{\varepsilon}(x_2 + z_2), \varepsilon), \\
\dot{y}_2 &= \sqrt{\varepsilon}\delta_2 y_2(1 + \mathcal{O}(\sqrt{\varepsilon})), \\
\dot{z}_2 &= x_2 - 2\delta_1 z_2 \gamma - z_2^2 + \mathcal{O}(\sqrt{\varepsilon}(z_2), \varepsilon).
\end{aligned}
$$

Lastly, setting $\Phi := (1+\mathcal{O}(\sqrt{\varepsilon}))^{-1} = 1+\mathcal{O}(\sqrt{\varepsilon})$ and rescaling time by Φ yields the result. $\square$

148

F   Proof of Proposition 7.6 and 7.7

Proof. To determine the direction of the flow of (7.41) along the axes, we must first derive expressions for the real and imaginary parts of Λ_1. From the definition of Λ_1 (7.33), we have that

$$
\begin{aligned}
\mathrm{Re}\Lambda_1 &= \frac{\delta_2 a}{a^2+b^2}\left[\delta_1(a^2-b^2-\alpha_2)+\left|\sqrt{1-\gamma^2}\right|\sin\left(Arg\sqrt{1-\gamma^2}\right)\right]\\
&\quad+\frac{\delta_2 b}{a^2+b^2}\left[2\delta_1 ab-\left|\sqrt{1-\gamma^2}\right|\cos\left(Arg\sqrt{1-\gamma^2}\right)\right],\\
\mathrm{Im}\Lambda_1 &= \frac{\delta_2 a}{a^2+b^2}\left[2\delta_1 ab-\left|\sqrt{1-\gamma^2}\right|\cos\left(Arg\sqrt{1-\gamma^2}\right)\right]\\
&\quad-\frac{\delta_2 b}{a^2+b^2}\left[\delta_1(a^2-b^2-\alpha_2)+\left|\sqrt{1-\gamma^2}\right|\sin\left(Arg\sqrt{1-\gamma^2}\right)\right].
\end{aligned}
\tag{7.66}
$$

Substituting $b=0$ into the above expressions, and carefully evaluating $Arg\sqrt{1-\gamma^2}$ along the various intervals of the a-axis, yields the desired results of Proposition 7.6. Likewise, substituting $a=0$ into (7.66) and evaluating $Arg\sqrt{1-\gamma^2}$ along the b-axis yields the results of Proposition 7.7. □

G   Proof of Proposition 7.8

Proof. From Appendix E in [66], we have

$$
\sqrt{1-\gamma^2} = \begin{cases} -i\delta_1\gamma\sqrt{1-\frac{1}{\gamma^2}}, & \mathrm{Im}(\delta_1\gamma) > 0,\\ i\delta_1\gamma\sqrt{1-\frac{1}{\gamma^2}}, & \mathrm{Im}(\delta_1\gamma) < 0, \end{cases}
\tag{7.67}
$$

where z has been replaced with $\delta_1\gamma = \delta_1(\alpha_2 - y_2^2)$. Using (7.67) and (7.25), we can rewrite $\Lambda_1 = \delta_2\lambda_1/y_2$,

$$
\Lambda_1 = \begin{cases} -\delta_1\delta_2\left(\frac{\alpha_2-y_2^2}{y_2}\right)\left(1+\sqrt{1-\frac{1}{(\alpha_2-y_2^2)^2}}\right), & \delta_1\mathrm{Re}(y_2)\mathrm{Im}(y_2) < 0,\\ -\delta_1\delta_2\left(\frac{\alpha_2-y_2^2}{y_2}\right)\left(1-\sqrt{1-\frac{1}{(\alpha_2-y_2^2)^2}}\right), & \delta_1\mathrm{Re}(y_2)\mathrm{Im}(y_2) > 0, \end{cases}
\tag{7.68}
$$

and expand for large $|y_2| \gg 1$,

$$
\Lambda_1 = \begin{cases} \delta_1\delta_2\left(2y_2 - \frac{2\alpha_2}{y_2} + \mathcal{O}\left(\frac{1}{y_2^3}\right)\right), & \delta_1\mathrm{Re}(y_2)\mathrm{Im}(y_2) < 0,\\ \delta_1\delta_2\left(\frac{1}{2y_2^3} + \frac{\alpha_2}{2y_2^5} + \mathcal{O}\left(\frac{1}{y_2^7}\right)\right), & \delta_1\mathrm{Re}(y_2)\mathrm{Im}(y_2) > 0. \end{cases}
\tag{7.69}
$$

Consider $\delta_1 = 1$ (Cases 1 and 2), and $y_2 = a + ib$ in the first or third quadrant. Using the appropriate expansion from (7.69), the system of ODEs (7.41) describing the elliptic contours becomes

$$
\begin{aligned}
a' &= -2\delta_2 b,\\
b' &= -2\delta_2 a,
\end{aligned}
$$

149

where $' = d/d\tau$. Eliminating τ and integrating gives the set of hyperbola (7.43). On the other hand, for y_2 in the second or third quadrant, (7.41) becomes

$$a' = -\frac{\delta_2}{2|y_2^3|^2}(b^3 - 3a^2b),$$

$$b' = -\frac{\delta_2}{2|y_2^3|^2}(a^3 - 3ab^2).$$

Eliminating τ gives

$$\frac{db}{da} = \frac{a(a^2 - 3b^2)}{b(b^2 - 3a^2)}. \tag{7.70}$$

Utilising the substitution $b = av$, $\frac{db}{da} = v + a\frac{dv}{da}$, equation (7.70) transforms to

$$a\frac{dv}{da} = \frac{1 - v^4}{v^3 - 3v},$$

which is separable. Thus

$$a + C = \int \frac{v^3}{1 - v^4} dv - \frac{3}{2} \int \left(\frac{v}{1 - v^2} + \frac{v}{1 + v^2} \right) dv,$$

$$= \frac{1}{2} \ln(1 - v^2) - \ln(1 + v^2),$$

$$\Rightarrow C_1 a^2 = \frac{1 - v^2}{(1 + v^2)^2}, \tag{7.71}$$

where $C_1 = e^{2C}$. Substituting $v = b/a$ into (7.71) and rearranging leads to the set of Lemniscate curves (7.42). Note that for $\delta_1 = -1$ (Cases 3 and 4), the conditions in (7.69) switch, but the resulting families of asymptotic curves are the same as those obtained for $\delta_1 = 1$. $\qquad\square$

H   Proof of Proposition 7.9

Proof. Let $F(y_2) = \int_\Gamma \Lambda_1(z) dz$, where we have suppressed the $\delta_{1,2}$ and α_2 dependence in Λ_1 for ease of notation. Like Λ_1, F is analytic everywhere except at the pole $(y_{2,p} = 0)$, and along the branch cuts (see Figure 7.8). We can write F as the sum of its real and imaginary parts

$$F(a + ib) = H(a, b) + iG(a, b),$$

where the functions H and G are defined as

$$H(a, b) = Re\left(\int_\Gamma \Lambda_1(z) dz \right),$$

$$G(a, b) = Im\left(\int_\Gamma \Lambda_1(z) dz \right).$$

Since F is analytic, it must satisfy the Cauchy-Riemann equations, and the complex derivative is given by

$$\frac{dF}{dy_2} = H_a + iG_a, \tag{7.72}$$

$$= H_a - iH_b.$$

From the fundamental theorem of calculus, we know that

$$\frac{dF}{dy_2} = \Lambda_1(z). \tag{7.73}$$

Comparing (7.72) and (7.73), we find that

$$H_a = Re\Lambda_1(z),$$
$$H_b = -Im\Lambda_1(z).$$

Substituting the above into (7.41) gives the Hamiltonian system

$$a' = H_b,$$
$$b' = -H_a.$$

$\square$

I Proof of Proposition 7.10

Proof. To calculate the growth rate, first note that

$$\lambda_{1,2} = z \mp i\sqrt{1-z^2},$$
$$= Re(z) \pm Im(\sqrt{1-z^2}) + i[Im(z) \mp Re(\sqrt{1-z^2})],$$

where $z = -\delta_1\gamma$, and $\gamma = \alpha_2 - y_2^2$. Then

$$-i\lambda_2\overline{\lambda}_1 = -i\left(Re(-\delta_1\gamma) - Im(\sqrt{1-\gamma^2}) + i\left[Im(-\delta_1\gamma) + Re(\sqrt{1-\gamma^2})\right]\right) \times$$
$$\left(Re(-\delta_1\gamma) + Im(\sqrt{1-\gamma^2}) - i\left[Im(-\delta_1\gamma) - Re(\sqrt{1-\gamma^2})\right]\right),$$
$$\Rightarrow Re(-i\lambda_2\overline{\lambda}_1) = \left(Im(-\delta_1\gamma) + Re(\sqrt{1-\gamma^2})\right)\left(Re(-\delta_1\gamma) + Im(\sqrt{1-\gamma^2})\right) -$$
$$\left(Re(-\delta_1\gamma) - Im(\sqrt{1-\gamma^2})\right)\left(Im(-\delta_1\gamma) - Re(\sqrt{1-\gamma^2})\right),$$
$$= -2\delta_1\left[Re(\gamma)Re(\sqrt{1-\gamma^2}) + Im(\gamma)Im(\sqrt{1-\gamma^2})\right],$$
$$\Rightarrow Im(-i\lambda_2\overline{\lambda}_1) = -\left[Re(\gamma)^2 + Im(\gamma)^2 - Re(\sqrt{1-\gamma^2})^2 - Im(\sqrt{1-\gamma^2})^2\right],$$
$$= \sqrt{1-\gamma^2}\overline{\sqrt{1-\gamma^2}} - \gamma\overline{\gamma}.$$

Finally, note that these real and imaginary parts need to be multiplied by $\varphi\overline{\varphi} = 1/(a^2 + b^2)$. $\square$

J Proof of Proposition 7.11

Proof. We wish to calculate the sign of

$$\Omega = -\frac{2\delta_1}{a^2 + b^2}\omega(\gamma),$$

in different regions of complex (a, b)-plane, where

$$\omega(y) := Re(\gamma)Re(\sqrt{1-\gamma^2}) + Im(\gamma)Im(\sqrt{1-\gamma^2}).$$

Clearly $1/(a^2 + b^2)$ is positive for all $a, b \in \mathbb{R}$, and it does not affect the sign of Ω. Now, using Lemmas 4.4 and 4.5 in [66], we know that

1. If $y = \alpha + i\beta$ is in the first quadrant, then $\omega(y) > 0$.
2. If $y = \alpha + i\beta$ is in the second quadrant, then $\omega(y) < 0$.

Replacing y with $\gamma = \alpha_2 - y_2^2 = \alpha_2 - (a + ib)^2$, we

$$\alpha = \text{Re}(\gamma) = \alpha_2 - (a^2 - b^2),$$
$$\beta = \text{Im}(\gamma) = -2ab.$$

Hence we have the following results:

1. If $y_2 = a + ib$ is in the second quadrant and $a^2 - b^2 < \alpha_2$, then $\alpha, \beta > 0$ and $\omega(\gamma) > 0$;
2. If $y_2 = a + ib$ is in the second quadrant and $a^2 - b^2 > \alpha_2$, then $\alpha < 0$, $\beta > 0$ and $\omega(\gamma) < 0$;
3. If $y_2 = a + ib$ is in the fourth quadrant and $a^2 - b^2 < \alpha_2$, then $\alpha, \beta > 0$ and $\omega(\gamma) > 0$;
4. If $y_2 = a + ib$ is in the fourth quadrant and $a^2 - b^2 > \alpha_2$, then $\alpha < 0$, $\beta > 0$ and $\omega(\gamma) < 0$.

Note that sgn $\Omega = -\text{sgn}\,(\delta_1\omega)$ and that due to the $\mathbb{Z}_2$-symmetry in y_2, we can obtain the sign of Ω in the first and third quadrants.

$\square$

K Proof of Proposition 7.13

Proof. We can make (7.51) integrable by multiplying through by an integrating factor $\exp(V(\tau, \tau_0))$, where

$$V(\tau, \tau_0) = \begin{pmatrix} \frac{i}{\sqrt{\varepsilon}} \int_{\tau_0}^{\tau} \Lambda_1(\sigma)\overline{\Lambda}_1(\sigma)d\sigma & 0 \\ 0 & \frac{i}{\sqrt{\varepsilon}} \int_{\tau_0}^{\tau} \Lambda_2(\sigma)\overline{\Lambda}_1(\sigma)d\sigma \end{pmatrix}.$$

Notice that

$$\exp(V(\tau, \tau_0)) = \Phi(\tau_0, \tau),$$

where Φ is the transition matrix, or fundamental solution matrix. Multiplying (7.51) by the integrating factor, we obtain

$$\sqrt{\varepsilon}U\Phi(\tau_0, \tau) - A(\tau)\Phi(\tau_0, \tau) = G(U, \tau)\Phi(\tau_0, \tau), \tag{7.74}$$

where $A(\tau)$ is the linear part of (7.51), i.e.

$$A(\tau) = \begin{pmatrix} -i\Lambda_1\overline{\Lambda}_1 & 0 \\ 0 & -i\Lambda_2\overline{\Lambda}_1 \end{pmatrix}.$$

Recall that the transition matrix has several useful properties: $\Phi(0,0) = I$, $\Phi^{-1}(\tau_0, \tau) = \Phi(\tau, \tau_0)$ and $\Phi(\tau, \tau_0)\Phi(\tau_0, \sigma) = \Phi(\tau, \sigma)$. Solving equation (7.74) leads to the solution

$$\frac{d}{d\tau}\left(\sqrt{\varepsilon}\Phi(\tau_0, \tau)U\right) = G(U, \tau)\Phi(\tau_0, \tau),$$

$$\Rightarrow \Phi(\tau_0, \tau)U(\tau) = \Phi(\tau_0, 0)U(0) + \frac{1}{\sqrt{\varepsilon}}\int_0^\tau G(U, \sigma)\Phi(\tau_0, \sigma)d\sigma,$$

$$\Rightarrow U(\tau, U_0) = U_0\Phi(\tau, 0) + \frac{1}{\sqrt{\varepsilon}}\int_0^\tau G(U, \sigma)\Phi(\tau, \sigma)d\sigma,$$

where $\tau_0 = 0$. □

Chapter 8

Conclusion and Future Work

In this thesis, we combined techniques from geometric singular perturbation theory (GSPT) and averaging to analyse torus canards and related problems in neural models. Torus canards are a relatively new phenomenon, which were first discovered in a model of neuronal activity in cerebellar Purkinje cells [60]. They are special solutions that follow a repelling manifold of periodic orbits of the layer problem for a significant amount of time and can be viewed as the averaged counterparts of canards. The main contribution of this thesis is two-fold. Firstly, we developed novel numerical averaging techniques that allow for a more precise study of torus canards, and oscillatory solutions in general, in singularly perturbed neural models. Secondly, our rigorous blow-up analysis of a novel FSN bifurcation (type III) expands current theory on the existence and behaviour of canards. We now provide a detailed summary of the main contributions and implications of this work with regards to each chapter. We also discuss open questions and future directions.

8.1 The Wilson-Cowan-Izhikevich Model

The Wilson-Cowan-Izhikevich (WCI) model is an extended version of the Wilson-Cowan model [113], first proposed by Izhikevich [54]. For a range of parameter values, the WCI model exhibits fold/fold-cycle bursting. Burke et al. [18] studied the WCI model in the fold/fold bursting regime, and numerically identified torus canards. Via a sequence of full system simulations, the authors demonstrated the existence of a torus canards explosion through the bursting to spiking transition. Finally, the authors also provided a two-parameter continuation of the layer problem bifurcation structures, thereby identifying parameter regimes corresponding to other types of bursting. Based on an averaged normal form, Vo [104] numerically identified the toral folded singularity responsible for the explosion and provided a continuation in two-parameter space that demarcated the singular limit bursting and spiking regions.

Like [104], our numerical methods enabled the identification and continuation of the toral folded singularity with respect to two system parameters. However, we were also able to continue equilibria of the averaged reduced system. Thus we improved on the work of Burke et al. and Vo by providing a complete two-parameter continuation of the averaged reduced structures in the WCI model. Our study focused on the fold/fold-cycle

bursting regime where torus canards were found. We showed that the transition from bursting to spiking occurred via a sequence of torus canards in an exponentially small parameter window (i.e. a torus canard explosion). However, the WCI model also exhibits fold/hopf and fold/homoclinic bursting in other parameter regimes. Desroches et al. [30] showed that complex bursting patterns known as canards of mixed type (CMT) occur at the transition from fold/hopf-cycle bursting to a state of fixed activity. Our numerical continuation methods could be used to identify the exact region in the (k, r_x)-plane where CMTs occur in the WCI model. From a more general point of view, numerical averaging may provide new insights into CMT and other types of bursting behaviour in a variety of neural models.

8.2 The Butera Model

The second model studied in this thesis, formulated by Butera et al. [20, 21], describes two synaptically coupled neurons in the pre-Bötzinger complex. Neurons in this region of the brainstem are essential to respiratory rhythm generation in mammals. While the single neuron version of the model exhibits fold/homoclinic (square wave) bursting, coupling with a second identical neuron produces fold/fold (top hat) bursting for a range of parameter values. Butera and colleagues showed that model neurons can exhibit quiescent, spiking and bursting behaviour. Furthermore, they used direct simulations on a grid to establish the regions in (g_{ton}, g_{syn}) parameter space where bursting occurred. Best et al. [11] refined this analysis by identifying additional types of bursting and spiking regimes of the two-neuron model. By combining geometric singular perturbation theory and averaging, Best et al. [11] formulated an averaged reduced model which they analysed. Numerical simulations were used to track nullclines of the averaged reduced system and identify intersections, i.e. averaged equilibria. By varying parameter values, they approximated boundary curves in (g_{ton}, g_{syn}) space which separated qualitatively different averaged reduced problem features, and corresponding solutions of the full system.

Our study builds on past work in several ways. Using numerical continuation in the software package AUTO [34], we identified and continued various bifurcations of the full two neuron model in (g_{ton}, g_{syn}) parameter space for the first time. Away from the weak coupling regime $g_{syn} \leq 1$, our numerical analysis established the connection between certain full system bifurcations and the transitions between different activity patterns. In particular, we found that some bifurcations were directly correlated with transitions, for example, the pitchfork bifurcation marked the transition between asymmetric and symmetric spiking. Other bifurcations, such as the two torus bifurcations, only approximately indicated the region where transitions occurred. Compared to earlier simulations, our full system continuation results provide an improved understanding of the boundaries in parameter space which mark the transitions between observed activity patterns. Furthermore, we also identified activity patterns near the bursting to spiking transition that were previously missed. Examples include amplitude modulate spiking and bursting, both hallmarks of torus canard behaviour [107].

In an effort to better understand the dynamic mechanisms responsible for activity patterns and transitions between them, we turned our attention to the averaged reduced system studied by Butera et al. While past analysis of this subsystem relied on numerical simula-

tions, we implemented a numerical continuation scheme in AUTO to locate and continue the averaged equilibria with respect to a system parameter. Subsequent bifurcation diagrams allowed us to identify the averaged reduced structures connected with each activity pattern of the full model. Our numerical methods also enabled the identification and continuation of toral folded singularities. This approach led to the new observation that the averaged equilibria and folded singularities interact in various folded saddle-node (FSN) bifurcations. We identified three different types of FSN bifurcations: type I, II and III. The FSN type III, a pitchfork bifurcation of two folded singularities and an ordinary singularity, arises due to the symmetry induced by coupling two identical neurons in the Butera model. To the best of our knowledge, this type of FSN bifurcation is novel and identified for the first time in our work. It remains to find more examples of the FSN III in other neural models.

Similar to the WCI model, we identified torus canards near the spiking to bursting transition in the Butera model. The transition occurs near a supercritical torus bifurcation of the full system, which corresponds to the FSN II bifurcation of the averaged reduced system. Unlike the WCI model, the Butera model has two slow variables; the addition of a second slow variable results in generic torus canards that occur on open parameter intervals. In the full system, the transition begins at the supercritical torus bifurcation, which gives birth to a phase space torus attractor, as shown in return maps. The attracting torus generates amplitude modulated spiking solutions. Under variation of g_{ton}, the torus quickly breaks down, and the system transitions to bursting via complex amplitude modulated bursting trajectories. We also identified a second (subcritical) torus bifurcation in the full Butera model that is associated with the FSN III, and approximates the symmetric to asymmetric bursting transition. As the torus bifurcation is supercritical, and we cannot numerically continue nearby quasi-periodic bursting solutions, little is known about how the bifurcation actually facilitates the transition.

Many more open problems have arisen from our study of the Butera model. Based on our full system analysis (and the canonical model – see the following section) we expect the pitchfork (PF), FSN II and FSN III bifurcations to coalesce at a codimension-two bifurcation. Ideally, we would like to construct a two-parameter bifurcation diagram of the averaged reduced system to further support this. In theory, the FSN II and III should be flagged by AUTO as bifurcations during the one-parameter continuation of averaged equilibria (a Floquet multiplier crosses the unit circle when the averaged equilibria interact with the SNPO). This would easily enable continuation in two parameters. Although AUTO's built in algorithms compute the Floquet multipliers, it fails to flag the the FSN II or III bifurcation. This problem can be circumvented by implementing the variational equation and explicitly calculating the Floquet multiplier μ_2, as was done in the toral folded singularity continuation (see Section 3.5.4). The FSN I, a saddle-node of two folded singularities, is far more problematic as it doesn't involve any equilibria. Althoughwe computed the FSN I for fixed values of g_{syn} corresponding to Cases 1-6, it remains to formally check via continuation if this bifurcation interacts with any other curves in the two-parameter continuation away from the organising centre (e.g., in the strong coupling regime).

Very little is understood about the weak coupling regime. As g_{syn} decreases, excursions away from the $h_1 = h_2$ symmetry axis in the asymmetric bursting regime become shorter and shorter. As such, it becomes increasingly difficult to qualitatively distinguish symmetric and asymmetric bursting. Furthermore, there seems to be a limited correlation between some

156

full system bifurcation curves and the transitions between activity patterns in the weak coupling regime. Although we can continue averaged reduced structures from $g_{syn} > 1$ into the weak coupling region, due to numerical difficulties, we cannot directly compute the averaged equilibria or folded singularities for $g_{syn} \lesssim 1$. Naturally, there may be equilibria or folded singularities that only exist in this region, which we have missed. Shedding light on the intricate dynamics of the weak coupling regime may require an altogether different approach.

8.3 Canonical Model of the Organising Centre

Our investigation of the Butera model identified four important codim-1 bifurcations, PF, FSN II, FSN III, and SN, as well as three related codim-2 bifurcations, PF–SN, FSN II–SN, and PF–FSN II–FSN III. Due to the proximity of the codim-2 points in (g_{ton}, g_{syn}) parameter space, we hypothesised that these three bifurcations were in fact the unfolding of a higher codimension bifurcation, the so-called organising centre. To support this theory, we formulated a canonical model, which comprised all the necessary bifurcations in the averaged reduced system. We found that the canonical system dynamics were consistent with the activity patterns observed in the full Butera model and it's associated averaged reduced system. We also identified paths in parameter space which corresponded to paths between activity patterns (under parameter variation) in the Butera model. Our results validate the GSPT/averaging analysis of the Butera model. While we identified a codim-3 bifurcation of the canonical model where all three codim-2 bifurcations coalesced, we did not provide any further analysis. A detailed blow-up of the canonical model, and in particular the codim-3 point, still needs to be tackled.

8.4 Folded Saddle-Node Type III

Folded node and folded saddle canards have been studied extensively in $\mathbb{R}^3$. Codimension-one bifurcations of folded singularities, folded saddle-nodes (FSN), come in three varieties. The FSN type I corresponds to a true saddle-node bifurcation of a folded node and folded saddle. The FSN type II corresponds to a transcritical bifurcation of an ordinary singularity (or equilibria) and a folded singularity. The third type, the FSN III, arises due to symmetry: it is a pitchfork bifurcation of two folded singularities and an ordinary singularity. The FSN I and II are common in neural applications and can generate complex behaviour. Both can play a role in the creation of MMO patterns [12, 46, 45, 13]. The FSN II is the dynamic unfolding of the 2D singular Andronov-Hopf bifurcation, which mediates the transition from small amplitude oscillations to relaxation oscillations in planar singularly perturbed systems [37, 64]. On the other hand, the FSN III is novel and was discovered in our study of the Butera model.

The local dynamics near the FSN I and FSN II limit has been analysed, and the existence of canards has been proven in both cases [108, 66]. Using a similar approach to past work, we performed a partial blow-up of the FSN III singularity and analytically extended the system into the complex plane. Using elliptic contours and other properties of the complexified system, we proved the existence of $\mathcal{O}(\sqrt{\varepsilon})$ canards and faux canards as intersections of

stable and unstable invariant manifolds. These canard solutions rotated about the primary weak canard of the folded node (Cases 1 and 4), or the primary faux canards of the folded saddle (Cases 2 and 3). Similar to the other FSN bifurcations, the FSN III gave rise to delay phenomena. Using a way-in/way-out function, we calculated maximal and minimal delay estimates. Like the FSN II, we showed that the FSN III possessed a pole in the complexified system which impacted the delay estimates. The positioning of this pole relative to attracting and repelling manifolds created some interesting points of difference with the other two cases. For example, trajectories with initial conditions sufficiently close to the pole experience an 'infinite delay', i.e. they trace the length of an infinite repelling manifold, having only tracked the attracting manifold for a finite amount of time. This sort of behaviour is not possible in the FSN I and II.

While our study of the novel FSN III is an important addition to the growing compendium of canard theory, it is by no means a complete analysis. Recent work [76, 78] has expanded our understanding of folded saddle canards and their behaviour. In particular, the authors identify new types of secondary folded saddle faux canards, characterise their rotational behaviour, and detail numerical methods for computing them. In addition, the authors also demonstrate how the secondary faux canards can generate complex dynamics near the FSN I limit in various neural models. As Cases 2 and 3 of the FSN III possess two folded saddles, it could be worthwhile to consider the dynamics of various secondary faux canards near the FSN III limit.

References

[1] V. Afraimovich and L. Shilnikov, *Invariant two-dimensional tori, their breakdown and stochasticity, methods of the qualitative theory of differential equations,,* Gos. Univ., Gorki, (1983), pp. 3–26.

[2] V. Afraimovich and L. P. Shilnikov, *Invariant two-dimensional tori, their breakdown and stochasticity,* Amer. Math. Soc. Transl, 149 (1991), pp. 201–212.

[3] A. Algaba, E. Freire, E. Gamero, and A. Rodrìguez-Luis, *A three-parameter study of a degenerate case of the hopf-pitchfork bifurcation,* Nonlinearity, 12 (1999), pp. 1177–1206.

[4] R. Ayoub, *The Lemniscate and Fagnano's Contributions to Elliptic Integrals,* Archive for history of Exact Sciences, 29 (1984), pp. 131–149.

[5] S. M. Baer and T. Erneux, *Singular Hopf bifurcation to relaxation oscillations II,* SIAM Journal on Applied Mathematics, 52 (1992), pp. 1651–1664.

[6] G. N. Benes, A. M. Barry, T. J. Kaper, M. A. Kramer, and J. Burke, *An elementary model of torus canards,* Chaos, 21 (2011).

[7] E. Benoît, J. L. Callot, Diener, Francine, and M. Diener, *Chasse au canards,* I-IV, Collect. Math, 32 (1981), pp. 37–119.

[8] N. Berglund and B. Gentz, *Noise-induced phenomena in slow-fast dynamical systems: a sample-paths approach,* Springer Science & Business Media, 2006.

[9] J. Bernoulli, *Curvatura laminae elasticae,* Acta eruditorum, 13 (1694), pp. 262–276.

[10] R. Bertram, M. J. Butte, T. Kiemel, and A. Sherman, *Topological and phenomenological classification of bursting oscillations,* Bulletin of mathematical biology, 57 (1995), pp. 413–439.

[11] J. Best, A. Borisyuk, J. Rubin, D. Terman, and M. Wechselberger, *The dynamic range of bursting in a model respiratory pacemaker network,* SIAM Journal on Applied Dynamical Systems, 4 (2005), pp. 1107–1139.

[12] K. Bold, C. Edwards, J. Guckenheimer, S. Guharay, K. Hoffman, J. Hubbard, R. Oliva, and W. Weckesser, *The forced van der Pol equation II: Canards in the reduced system,* SIAM Journal on Applied Dynamical Systems, 2 (2003), pp. 570–608.

[13] B. BRAAKSMA, *Singular hopf bifurcation in systems with fast and slow variables*, Journal of Nonlinear Science, 8 (1998), pp. 457–490.

[14] R. BRETTE AND W. GERSTNER, *Adaptive exponential integrate-and-fire model as an effective description of neuronal activity*, Journal of neurophysiology, 94 (2005), pp. 3637–3642.

[15] M. BRØNS, T. J. KAPER, AND H. G. ROTSTEIN, *Introduction to focus issue: Mixed mode oscillations: Experiment, computation, and analysis*, Chaos, 18 (2008), pp. 67–70.

[16] M. BRØNS, M. KRUPA, AND M. WECHSELBERGER, *Mixed mode oscillations due to the generalized canard phenomenon*, Fields Institute Communications, 49 (2006), pp. 39–63.

[17] N. BRUNEL AND M. C. VAN ROSSUM, *Lapicque's 1907 paper: From frogs to integrate-and-fire*, Biological Cybernetics, 97 (2007), pp. 337–339.

[18] J. BURKE, M. DESROCHES, A. M. BARRY, T. J. KAPER, AND M. A. KRAMER, *A showcase of torus canards in neuronal bursters*, The Journal of Mathematical Neuroscience, 2 (2012), p. 3.

[19] J. BURKE, M. DESROCHES, A. GRANADOS, T. J. KAPER, M. KRUPA, AND T. VO, *From canards of folded singularities to torus canards in a forced van der Pol equation*, Journal of Nonlinear Science, 26 (2016), pp. 405–451.

[20] R. J. BUTERA, J. RINZEL, AND J. C. SMITH, *Models of respiratory rhythm generation in the pre-Bötzinger complex. I. Bursting pacemaker neurons*, Journal of Neurophysiology, 82 (1999), pp. 382–397.

[21] ——, *Models of respiratory rhythm generation in the pre-Bötzinger complex. II. Populations of coupled pacemaker neurons*, Journal of Neurophysiology, 82 (1999), pp. 398–415.

[22] R. J. BUTERA, J. RUBIN, D. TERMAN, AND J. SMITH, *Oscillatory bursting mechanisms in respiratory pacemaker neurons and networks*, Bursting: the genesis of rhythm in the nervous system, (2005), pp. 303–347.

[23] R. BUTERA JR., J. CLARK JR., AND J. BYRNE, *Transient responses of a modeled bursting neuron: Analysis with equilibrium and averaged nullclines*, Biological Cybernetics, 77 (1997), pp. 307–322.

[24] C.-T. CHEN, *Linear system theory and design*, Oxford University Press, Inc., 3rd ed., 1998.

[25] R. CURTU AND J. RUBIN, *Interaction of canard and singular Hopf mechanisms in a neural model*, SIAM Journal on Applied Dynamical Systems, 10 (2011), pp. 1443–1479.

[26] G. Cymbalyuk and A. Shilnikov, *Coexistence of tonic spiking oscillations in a leech neuron model*, Journal of Computational Neuroscience, 18 (2005), pp. 255–263.

[27] C. A. Del Negro, C.-F. Hsiao, S. H. Chandler, and A. Garfinkel, *Evidence for a novel bursting mechanism in rodent trigeminal neurons*, Biophysical journal, 75 (1998), pp. 174–182.

[28] C. A. Del Negro, C. G. Wilson, R. J. Butera, H. Rigatto, and J. C. Smith, *Periodicity, mixed-mode oscillations, and quasiperiodicity in a rhythm-generating neural network*, Biophysical Journal, 82 (2002), pp. 206–214.

[29] Z. Denkowska and R. Roussarie, *A method of desingularization for analytic two-dimensional vector field families*, Boletim da Sociedade Brasileira de Matemática, 22 (1991), pp. 93–126.

[30] M. Desroches, J. Burke, T. J. Kaper, and M. A. Kramer, *Canards of mixed type in a neural burster*, Physical Review E, 85 (2012), pp. 1–6.

[31] M. Desroches, J. Guckenheimer, B. Krauskopf, C. Kuehn, H. M. Osinga, and M. Wechselberger, *Mixed-mode oscillations with multiple time scales*, SIAM Review, 54 (2012), pp. 211–288.

[32] F. Diener and M. Diener, *Chasse au canard. I. Les canards*, Collect. Math, 32 (1981), pp. 37–74.

[33] M. Diener, *The canard unchained or how fast/slow dynamical systems bifurcate*, The Mathematical Intelligencer, 6 (1984), pp. 38–49.

[34] E. J. Doedel, T. F. Fairgrieve, B. Sandstede, A. R. Champneys, Y. A. Kuznetsov, and X. Wang, *AUTO-07P: Continuation and bifurcation software for ordinary differential equations*, 2007.

[35] E. J. Doedel, B. W. Kooi, Y. A. Kuznetsov, and G. A. K. Van Voorn, *Continuation of connecting orbits in 3D-ODEs: (II) Cycle-to-cycle connections*, International Journal Of Bifurcation And Chaos, 19 (2008), pp. 159–169.

[36] F. Dumortier, *Techniques in the theory of local bifurcations: Blow-up, normal forms, nilpotent bifurcations, singular perturbations*, in Bifurcations and periodic orbits of vector fields, D. Schlomiuk, ed., vol. 408, Springer Science & Business Media, 1993, pp. 19–73.

[37] F. Dumortier and R. H. Roussarie, *Canard cycles and center manifolds*, American Mathematical Soc., 1996.

[38] W. Eckhaus, *Relaxation oscillations including a standard chase on french ducks*, Asymptotic Analysis II, (1983), pp. 449–494.

[39] B. Ermentrout and M. Wechselberger, *Canards, clusters, and synchronization in a weakly coupled interneuron model*, SIAM Journal on Applied Dynamical Systems, 8 (2009), pp. 253–278.

[40] N. Fenichel, *Geometric singular perturbation theory for ordinary differential equations*, Journal of Differential Equations, 31 (1979), pp. 53–98.

[41] N. Fenichel and J. Moser, *Persistence and smoothness of invariant manifolds for flows*, Indiana University Mathematics Journal, 21 (1971), pp. 193–226.

[42] G. Floquet, *Sur les équations différentielles linéaires à coefficients périodiques*, Annales scientifiques de l'École normale supérieure, 12 (1883), pp. 47–88.

[43] P. A. Gray, W. A. Janczewski, N. Mellen, D. R. McCrimmon, and J. L. Feldman, *Normal breathing requires pre-Bötzinger complex neurokinin-1 receptor-expressing neurons*, Nature neuroscience, 4 (2001), pp. 927–30.

[44] R. E. Griffiths and M. Pernarowski, *Return map characterizations for a model of bursting with two slow variables*, SIAM Journal on Applied Mathematics, 66 (2006), pp. 1917–1948.

[45] J. Guckenheimer, *Singular Hopf bifurcation in systems with two slow variables*, SIAM Journal on Applied Dynamical Systems, 7 (2008), pp. 1355–1377.

[46] J. Guckenheimer, K. Hoffman, and W. Weckesser, *The forced van der Pol equation I: The slow flow and its bifurcations*, SIAM Journal on Applied Dynamical Systems, 2 (2003), pp. 1–35.

[47] J. Guckenheimer and P. J. Holmes, *Nonlinear oscillations, dynamical systems, and bifurcations of vector fields*, Springer Science & Business Media, 2013.

[48] I. Gucwa and P. Szmolyan, *Geometric singular perturbation analysis of an autocatalator model*, Discrete and Continuous Dynamical Systems - Series S, 2 (2009), pp. 783–806.

[49] X. Han and Q. Bi, *Slow passage through canard explosion and mixed-mode oscillations in the forced Van der Pol's equation*, Nonlinear Dynamics, 68 (2012), pp. 275–283.

[50] E. Harvey, V. Kirk, M. Wechselberger, and J. Sneyd, *Multiple timescales, mixed mode oscillations and canards in models of intracellular calcium dynamics*, Journal of Nonlinear Science, 21 (2011), pp. 639–683.

[51] M. Hayes, T. Kaper, P. Szmolyan, and M. Wechselberger, *Geometric desingularization of degenerate singularities in the presence of fast rotation: A new proof of known results for slow passage through Hopf bifurcations*, Indagationes Mathematicae, 27 (2016), pp. 1184–1203.

[52] V. A. Iakubovich and V. M. Starzhinskii, *Linear differential equations with periodic coefficients*, vol. 1, Wiley, 1975.

[53] N. Inaba, Y. Nishio, and T. Endo, *Chaos via torus breakdown from a four-dimensional autonomous oscillator with two diodes*, Physica D: Nonlinear Phenomena, 240 (2011), pp. 903–912.

[54] E. M. Izhikevich, *Neural excitability, spiking and bursting*, International Journal of Bifurcation and Chaos, 10 (2000), pp. 1171–1266.

[55] E. M. Izhikevich, *Dynamical systems in neuroscience*, MIT press, 2007.

[56] C. Jones, *Geometric singular perturbation theory*, in Dynamical systems, Springer, Berlin Heidelberg, 1995, pp. 44–118.

[57] L. V. Kibiuk, D. Stuart, M. Miller, et al., *Brain facts: A primer on the brain and nervous system*, The Society For Neuroscience, 2008.

[58] B. W. Knight, *Dynamics of encoding in a population of neurons*, The Journal of General Physiology, 59 (1972), pp. 734–766.

[59] I. Kosiuk and P. Szmolyan, *Scaling in singular perturbation problems: blowing up a relaxation oscillator*, SIAM J. Appl. Dyn. Syst., 10 (2009), pp. 1307–1343.

[60] M. A. Kramer, R. D. Traub, and N. J. Kopell, *New dynamics in cerebellar purkinje cells: Torus canards*, Physical Review Letters, 101 (2008), p. 068103.

[61] B. Krauskopf and T. Riess, *A Lin's method approach to finding and continuing heteroclinic connections involving periodic orbits*, Nonlinearity, 21 (2008), pp. 1655–1690.

[62] B. Krauskopf and C. Rousseau, *Codimension-three unfoldings of reflectionally symmetric planar vector fields*, Nonlinearity, 10 (1997), p. 1115.

[63] M. Krupa and M. Brøns, *Extending slow manifolds near transcritical and pitchfork singularities*, Nonlinearity, 14 (2001), pp. 1473–1491.

[64] M. Krupa and P. Szmolyan, *Extending geometric singular perturbation theory to nonhyperbolic points – fold and canard points in two dimensions*, SIAM Journal on Mathematical Analysis, 33 (2001), pp. 286–314.

[65] M. Krupa and P. Szmolyan, *Relaxation oscillation and canard explosion*, Journal of Differential Equations, 174 (2001), pp. 312–368.

[66] M. Krupa and M. Wechselberger, *Local analysis near a folded saddle-node singularity*, Journal of Differential Equations, 248 (2010), pp. 2841–2888.

[67] C. Kuehn, *From first Lyapunov coefficients to maximal canards*, International Journal of Bifurcation and Chaos, 20 (2010), pp. 1467–1475.

[68] ——, *Multiple time scale dynamics*, vol. 191, Springer, 2015.

[69] A. Kuznetsov, S. Kuznetsov, E. Mosekilde, and N. Stankevich, *Generators of quasiperiodic oscillations with three-dimensional phase space*, The European Physical Journal Special Topics, 222 (2013), pp. 2391–2398.

[70] Y. A. Kuznetsov, *Elements of applied bifurcation theory*, vol. 112, Springer Science & Business Media, 2013.

[71] J. Lagrange, *Mécanique analytique (2 vols.), edition Albert Blanchard*, 1788.

[72] L. Lapique, *Recherches quantitatifs sur l'excitation des nerfs traitee comme une polarisation*, J Physiol Pathol Gen, 9 (1907), pp. 620–635.

[73] D. A. McCormick and H.-C. Pape, *Properties of a hyperpolarization-activated cation current and its role in rhythmic oscillation in thalamic relay neurones.*, The Journal of physiology, 431 (1990), pp. 291–318.

[74] J. D. Meiss, *Differential dynamical systems*, Society for Industrial and Applied Mathematics, 2007.

[75] E. Mishchenko and N. K. Rozov, *Differential equations with small parameters and relaxation oscillations (translated from russian)*, Plenum Press, (1980).

[76] J. Mitry, *A geometric singular perturbation approach to neural excitability*, PhD thesis, University of Sydney, Australia, 2016.

[77] J. Mitry, M. McCarthy, N. Kopell, and M. Wechselberger, *Excitable neurons, firing threshold manifolds and canards*, The Journal of Mathematical Neuroscience, 3 (2013), p. 12.

[78] J. Mitry and M. Wechselberger, *Folded saddles and faux canards*, SIAM Journal on Applied Dynamical Systems, 16 (2017), pp. 546–596.

[79] A. I. Neishtadt, *Persistence of stability loss for dynamical bifurcations I*, Differential Equations, 23 (1987), pp. 1385–1393.

[80] ——, *Persistence of stability loss for dynamical bifurcations II*, Differential Equations, 24 (1988), pp. 171–176.

[81] L. G. Nowak, R. Azouz, M. V. Sanchez-Vives, C. M. Gray, and D. A. McCormick, *Electrophysiological classes of cat primary visual cortical neurons in vivo as revealed by quantitative analyses*, Journal of neurophysiology, 89 (2003), pp. 1541–1566.

[82] I. Parasyuk and B. Repeta, *Hyperbolic invariant tori of a fast-slow system with dynamic bifurcation of multifrequency oscillations*, Journal of Mathematical Sciences, 3 (2017), pp. 312–335.

[83] L. Pontryagin and L. Rodygin, *Approximate solution of a system of ordinary differential equations involving a small parameter using derivatives*, Soviet Math. Dokl., 1 (1960), pp. 237–240.

[84] J. C. Rekling and J. L. Feldman, *Pre-bötzinger complex and pacemaker neurons: hypothesized site and kernel for respiratory rhythm generation*, Annual review of physiology, 60 (1998), pp. 385–405.

[85] J. Rinzel, *Bursting oscillations in an excitable membrane model*, in Ordinary and partial differential equations, Springer, 1985, pp. 304–316.

[86] ——, *A formal classification of bursting mechanisms in excitable systems*, in Mathematical topics in population biology, morphogenesis and neurosciences, Springer, 1987, pp. 267–281.

[87] K.-L. Roberts, J. E. Rubin, and M. Wechselberger, *Averaging, folded singularities, and torus Canards: explaining transitions between bursting and spiking in a coupled neuron model*, SIAM Journal on Applied Dynamical Systems, 14 (2015), pp. 1808–1844.

[88] H. G. Rotstein, M. Wechselberger, and N. Kopell, *Canard induced mixed-mode oscillations in a medial entorhinal cortex layer II stellate cell model*, SIAM Journal on Applied Dynamical Systems, 7 (2008), pp. 1582–1611.

[89] R. Roussarie, *Techniques in the theory of local bifurcations: cyclicity and desingularization*, in Bifurcations and Periodic Orbits of Vector Fields, D. Schlomiuk, ed., Springer Science & Business Media, 1993, pp. 347–382.

[90] J. Rubin and M. Wechselberger, *Giant squid-hidden canard: The 3D geometry of the Hodgkin-Huxley model*, Biological Cybernetics, 97 (2007), pp. 5–32.

[91] ——, *The selection of mixed-mode oscillations in a Hodgkin-Huxley model with multiple timescales*, Chaos, 18 (2008).

[92] J. a. Sanders, F. Verhulst, and J. Murdock, *Averaging methods in nonlinear dynamical systems*, vol. 59, Springer Science & Business Media, 2nd ed., 2007.

[93] A. Shilnikov, *Complete dynamical analysis of a neuron model*, Nonlinear Dynamics, 68 (2012), pp. 305–328.

[94] A. Shilnikov and M. Kolomiets, *Methods of the qualitative theory for the hindmarsh–rose model: A case study–a tutorial*, International Journal of Bifurcation and chaos, 18 (2008), pp. 2141–2168.

[95] J. C. Smith, H. H. Ellenberger, K. Ballanyi, D. W. Richter, and J. L. Feldman, *Pre-Bötzinger complex : a brainstem region that may generate respiratory rhythm in mammals*, Science, 254 (1991), pp. 726–729.

[96] P. Smolen, D. Terman, and J. Rinzel, *Properties of a bursting model with two slow inhibitory variables*, SIAM J. Appl. Math., 53 (1993), pp. 861–892.

[97] M. Steriade, *Neuronal substrates of sleep and epilepsy*, Cambridge University Press, 2003.

[98] R. Straube, D. Flockerzi, and M. J. B. Hauser, *Sub-Hopf/fold-cycle bursting and its relation to (quasi-)periodic oscillations*, Journal of Physics: Conference Series, 55 (2006), pp. 214–231.

[99] P. Szmolyan and M. Wechselberger, *Canards in $\mathbb{R}^3$*, Journal of Differential Equations, 177 (2001), pp. 419–453.

[100] P. Szmolyan and M. Wechselberger, *Relaxation oscillations in $\mathbb{R}^3$*, Journal of Differential Equations, 200 (2004), pp. 69–104.

[101] W. Teka, J. Tabak, T. Vo, M. Wechselberger, and R. Bertram, *The dynamics underlying pseudo-plateau bursting in a pituitary cell model.*, Journal of mathematical neuroscience, 1 (2011), pp. 1–23.

[102] A. Tikhonov, *On the dependence of the solutions of differential equations on a small parameter*, Matematicheskii sbornik, 64 (1948), pp. 193–204.

[103] B. Van der Pol, *Lxxxviii. on relaxation-oscillations*, The London, Edinburgh, and Dublin Philosophical Magazine and Journal of Science, 2 (1926), pp. 978–992.

[104] T. Vo, *Generic torus canards*, Physica D: Nonlinear Phenomena, (2017).

[105] T. Vo, R. Bertram, and M. Wechselberger, *Bifurcations of canard-induced mixed mode oscillations in a pituitary lactotroph model*, Discrete and Continuous Dynamical Systems, 32 (2012), pp. 2879–2912.

[106] ——, *Multiple geometric viewpoints of mixed mode dynamics associated with pseudo-plateau bursting*, SIAM Journal on Applied Dynamical Systems, 12 (2013), pp. 789–830.

[107] T. Vo, M. A. Kramer, and T. J. Kaper, *Amplitude-modulated bursting: A novel class of bursting rhythms*, Physical Review Letters, 117 (2016), pp. 1–5.

[108] T. Vo and M. Wechselberger, *Canards of folded saddle-node type I*, SIAM Journal on Mathematical Analysis, 47 (2015), pp. 3235–3283.

[109] M. Wechselberger, *Extending Melnikov theory to invariant manifolds on non-compact domains*, Dynamical Systems, 17 (2002), pp. 215–233.

[110] ——, *Existence and bifurcation of canards in $\mathbb{R}^3$ in the case of a folded dode*, SIAM Journal on Applied Dynamical Systems, 4 (2005), pp. 101–139.

[111] ——, *À propos de canards (Apropos canards)*, Transactions of the American Mathematical Society, 364 (2012), pp. 3289–3309.

[112] M. Wechselberger, J. Mitry, and J. Rinzel, *Canard theory and excitability*, in Nonautonomous dynamical systems in the life sciences, 2013, pp. 89–132.

[113] H. R. Wilson and J. D. Cowan, *Excitatory and inhibitory interactions in localized populations of model neurons*, Biophysical Journal, 12 (1972), pp. 1–24.

[114] J. Wojcik and A. Shilnikov, *Voltage interval mappings for activity transitions in neuron models for elliptic bursters*, Physica D: Nonlinear Phenomena, 240 (2011), pp. 1164–1180.